Population of Obscured Active Galactic Nuclei

a thesis submitted

in partial fulfilment of the requirements

for the degree of

Doctor of Philosophy

by

Abhijit Kayal

(Roll No. 17330003)

under the supervision of

Dr. Veeresh Singh

Assistant Professor

Astronomy & Astrophysics Division

Physical Research Laboratory, Ahmedabad, India

Department of Physics

INDIAN INSTITUTE OF TECHNOLOGY GANDHINAGAR

2023

Dedicated to my Maa,

Smt. Kalyani Kayal

who gave all the little she had, so that I could explore the infinite!

DECLARATION

I, **Abhijit Kayal (Roll No: 17330003)**, hereby declare that, this thesis titled **"Population of Obscured Active Galactic Nuclei"** submitted to the Indian Institute of Technology Gandhinagar towards partial fulfilment for the award of **Doctor of Philosophy** in **Physics** is an original work carried out by me under the supervision of **Dr. Veeresh Singh** at the Physical Research Laboratory, Ahmedabad, India. I have sincerely tried to uphold the academic ethics and honesty. Whenever an external information or statement, or result is used, every effort is made to indicate this clearly, with due reference to the literature.

July, 2023

Abhijit Kayal

CERTIFICATE

This is to certify that, the work presented in this thesis titled **"Population of Obscured Active Galactic Nuclei"** submitted by **Abhijit Kayal** (**Roll No: 17330003**) to the Indian Institute of Technology, Gandhinagar, has been carried out by him under my supervision, and it has not been submitted elsewhere for the award of any degree/diploma.

July, 2023

Dr. Veeresh Singh

(Thesis Supervisor)

Assistant Professor

Astronomy & Astrophysics Division

Physical research Laboratory

Ahmedabad, India

ACKNOWLEDGEMENT

Throughout the five years of my research, I learnt many times and realised that doing a PhD is a marathon, not a race. Many times I felt like I was sprinting, fueled by the high of my complex codes and script working; going several days even though multiple times errors in running codes tried to put a break on me (challenges excite me even more). And many other times, I felt exhausted, frustrated and out of breath, wondering if I really could make it to the finish line. Well, I have completed the marathon, and I could not make it possible without having constantly encouraging and supportive people around me who have trained me and cheered for me along the way. I take this opportunity to acknowledge them and extend my humble and sincere gratitude for helping me to make this thesis a possibility.

The first name, I would like to place on record and thank my research supervisor, Dr. Veeresh Singh, for providing me with a healthy environment where I could work as an independent researcher. You made me realize how much I had learned and made me feel empowered in my ability to learn independently. You have always been extremely supportive, and have been particularly understanding about receiving last-minute emails and reading over the past few months. Words cannot express my gratitude to you for your invaluable patience, help and feedback. For every new idea in this thesis, I owe you a lot. Additionally, this endeavour would not have been possible without the generous support from my institute Physical Research Laboratory (PRL) and the Indian Institute of Technology, Gandhinagar (IIT GN), who financed and facilitated my research.

I also could not have undertaken this journey without the collaborators Prof. C. H. Ishwara Chandra, Prof. Yogesh Wadadekar , Prof. Santosh Vadawale, Mr. N.P.S. Mithun, Prof. Gulab Dewangan and Prof. Poshak Gandhi, who generously provided knowledge and expertise. I would like to express my deepest gratitude and appreciation to Prof. Claudio Ricci for always being very helpful and responding swiftly to my queries whenever I was stuck.

I am also grateful to my Doctoral Studies Committee (DSC) members - Prof. Santosh Vadawale, Dr. Mudit Srivastava and Dr. Bhalamurugan Sivaraman, for examining my research progress and for their suggestions regarding my work and future plans throughout my PhD tenure. I sincerely thank the Academic Committee for their rigorous annual reviews and valuable feedback. I acknowledge the support I received from my coursework instructors - Dr. Veeresh Singh, Dr. Mudit K. Srivastava, Prof. Shashikiran Ganesh, Dr. Lokesh Kumar Dewangan, Dr. Vishal Joshi, Dr. Aveek Sarkar, Dr. Arvind Singh Rajpurohit and Prof. Sachindra Naik, who gave me a basic understanding of Astronomy and Astrophysics. I am also thankful to the Director of PRL, Prof. Anil Bhardwaj. Thanks should also go to the librarians, research assistants, and study participants from the PRL, who impacted and inspired me. You all have added meaning to my PhD experience in different ways.

I would like to thank "The Committee on Space Research" (COSPAR) for providing me with an opportunity to attend the workshop on X-ray astronomy held in IISER Mohali. I would specially thank Prof. Keith Arnaud and Prof. Matteo Guainazzi who taught me X-ray data reduction and data analysis. I would also like to acknowledge Radio Astronomy School (RAS) at NCRA, Pune, where I learnt radio interferometry and observational techniques. I also learnt how to reduce and analyse radio data, especially from the Giant Metrewave Radio Telescope (GMRT). I thank all the staff of the GMRT for providing us with GMRT observations. Next, I acknowledge that I have used data from the AstroSat mission of the Indian Space Research Organization (ISRO), archived at the Indian Space Science Data Centre (ISSDC). Also, I made use of *Chandra* and *XMM-Newton* archives, the HEASARC website for X-ray archival data and Software, NASA's Astrophysics Data System and the NASA/IPAC Extragalactic Database (NED) in my research work. I also used data obtained with the LOw Frequency ARray (LOFAR) and with the Very Large Array (VLA).

Thank you to the wonderful people - my batchmates - Sushant Dutta and Vipin Kumar for their editing help, late-night help, and moral support. It would be a miss if I do not mention my office mates, Sushant, Vipin, my juniors; Naval and Arup with whom I always enjoyed interactions, fun time and indoor games. Thank you to everyone who I have connected within a group: my batchmates and friends - Abhay Kumar, Neeraj Kumari, Biswajit Mondal, Shanwlee Sow Mondal, Aravind K; my seniors - Parveen Kumar, JNHS Aditya, Sandeep Rout, Vineet Ojha; my juniors - Naval, Arup, Birendra, Akanksha, Namita; Other batchmates from different divisions and my hostel friends- Deepak, Vishal, Ramanuj, Sovan, Tanmay, Suraj, Sana, Milan, Ankit, Alka, Anshika, Sarika, Rituparna, Madhusudhan, Satyajeet, Kamlesh, Subith, Partha, Himanshu, Shivani, Atif, Amit, Hrushikesh. Many thanks to Pravin and Sudipta for becoming my family at the hostel and being my big supporter and caretaker in the ups and downs of my life, in my health issues during my PhD tenure. Hirdesh, even though we joined different divisions at PRL, we always stayed connected over phone. I was grateful to have my school friends- Shankhadeep Naskar and Priyabrata Sahoo; Special thanks to my college friend, the Physics expert, and a very good poet, Somajit Dey, for helping me to understand many concepts in physics and I had wonderful, entertaining moments while composing your extraordinary poems. I also thank my other college friends - Tanmoy Bar, Avik Paul and Apu Mondal. Thank you all for helping me on this journey.

I am extremely grateful to my Bengali and Physics teachers: Dr. Priyatosh Basu and Dr. Atishdipankar Jana. Without your teachings, training, guidance and blessings; I would not have reached such a higher level of academics and accomplished my thesis.

Most of my gratitude is reserved for my family. I would be remiss in not mentioning my family, especially my Maa, my brother Boro, and my younger sister Puja. You have always been there like a big banyan tree to protect me under your soothing shadow from social and any other issues so that I could focus on my research without any disturbances. You have always provided me with emotional, motivational and financial support to ensure that I do not have to suffer or struggle with anything. Your belief in me has kept my spirits and motivation high during my PhD. I am thankful to my parents-in-law for their care and for always giving homely feelings as I am away from my own home.

Lastly, I would like to thank the one special person in my life, my wife Ghazal, without whom not only this acknowledgement but also my life would not be complete. Thank you so much for your hardships behind me to keep me going on, to keep me motivated through my late working hours, for being my odd hours' proofreader, editor, my late-night discussion buddy and most of all for being my best friend. Thank you so much for everything, even though I know thank you is not enough.

Abhijit Kayal

ABSTRACT

Active Galactic Nuclei (AGN) are the manifestation of accretion onto the supermassive black holes (SMBHs) located at the centres of galaxies. AGN emit copiously across a wide range of wavelengths via various processes occurring in the material present around the accreting SMBHs. Moreover, the enormous radiative power in most AGN is often obscured by the gas and dust present in the circumnuclear environment and in the large-scale interstellar medium of the host galaxy. Thus, obscuration poses a challenge for uncovering the complete AGN population and understanding their cosmic evolution, in particular at high redshifts. The dust-obscured galaxies (DOGs), which are bright in the infrared wavelengths but relatively much faint in the optical wavelengths can be the potential hosts for obscured AGN. Due to the large content of dust and gas, the optical and UV emission from AGN gets heavily absorbed. Hence, optical and UV surveys can miss the AGN population residing in dusty environments. However, radio, infrared and X-ray surveys being less susceptible to absorption, can detect obscured AGN.

This thesis work delves into unveiling and understanding of a new population of AGN in DOGs using different observational techniques based on the deep radio, mid-IR and X-ray observations. Using deep radio observations from the upgraded Giant Metrewave Radio Telescope at 400 MHz, our study demonstrates that sensitive radio observations are one of the most efficient methods for detecting radio-emitting AGN residing in dusty environments. Our deep uGMRT observations have resulted in 29 per cent radio detection rate of DOGs, which is the highest among all the literature studies performed till date. With multi-frequency radio observations, we find that radio sources in DOGs are mainly compact steep spectra sources and peaked spectrum sources, which further infers that the radio sources are likely to be in the early phase of their evolution. Unlike our radio

observations, we find that deep XMM-Newton X-ray observations detect a much smaller fraction (8 per cent) of AGN and the detections are limited only to the X-ray luminous AGN.

We performed X-ray spectral modelling of 34 DOGs ($0.59 \leq z \leq 4.65$) using all the existing *XMM-Newton* data, and *Chandra*/ACIS data, whenever available in the XMM-SERVS extragalactic field. The X-ray spectra of our DOGs can be well described with an absorbed power law and reflection component. The column densities derived from the spectral modellings show that all but four of our DOGs are moderately obscured ($N_{\rm H} < 10^{23}$ cm^{-2}) and the fraction of heavily obscured DOGs is limited only to 11.7%. The high absorption corrected 2.0−10 keV X-ray luminosities ($10^{43} - 10^{45}$ erg s^{-1}) suggest for the presence of luminous AGN. The $N_{\rm H}$ versus Eddington ratio diagnostic plot infers that our DOGs represent a heterogeneous population containing Hot DOGs as well as reddened quasars. Only a few of our DOGs are likely to belong to an early phase (Hot DOGs) during which accretion and obscuration peak, while the remaining DOGs possibly belong to a late phase during which radiative feedback from the dominant AGN blows away obscuring material.

In order to constraint the geometry of the circumnuclear obscuring material, we performed a detailed study of the multi-epoch broadband spectra of the heavily obscured AGN hosted in the nearby Circinus galaxy. We utilised all the available hard X-ray (> 10 keV) observations taken at ten different epochs in the span of 22 years from 1998 to 2020 from *BeppoSAX*, *Suzaku*, *NuSTAR* and *AstroSat*. The 3.0-79 keV broadband X-ray spectral modelling using physically motivated models infers the presence of a torus viewed edge-on (inclination angle of 77°-81°) with a low covering factor of 0.28, and Compton-thick line-of-sight column densities ($N_{H,LOS} = 4.13{-}9.26 \times 10^{24}$ cm^{-2}) in all the epochs. The joint multi-epoch spectral modelling suggests that the overall structure of the torus is likely to remain unchanged. However, we find tentative evidence for the variable line-of-sight column density on time scales ranging from 1 day to 1 week to a few years, suggesting a clumpy circumnuclear material located at subparsec to tens of parsec scales.

List of Publications

1. **Abhijit Kayal**, Veeresh Singh, C.H. Ishwara Chandra, Yogesh Wadadekar and Sushant Dutta, 2022, "Detection of radio-AGN in dust-obscured galaxies using deep uGMRT radio continuum observations", *Journal of Astrophysics and Astronomy*, 43, 82, https://doi.org/10.1007/s12036-022-09873-0.

2. **Abhijit Kayal**, Veeresh Singh, Claudio Ricci, N. P. S. Mithun, Santosh Vadawale, Gulab Dewangan and Poshak Gandhi, 2023, "Multi-epoch hard X-ray view of Compton-thick AGN Circinus Galaxy" *Monthly Notices of the Royal Astronomical Society*, Volume 522, Issue 3, pp.4098-4115, https://doi.org/10.1093/mnras/stad1216.

3. **Abhijit Kayal** and Veeresh Singh, "X-ray spectral properties of dust-obscured galaxies in the XMM-SERVS region of XMM-LSS field" (*Submitted in Monthly Notices of the Royal Astronomical Society*).

Contributory

1. Sushant Dutta, Veeresh Singh, C.H. Ishwara Chandra, Yogesh Wadadekar, **Abhijit Kayal** and Ian Heywood, 2023, "Search and Characterization of Remnant Radio Galaxies in the XMM-LSS Deep Field", *The Astrophysical Journal*, Volume 944, Issue 2, id.176, 19 pp, https://iopscience.iop.org/article/10.3847/1538-4357/acaf01.

2. Sushant Dutta, Veeresh Singh, C.H. Ishwara Chandra, Yogesh Wadadekar and **Abhijit Kayal**, 2022, "Characteristics of Remnant Radio Galaxies Detected in the Deep Radio Continuum Observations from the SKA

Pathfinders", *Journal of Astrophysics and Astronomy*, 43, 96, https://doi.org/10.1007/s12036-022-09883-y.

List of Figures

List of Tables

Contents

List of Abbreviations

ACIS	Advanced CCD Imaging Spectrometer
ADAF	Advection-Dominated Accretion Flow
AIPS	Astronomical Image Processing System
AGN	Active Galactic Nuclei
ALMA	Atacama Large Millimeter Array
ASKAP	Australian SKA Pathfinder
B−DOG	Bump Dust-Obscured Galaxy
BLR	Broad Line Region
CALDB	Calibration Database
CASA	Common Astronomy Software Applications
CCD	Charge-Coupled Device
CIAO	Chandra Interactive Analysis of Observations
CMB	Cosmic Microwave Background
CNN	Convolutional Neural Network
CSM	Circum-Stellar Medium
CSO	Compact Symmetric Object
CSS	Compact Steep Spectrum

CT	Compton-Thick
CTI	Charge Transfer Inefficiency
CXC	Chandra X-ray Center
CZTI	Cadmium Zinc Telluride Imager
DB	Dirty Beam
DOG	Dust-Obscured Galaxy
e−MERLIN	enhanced Multi-Element Radio Linked Interferometer Network
EMU	Evolutionary Map of the Universe
EPIC	European Photon Imaging Camera
EVN	European VLBI Network
FWHM	Full Width Half Maximum
FIRST	Faint Images of the Radio Sky at Twenty-Centimeters
FoV	Field of View
FPM	Focal Plane Module
FIR	Far-Infrared
FR	Fanaroff & Riley
GMRT	Giant Meterwave Radio Telescope
GPS	GHz-Peaked-Spectrum
GTI	Good Time Interval
HEASARC	High Energy Astrophysics Science Archive Research Center
HFP	High-Frequency-Peaker
HLIRG	Hyper-Luminous Infrared Galaxy

HSC−SSP	Hyper Suprime−Cam Subaru Strategic Program
HXD	Hard X-ray Detector
IC	Inverse-Compton
IR	Infrared
IRAC	Infrared Array Camera
ISM	Inter-Stellar Medium
ISRO	Indian Space Research Organisation
ISSDC	Indian Space Science Data Centre
JWST	James Webb Space Telescope
JVLA	Jansky Very Large Array
LAXPC	Lrage-Area Porportional Counter
LINER	Low-Ionization Nuclear Emission Region
LIRG	Luminous Infrared Galaxy
LOFAR	LOw Frequency ARray
LOS	Line-Of-Sight
MECS	Medium Energy Concentrator Spectrometers
MEM	Maximum Entropy Method
MHD	Magneto-Hydrodynamics
MIDI	VLTI mid-infrared interferometric instrument
MIGHTEE	MeerKAT International GHz Tiered Extragalactic Exploration
MIPS	Multi-band Imaging Photometer for *Spitzer*
MIR	Mid-Infrared

MOS Metal-Oxide-Semiconductor

MPS MHz-Peaked-Spectrum

NLR Narrow Line Region

NRAO National Radio Astronomical Observatory

NuSTAR Nuclear Spectroscopic Telescope Array

NUSTARDAS NuSTAR Data Analysis Software

NVSS NRAO VLA Sky Survey

NXB Non X-ray Background

PDS Phoswich Detector System

PHA Pulse Height Amplitude

PL−DOG Power-law Dust-Obscured Galaxy

PRIMUS PRIsm MUlti-object Survey

PSF Point Spread Function

PyBDSF Python Blob Detector and Source Finder

RL Radio Loud

RQ Radio Quiet

RFI Radio Frequency Interference

SAS Science Analysis System

SMBH Supermassive Black Hole

SSC Synchrotron Self-Compton

SSA Synchrotron Self-Absorption

SKA Square Kilometer Array

SFG	Star-Forming Galaxy
SED	Spectral Energy Distribution
SNR	Signal-to-Noise Ratio
SWIRE	*Spitzer* Wide-area Infrared Extragalactic Survey
SXT	Soft X-ray Telescope
ULIRG	Ultra-Luminous Infrared Galaxy
ULX	Ultra-Luminous X-ray
UV	Ultraviolet
uGMRT	upgraded Giant Meterwave Radio Telescope
VIPERS	VIMOS Public Extragalactic Redshift Survey
VLASS	Very Large Array Sky Survey
VLBA	Very Long Baseline Array
VLBI	Very-Long-Baseline Interferometery
VLTI	Very Large Telescope Interferometer
VVDS	VIMOS-VLT Deep Survey
WISE	Wide-field Infrared Survey Explorer
XIS	X-ray Imaging Spectrometer
XMM	X-ray Mulit-Mirror Mission
XMM−LSS	XMM-*Newton* Large−Scale Structure
XMM−SERVS	XMM-*Spitzer* Extragalactic Representative Volume Survey

Chapter 1

Introduction

1.1 Active Galactic Nuclei (AGN)

Active Galactic Nuclei (AGN) are luminous compact cores of galaxies which emit radiation over the whole electromagnetic spectrum starting from radio to gamma rays. The main energy generation mechanism is the accretion of matter onto the supermassive black holes (Lyden-Bell, 1969; Pringle et al., 1973; Rees, 1984) producing a high luminosity ($L_{\rm bol} \approx 10^{42} - 10^{48}$ erg s^{-1}; Krolik, 1999) such that they often outshine their host galaxies. Observations in different wavelengths provide information about different aspects of AGN, *e.g.*, optical, UV and X-ray continuum arise from the accretion processes, infrared (IR) traces the circum-nuclear dust content and radio emission comes from the jet and lobes. Thus, multiwavelength studies trace different morphological components of AGN. In the following section, we provide a brief description of AGN components. For a better understanding, we show various AGN components in Figure 1.1.

1.2 AGN components

1.2.1 Supermassive black hole

Supermassive black hole (SMBH) is one of the fundamental components of AGN. It is widely accepted that every massive galaxy contains SMBHs ($M_{SMBH} \sim 10^6 - 10^{10} M_\odot$) at their centres (Kormendy & Richstone, 1995; Magorrian et al., 1998; Greene et al., 2008; Kormendy & Ho, 2013; Koss et al., 2017). Various studies suggest that tight correlations between the mass of SMBHs and galaxy properties (*e.g.*, mass and the luminosity of the host galaxy bulge, stellar velocity dispersion) exist (Richstone et al., 1998; Kormendy & Gebhardt, 2001; Merritt & Ferrarese, 2001; McConnell & Ma, 2013; Kormendy & Ho, 2013), which indicates the co-evolution of galaxy and SMBH growth. The nuclear activity is triggered due to the large inflow of matters towards the SMBH (Hopkins et al., 2006), inducing the rapid black hole growth, which in turn affects the galaxy evolution through feedback processes. The galaxies hosting highly luminous ($L_{\rm bol} \gtrsim 10^{42}$ erg s^{-1}) accreting SMBHs are commonly termed as 'active galaxies'.

1.2.2 Accretion disk

The infalling matter onto SMBH possesses non-zero angular momentum, hence it does not fall directly onto the SMBH due to the conservation of angular momentum. Instead, the infalling matter forms a rotating disk-like geometry known as accretion disk, oriented perpendicular to the direction of angular momentum (Lyden-Bell, 1969; Pringle et al., 1972; Shakura & Sunyaev, 1973). The gravitational potential energy of the infalling matter gets converted into heat through turbulence, viscosity and magnetic processes which cause emission of radiation from the accretion disk (Pringle et al., 1973; Rees, 1984).

The energy released due to the accretion of mass m at a distance R from a black hole of mass M can be expressed as,

$$\Delta E = \frac{GMm}{R} \tag{1.1}$$

The luminosity associated with the energy released can be expressed as (Longair, 2011),

$$L = \frac{GM\dot{m}}{R} = \epsilon \dot{m} c^2 \tag{1.2}$$

where, $\dot{m}$ is the mass accretion rate. $\epsilon = GM/Rc^2$, is related to the efficiency of conversion of mass into radiation in the accretion process which depends on the black hole spin. The value ϵ is 0.06 for a non-rotating Schwarzschild black hole, while it increases to 0.42 in case of a maximally rotating Kerr black hole (Eardley & Press, 1975; Pringle, 1981; Shapiro et al., 1983; Longair, 2011). The maximum efficiency achieved in case of nuclear fusion is only $\epsilon \sim 0.007$ (Davis & Laor, 2011). Thus, accretion onto SMBH is a more efficient process of mass to energy conversion and it is considered to be the main emission mechanism of AGN which was first proposed by Lyden-Bell (1969). The accretion disk in AGN has a typical temperature of $T \approx 10^4 - 10^5$ K (Longair, 2011; Netzer, 2013) yielding thermal emission in the optical and UV wavebands, which are responsible for the observed "big blue bump" in the SED of AGN (Shields, 1978; Malkan, 1983). In the literature, there are several proposed models which describe different kinds of accretion flows For instance, the Advection-Dominated Accretion Flow (ADAF) model is proposed for an optically-thin accretion disk accreting at sub-Eddington rate (Narayan & Yi, 1994) as well as an optically-thick accretion disk accreting at super-Eddington rate (Abramowicz et al., 1988).

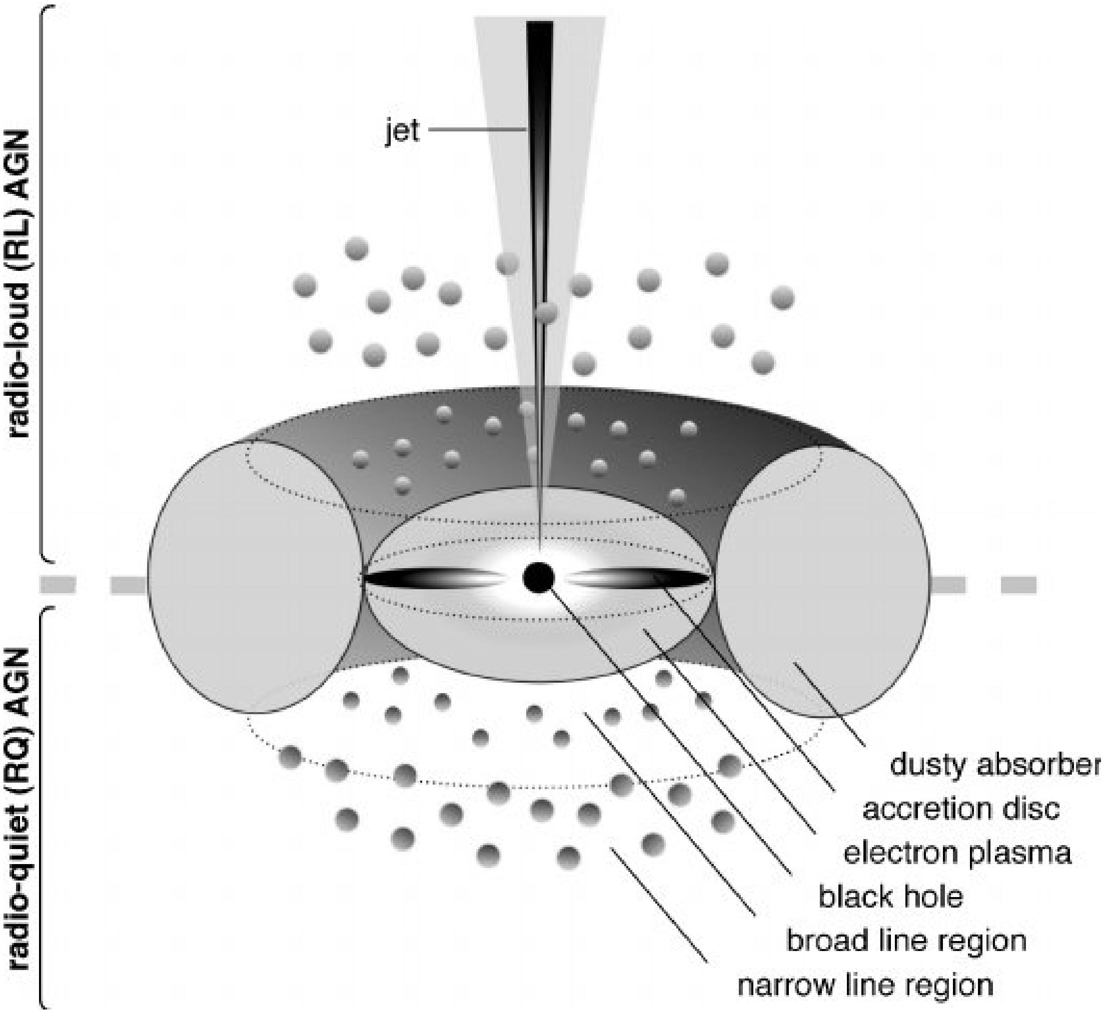

Figure 1.1: A schematic representation of AGN components. This is a cartoon image and not to scale. Courtesy: Marie-Luise Menzel.

1.2.3 Hot corona

The X-ray spectra of AGN showing a power-law continuum suggest for the presence of a hot plasma region named corona, located at the innermost regions near the SMBH (Haardt & Maraschi, 1991; Haardt et al., 1994). The high temperature of the corona ($\sim 10^8$ K, Netzer, 2013) is thought to be due to the deposition of a significant fraction of accretion energy in the corona (Haardt et al., 1994). However, the formation process, geometry and the location of the corona are still not very well understood. Studies based on the microlensing variability of strongly lensed quasars (Chartas et al., 2009, 2016) and X-ray reverberation showing lags between the direct X-ray continuum and their reflection from the accretion disk (Fabian et al., 2009; Kara et al., 2016; De Marco & Ponti, 2019) suggest for a compact X-ray emitting region of the order of a few tens of gravitational radii (Reis & Miller, 2013). There are several models available in the literature that suggest different geometries for the corona, *e.g.*, a hot layer of optically thin plasma located above the accretion disk (two phase model; Haardt & Maraschi, 1991; Haardt et al., 1994), a compact X-ray source located on the black hole spin axis (the lamp-post model; Matt et al., 1991; Miniutti & Fabian, 2004), patchy corona model (Wilkins & Gallo, 2015).

The power-law continuum emitted from the corona interacts with circumnuclear region (*e.g.*, accretion disk, broad line region and torus) and gives rise to a reflection component. In the circumnuclear material, low energy (< 10 keV) X-ray photons suffer photoelectric absorption while high energy (> 10 keV) photons suffer Compton down-scattering which in turn produces a hump-like feature (known as Compton hump) at around ~ 30 keV in the X-ray spectrum (see Figure 1.2).

1.2.4 Broad-line and narrow-line regions

One of the characteristic features of the AGN spectra is the presence of broad and narrow emission lines (Barthel et al., 1990). The different line widths lead to the conclusion that the regions responsible for giving rise to such emission lines have different physical properties, *e.g.*, geometry, velocity and density. In the following subsections, we briefly discuss about these regions.

1.2.4.1 Broad-line region (BLR)

The optical and UV spectra of AGN show prominent broad emission lines, *e.g.*, Lyα 1216Å, Hα 6563Å, Hβ 4861Å, C IV 1548Å, 1551Å, Mg II 2796Å, 2804Å and multiplets of Fe II (Krolik, 1999; Tang et al., 2012). Along with the allowed transition lines, semi-forbidden lines (*e.g.*, C III] λ1909Å, C II] λ2326Å etc) are also observed. The typical widths ($5000 - 10000$ km s^{-1}) of broad emission lines (Peterson, 2006) are explained by the Doppler effect wherein the line emitting clouds present in a region named as 'broad-line region' (BLR) orbit around SMBH (see Gaskell, 2009, for a review on BLR). The absence of the forbidden lines places a lower limit on the BLR gas density. The typical gas density of the BLR is found to be $\sim 10^9$ cm^{-3}. The broad emission lines are originated due to the photo-ionization of the BLR gas (Stein & Weedman, 1976; Osterbrock, 1978) by the UV continuum emission arising from the accretion disk (Bahcall et al., 1972; Davidson & Netzer, 1979). The photo-ionization is balanced by the recombination, thus making the BLR gas to be in photo-ionization equilibrium (Peterson, 2006). It is found that a typical temperature of $T \approx 10^4$ K is required for the photo-ionized gas in BLR to achieve photo-ionization equilibrium (Ghisellini, 2013).

The extent of BLR is estimated from a technique called 'reverberation mapping', which utilizes the fact that due to the finite size of the BLR, there would be a time delay for the variations in the emission lines to show up in response to the changes in the ionizing continuum (see Peterson, 2008, for more discussion on reverberation mapping). The time delay is determined as, $\tau = R_{\rm BLR}/c$, where, $R_{\rm BLR}$ is the size of the BLR and c is the speed of light. The typical size of the BLR scales from light days ($\sim 10^{16}$ cm) to light weeks ($\sim 10^{16} - 10^{17}$ cm) for low luminosity AGN and extends to light years ($\gtrsim 10^{17}$ cm) for high luminosity AGN (10^{44} erg s^{-1}) (Kaspi et al., 2000; Hoormann et al., 2019).

1.2.4.2 Narrow-line region (NLR)

In addition to the broad emission lines, the optical spectra of most AGN also show narrow emission lines, which include permitted emission lines, *e.g.*, Hi, Hei, Heii as well as forbidden emission lines, *e.g.*, [Nev] 3426Å, [NeIII] 3869Å, [OII] 3727Å, [OIII] 4959Å, 5007Å, [NII] 6548Å, 6583Å, [SII] 6716Å, 6731Å(Peterson, 1997). The line widths ($\Delta v_{\rm FWHM}$) of the narrow emission lines lies within a range of $200-900$ km s^{-1}, much smaller as compared to broad emission lines, suggesting that the narrow-line region (NLR) resides far away from the central SMBH. Further, the presence of forbidden emission lines suggests that the density of the NLR should be much lower, having a typical value of $n_e \approx 10^2 - 10^4$ cm^{-3} (Osterbrock & Ferland, 2006). The temperature of the NLR gas falls in the range $10000 - 25000$ K with a typical value of $T_{\rm e} \approx 16000$ K (Peterson, 1997).

The extent of the NLR can be determined from the correlation between the NLR size and the luminosities of the strong emission lines, *e.g.*, [OIII], and is found to be spread across $\sim 100 - 1000$ pc. Due to such a large extent, NLR is usually resolved in the visible wavelengths revealing an axisymmetric morphology which appears as a biconical region (Tadhunter & Tsvetanov, 1989) having opening angles in the range $\sim 30^\circ - 100^\circ$ (Bennert et al., 2006; Peterson et al., 2013). The sharp edges of the cone are formed due to the collimated radiation from AGN and an obscuring structure called 'torus' around it. In the next Section 1.2.5, I describe obscuring torus.

1.2.5 Torus

The existence of torus was proposed to explain the spectropolarimetric observations of NGC 1068, a type 2 AGN, showing the presence of broad emission lines in the polarised light which were otherwise absent in the optical spectra of type 2 AGN (Antonucci & Miller, 1985). Later on, more observations favoured the presence of a geometrically thick, axisymmetric dusty molecular structure namely torus, surrounding the central region of AGN hiding the SMBH, accretion disk and BLR (the unification model; Antonucci, 1993; Urry & Padovani, 1995; Ramos Almeida & Ricci, 2017). Thus, the torus causes obscuration of the direct emission from the BLR as well as the central region (*e.g.*, accretion disk, corona). The torus has a typical gas density of $10^4 - 10^7$ cm^{-3} moving with Keplerian velocities of 1000 km s^{-1} as suggested by the interpolation between BLR and NLR. From X-ray observations, obscuration in the torus can be quantified in terms of equivalent hydrogen column density ($N_{\rm H}$) and is usually found in the range of 10^{22} cm^{-2} - 10^{24} cm^{-2} and even larger (Singh et al., 2011; Ricci et al., 2017a).

High resolution mid-IR imaging (Packham et al., 2005; Elitzur & Shlosman, 2006) and sub-mm interferometric observations (Combes et al., 2019; Alonso-Herrero et al., 2019) have been performed for some nearby AGN. These observations are able to spatially resolve torus and constrain its size to a few parsec. The classical picture of the torus was assumed to be composed of smooth and homogeneous distribution of dust (Efstathiou & Rowan-Robinson, 1995; Fritz et al., 2006), however more recent studies suggest for a clumpy torus (Nenkova et al., 2008; Hönig & Kishimoto, 2010). In this thesis, I present a detailed study of the circumnuclear environment around AGN in Circinus galaxy demonstrating evidence in supporting clumpy torus (see Chapter 5).

1.2.6 Jets and lobes

Some AGN show extended radio emission, which originates from the nuclear region and extends up to large distances of hundreds of kpc. These AGN, termed as radio galaxies, show a pair of highly collimated 'jets' which terminate into cocoons of plasma named as 'lobes'. The jet-lobe structure prominently seen at radio wavelengths is also present in other classes of AGN but often appears small in size due to the orientation or evolutionary effects (Padovani et al., 2017). The AGN jets are known to be collimated, outflowing high energetic plasma moving with a relativistic speed (Rees, 1971). In general, bipolar jets emanating from the central region of AGN in the two opposite directions are likely to be oriented in the direction perpendicular to the plane of accretion (Blandford & Rees, 1974; Wiita, 1978). Due to the relativistic speed, jets create shock waves at the edges of the lobes and form bright and compact regions at the edges of lobes (Begelman & Cioffi, 1989; Kaiser & Alexander, 1997) which are known as hotspots (Swarup et al., 1984). Jets also suffer deceleration via interaction with the interstellar as well as intergalactic medium and eventually gets diffuse to form lobes.

The AGN jets emit radiation across radio to γ-rays. The radio emission is produced via non-thermal Synchrotron emission, where the high energetic particles gyrate in the magnetic field. On the other hand the higher energy X-rays to γ-rays are thought to be produced via inverse Compton emission (IC), where the low energy photons get upscattered by the relativistic particles in the jet, and thus, gain energy and radiate at higher frequencies. The low energy photons that get upscattered could be radio photons generated in situ via Synchrotron emission (Synchrotron Self-Compton; Maraschi et al., 1992; Bloom & Marscher, 1996) or could be external photons such as from the Cosmic Microwave Background (CMB) (Dermer & Schlickeiser, 1993).

The mechanisms responsible for jet launching and collimation are not well understood. Most of the theoretical models suggest that the magneto-hydrodynamic (MHD) processes are responsible for launching the relativistic jets. Also, jet launching mechanisms involve the energy extraction from the spinning SMBH (Blandford-Znajek mechanism, Blandford & Znajek, 1977) where the magnetic field lines get dragged due to the rotating black hole and the matter gets accelerated along the field lines. The jet can also extract energy from the accretion disk which is responsible for generating the magnetic field lines (Blandford-Payne mechanism, Blandford & Payne, 1982). A detailed review on AGN-jets can be found in Blandford et al. (2019).

1.3 Obscuration around AGN

Obscuration plays an important role in our understanding about the growth of SMBHs and their connections to the cosmological evolution of galaxies hosting them. The presence of a large amount of matter in the circumnuclear environment is responsible for AGN obscuration. The inflow of the same matter on to the SMBH also fuels AGN activity. Earlier studies suggested that the AGN obscuration can be explained by a single parsec-scale obscuring torus (Antonucci & Miller, 1985; Urry & Padovani, 1995; Matt et al., 1997; Guainazzi et al., 2005; Noguchi et al., 2010; Mateos et al., 2017). However, there are an increasing amount of evidence, coming from mostly X-ray and IR observations, suggest that obscuration on different spatial scales, including multiple obscuring regions is likely to exist around SMBH (Davies et al., 2007; Ballantyne, 2008; Alexander

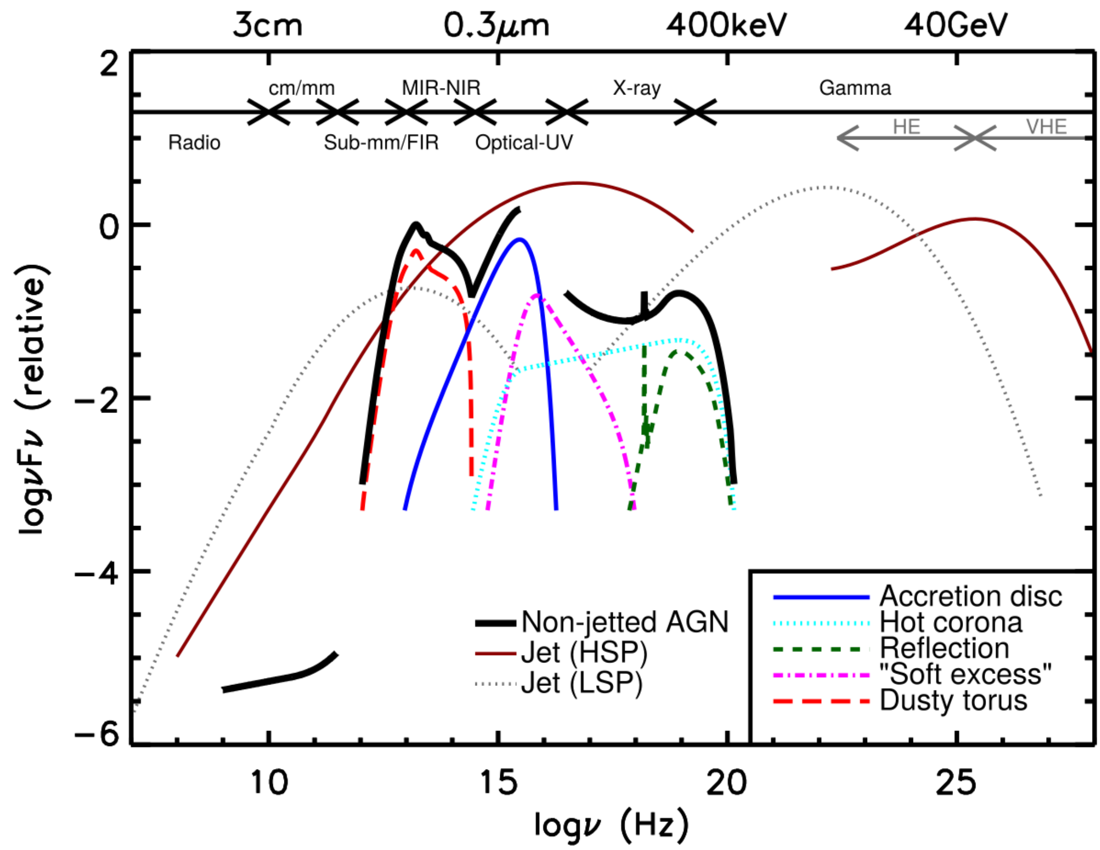

Figure 1.2: A schematic representation of the spectral energy distribution (SED) of different types of AGN. The SEDs are shown for a high Synchrotron peaked blazar (HBL; based on Mrk 421 SED) and a low Synchrotron peaked blazar (LBL; based on 3C 454.3 SED). The black solid curve represents the total emission and the various coloured curves represent the individual components. This image is adapted from Bianchi et al. (2022).

& Hickox, 2012). In major galaxy-mergers, a large amount of obscuring matter is expected to be present at even larger scales ($\approx$ 100 parsec to several kpc) for some sight lines. Thus, obscuration can be expected over a wide range of regions extending from sub-parsec to kpc.

Obscuration can also occur due to the larger scale material spread across the entire galaxy ($\sim$ 1 kpc). The merger-induced evolutionary picture suggests that the presence of a large amount of dust and gas on a galaxy-scale could lead to the triggering of nuclear activity (Hopkins et al., 2008; Alexander & Hickox, 2012) and an obscured AGN. Studies of heavily obscured luminous AGN suggested for a close association of the nuclear triggering with the major mergers (Cooke et al., 2019). However, it is still not well understood whether the large-scale dust and gas associated with the mergers are indeed responsible for obscuration of AGN in such systems.

1.4 Motivation

It has been well known that optical, UV and even X-ray observations tend to miss obscured AGN as their dusty environments absorb these emissions (Della Ceca et al., 2015; Vito et al., 2018). The thesis work aims to unveil a new population of AGN residing in dust-obscured galaxies (DOGs) that are bright in the mid-IR but faint in the optical (see Section 3.1 for more details). By utilising deep radio and X-ray surveys in the *XMM-Newton* Large Scale Structure survey (XMM-LSS) field, we identify and constrain the fraction of AGN hosted in DOGs. We also attempt to understand the nature of AGN residing in obscured environments, by examining various properties such as radio sizes, radio luminosities, radio spectra, MIR colours, X-ray hardness ratios, X-ray luminosities and X-ray absorbing column densities. We use the stacking technique to detect radio emission in DOGs that remained undetected in our uGMRT and VLA radio observations. Notably, we reveal the presence of radio emission in the stacked images suggesting the possible existence of AGN in DOGs that couldn't be detected due to the limited sensitivity of our observations (Chapter 3). Thus, our work presented in the thesis acts as a test-bed for future upcoming deeper radio surveys. For AGN with relatively bright X-ray emission ($F_{0.5-10\ \rm keV} \geq 10^{-13}$ erg s^{-1} cm^{-2}) we characterize their X-ray spectral properties with an aim to constrain their absorbing column density (Chapter 4). To probe the changes in column density and geometry of obscuring material, we performed a detailed study of the nearby Compton-Thick AGN (CT-AGN $N_{\rm H,\ LOS} \geq 10^{24}$ cm^{-2}; Comastri, 2004) in the Circinus galaxy using multi-epoch hard X-ray observations (Chapter 5). The motivations for our work presented in the thesis are outlined as below.

- The large reservoirs of gas and dust in galaxies absorb the optical and UV emission arising from the AGN and re-radiate it at IR wavelengths. Hence, the AGN population residing in dusty galaxies can be missed by the optical and UV surveys. It is unclear that what fraction of DOGs host AGN and what is their nature. Radio emission is insensitive to the dust-obscuration, and hence, radio observations can be used to unveil the population of radio AGN residing in dust-obscured galaxies.

- In principle, observations in a single wave band can miss to identify the complete AGN population. For instance, radio-quiet AGN with nearly insignificant radio emission can be missed even in deep radio observations. Hence, in addition to deep radio observations, we also use deep *XMM-Newton* survey and *Spitzer* MIR observations to obtain a complete census of AGN in dust-obscured galaxies.

- We point out that the previous radio studies of DOGs have been limited mainly to the radio-powerful sources or suffer from the shallow flux density limits of radio surveys. For instance, Gabányi et al. (2021) studied the radio properties of 661 DOGs with the FIRST survey and found only 2 per cent sources of their sample, exclusively power law (PL) DOGs, detected in the FIRST with 5σ sensitivity limited to 1.0 mJy beam^{-1}. Therefore, recent deep radio observation with 5σ sensitivity of $0.1 - 0.15$ mJy beam^{-1} have the potential to unveil a new population of AGN, even in the relatively faint DOGs at higher redshifts ($z > 1.0$).

- The radiative feedback from rapidly accreting AGN in dusty environments is poorly understood. Hence, the study of X-ray luminous AGN hosted in DOGs can offer us better insights into the rapid evolution of the early phase of quasars. The deep X-ray observations can allow us to obtain an accurate measurement of absorbing column density and the intrinsic absorption-corrected luminosity. Further, it can enable us to place constraints on the geometry and location of the obscuring media.

- Despite a large number of studies, the location, geometry, and physical state of the obscuring material are still widely debated even in the nearby CT-AGN. To constrain the geometry of circumnuclear obscuring media, we attempt to model the multi-epoch broad-band X-ray spectra of the nearby AGN in the Circinus galaxy.

1.5 Thesis Organisation

The structure of the thesis is outlined as follows.

Chapter 2: Radio and X-ray observational techniques and telescopes

This chapter describes observational techniques, telescopes and our observations in the radio and X-ray domains. I have given a detailed description of the radio synthesis imaging and standard data reduction procedure for radio continuum imaging. The brief details of uGMRT and VLA radio interferometers are also provided. Further, I have elaborated upon the X-ray observational techniques, spectral modelling, and data reduction procedure. I have also provided a brief description of various X-ray telescopes (*Chandra*, *XMM-Newton*, *NuSTAR* and *AstroSat*) from which data are used to study the X-ray spectral properties of our sample sources and Circinus galaxy.

Chapter 3: Detection of radio-AGN in dust-obscured galaxies

This chapter focuses on unveiling a new population of radio-emitting AGN hosted in DOGs. We have used deep radio observations from uGMRT and demonstrated the existence of AGN in nearly 28 per cent of DOGs. Unlike previous studies, our study reveals the highest fraction of AGN in DOGs. We have also investigated radio characteristics, MIR colours, X-ray absorbing column densities and X-ray luminosities to understand the nature of these sources. We conclude that the majority of radio-detected sources in DOGs are likely to be young radio AGN with radio jets confined within the hosts.

Chapter 4: X-ray spectral characteristics of AGN in dust-obscured galaxies

In this chapter, we present X-ray spectral analysis of a sample of 34 DOGs using all the existing *XMM-Newton* data, and *Chandra*/ACIS data, whenever available in the *XMM-SERVS* extragalactic field. This study is limited to only those sources that are relatively bright in the *XMM-Newton* observations such that their spectral analysis is feasible. Also, sources have accurate photometric or spectroscopic redshifts to enable us to make redshift-correction. We find that, the X-ray spectra of our DOGs can be well described with an absorbed power law and reflection component. This study helps us to characterize poorly explored high-redshift AGN residing in dusty environments.

Chapter 5: Multi-epoch hard X-ray view of the heavily obscured AGN in the Circinus Galaxy

This chapter presents a case study of a nearby ($z = 0.0014$) luminous, heavily obscured Compton-thick AGN, Circinus galaxy. Using all the available hard X-ray observations till date from the *BeppoSAX*, *Suzaku*, *NuSTAR* and *AstroSat*/LAXPC observations, we have modelled the multi-epoch hard X-ray spectra of the heavily obscured AGN in the Circinus galaxy. We utilised *Chandra* and *XMM-Newton* X-ray observations to assess the contamination from neighbouring off-nuclear sources. We demonstrated that AGN is found to be obscured with CT absorbing column densities across all the epochs. We also find tentative evidence for change in column density favouring a clumpy obscuring material around AGN.

Chapter 6: Summary and future work

This chapter provides a summary of the thesis work. I list the results and discuss their importance and implications. I emphasize the role of our deep uGMRT observations in unveiling a new population of AGN. I highlight the fact that our study can be used as a test-bed for planned and upcoming deeper radio and X-ray surveys. This chapter also delves into our future plan that has emerged from the thesis work. For instance, our stacking analysis has revealed the presence of a faint radio population in DOGs. So, I plan to use deeper radio surveys to unveil and better constrain the AGN population hosted in DOGs. I also emphasize the importance of sub-arcsec radio observations needed to detect compact jet-lobe structures and to constrain the timescales during the early phase of AGN evolution.

Chapter 2

Radio and X-ray observational techniques and telescopes

In this thesis work, I have used mainly radio and X-ray observations to identify and unveil the nature of obscured AGN. Thus, I devote this chapter for describing radio and X-ray observational techniques and data reduction procedures. I also provide brief details about the telescopes from which we obtained our observations.

2.1 Radio observational techniques

2.1.1 Aperture Synthesis

According to the diffraction-limited Rayleigh criterion, the angular resolution achieved by an instrument is limited to the size of the instrument aperture as well as the wavelength at which observation is performed,

$$\theta \sim \lambda/D \tag{2.1}$$

where, D is the aperture size of the instrument. Thus, the longer wavelength radio observations require a larger aperture size to obtain the same angular resolution that can be achieved by a smaller telescope observing in shorter wavelength. For example, the recently launched NASA's James Webb Space Telescope (JWST) has an aperture size of 6.5m which provides observations in the range 0.6 μm – 28.5 μm. Hence, it would achieve an angular resolution of $\sim 0''.02$ at 0.6 μm. In order to achieve the very same angular resolution with a radio telescope at 21 cm (1.4 GHz) it would require an aperture size of nearly 230 km. Such a large telescope is impractical to build as the increased gravitational and wind loads become difficult to handle.

In radio astronomy, high angular resolution is achieved by using the interferometric technique. In this technique, radio observations are performed simultaneously with an array of smaller radio antennas spread over a large region, and then the radio signals of each pair of antennas are combined interferometrically. The combined signal from each pair of radio antennas produces interference pattern that is directly related to the source brightness distribution. According to *van Cittert-Zernike* theorem, spatial correlation of the electric field in $u - v$ plane is the Fourier transform of the source brightness distribution,

$$V_\nu(u, v) = \int_{-\infty}^{+\infty} \int_{-\infty}^{+\infty} I_\nu(l, m) e^{-i2\pi(ul+vm)} dl\ dm \tag{2.2}$$

where, $V_\nu(u, v)$ is the spatial coherence function (also known as complex visibility), $I_\nu(l, m)$ brightness distribution of the source, ν is the observing frequency (see Thompson et al., 2017, page 94). Hence, according to the Equation 2.2, each pair of radio antennas allows for the measurement of a single Fourier component of the source brightness distribution, *i.e.*, one sample at the $u - v$ plane at a time. If there is a large number of samples (*i.e.*, interferometric measurements) are available in the $u - v$ plane, then the brightness distribution of the source can be reconstructed from the Fourier transform.

An array containing N number of radio antennas would measure $N(N-1)/2$ number of samples (*i.e.*, visibilities) in the $u - v$ plane (or Fourier plane). The $u - v$ coverage can also be increased by using only two-element radio interferometers due to Earth's rotation. This is because Earth's rotation makes the baseline projections appear differently if seen from the source position. This resulted in a different (u, v) points in the Fourier plane. This is known as "Earth rotation aperture synthesis" which was first proposed by (Ryle & Hewish, 1960). In recent times this is referred to as simply "aperture synthesis". Thus, in "aperture synthesis" method, if all the Fourier components are measured upto a baseline length of two extreme-end antennas (which can be as large as the diameter of the Earth) in an array, then it could be possible to reconstruct the sky image having the same resolution as would be obtained with a single radio telescope of aperture size equal to the baseline length.

2.2 Radio data reduction

The basic steps of radio data reduction procedure include flagging, calibration, imaging, deconvolution and self-calibration (see Fomalont & Perley, 1999, for more details). In the following subsections, I briefly describe these steps.

2.2.1 Flagging

Data are subjected to initial flagging before passing through the calibration process. "Flagging" is basically identifying and removing bad data from the observations. There are several factors that are responsible for corrupting the data which includes various equipment malfunctions (*e.g.*, receiver failure, tracking inaccuracies in antennas etc.), signals from terrestrial radio sources, radio frequency interferences (RFI) from human-made devices etc. RFI can be identified as anomalous spikes in the amplitude vs baseline plot (Fridman & Baan, 2001). Generally, RFI are searched both at the start and at the end of the channels but can also be searched in between channels. Once, the RFI are identified, the corresponding frequency ranges are flagged. Once, the data is free from bad data, they are ready to be calibrated.

2.2.2 Calibration

As discussed in Section 2.1.1, the interference pattern recorded by each pair of radio antennas in an array lie on an $u-v$ plane can reconstruct the sky brightness distribution through Fourier transform. The measurement of such interference pattern of a two-element interferometer is called the spatial coherence function or visibility. Since, the visibility from each pair of antennas is sampled at discrete times hence, the Equation 2.2 can be written as,

$$V_\nu(i,j)(t) = \int_{-\infty}^{+\infty}\int_{-\infty}^{+\infty} I_\nu(l,m)e^{-i2\pi(u_{ij}(t)l+v_{ij}(t)m)}dl\ dm \tag{2.3}$$

The visibility recorded by each pair of radio antennas is usually referred to as the "observed" visibility (denoted by $V_{ij}^{\rm obs}$; i, j being the ith and jth antennas) (see Fomalont & Perley, 1999). Generally, the 'observed' visibility differs from the 'true' visibility ($V_{ij}^{\rm true}$). The aim of the calibration is to make necessary corrections to $V_{ij}^{\rm obs}$ in order to recover $V_{ij}^{\rm true}$. Since, to a good approximation the arrays are linear devices (output being a linear function of input) and the individual measurements are isolated hence, $V_{ij}^{\rm obs}$ can be considered as a linear function of $V_{ij}^{\rm true}$ which can be expressed as,

$$V_{ij}^{\rm obs}(t) = G_{ij}(t)V_{ij}^{\rm true}(t) + \epsilon_{ij}(t) + \eta_{ij}(t) \tag{2.4}$$

where, t is the time of the observation, $G_{ij}(t)$ is the baseline-based complex gain, $\epsilon_{ij}(t)$ is the baseline-based complex offset and $\eta_{ij}(t)$ is a stochastic complex noise.

The major part of the data corruption occurs before the cross-correlation of the signals from the antenna-pair. Hence, $G_{ij}(t)$ can be approximated as the product of the antenna-based complex gains $g_i(t)$ and $g_j(t)$, and can be expressed as,

$$G_{ij}(t) = g_i(t)g_j^*(t) = a_i(t)a_j(t)e^{i(\phi_i(t)-\phi_j(t))} \tag{2.5}$$

where, $a(t)$ and $\phi(t)$ are the antenna-based amplitude and phase corrections of the respective antennas, respectively.

2.2.2.1 Amplitude (or Flux) calibration

The complex gain $G_{ij}(t)$ can be determined by observing the calibrator sources. The standard calibrator sources are bright point radio sources with known and constant flux densities and well-known sky-positions and are well isolated to avoid confusion from the nearby sources (Klein & Stelzried, 1976). For a standard flux calibrator $V_{ij}^{\rm true}(t)$ is known, hence, $V_{ij}^{\rm obs}(t)$ can be obtained by observing the source. Now, if a calibrator source has flux density measurement S with it's position accurately known then the amplitude of the true complex visibility ($V_{ij}^{\rm true}(t)$) is S and the phase is zero degrees. Hence, the baseline-based complex gain at the time of observation can be written from Equation 2.4 as,

$$G_{ij}(t) = \frac{V_{ij}^{\rm obs}(t)}{S} \tag{2.6}$$

where, the complex offset term $\epsilon_{ij}(t)$ is assumed to be negligible and the complex noise term $\eta_{ij}(t)$ becomes negligible after proper averaging of the data in a scan.

2.2.2.2 Phase calibration

The incoming wavefront of radio waves coming from an astrophysical source suffers distortion as it passes through the Earth's ionosphere. These distributions introduce phase errors across the wavefront and they vary rapidly with time and across the telescope array. To correct for the phase errors we perform phase calibration by observing a phase calibrator. Unlike the flux calibrator, a phase calibrator may be variable on much shorter timescales, but they must lie close to the source which is being observed. Generally, during the observation, a flux calibrator is observed first which is then utilised to calibrate the amplitude of the phase calibrator. The phase calibrator is then utilised to calibrate the visibility amplitudes and phase for the rest of the observations. A frequent short scans of the phase calibrator are generally intermixed throughout the observation period where the gain values are interpolated to calibrate the visibility data of the observed source (Browne et al., 1998; Winn et al., 2003). The frequency and the time interval of the short scans depend on several factors, *e.g.*, the frequency of the observation, the length of the baseline and the weather condition.

2.2.2.3 Bandpass calibration

Bandpass calibration is required for correcting the complex gain variations as a function of frequency across the bandwidth of the receiver (Yamaki et al., 2012; Patra et al., 2017). The bandpass calibration is essential for spectral line as well as wide-band radio continuum observations. The aim of the bandpass calibration is to compensate for the changes in the gain with frequency. In order to estimate the changes in antenna gain with frequency, the baseline-based complex gain can be considered as a function of frequency ($G_{ij}(\nu)$). In order to determine the relative frequency response of the frequency band, a strong calibrator source is observed which may not be a point source but have a flat spectrum over the frequency band. Since, the true visibility is identical in all the channels over the frequency bandwidth hence, the complex correlator-based gain function for $i-j$ baseline and kth frequency channel is given by,

$$G_{ij}(\nu_k) = \frac{V_{ij}^{\mathrm{obs}}(\nu_k)}{V_{ij}^{\mathrm{true}}(\nu_k)} \tag{2.7}$$

The frequency-dependent, baseline-dependent bandpass can be expressed as the products of the antenna-based gains which then can be converted into antenna-based bandpass amplitude and phase calibrations. The bandpass calibration scan follows the same methods as the flux and phase calibration scans however, due to the slow time variations of the bandpass functions, one bandpass calibration per observing run is sufficient for most observations.

2.2.3 Imaging and Deconvolution

As described earlier (see Section 2.1.1), each pair of radio antennas measures one sample in the $u - v$ plane at a time. A large no of samples in the $u - v$ plane can reproduce the sky brightness distribution through Fourier transform,

$$I_\nu(l,m) = \int_{-\infty}^{+\infty}\int_{-\infty}^{+\infty} V_\nu(u,v)e^{+i2\pi(ul+vm)}du\ dv \tag{2.8}$$

However, the spatial coherence function $V_\nu(u,v)$ is not known everywhere but rather sampled at discrete places in the Fourier plane (*i.e.*, $u - v$ plane). Hence, the observed sky brightness distribution can be expressed as,

$$I_\nu^D(l,m) = \int_{-\infty}^{+\infty}\int_{-\infty}^{+\infty} V_\nu(u,v)S(u,v)e^{+i2\pi(ul+vm)}du\ dv \tag{2.9}$$

where, $S(u,v)$ is the sampling function which the value is one where the data is present and is zero in case of no data (Perley et al., 1986). $I_\nu^D(l,m)$ is referred to as "dirty image" or "dirty map" which is related to the true $I_\nu(l,m)$ by the convolution equation,

$$I_\nu^D = I_\nu * DB \tag{2.10}$$

where $*$ denotes the convolution. DB is the inverse Fourier transform of the sampling function $S(u,v)$ and is termed as "dirty beam" which is basically PSF of the synthesized array, corresponding to the sampling function.

Hence, in order to obtain the true brightness distribution the "dirty beam" needs to be deconvolved with the observed brightness distribution. There are different deconvolution algorithms available *viz*., 'CLEAN' (Högbom, 1974; Högbom & Cornwell, 2009), Maximum Entropy Method (MEM; Frieden, 1972; Wernecke, 1977; Gull & Daniell, 1978), Adaptive Scale Pixel CLEAN (ASP-CLEAN; Bhatnagar & Cornwell, 2004), Multi-Scale CLEAN (MS-CLEAN Cornwell, 2008).

2.2.4 Self-calibration

After deconvolution, there could be residual calibration errors that can still degrade the image. However, a major role is played by the variable and non-uniform troposphere and ionosphere due to which calibration gains change significantly during the observations. A simple interpolation of gains as obtained by observing the calibrator source at the start and at the end of the target source observations would not properly correct the observed data. However, these effects can be eliminated by a technique called Self-calibration (or *Selfcal*) that uses a model of the target source based on the visibilities of the same target source to reduce the calibration errors (Cornwell, 1982). In other words, *Selfcal* is analogous to the standard calibration but unlike in the standard calibration, *Selfcal* uses the target source itself as a calibrator to correct the data (hence the name "Self-calibration").

Selfcal uses *phase closure* and *amplitude closure* iteratively to correct for antenna gain and *a prior* flux calibration, respectively. In *phase closure*, the visibility phases are summed over any triangle baseline (three antennas), whereas in *amplitude closure*, the ratio of the visibility amplitudes is taken over any rectangle baseline containing four antennas. In an interferometric array containing N radio antennas, there would be N complex gain that could corrupt the $N(N-1)/2$ complex visibility measurement at any given time. So, constraints on the amplitude would be $N(N-1)/2-N$ and constraints on the phase would be $N(N-1)/2-(N-1)$. If the number of elements of an interferometric array becomes very large, then the following iterative scheme is adapted.

1. An initial model of the target source is assumed and the visibilities based on the assumed model are calculated

2. Antenna gains are solved for the model

3. The gain corrections are applied to correct the visibility data

4. A new model is formed based on the corrected data for the next iteration

Steps 1 - 4 are repeated until the desired model is achieved. The iterative deconvolution algorithm 'CLEAN' can be utilised to obtain the model of the target source to be used in the *Selfcal* procedure.

2.3 Radio telescopes

For our work, we have used radio observations mainly from upgraded GMRT and VLA. Herewith, I give a brief description about these telescopes.

2.3.1 Giant Metrewave Radio Telescope (GMRT)

The Giant Metrewave Radio Telescope (GMRT; Swarup, 1991) is a fully operational Indian low-frequency radio telescope facility located near Pune. It consists of an array of 30 antennas providing a collecting area of 30,000 square metres at metre wavelength. Each antenna is a fully steerable but non-movable parabolic dish having a diameter of 45m. The distance between the two extreme antennas is $\sim$ 25 km which corresponds to the longest baseline of the GMRT. The

14 out of 30 antennas are randomly distributed in a central ~ 1 square km region, constituting several short baselines which are suitable to study large and extended sources. The remaining 16 antennas are distributed in three arms (in 'Y' shape) called 'East', 'West' and 'South' where each arm has a length of ~ 14 km (see Figure 2.1). The GMRT currently performs radio observations in the frequency range of 150 MHz - 1450 MHz in five frequency bands centered at 153 MHz, 233 MHz, 325 MHz, 610 MHz and 1420 MHz where each band have a bandwidth of 32 MHz.

Recently, GMRT has been upgraded with improved receiver systems which have wider frequency bands to provide nearly seamless frequency coverage between 50 MHz to 1450 MHz (Gupta et al., 2017). The upgraded GMRT (uGMRT) provides more sensitive radio observations in five frequency bands; 50 MHz−80 MHz (band-1), 120 MHz−250 MHz (band-2), 250 MHz−550 MHz (band-3), 550 MHz−850 MHz (band-4) and 1050 MHz−1450 MHz (band-5) having maximum bandwidth of 400 MHz.

2.3.2 Very Large Array (VLA)

The Karl G. Jansky Very Large Array (VLA; Thompson et al., 1980) is one of the widely-used centimeter-wavelength radio telescopes, situated in New Mexico, northwest of Socorro. This interferometric array consists of 28 antennas each having a diameter of 25m. All the antennas are fully steerable on an altitude-azimuth mount. The 27 antennas which are operational are distributed in Y-shape, where each of the three arms contains nine telescopes. The observing frequency range is 1.0 GHz−50.0 GHz. With antennas movable on railway tracks, VLA allows observations in four principal array configurations 'A', 'B', 'C' and 'D' where each configuration have different baselines of 36.0 km, 11.4 km, 3.4 km and 1.0 km, respectively. Depending on the array configurations for an

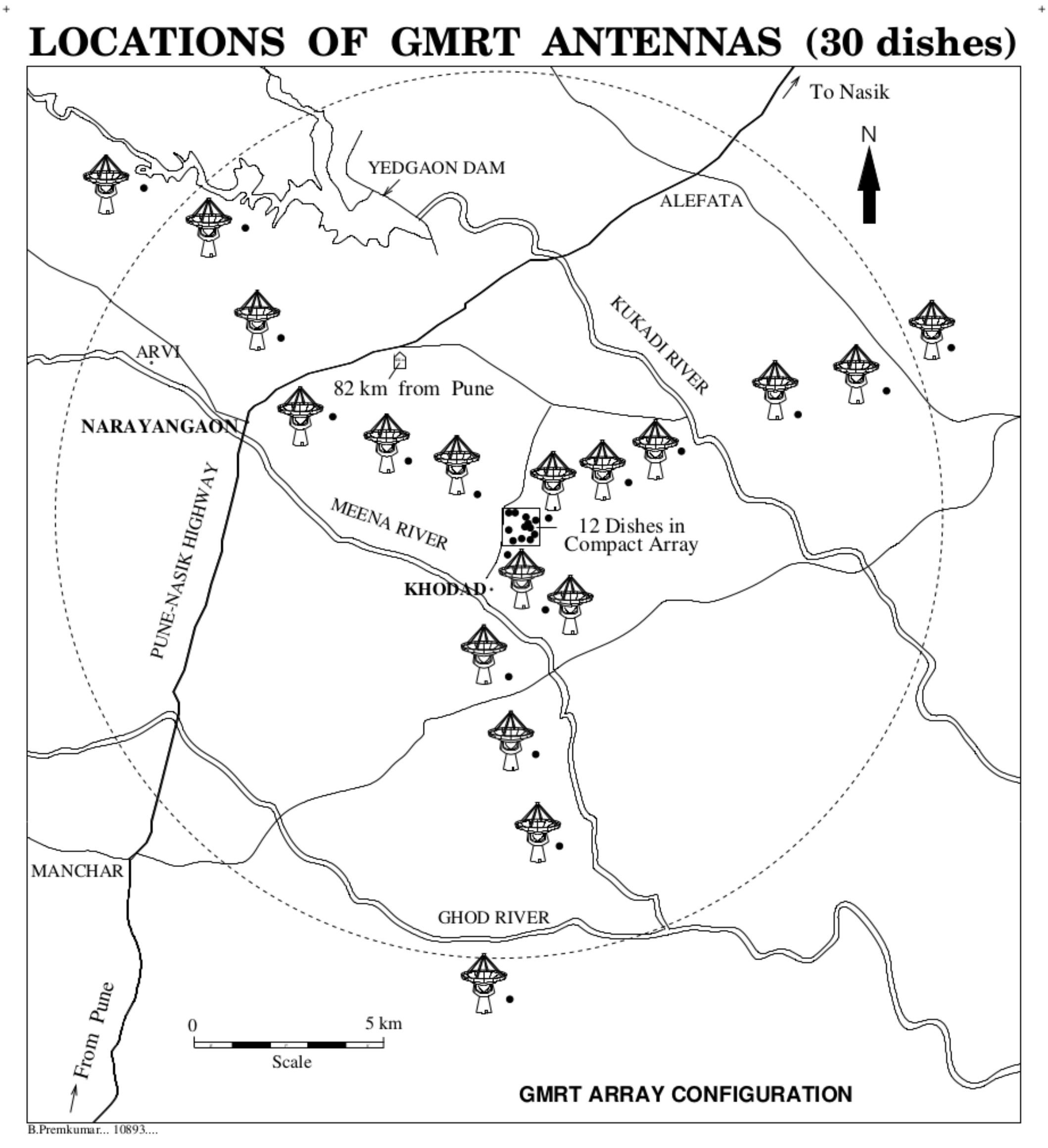

Figure 2.1: The GMRT array configuration. Image credit: http://www.ncra.tifr.res.in/ncra/gmrt/gmrt-users/low-frequency-radio-astronomy/ch18.pdf

observation, VLA provides angular resolutions in the range $0''.04$ to $0''.2$ where the highest angular resolution is achieved in the 'A' configuration.

2.4 Radio observations

To study the radio properties of DOGs, we have utilised 400 MHz band$-$3 uGMRT observations covering a sky area of 2.4 deg^2 in the XMM-LSS field centered at RA = 02^h 26^m 45^s and DEC = -04^0 $41'$ $30''$ (J2000). Apart from uGMRT, we have used existing multi-frequency radio observations at 1.5 GHz from VLA and at 150 MHz from LOFAR. We have also utilised shallow large-area surveys like 1.4 GHz FIRST and 3.0 GHz VLASS observations overlapping with the uGMRT coverage. More details on the radio observations are described in Section 3.2.1.

2.5 X-ray observational techniques

In X-ray astronomy, X-ray detectors are designed to measure and store the information regarding the position, time and the energy of an incident X-ray photon. Thus, X-ray detectors are different from the detectors operating in the longer wavelengths, *e.g.*, optical, infrared; where the integrated flux is measured instead of individual photons. This is owing to the fact that X-ray photons have relatively high energies and low flux which makes them easy to be detected and counted individually. To record X-ray events, various types of X-ray detectors such as Proportional Counters, Charge Coupled Devices (CCDs) etc. have been developed (see Knoll, 2000, for more details on X-ray detectors).

Proportional counters are among the simplest X-ray detectors in X-ray astronomy. There are several X-ray telescopes that have onboard proportional counters as X-ray detectors, *e.g.*, LAXPC onboard *AstroSat* (see Section 2.7.3). A typical proportional counter contains a windowed gas-filled chamber where a mixture of inert gasses is kept at high pressure. The incident X-ray photons after traversing through the window, interacts with the gas mixture via photoelectric effect. This generates primary photo-electrons which are then drifted towards the positive anode wire placed at the centre of the chamber. These drifting electrons on their way towards the anode ionize the other gas atoms along their paths producing more number of Auger electrons and/or fluorescent photons which in turn ionizes the gas further causing an avalanche. Thus, a cascade of electrons that reaches to the anode represents the amplification of the charge produced during the initial interaction of the X-ray photons with the gas. Hence, the signal induced at the anode is proportional to the absorbed energy incident on the detector and contains information about the energies, arrival times and interaction positions of X-ray photons.

Another most commonly used X-ray detectors are Charge Coupled Devices (CCDs). Owing to their high dynamic range, sensitivity and linear responses, they are now become the popular choice of detectors to be used in ground-based as well as space-based astronomical observatories operating in optical, infrared and even in X-ray. There are several currently active X-ray observatories that have CCDs as onboard X-ray detectors, *e.g.*, SXT on *AstroSat* (Singh et al., 2017), EPIC on *XMM-Newton* (Strüder et al., 2001; Turner et al., 2001), ACIS on *Chandra* (Garmire et al., 2003) etc. A CCD is an array of “coupled” capacitors which could be either a metal-oxide-semiconductor (MOS) or p-n junction. When X-ray photons are incident on a CCD detector, they get photoelectrically absorbed in the semiconductor substrate and generate electron-hole pairs. The generated charges are then stored in pixels by employing an electric field which is then transferred to neighbouring pixels to be finally read and digitized at the readout amplifier. X-ray CCDs operate in photon counting mode where the energy, position and arrival time of each X-ray photon are recorded. In X-ray photon counting mode, the frame time is such that not more than a single photon should fall on the detector. In case of timing analysis, the fast time resolution can be achieved by sacrificing the spatial information. Although, CCDs provide many advantages and flexibility as X-ray detectors, but owing to the depth of their active regions their sensitivities are limited from a few hundreds eV to 10 keV.

CZT or CdZnTe detectors are used to detect X-ray at higher energies ($>$ 10 keV) owing to their higher cross-section as compared to silicon CCDs which provides a better quantum efficiency in hard X-ray. The currently active hard X-ray telescopes have CZT detectors at their focal plane, *e.g.*, CZTI onboard *AstroSat* (Bhalerao et al., 2017), Focal Plane Modules (FPMs) onboard *NuSTAR* (Harrison et al., 2013) etc. Since, CZT detectors are semiconductor devices hence, their working functions are similar to CCD detectors except that each pixel in CZT detectors are read independently instead of row-wise charge transfer in CCDs.

2.6 X-ray data reduction and analysis

2.6.1 Data reduction

The X-ray scientific products *e.g.*, images, spectra, lightcurves are essential for decoding underlying physical mechanisms of any astrophysical phenomena. The major part of the X-ray data reduction process involves generating cleaned and calibrated data which can be utilised to extract such scientific products through processing and cleaning of raw data obtained from the X-ray observations carried out by any X-ray telescope. The X-ray detectors detect individual X-ray photons that hit the detector and store various information of the incoming photons in a raw event file (generally called as Level-1 event file).

The basic data structure of a Level-1 raw event file is a list of detected events where each event contains a set of attributes (Arnaud et al., 2011) such as the photon arrival time, the amount of charge generated by the photon interaction (known as Pulse Height Amplitude or PHA) which in turn is related to the photon energy, the position of the photon interaction on the detector along with several other information regarding the satellite orbit, status of the detectors etc. The raw Level-1 event file also contains events due to the interaction of high energy particles like cosmic rays, charged particles trapped in the Earth's magnetosphere etc. that can mimic as an X-ray source. Not only so but also spurious signals generated due to the bad (hot and/or flickering) pixels, afterglows etc. may introduce artifacts during the observations which need to be eliminated. Thus, the raw Level-1 event file is not suitable for scientific analysis and requires reprocessing. The reprocessing is done through cleaning and filtering criteria which produces a cleaned and calibrated Level-2 event file. A standard X-ray data reduction pipeline applies such filtering criteria using the informations that are stored in the Calibration Database (CALDB) files provided by the instrument team of the respective X-ray observatories. However, provisions for incorporating user-defined cleaning and filtering criteria for specific observations are also included in the pipeline. Finally, the images, spectra and lightcurves suitable for scientific analysis can be extracted from the cleaned and calibrated Level-2 event file. The data analysis procedures of specific X-ray telescopes are described in detail in Section 4.3 and Section 5.3.

2.6.2 X-ray spectral fitting

In X-ray astronomy, the actual X-ray spectrum of a source is not recorded. Instead, the count spectrum is observed where photon counts are recorded within some specific instrument channels of the X-ray detector that is performing the observation. The actual spectrum $F(E)$ is related to the observed count spectrum $C(I)$ by the following relation,

$$C(I) = \int F(E)R(I,E)dE \tag{2.11}$$

where, $R(I,E)$ is related to the response of the X-ray instrument which is proportional to the probability for a photon with given energy E to be detected in channel I of the detector (Arnaud et al., 2011). Equation 2.11 indicates that the actual spectrum $F(E)$ can be obtained through a simple inversion of the equation. However, such inversion is non-unique and is very much unstable to small changes in $C(I)$. In order to deal such cases, a 'forward-fitting' approach is adopted where a model spectrum in terms of some parameters describing the underlying physical mechanisms is assumed. Such model spectrum is then convolved with the detector response and is compared with the observed count spectrum using a fit-statistics. The initial model parameters are varied until the best value of the fit-statistics is obtained (which in case of χ^2-statistics is the minimum value of

χ^2). Once the best-fit is obtained, the confidence regions of the model parameters are calculated. The most widely used fit-statistics is χ^2-statistics which is defined as,

$$\chi^2 = \sum_{I=1}^{\nu} \frac{(C(I) - C_p(I))^2}{(\sigma(I))^2} \tag{2.12}$$

where, $C_p(I)$ is the model predicted count rate in the channel I, $C(I)$ is the observed count rate in channel I and $\sigma(I)$ is the error in the channel I (usually estimated as $\sqrt{C(I)}$) and ν is the degrees-of-freedom (Arnaud et al., 2011).

Once the best-fit parameters of a model are obtained, the next step is to find out that how good the model is fitting the data. This is determined by the goodness-of-fit statistics. In case χ^2-statistics is used to measure the goodness-of-fit statistics, we find the value of reduced χ^2 defined as χ^2/ν, where ν is the degrees-of-freedom obtained by subtracting the number of model parameters that are freely varied during the fit from the number of channels. Generally, for a data set following a Gaussian distribution, a good-fit is expected to yield model-predicted count rates which are within 1σ deviation from the observed count rates. The equation 2.12 then reduces to $\chi^2 \sim \nu$ which in turn gives reduced $\chi^2 \sim 1$. Thus, in case of a good-fit one would expect reduced χ^2 value approaching to one, although the main criterion is to achieve minimum χ^2. Also, it is to be noted that the statistical test is not the only measure of a best-fit model but also has to be scientifically relevant in order to properly explain the physical mechanisms responsible for the observing phenomena. For the spectral analysis, we have used the X-ray spectral fitting package `xspec` (Arnaud, 1996).

2.7 X-ray telescopes

In the following subsections, I provide a brief description about the X-ray telescopes from which we have used observations.

2.7.1 *Chandra*

The *Chandra* X-ray observatory, one of the NASA's flagship missions, was launched on 23 July 1999. It carries three major instruments, *i.e.*, Advanced CCD Imaging Spectrometer (ACIS), High Energy Transmission Grating (HETG) and Low Energy Transmission Grating (LETG). The ACIS (Garmire et al., 2003) contains a total of 10 CCD chips arranged in two configurations, a 2×2 configuration (ACIS I-array; FoV $16'.9\times16'.9$) and 1×6 configuration (ACIS S-array; FoV $8'.3\times50'.6$) enabling both imaging as well as spectroscopic observations with an unprecedented angular resolution of $0''.5$. The *Chandra* X-ray observatory, with it's unique high resolution imaging and spectroscopic abilities, provides sensitive X-ray observations in $0.1-10$ keV energy range.

2.7.2 *XMM-Newton*

The X-ray Multi-Mirror Mission (*XMM-Newton*) observatory was launched by European Space Agency (ESA) on 10 December 1999. It contains three focusing X-ray telescopes, European Photon Imaging Camera (EPIC; Strüder et al., 2001), Reflection Grating Spectrometer (RGS; den Herder et al., 2001), and Optical Monitor (OM; Mason et al., 2001). The EPIC cameras are equipped with two different types of CCD arrays, Metal Oxide Semiconductor (*MOS*) in two CCD arrays and *pn* in one CCD array. It provides sensitive observations over a $30'$ FoV with a spectral resolution of $(E/\Delta E)\sim20-50$ and an on-axis angular resolution of (FWHM) $\sim6''$. For EPIC *pn,* the X-ray photons coming from the mirror assembly focused uninterruptedly on the CCD. In case of EPIC MOS, only 44% of the incoming photons are focused on the *MOS* CCD while 40% of the incoming photons are intercepted by the *RGS* assembly installed before the *MOS* CCD arrays. Unlike *Chandra,* which has an on-axis effective area of 600 cm^2 at

1.5 keV, the *XMM-Newton* has a total effective area of 4650 cm^2 at 1.5 keV. Due to the large effective area *XMM-Newton* /EPIC provides better quality spectra in $0.15 - 12$ keV energy range.

2.7.3 *AstroSat*

The *AstroSat* (Agrawal, 2006; Singh et al., 2014a) is the first Indian multiwavelength space-based observatory, which was launched by Indian Space Research Organisation (ISRO) on 28 September 2015. There are five onboard telescopes, *i.e.*, Soft X-ray Telescope (SXT; Singh et al., 2016, 2017), Large Area X-ray Proportional Counter (LAXPC; Yadav et al., 2016; Agrawal et al., 2017), Ultra Violet Imaging Telescope (UVIT; Kumar et al., 2012; Subramaniam et al., 2016), Cadmium-Zinc-Telluride Imager (CZTI; Bhalerao et al., 2017) and Scanning Sky Monitor (SSM). Therefore, *AstroSat* has capability to perform simultaneous multiwavelength observations in the optical, UV and X-ray bands.

The SXT is a grazing incidence focusing X-ray telescope which operates in the energy range of 0.3–8 keV with an energy resolution of 5–6% at 1.5 keV. In the focusing X-ray telescopes such as *SXT*, *XMM-Newton* and *Chandra*, an X-ray beam is completely reflected from the vacuum–mirror interface when it incidents within the range of grazing angles. Therefore, a mirror assembly containing concentric hyperbolic shells is used to focus incident X-ray photons. More details on the SXT and LAXPC are given in Section 5.3.3.

2.7.4 *NuSTAR*

Nuclear Spectroscopic Telescope Array (*NuSTAR* ; Harrison et al., 2013) is the first focusing high-energy X-ray telescope with an energy coverage of 3 - 79 keV, was launched on 13 June 2012. It consists of two co-aligned X-ray telescopes each of 10.14m focal length. At the focal plane, there are 4 CdZnTe pixel detectors providing an energy resolution of 400 eV at 10 keV and 900 eV at 68 keV and an angular resolution of 18″ over the FoV of 12′.5. As a focusing X-ray telescope, *NuSTAR* provides more than 100-fold increased sensitivity in the hard X-ray as compared to any other current or previous X-ray telescope in this energy range.

2.8 X-ray observations

To study the X-ray spectral properties of AGN hosted in DOGs, we have used all the existing *XMM-Newton* and *Chandra* observations available in the XMM-SERVS region. More details can be found in Chapter 4. To probe multi-epoch spectral and timing properties of the nearby Compton-thick AGN in the Circinus galaxy, we have also utilised multi-epoch X-ray observations from the *BeppoSAX*, *Suzaku*, *NuSTAR* , *XMM-Newton* , *Chandra* and *AstroSat* (see Chapter 5).

Chapter 3

Detection of radio-AGN in dust-obscured galaxies †

3.1 Introduction

AGN, a manifestation of accretion onto the SMBH, is believed to be triggered by the inflow of matter into the central region of galaxies. One of the most favored scenarios for AGN triggering is galaxy-galaxy interaction or merger that also causes the enhancement in star-formation (SF) activity (Hopkins et al., 2006). The inter-link between AGN and SF activity is indicated by the similarity in the cosmological evolution of co-moving space-densities of AGN and star-forming galaxies that peak at redshift (z) $2-3$ (Kauffmann & Haehnelt, 2000). It is well established that the intensely star-forming galaxies containing a large amount of gas and dust can potentially host obscured AGN (Lacy & Sajina (2020) and references therein). The large reservoirs of gas and dust absorb the optical and

† **Abhijit Kayal**, Veeresh Singh, C. H. Ishwara Chandra, Yogesh Wadadekar and Sushant Dutta, 2022, *Journal of Astrophysics and Astronomy*, 43, 84, https://doi.org/10.1007/s12036-022-09873-0

UV emission arising from the AGN and stars, and re-radiate it at infrared (IR) wavelengths. Therefore, the AGN population residing in dusty galaxies can be missed by the optical and UV surveys (see Truebenbach & Darling, 2017). The Far-IR (FIR) and Mid-IR (MIR) surveys have been advantageous in detecting DOGs that are bright in the mid-IR but faint in the optical with the ratio of 24 μm to r-band fluxes $\geq$1000 (see Section 3.3.1). Moreover, the identification of obscured AGN is often challenging. To uncover the obscured AGN, various methods, *e.g.*, hard X-ray detection of AGN emission (Ricci et al., 2021), colour selection techniques (Noboriguchi et al., 2019), MIR emission characterized by a power$-$law (Farrah et al., 2017), have been employed. Albeit, all these methods suffer from certain limitations; for instance, hard X-ray observations are unable to detect AGN with column densities ($N_{\rm H}$) $\geq$ 10^{26} cm^{-2} due to dominant Compton down-scattering, colour selection techniques for the AGN hosted in DOGs can be valid up to z $\leq$ 2.0 due to the redshift related systemic shift in SEDs (Donley et al., 2012), and the MIR spectral energy distributions (SEDs) of intensely star-forming galaxies hosting obscured AGN can be fitted equally well with the templates of SFGs as well as of AGN (Shanks et al., 2021).

The *Spitzer* and *Herschel* observations confirmed that DOGs are a subset of optically-faint high-redshift (z $\sim$ 1.5 $-$ 2.5) galaxies with their total (8 $-$ 1000 μ m) IR luminosities in the range of $10^{11.5}$ $L_{\odot}$ $-$ 10^{14} $L_{\odot}$ (see Melbourne et al., 2012). Thus, based on their IR luminosities, DOGs are the most luminous galaxies at their redshifts and can be classified as luminous infrared galaxies (LIRGs; $L_{8-1000~\mu{\rm m}}$ $\geq$ 10^{11} $L_{\odot}$ $-$ 10^{12} $L_{\odot}$), ultra-luminous infrared galaxies (ULIRGs; $L_{8-1000~\mu{\rm m}}$ $\geq$ 10^{12} $L_{\odot}$ $-$ 10^{13} $L_{\odot}$), and hyper-luminous infrared galaxies (HLIRGs; $L_{8-1000~\mu{\rm m}}$ $\geq$ 10^{13} $L_{\odot}$) (see Rowan-Robinson, 2000; Farrah et al., 2017). In general, DOGs detected in the *Herschel* SPIRE (Griffin et al., 2010), bands *i.e.*, 250 μm, 350 μm, and 500 μm have cooler dust with the temperature of $20 - 40$ K (Riguccini et al., 2015) than those not detected in the FIR bands. To explain the high IR luminosity of DOGs, theoretical models invoke gas-rich major merger leading to an intensely star-forming dusty merged system (Hopkins et al., 2008; Yutani et al., 2022). The merged system, in the early phase, can be classified as a star-forming DOG, while AGN activity can begin once gaseous and dusty material is being fed into the central region hosting SMBH. Thus, star-forming DOGs are likely to evolve into AGN-dominated DOGs before eventually turning into quasars or red ellipticals (see Dey et al., 2008). In the literature, DOGs have been divided into two categories *viz.* 'bump' DOGs (B-DOGs) showing a bump feature centered at 1.6 μm in the rest frame, and 'power−law' DOGs (PL-DOGs) showing a power−law MIR SED (Melbourne et al., 2012). The MIR emission in PL-DOGs is dominated by AGN heated dust, while MIR emission in B-DOGs is mostly powered by star-formation (Farrah et al., 2008). The obscured AGN are detected more commonly among the extreme population of PL-DOGs characterized by relatively hot dust emission, also known as the 'Hot DOGs' or hyper luminous infrared galaxies ($L_{\rm IR} > 10^{13}\ L_{\odot}$) residing mostly at high-redshifts ($z \sim 2$) (Tsai et al., 2015; Farrah et al., 2017). However, we cannot rule out the possibility of the existence of obscured AGN in B-DOGs with a less dominant contribution to the MIR emission. The obscured AGN with radio jets can easily be detected with radio observations as the gas and dust are optically thin at radio wavelengths. Therefore, radio observations of DOGs can enable us to unveil hitherto the unexplored population of obscured AGN. The popular radio−FIR correlation (Helou et al., 1985; Condon, 1992) observed in SFGs can also be exploited to identify radio powerful AGN as they are likely to show significant excess in radio emission (Morić et al., 2010). However, it would be challenging to identify less powerful radio AGN that show only a small deviation in the radio−FIR correlation (Zakamska et al., 2016). Therefore, to ascertain the presence of AGN in DOGs we investigate various properties *i.e.*, spectra, and luminosities.

The previous radio studies of DOGs have been limited mainly to the radio-powerful PL-DOGs or suffer from the shallow flux density limits of radio surveys. For instance, Lonsdale et al. (2015) performed Atacama Large Millimeter/sub-millimeter Array (ALMA) observations at 345 GHz (870 μm) for a sample of 49 dust-obscured quasars selected with ultra-red WISE colour ((W2 - W3) + 1.25 (W1 - W2) $>$ 7) similar to Hot DOGs (Wu et al., 2012) and compact radio emission in the 1.4 GHz Faint Images of the Radio Sky at Twenty-Centimeters (FIRST; Helfand et al., 2015)and NRAO VLA Sky Survey (NVSS; Condon et al., 1998). They found 345 GHz ALMA detection in only 26/49 sources (with a detection level $\geq 3\sigma$) having high star formation rates of several thousand $M_{\odot}$ yr^{-1} concurrent with the highly obscured quasar. Using 10 GHz Karl G. Jansky Very Large Array (VLA) observations of these radio-powerful dust-obscured quasars, Patil et al. (2020) reported the evidence for young jets with angular sizes of $< 0.2''$. More recently, Gabányi et al. (2021) studied the radio properties of 661 DOGs with the FIRST survey and found only 2% sources of their sample, exclusively PL-DOGs, detected in the FIRST with 5σ sensitivity limited to 1.0 mJy beam^{-1}. The stacking of FIRST image cutouts at the positions of the radio-undetected DOGs revealed radio emission only in PL-DOGs at the level of 0.16 mJy beam^{-1} flux density. Thus, it is evident that the radio emission in a large fraction of DOGs, even among AGN-dominated DOGs, remained undetected due to the relatively shallow detection limit of the FIRST survey. With our deep radio observations from the upgraded Giant Metrewave Radio Telescope (uGMRT) we aim to detect radio emission in DOGs at much fainter levels and unveil a new population of obscured AGN.

3.2 Multiwavelength observations

We have used multiwavelength surveys across radio, IR, optical and X-ray wavelengths that are available in the XMM-LSS field. To unveil the population of AGN in DOGs, we have used our band-3 uGMRT observations along with the existing auxiliary data. The footprints band-3 uGMRT observations, 1.5 GHz VLA observations, deep HSC-SSP survey, SWIRE survey and XMM-SERVS are shown in Figure 3.1. Here, we provide a brief description of the observations used for the thesis work.

3.2.1 Radio observations

400 MHz band-3 uGMRT observations: Our band-3 ($250\text{MHz} - 550\text{MHz}$) continuum imaging observations with the uGMRT were carried out during 11 September 2017 under the proposal code 32_066. These observations of one pointing centered at RA = $02^h\ 26^m\ 45^s.0$ and DEC = $-04^\circ\ 41'\ 30''.0$ were performed in the full synthesis mode with a total observing time of 10 hours. The flux calibrators 3C48 and 3C147 were observed for $15 - 20$ minutes at the beginning and end of the observing session, respectively. The phase calibrators $0116 - 0208$ and $0323 + 055$ were observed for $5 - 6$ minutes with each scan inter-leaved with 30 minutes scan of the target field. The data were reduced using a Common Astronomy Software Applications (CASA[1]) based pipeline. The standard data reduction procedure includes flagging of bad data, calibration of visibilities, and imaging of calibrated-visibilities. The final image was obtained after applying four iterations of 'phase-only' and one round of 'phase-and-amplitude' self-calibration which helped us for correcting artifacts arising from the residual calibration errors. The primary beam correction was applied to correct for underestimated

[1] https://casa.nrao.edu/

flux densities in the outer regions. Our final image has a median noise-rms of 30 μJy beam^{-1}, although noise-rms around relatively bright sources ($>$ 100 mJy) and at the peripheral regions is higher. The final image has synthesized beam of $6''.7 \times 5''.3$ with position angle of $71^{\circ}.7$, and covers a total sky area of nearly 2.4 deg^2 consisting a deeper central region of 1.3 deg^2 with noise-rms $\leq$ 30 μJy beam^{-1}.

We created the source catalogue by using the Python Blob Detector and Source Finder (PyBDSF; Mohan & Rafferty, 2015) algorithm. While running the PyBDSF we set the source detection limit to 5σ for peak pixel and 3σ for island boundary and grouped overlapping Gaussians into a single source. To minimize the number of spurious sources around bright sources we adopt smaller rms box of 33×33 pixel^2 with sliding of 11 pixels in the regions containing bright sources, while rms box size of 40×40 pixel^2 with sliding of 13 pixels was used in the remaining part of the image , where 1 pixel corresponds to 1 arcsec. With the aforementioned parameters we obtain a catalogue of 2332 sources detected at $\geq 5\sigma$ level.

Ancillary radio data: For our study, we also used the radio data at other frequencies. The footprints of uGMRT observations are covered with the 1.5 GHz Jansky Very Large Array (VLA) and 150 MHz LOw Frequency ARray (LOFAR) observations available in the *XMM-LSS* field. The 1.5 GHz wide-band ($0.994 - 2.018$ GHz) VLA radio observations achieved a median noise-rms of 16 μJy beam^{-1} and angular resolution of $4''.5$ (Heywood et al., 2020). The 150 MHz LOFAR observations reported by Hale et al. (2019) cover the sky-area of 27 deg^2 with mosaiced image having a median noise-rms in the range of 0.28 mJy beam^{-1} to 0.40 mJy beam^{-1} and the synthesized beam of $7''.5 \times 8''.5$. We note that the sky-area of our uGMRT observations is also covered by the shallow large-area surveys such as 1.4 GHz FIRST and 3.0 GHz Very Large Area Sky Survey (VLASS).

The FIRST performed with VLA B-configuration has the resolution of $5''.0$ and noise-rms 0.15 mJy beam^{-1} (Becker et al., 1995). The more recent VLASS is a high-frequency analogue of the FIRST and provides a median noise-rms of 0.12 mJy beam^{-1} and angular resolution of $2''.5$ (Lacy et al., 2020).

3.2.2 IR data from SWIRE survey

To select DOGs, we use data from the *Spitzer* Wide−area InfraRed Extragalactic survey (SWIRE; Lonsdale et al., 2003) and the Hyper Supreme Cam - Subaru Strategic Program (HSC-SSP; Aihara et al., 2022) optical survey. The SWIRE performed imaging in all four bands of the Infrared Array Camera (IRAC), *viz.*, 3.6 μm, 4.5 μm, 5.8 μm and 8.0 μm, and in all three bands of the Multi-band Imaging Photometer (MIPS) *viz.*, 24 μm, 70 μm, and 160 μm. The 5σ sensitivity of SWIRE is 7.3 μJy beam^{-1}, 9.7 μJy beam^{-1}, 27.5 μJy beam^{-1} and 32.5 μJy beam^{-1} in the four IRAC bands, respectively, and 0.45 mJy beam^{-1}, 2.75 mJy beam^{-1} and 17.5 mJy beam^{-1} in three MIPS bands, respectively. In the *XMM-LSS* field, the SWIRE is centered at RA = 02^h 21^m 00^s and DEC = -04° 30′ 00′ (J2000) and covers a total sky−area of 8.7 deg^2 with the IRAC bands and 9.0 deg^2 in the MIPS bands.

3.2.3 Optical data from HSC-SSP survey

In our study, we used optical data from the HSC-SSP[2] survey, which is a multi-band (g, r, i, z, y and four narrow-band filters) imaging survey carried out with the Hyper Suprime-Cam (HSC) wide-field camera (FOV $\sim$ 1.5 deg^2) installed on the 8.2-m Subaru telescope (Aihara et al., 2022). The HSC-SSP survey has three components, *i.e.*, wide, deep, and ultra-deep, forming a nested coverage wherein

[2] https://hsc.mtk.nao.ac.jp/ssp/survey/

the footprints of deeper components lie within the footprint of less deep component. The wide component covers nearly 1400 deg^2 around the celestial equator with i band limiting magnitude of 26.2 mag, while the deep survey component covers a total sky-area of only 27 deg^2 in four different extragalactic fields, including the *XMM-LSS* with the limiting magnitude of $m_i = 26.8$ (Aihara et al., 2022). The ultra-deep component covers a total area of only 3.5 deg^2 in two sub-fields with the limiting magnitude of $m_i = 27.4$. We note that the limiting magnitudes are measured with $2''.0$ aperture at 5σ level.

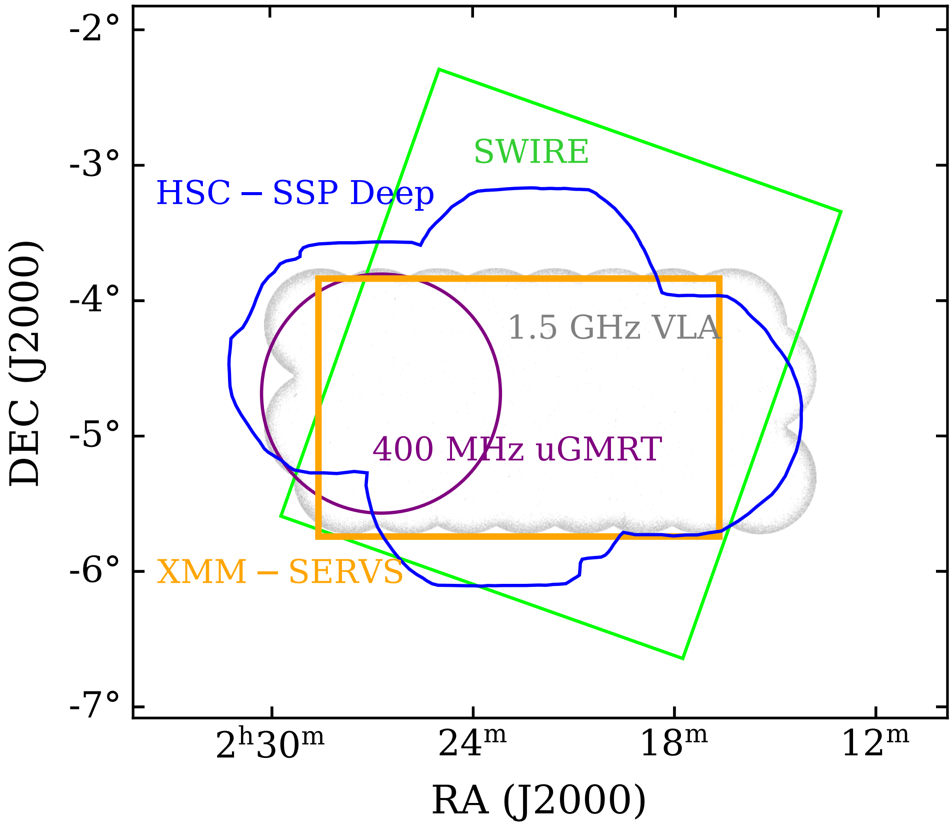

Figure 3.1: The footprints of multiwavelength surveys in the XMM-LSS field. Our study on the radio properties of DOGs is limited to 400 MHz uGMRT region.

3.3 The sample and selection criteria of DOGs

3.3.1 Selection criteria

In the literature, DOGs have been identified by using the flux ratio of FIR to optical (Toba et al., 2015). Using *Spitzer* survey data Fiore et al. (2008) demonstrated that the flux ratio of 24 μm to R band optical ($S_{24\ \mu\text{m}}/S_{\text{R}}$) $\geq$ 1000 can efficiently select DOGs. The cutoff limit of 1000 is based on the fact that it selects sources redder than the colour of most ULIRGs at all redshifts (Dey et al., 2008). The flux ratio criterion corresponds to the colour cut of $R-[24] \geq 7.5$; where magnitudes are measured in the AB system (Oke & Gunn, 1983). To select DOGs, we first identified the optical counterparts of 24 μm sources by cross-matching the 24 μm SWIRE catalogue with the HSC-SSP optical catalogue. We use IRAC 3.6 μm counterparts positions of 24 μm sources, whenever available, considering the fact that the 3.6 μm IRAC observations provide better angular resolution ($2''.0$) than that of the MIPS at 24 μm ($5''.6$). Thus, the optical counterpart is searched around the 3.6 μm source position within a radius of $1''.0$ and the closest source is being considered as the true counterpart. In case of the unavailability of IRAC coverage we search optical counterparts around the 24 μm source position within a search radius of $2''.0$. In our cross-matching exercise, we followed the method described in Singh et al. (2015) to choose the optimum search radius which in turn ensures maximum completeness with minimum contamination by random matches. After identifying the optical counterparts of 24 μm sources, we derive a sample of 321 DOGs that satisfy the following criteria : (i) $S_{24\ \mu\text{m}}/S_r \geq 1000$, where $S_{24\ \mu\text{m}}$ and S_r are 24 μm and r band fluxes, respectively; (ii) $S_{24\ \mu\text{m}} \geq 0.4$ mJy (24 μm sample suffers incompleteness below this flux limit); (iii) sources fall within the region covered by our 400 MHz uGMRT observations. Table 3.1 shows a sample of 109 DOGs detected at radio wavelengths (see Section 3.4.1 for more details).

We note that the DOGs with no optical (r band) counterparts can be extremely obscured galaxies, although, we find that all our sample sources show optical counterparts in the HSC-SSP. We excluded sources falling within the masked regions in the HSC-SSP optical image. From $S_{24\ \mu\mathrm{m}}/S_r$ versus r band magnitude (m_r) plot (see Figure 3.2, left panel) it is evident that the DOGs in our sample are generally faint in the optical with r band magnitude distributed in the range of 22.63 to 26.97 with a median value of 25.20. We also find that the faint optical counterparts have apparently higher values of $S_{24\ \mu\mathrm{m}}/S_r$ due to the 24 μm flux cutoff limit applied in our sample selection criteria. We find that 24 μm luminosities for our sample sources, with available redshifts (see Section 3.3.2), are found to be in the range of 7.96 $\times$ 10^7 $L_{\odot}$ to 2.35 $\times$ 10^{12} $L_{\odot}$ with a median value of 1.56 $\times$ 10^{11} $L_{\odot}$. All but one of our sources with available redshifts have 24 μm luminosity higher than 4.8 $\times$ 10^{10} $L_{\odot}$ (see Table 3.1). Therefore, based on the total IR luminosities, our sources can be classified as LIRGs and ULIRGs.

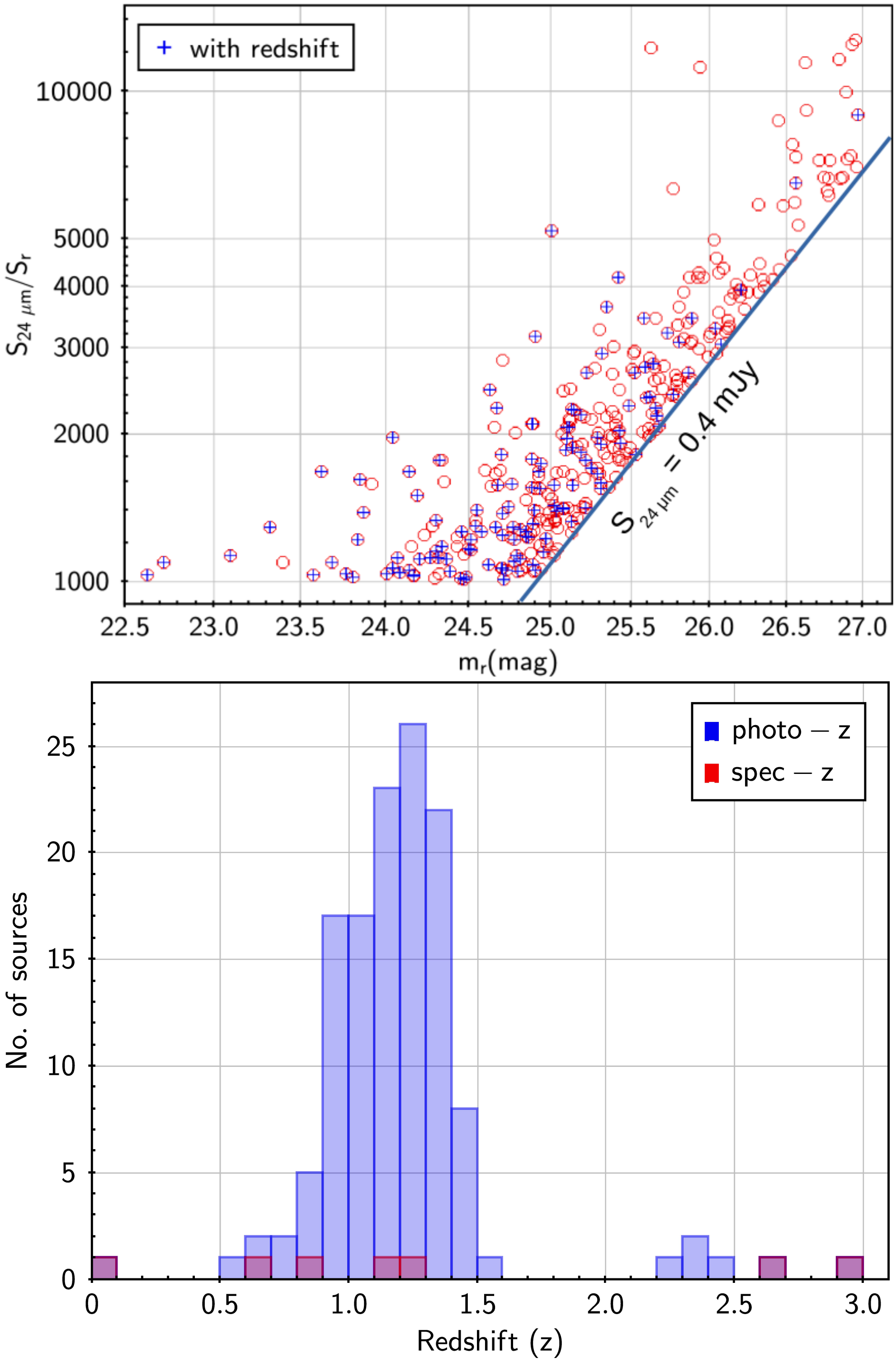

Figure 3.2: *Top panel*: The flux ratio of 24 μm to r band ($S_{24\ \mu\mathrm{m}}/S_r$) versus r band magnitude (m_r). As expected, sources with redshifts are relatively bright and have lower value of 24 μm mid-IR to r band optical flux ratio. *Bottom panel*: The histogram of available redshift estimates for our sample DOGs. The redshifts are based on the HSC-SSP PDR 3 redshift catalogue.

Table 3.1: The sample of radio-detected DOGs

RA (h m s)	DEC (d m s)	S_{24} (mJy)	S_r (mag)	S_{24}/S_r (10^3)	$S_{400\ \mathrm{MHz}}$ (mJy)	$S_{1.5\ \mathrm{GHz}}$ (mJy)	$\alpha_{400\ \mathrm{MHz}}^{1.5\ \mathrm{GHz}}$	z	$\log L_{400\ \mathrm{MHz}}$ (W Hz^{-1})	$\log L_{1.5\ \mathrm{GHz}}$ (W Hz^{-1})
02 : 23 : 23	−04 : 49 : 26	0.52 ± 0.02	24.93 ± 0.03	1.34	1.37 ± 0.17	0.38 ± 0.01	-0.96 ± -0.22	> 1.0	> 24.85	> 24.3
02 : 23 : 24	−04 : 26 : 03	0.55 ± 0.03	24.81 ± 0.03	1.27	0.75 ± 0.15	0.29 ± 0.01	-0.71 ± -0.36	1.17 ± 0.12 (p)	24.76 ± 0.2	24.35 ± 0.03
02 : 23 : 42	−04 : 43 : 56	0.8 ± 0.02	24.63 ± 0.04	1.57	0.65 ± 0.2	0.18 ± 0.004	-0.99 ± -0.54	> 1.0	> 24.53	> 23.97
02 : 23 : 44	−04 : 56 : 34	0.52 ± 0.03	25.4 ± 0.08	2.09	—	0.07 ± 0.005	—	> 1.0	—	> 23.57
02 : 23 : 47	−04 : 20 : 46	0.92 ± 0.03	24.3 ± 0.03	1.34	0.57 ± 0.15	0.1 ± 0.005	-1.33 ± -0.48	1.26 ± 0.13 (p)	24.72 ± 0.26	23.97 ± 0.05
02 : 23 : 49	−05 : 04 : 53	0.94 ± 0.02	24.01 ± 0.02	1.03	0.89 ± 0.14	0.35 ± 0.01	-0.71 ± -0.28	0.0337 ± 0.0001 (s)	21.37 ± 0.16	21.0 ± 0.03
02 : 23 : 49	−04 : 59 : 16	0.51 ± 0.03	24.99 ± 0.07	1.38	—	0.14 ± 0.005	—	> 1.0	—	> 23.86
02 : 23 : 54	−04 : 14 : 37	1.34 ± 0.03	23.68 ± 0.01	1.1	0.57 ± 0.17	0.13 ± 0.004	-1.11 ± -0.54	1.32 ± 0.12 (p)	24.77 ± 0.3	24.13 ± 0.03
02 : 23 : 55	−04 : 50 : 34	0.61 ± 0.03	24.45 ± 0.03	1.02	—	0.14 ± 0.005	—	1.55 ± 0.12 (p)	—	24.34 ± 0.04
02 : 23 : 57	−04 : 36 : 00	0.44 ± 0.03	24.98 ± 0.04	1.19	—	0.05 ± 0.003	—	> 1.0	—	> 23.41
02 : 23 : 57	−04 : 45 : 54	0.66 ± 0.03	24.74 ± 0.04	1.42	—	0.06 ± 0.004	—	1.22 ± 0.09 (p)	—	23.71 ± 0.07
02 : 24 : 00	−04 : 31 : 26	0.58 ± 0.03	26.06 ± 0.1	4.27	—	0.15 ± 0.004	—	> 1.0	—	> 23.89
02 : 24 : 03	−04 : 38 : 53	0.82 ± 0.03	24.66 ± 0.02	1.66	—	0.24 ± 0.01	—	> 1.0	—	> 24.1
02 : 24 : 11	−04 : 42 : 32	0.88 ± 0.03	24.08 ± 0.02	1.04	—	0.03 ± 0.003	—	1.01 ± 0.22 (p)	—	23.2 ± 0.1
02 : 24 : 15	−04 : 41 : 02	0.72 ± 0.02	25.13 ± 0.04	2.24	—	0.13 ± 0.01	—	1.22 ± 0.2 (p)	—	24.05 ± 0.08
02 : 24 : 24	−05 : 08 : 37	0.56 ± 0.03	25.85 ± 0.15	3.38	0.57 ± 0.15	0.15 ± 0.004	-1.01 ± -0.46	> 1.0	> 24.47	> 23.89
02 : 24 : 26	−04 : 48 : 29	0.6 ± 0.03	25.13 ± 0.06	1.88	1.06 ± 0.09	0.33 ± 0.005	-0.89 ± -0.16	1.12 ± 0.12 (p)	24.87 ± 0.08	24.36 ± 0.02
02 : 24 : 28	−04 : 33 : 53	0.63 ± 0.03	26.05 ± 0.17	4.58	0.52 ± 0.11	0.15 ± 0.004	-0.94 ± -0.37	> 1.0	> 24.43	> 23.89
02 : 24 : 35	−05 : 11 : 27	0.63 ± 0.02	26.32 ± 0.12	5.88	0.79 ± 0.1	0.2 ± 0.004	-1.02 ± -0.22	> 1.0	> 24.62	> 24.02
02 : 24 : 35	−04 : 56 : 09	0.45 ± 0.02	26.58 ± 0.21	5.33	—	0.05 ± 0.004	—	> 1.0	—	> 23.41
02 : 24 : 36	−04 : 13 : 01	0.53 ± 0.03	25.49 ± 0.07	2.29	2.4 ± 0.12	0.67 ± 0.01	-0.97 ± -0.09	1.39 ± 0.23 (p)	25.45 ± 0.05	24.9 ± 0.01
02 : 24 : 37	−05 : 06 : 09	0.64 ± 0.03	24.93 ± 0.06	1.64	0.33 ± 0.08	0.12 ± 0.005	-0.77 ± -0.44	> 1.0	> 24.24	> 23.8
02 : 24 : 37	−04 : 03 : 34	0.48 ± 0.03	26.13 ± 0.11	3.78	—	0.1 ± 0.004	—	> 1.0	—	> 23.72
02 : 24 : 40	−04 : 59 : 27	0.56 ± 0.02	24.98 ± 0.04	1.51	0.27 ± 0.07	0.13 ± 0.005	-0.57 ± -0.43	> 1.0	> 24.15	> 23.83
02 : 24 : 44	−04 : 49 : 56	0.68 ± 0.03	25.87 ± 0.13	4.18	0.19 ± 0.06	—	—	> 1.0	> 24.0	—
02 : 24 : 44	−04 : 43 : 35	0.68 ± 0.02	25.07 ± 0.04	2.0	0.34 ± 0.06	0.06 ± 0.004	-1.27 ± -0.32	> 1.0	> 24.25	> 23.49
02 : 24 : 48	−04 : 43 : 35	0.43 ± 0.02	25.61 ± 0.07	2.06	0.25 ± 0.05	0.09 ± 0.01	-0.74 ± -0.39	> 1.0	> 24.12	> 23.67
02 : 24 : 48	−04 : 36 : 08	0.44 ± 0.02	24.89 ± 0.03	1.08	—	0.06 ± 0.003	—	1.23 ± 0.22 (p)	—	23.72 ± 0.05
02 : 24 : 48	−04 : 58 : 51	0.48 ± 0.03	25.07 ± 0.05	1.42	0.45 ± 0.07	0.26 ± 0.01	-0.42 ± -0.29	1.31 ± 0.3 (p)	24.66 ± 0.16	24.42 ± 0.04
02 : 24 : 51	−05 : 08 : 49	0.59 ± 0.03	24.48 ± 0.05	1.02	0.46 ± 0.11	0.1 ± 0.004	-1.16 ± -0.42	0.99 ± 0.12 (p)	24.37 ± 0.24	23.71 ± 0.04
02 : 24 : 57	−04 : 21 : 26	0.54 ± 0.02	25.41 ± 0.06	2.16	2.71 ± 0.09	2.8 ± 0.01	0.02 ± -0.06	> 1.0	> 25.15	> 25.17

Table 3.1 – *Continued*

RA (h m s)	DEC (d m s)	S_{24} (mJy)	S_r (mag)	S_{24}/S_r (10^3)	$S_{400\ \mathrm{MHz}}$ (mJy)	$S_{1.5\ \mathrm{GHz}}$ (mJy)	$\alpha_{400\ \mathrm{MHz}}^{1.5\ \mathrm{GHz}}$	z	log $L_{400\ \mathrm{MHz}}$ (W Hz^{-1})	log $L_{1.5\ \mathrm{GHz}}$ (W Hz^{-1})
02 : 24 : 59	−04 : 14 : 13	3.24 ± 0.03	22.72 ± 0.01	1.09	0.9 ± 0.1	0.3 ± 0.004	-0.83 ± -0.2	1.9 ± 0.57 (p)	25.36 ± 0.11	24.88 ± 0.01
02 : 25 : 02	−05 : 10 : 20	0.47 ± 0.03	26.78 ± 0.25	6.64	0.35 ± 0.1	—	—	> 1.0	> 24.26	—
02 : 25 : 02	−04 : 46 : 06	0.63 ± 0.03	24.88 ± 0.03	1.55	0.45 ± 0.1	0.19 ± 0.01	-0.66 ± -0.38	1.06 ± 0.08 (p)	24.43 ± 0.22	24.06 ± 0.05
02 : 25 : 05	−04 : 40 : 17	0.51 ± 0.03	26.78 ± 0.25	7.24	—	0.09 ± 0.004	—	> 1.0	—	> 23.67
02 : 25 : 09	−04 : 45 : 50	0.41 ± 0.03	25.88 ± 0.09	2.56	0.29 ± 0.07	—	—	> 1.0	> 24.18	—
02 : 25 : 09	−05 : 00 : 33	2.2 ± 0.02	23.32 ± 0.01	1.29	0.74 ± 0.09	0.2 ± 0.004	-1.01 ± -0.22	1.03 ± 0.23 (p)	24.62 ± 0.12	24.05 ± 0.02
02 : 25 : 10	−04 : 04 : 01	0.66 ± 0.02	25.51 ± 0.06	2.92	5.36 ± 0.14	1.44 ± 0.01	-0.99 ± -0.05	> 1.0	> 25.45	> 24.88
02 : 25 : 12	−04 : 47 : 22	0.69 ± 0.03	25.12 ± 0.04	2.13	0.36 ± 0.07	—	—	1.76 ± 0.10 (p)	24.88 ± 0.19	—
02 : 25 : 14	−04 : 34 : 19	2.38 ± 0.04	23.09 ± 0.01	1.13	1.08 ± 0.07	0.27 ± 0.004	-1.03 ± -0.12	3.54 ± 0.14 (p)	26.09 ± 0.06	25.49 ± 0.01
02 : 25 : 15	−04 : 32 : 34	0.42 ± 0.03	26.22 ± 0.11	3.59	—	0.06 ± 0.004	—	> 1.0	—	> 23.49
02 : 25 : 21	−04 : 08 : 44	1.25 ± 0.03	24.9 ± 0.03	3.16	0.33 ± 0.1	0.13 ± 0.01	-0.72 ± -0.53	1.60 ± 0.26 (p)	24.74 ± 0.3	24.34 ± 0.08
02 : 25 : 21	−05 : 22 : 19	0.43 ± 0.02	25.31 ± 0.04	1.59	—	0.1 ± 0.004	—	1.29 ± 0.26 (p)	—	23.99 ± 0.04
02 : 25 : 24	−05 : 28 : 28	2.16 ± 0.03	23.62 ± 0.02	1.67	1.3 ± 0.23	0.34 ± 0.01	-1.02 ± -0.31	1.00 ± 0.12 (p)	24.83 ± 0.18	24.25 ± 0.03
02 : 25 : 26	−04 : 30 : 58	0.66 ± 0.03	25.93 ± 0.1	4.28	0.17 ± 0.05	—	—	> 1.0	> 23.95	—
02 : 25 : 26	−04 : 32 : 35	0.79 ± 0.03	25.22 ± 0.06	2.67	0.27 ± 0.05	0.07 ± 0.004	-0.99 ± -0.33	1.35 ± 0.29 (p)	24.47 ± 0.19	23.89 ± 0.06
02 : 25 : 31	−05 : 07 : 09	0.67 ± 0.03	24.5 ± 0.03	1.16	0.2 ± 0.06	—	—	0.96 ± 0.12 (p)	23.98 ± 0.3	—
02 : 25 : 37	−05 : 23 : 05	0.7 ± 0.02	25.11 ± 0.07	2.14	0.5 ± 0.11	0.21 ± 0.01	-0.66 ± -0.39	> 1.0	> 24.42	> 24.04
02 : 25 : 45	−04 : 55 : 20	0.51 ± 0.03	24.7 ± 0.03	1.07	0.14 ± 0.04	—	—	0.99 ± 0.06 (p)	23.85 ± 0.29	—
02 : 25 : 45	−04 : 06 : 47	1.18 ± 0.02	23.76 ± 0.02	1.04	0.77 ± 0.07	0.3 ± 0.01	-0.71 ± -0.18	2.6427 ± 0.0001 (s)	25.64 ± 0.09	25.23 ± 0.03
02 : 25 : 46	−04 : 48 : 10	0.55 ± 0.03	26.71 ± 0.13	7.26	0.55 ± 0.04	0.29 ± 0.01	-0.48 ± -0.14	> 1.0	> 24.46	> 24.18
02 : 25 : 46	−04 : 04 : 58	0.68 ± 0.03	24.58 ± 0.03	1.27	0.35 ± 0.07	0.22 ± 0.01	-0.33 ± -0.36	2.28 ± 0.43 (p)	25.14 ± 0.2	24.94 ± 0.05
02 : 25 : 47	−04 : 28 : 09	0.62 ± 0.03	25.96 ± 0.09	4.18	0.37 ± 0.06	0.1 ± 0.004	-1.02 ± -0.29	> 1.0	> 24.29	> 23.72
02 : 25 : 49	−05 : 29 : 33	0.48 ± 0.02	25.39 ± 0.1	1.88	—	0.08 ± 0.005	—	> 1.0	—	> 23.62
02 : 25 : 52	−04 : 37 : 42	0.55 ± 0.03	25.65 ± 0.1	2.74	0.95 ± 0.04	0.37 ± 0.004	-0.71 ± -0.08	> 1.0	> 24.7	> 24.29
02 : 25 : 53	−05 : 04 : 46	0.56 ± 0.02	25.18 ± 0.07	1.83	0.27 ± 0.06	—	—	1.35 ± 0.22 (p)	24.47 ± 0.22	—
02 : 25 : 55	−04 : 50 : 34	0.42 ± 0.03	25.8 ± 0.13	2.41	0.18 ± 0.05	—	—	> 1.0	> 23.97	—
02 : 25 : 55	−05 : 02 : 13	0.6 ± 0.02	24.7 ± 0.03	1.25	0.55 ± 0.07	0.1 ± 0.01	-1.28 ± -0.26	1.11 ± 0.21 (p)	24.57 ± 0.13	23.83 ± 0.1
02 : 25 : 59	−04 : 25 : 10	0.43 ± 0.03	25.58 ± 0.1	2.02	1.21 ± 0.05	0.64 ± 0.005	-0.49 ± -0.08	> 1.0	> 24.8	> 24.52
02 : 25 : 59	−04 : 16 : 50	0.7 ± 0.03	26.03 ± 0.1	4.98	0.27 ± 0.06	0.06 ± 0.004	-1.14 ± -0.43	> 1.0	> 24.15	> 23.49
02 : 25 : 59	−04 : 41 : 36	0.48 ± 0.02	25.07 ± 0.06	1.41	0.29 ± 0.04	0.13 ± 0.004	-0.61 ± -0.23	1.1439 ± 0.0001 (s)	24.32 ± 0.14	23.98 ± 0.03
02 : 26 : 03	−04 : 29 : 30	1.42 ± 0.02	23.87 ± 0.01	1.38	5.75 ± 0.13	1.46 ± 0.01	-1.03 ± -0.04	1.10 ± 0.07 (p)	25.58 ± 0.02	24.98 ± 0.01
02 : 26 : 05	−04 : 44 : 21	0.77 ± 0.03	25.27 ± 0.08	2.72	0.32 ± 0.06	0.13 ± 0.01	-0.68 ± -0.31	> 1.0	> 24.22	> 23.83
02 : 26 : 06	−04 : 29 : 03	1.87 ± 0.03	25.01 ± 0.04	5.19	0.87 ± 0.06	0.36 ± 0.004	-0.67 ± -0.12	1.31 ± 0.22 (p)	24.95 ± 0.07	24.56 ± 0.01

Table 3.1 – *Continued*

RA (h m s)	DEC (d m s)	S_{24} (mJy)	S_r (mag)	S_{24}/S_r (10^3)	$S_{400\ \mathrm{MHz}}$ (mJy)	$S_{1.5\ \mathrm{GHz}}$ (mJy)	$\alpha_{400\ \mathrm{MHz}}^{1.5\ \mathrm{GHz}}$	z	$\log L_{400\ \mathrm{MHz}}$ (W Hz^{-1})	$\log L_{1.5\ \mathrm{GHz}}$ (W Hz^{-1})
02 : 26 : 09	−04 : 33 : 35	0.52 ± 0.02	25.31 ± 0.06	1.9	26.88 ± 0.71	9.33 ± 0.01	-0.8 ± -0.05	0.8979 ± 0.0001 (s)	26.03 ± 0.03	25.57 ± 0.001
02 : 26 : 10	−04 : 04 : 32	1.29 ± 0.03	23.84 ± 0.02	1.21	0.75 ± 0.09	0.12 ± 0.005	-1.38 ± -0.22	0.74 ± 0.12 (p)	24.28 ± 0.12	23.48 ± 0.04
02 : 26 : 11	−04 : 51 : 55	0.48 ± 0.03	26.32 ± 0.13	4.45	0.43 ± 0.05	0.21 ± 0.005	-0.53 ± -0.19	> 1.0	> 24.35	> 24.04
02 : 26 : 15	−04 : 47 : 26	0.41 ± 0.03	25.53 ± 0.09	1.82	0.17 ± 0.05	0.09 ± 0.01	-0.51 ± -0.49	2.35 ± 0.12 (p)	24.86 ± 0.29	24.59 ± 0.11
02 : 26 : 19	−04 : 42 : 26	0.49 ± 0.02	26.75 ± 0.23	6.69	0.3 ± 0.05	—	—	> 1.0	> 24.2	—
02 : 26 : 19	−04 : 15 : 05	0.92 ± 0.03	24.28 ± 0.04	1.3	0.34 ± 0.07	0.09 ± 0.01	-1.01 ± -0.41	> 1.0	> 24.25	> 23.67
02 : 26 : 20	−04 : 45 : 36	0.8 ± 0.02	24.3 ± 0.03	1.15	0.22 ± 0.05	—	—	1.2706 ± 0.0001 (s)	24.32 ± 0.23	—
02 : 26 : 22	−05 : 04 : 21	1.03 ± 0.03	24.65 ± 0.02	2.07	0.27 ± 0.07	0.08 ± 0.004	-0.93 ± -0.47	3.77 ± 0.3 (p)	25.56 ± 0.26	25.03 ± 0.05
02 : 26 : 23	−04 : 33 : 41	0.58 ± 0.03	25.19 ± 0.07	1.9	0.19 ± 0.05	—	—	> 1.0	> 24.0	—
02 : 26 : 25	−04 : 23 : 12	0.43 ± 0.03	25.5 ± 0.07	1.88	0.21 ± 0.06	0.09 ± 0.005	-0.59 ± -0.53	> 1.0	> 24.04	> 23.67
02 : 26 : 31	−05 : 00 : 44	0.45 ± 0.03	25.3 ± 0.09	1.66	0.35 ± 0.06	0.06 ± 0.004	-1.39 ± -0.34	> 1.0	> 24.26	> 23.49
02 : 26 : 31	−04 : 59 : 00	0.84 ± 0.03	24.2 ± 0.03	1.11	0.44 ± 0.05	0.15 ± 0.004	-0.79 ± -0.21	1.01 ± 0.1 (p)	24.37 ± 0.11	23.9 ± 0.03
02 : 26 : 33	−04 : 43 : 06	0.76 ± 0.02	24.43 ± 0.04	1.23	0.89 ± 0.05	0.4 ± 0.01	-0.6 ± -0.1	2.33 ± 0.65 (p)	25.57 ± 0.06	25.22 ± 0.02
02 : 26 : 35	−04 : 20 : 49	0.45 ± 0.02	25.65 ± 0.13	2.26	0.34 ± 0.05	—	—	1.02 ± 0.24 (p)	24.27 ± 0.15	—
02 : 26 : 37	−04 : 19 : 28	0.84 ± 0.02	24.89 ± 0.04	2.09	0.29 ± 0.08	—	—	1.43 ± 0.12 (p)	24.57 ± 0.28	—
02 : 26 : 41	−04 : 46 : 07	0.46 ± 0.03	26.03 ± 0.1	3.29	2.08 ± 0.07	0.45 ± 0.005	-1.16 ± -0.07	1.27 ± 0.3 (p)	25.29 ± 0.03	24.63 ± 0.01
02 : 26 : 43	−04 : 42 : 06	0.43 ± 0.03	25.47 ± 0.12	1.83	3.82 ± 0.13	0.31 ± 0.01	-1.89 ± -0.07	> 1.0	> 25.3	> 24.21
02 : 26 : 45	−04 : 11 : 11	0.47 ± 0.03	24.87 ± 0.05	1.14	0.6 ± 0.07	0.19 ± 0.01	-0.86 ± -0.2	> 1.0	> 24.5	> 24.0
02 : 26 : 46	−04 : 50 : 53	0.53 ± 0.03	24.84 ± 0.04	1.26	0.43 ± 0.06	0.16 ± 0.01	-0.74 ± -0.23	1.30 ± 0.13 (p)	24.63 ± 0.14	24.2 ± 0.06
02 : 26 : 48	−04 : 59 : 13	0.49 ± 0.02	24.98 ± 0.05	1.33	0.15 ± 0.04	0.08 ± 0.01	-0.52 ± -0.53	> 1.0	23.89 ± 0.27	23.62 ± 0.12
02 : 26 : 49	−05 : 19 : 38	0.67 ± 0.02	24.94 ± 0.24	1.74	0.37 ± 0.1	0.12 ± 0.005	-0.88 ± -0.49	1.16 ± 0.27 (p)	24.45 ± 0.27	23.96 ± 0.04
02 : 26 : 51	−04 : 19 : 54	0.73 ± 0.03	25.58 ± 0.13	3.45	0.39 ± 0.06	0.11 ± 0.005	-0.94 ± -0.28	1.28 ± 0.29 (p)	24.57 ± 0.15	24.03 ± 0.05
02 : 26 : 53	−04 : 33 : 13	0.85 ± 0.02	24.14 ± 0.02	1.06	0.37 ± 0.06	—	—	0.64 ± 0.09 (p)	23.81 ± 0.16	—
02 : 26 : 53	−04 : 41 : 30	0.74 ± 0.02	26.63 ± 0.12	9.14	0.31 ± 0.04	—	—	> 1.0	> 24.21	—
02 : 27 : 04	−05 : 17 : 34	1.18 ± 0.02	24.34 ± 0.06	1.77	—	0.13 ± 0.004	—	> 1.0	—	> 23.83
02 : 27 : 10	−04 : 35 : 14	0.44 ± 0.03	25.79 ± 0.13	2.52	0.31 ± 0.05	—	—	> 1.0	> 24.21	—
02 : 27 : 11	−04 : 47 : 29	1.72 ± 0.02	24.04 ± 0.01	1.96	0.18 ± 0.06	0.12 ± 0.005	-0.29 ± -0.57	0.95 ± 0.08 (p)	23.92 ± 0.33	23.74 ± 0.04
02 : 27 : 13	−05 : 27 : 00	1.14 ± 0.03	25.76 ± 0.17	6.34	0.63 ± 0.13	0.18 ± 0.01	-0.94 ± -0.38	> 1.0	> 24.52	> 23.97
02 : 27 : 16	−05 : 02 : 53	0.55 ± 0.03	24.92 ± 0.03	1.39	0.22 ± 0.05	0.06 ± 0.004	-0.92 ± -0.42	> 1.0	> 24.06	> 23.49
02 : 27 : 16	−04 : 55 : 51	0.65 ± 0.02	25.93 ± 0.12	4.19	0.21 ± 0.05	0.06 ± 0.003	-0.91 ± -0.45	> 1.0	> 24.04	> 23.49
02 : 27 : 16	−04 : 32 : 42	0.89 ± 0.03	24.59 ± 0.01	1.68	0.16 ± 0.04	—	—	1.45 ± 0.19 (p)	24.32 ± 0.25	—
02 : 27 : 19	−05 : 11 : 09	0.61 ± 0.03	24.91 ± 0.05	1.55	—	0.07 ± 0.004	—	> 1.0	—	> 23.57
02 : 27 : 20	−04 : 57 : 00	1.35 ± 0.03	24.14 ± 0.03	1.68	0.16 ± 0.05	—	—	1.31 ± 0.15 (p)	24.21 ± 0.31	—

Table 3.1 – *Continued*

RA (h m s)	DEC (d m s)	S_{24} (mJy)	S_r (mag)	S_{24}/S_r (10^3)	$S_{400\ \mathrm{MHz}}$ (mJy)	$S_{1.5\ \mathrm{GHz}}$ (mJy)	$\alpha^{1.5\ \mathrm{GHz}}_{400\ \mathrm{MHz}}$	z	log $L_{400\ \mathrm{MHz}}$ (W Hz^{-1})	log $L_{1.5\ \mathrm{GHz}}$ (W Hz^{-1})
02 : 27 : 20	−04 : 58 : 04	0.42 ± 0.03	24.91 ± 0.05	1.05	0.16 ± 0.04	—	—	1.32 ± 0.12 (p)	24.22 ± 0.25	—
02 : 27 : 25	−04 : 46 : 35	0.57 ± 0.03	25.08 ± 0.05	1.68	0.16 ± 0.04	—	—	> 1.0	> 23.92	—
02 : 27 : 26	−04 : 54 : 04	0.41 ± 0.03	25.36 ± 0.09	1.55	0.28 ± 0.05	—	—	> 1.0	> 24.17	—
02 : 27 : 34	−04 : 53 : 30	0.95 ± 0.03	24.07 ± 0.02	1.11	0.4 ± 0.07	0.07 ± 0.004	-1.34 ± -0.32	1.12 ± 0.08 (p)	24.44 ± 0.17	23.68 ± 0.06
02 : 27 : 48	−04 : 46 : 39	0.44 ± 0.03	24.95 ± 0.05	1.15	0.19 ± 0.06	—	—	1.37 ± 0.12 (p)	24.34 ± 0.32	—
02 : 27 : 52	−05 : 01 : 19	0.6 ± 0.03	24.47 ± 0.05	1.01	0.37 ± 0.09	0.09 ± 0.005	-1.03 ± -0.44	0.91 ± 0.09 (p)	24.18 ± 0.24	23.57 ± 0.06
02 : 27 : 52	−04 : 59 : 16	0.5 ± 0.03	25.68 ± 0.07	2.6	0.17 ± 0.06	—	—	> 1.0	> 23.95	—
02 : 27 : 53	−04 : 45 : 59	1.35 ± 0.03	24.7 ± 0.03	2.83	0.24 ± 0.06	—	—	> 1.0	> 24.1	—
02 : 27 : 58	−05 : 10 : 29	0.51 ± 0.03	24.7 ± 0.04	1.07	0.32 ± 0.06	0.1 ± 0.01	-0.91 ± -0.35	1.65 ± 0.08 (p)	24.76 ± 0.19	24.26 ± 0.1
02 : 27 : 59	−05 : 12 : 49	0.77 ± 0.03	24.67 ± 0.06	1.58	0.36 ± 0.07	—	—	0.98 ± 0.14 (p)	24.25 ± 0.19	—
02 : 28 : 10	−05 : 11 : 56	0.48 ± 0.03	24.98 ± 0.07	1.3	0.47 ± 0.07	0.14 ± 0.01	-0.9 ± -0.26	> 1.0	> 24.39	> 23.86
02 : 28 : 15	−04 : 57 : 54	2.49 ± 0.03	25.63 ± 0.06	12.25	1.46 ± 0.07	0.41 ± 0.01	-0.96 ± -0.09	> 1.0	> 24.88	> 24.33

Notes: Sources are listed in the increasing order of RA. The spectroscopic and photometric redshifts are indicated, within brackets, by ‘s’ and ‘p’, respectively.

3.3.2 Redshift estimates

We checked the availability of redshifts for our DOGs using spectroscopic and photometric redshift catalogues given in the HSC-SSP data access site[3]. The HSC−SSP PDR3 provides spectroscopic redshifts for the HSC-SSP sources, whenever available (spec-z table). The spectroscopic redshifts are gleaned from the publicly available spectroscopic redshifts surveys such as the VIMOS-VLT Deep Survey (VVDS; Le Fèvre et al., 2013), PRIsm MUlti-object Survey (PRIMUS) DR1 (Cool et al., 2013), VIMOS Public Extragalactic Redshift Survey (VIPERS; Garilli et al., 2014) in the *XMM-LSS* field. We also used the HSC-SSP PDR2 photometric redshift (photo-z) catalogue that provides redshifts obtained by using five-band HSC photometry. The photometric redshifts are derived from a photo-z code (MIZUKI; Tanaka et al., 2018) based on the SED fitting technique. To avoid highly inaccurate photo-z estimates we used photo-z estimates with reduced $\chi^2 \leq 1.5$ in the template fitting, and the fractional error on the derived redshift $\sigma_z/z \leq 0.25$. For our sample sources with no available redshifts in the photo-z catalogue, we used the photo-z catalogue provided by (Schuldt et al., 2021), who derived redshift by using a Convolutional Neural Network (CNN) method that uses galaxy images in addition to five band HSC-SSP photometric points. The CNN based photo-z estimates have an accuracy of $|z_{\rm pred} - z_{\rm ref}| = 0.12$ for the full HSC-SSP photometric in the redshift range of 0 to 4.0.

We attempt to find redshift estimates of our sample sources by cross-matching them with the available spectroscopic and photometric redshift catalogues. Following Tanaka et al. (2018) we considered the closest match within $1''.0$ radius centered at the optical positions of our sample sources. Given the high positional

[3]https://hsc.mtk.nao.ac.jp/ssp/data-release/

accuracy ($< 1''.0$) of HSS-SSP sources as well as spec$-z$ sources the optimum radius is only $1''.0$ which helps us to minimise the contamination and maximise the completeness. The cross-matching yielded spectroscopic redshifts for only seven sources that are derived from the VVDS (for five sources) and the PRIMUS (for two sources), while photometric redshifts are found for 124 sources. Thus, redshift estimates are available for only 131/321 (40.8%) of our DOGs. Using both spec$-z$ and photo$-z$ estimates we would desire to assess the reliability of redshift estimates and fraction of outliers. However, only seven of our DOGs have both spec$-z$ and photo$-z$ estimates. Therefore, due to small number statistics it is not possible to obtain an accurate assessment of the reliability of the photo$-z$ our DOGs.

Figure 3.2 (*right panel*) shows the redshift distribution spanning in the range 0.03 to 2.99 with a median value of 1.19. We find that the redshifts are mostly limited up to 1.5, and only seven sources have redshifts higher than 1.5. The lack of sources at higher redshift may be attributed to the larger inaccuracy in photo-z estimates and the faintness in the optical band for high-z sources. The comparison of r band magnitudes shows that the sources with redshift estimates have m_r in the range of 22.63 to 26.97 with a median value of 24.88, while sources with no redshifts are systematically fainter in the optical bands with m_r lying in the range of 23.39 to 26.96 with a median value of 25.49. Also, for high-z sources ($z > 2.0$) optical bands would sample the rest-frame UV light, which is strongly obscured by the dust present in host galaxies. Thus, in comparison to their low-z counterparts, the high-z DOGs are expected to be even much fainter in the optical.

3.4 Radio characteristics of DOGs

To investigate the radio emission characteristics of DOGs, we identified the radio counterparts of DOGs using 400 MHz uGMRT, 1.5 GHz VLA, and 150 MHz LOFAR observations.

3.4.1 Radio detection rates

We cross-matched our sample sources with the 400 MHz uGMRT, 1.5 GHz VLA and 150 MHz LOFAR source catalogues using an optimum search radius of $2''.0$ to $2''.5$. To ascertain the optimum value for cross-matching radius we inspected the histogram of the difference between the source positions in the two surveys and corrected for systemic positional offset, whenever found. Histograms show a sharp decline and become nearly constant after a certain radius beyond which cross-matched sources are only random matches. The same strategy has been followed in other studies (e.g., Singh et al., 2015). Further, to ensure the reliable cross-matching we also visually inspected the uGMRT and VLA radio images of our DOGs counterparts. We find that only 91/321 (28.3 per cent) DOGs are detected in the 400 MHz uGMRT observations. The detection rate in the 1.5 GHz VLA observations is a little lower, with only 83/321 (25.8 per cent) detected sources. Notably, only 65 sources are detected in both uGMRT and VLA observations, while 26 sources are detected in the uGMRT observations but not in the VLA observations, and 18 sources are detected in the VLA observations but not in the uGMRT observations. Thus, the radio detection rate of our sample DOGs is 109/321 $\simeq$ 34 per cent if detection at one frequency (either 400 MHz or 1.5 GHz) is considered. We note that our detections are limited to $\geq 5\sigma$ level, and hence, non-detection can still show a faint emission falling below the 5σ limit. In Figure 3.3 we show 24 μm MIPS, r band HSC-SSP, 400 MHz uGMRT and 1.5

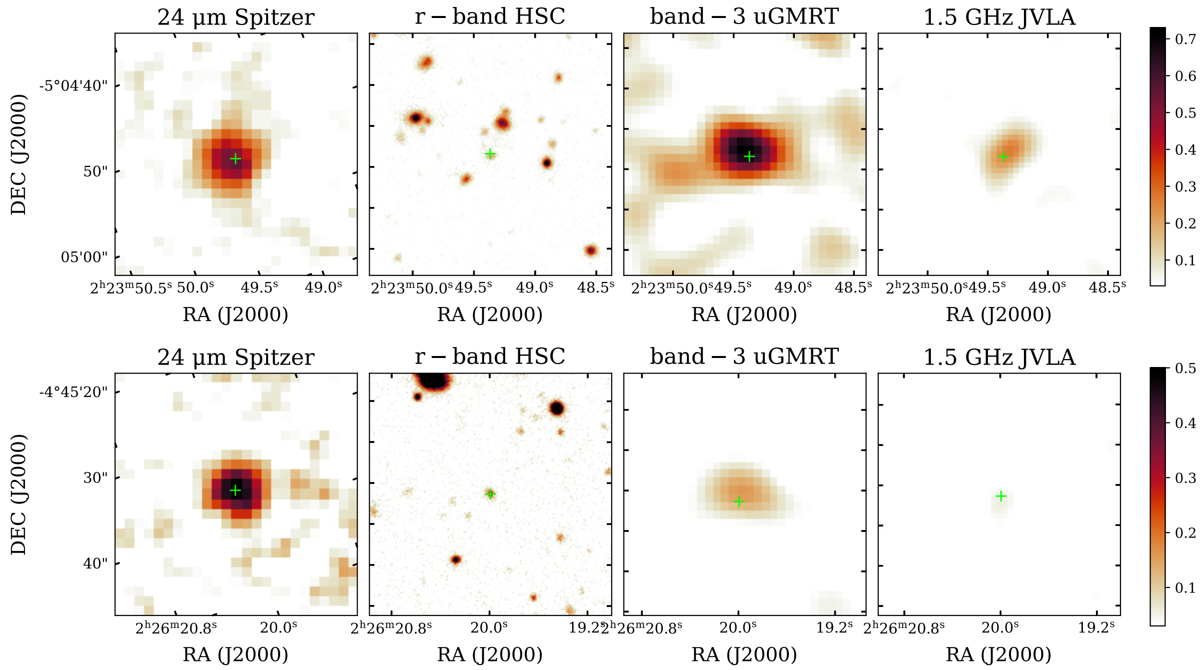

Figure 3.3: The 24 μm FIR, r band optical, 400 MHz uGMRT and 1.5 GHz VLA radio images of two representative DOGs from our sample. The upper panel shows a case where source is detected in both 400 MHz uGMRT ($S_{400\ \mathrm{MHz}} = 0.89 \pm 0.14$ mJy) and 1.5 GHz VLA ($S_{1.5\ \mathrm{GHz}} = 0.35 \pm 0.01$ mJy). The lower panel presents a case where source is detected only in the uGMRT ($S_{400\ \mathrm{MHz}} = 0.22 \pm 0.04$ mJy) but falls below the 5σ detection limit of the VLA, although a faint emission is apparent. All the images are of $30'' \times 30''$. The plus symbol represents the optical position of sources. A vertical colour bar indicates intensity level in mJy beam^{-1}.

GHz VLA images of the two of our sample sources. In J022349-050453, we detect radio counterparts in both 400 MHz uGMRT and 1.5 GHz VLA observations (see Figure 3.3 *upper panel*). While, in J022619-044536, we detect only a faint emission at 1.5 GHz falling below the 5σ detection limit (see Figure 3.3 *bottom panel*).

Table 3.2: The radio detection rates in different surveys.

Radio observations	Frequency (MHz)	BW (MHz)	5σ depth (mJy beam^{-1})	Resolution ($'' \times ''$)	$N_{\rm Detected}$	Detection rate (per cent)
uGMRT	400	200	0.15	6.7 $\times$ 5.3	91/321	28.3
VLA	1500	1000	0.08	4.5 $\times$ 4.5	83/321	25.8
LOFAR	150	130	1.4-1.97	7.5 $\times$ 8.5	11/316	3.5
FIRST	1400	128	1.0	5.0 $\times$ 5.0	02/321	0.6
VLASS	3000	2000	0.6	2.5 $\times$ 2.5	03/321	0.9
All (uGMRT or VLA)					109/321	34

In Table 3.2 we list the basic parameters (frequency, bandwidth, sensitivity and resolution) of different radio observations and the detection rates of our sample DOGs in them. We note that a somewhat higher detection rate in the 400 MHz uGMRT observations than that in the 1.5 GHz VLA can be attributed to its better sensitivity. The 5σ median sensitivity of 0.15 mJy beam^{-1} of our 400 MHz uGMRT observations correspond to 0.06 mJy beam^{-1} at 1.5 GHz, assuming a typical spectral index of -0.7. Thus, our 400 MHz uGMRT observations are deeper than 1.5 GHz VLA observations having an average 5σ depth 0.08 mJy beam^{-1}. Moreover, the detection of several sources at only one frequency (in 400 MHz uGMRT but not in 1.5 GHz VLA or vice versa) can be due to the diverse spectral properties of radio sources, *i.e.*, steep sources are preferentially detected in the uGMRT observations while VLA observations can detect flat spectrum sources (see Section 3.4.4 for more discussion).

We note that (316/321) majority of our sample sources fall within the 150 MHz LOFAR footprints; however, only 11/316 (3.5 per cent) sources show detection in the LOFAR observations. All the sources detected in the LOFAR observations are relatively bright ($S_{150\ \rm MHz} > 1.5$ mJy) and are also detected in both 400 MHz uGMRT as well as 1.5 GHz VLA observations. A much lower detection rate in the LOFAR observations is due to its relatively low sensitivity and the faintness of radio emission in our sample DOGs. We also checked the radio counterparts of our sample sources in the 1.4 GHz FIRST and 3 GHz VLASS, and found only two and three sources, respectively. Thus, the detection rate of our sample sources in the FIRST and VLASS is $<$ 1.0 per cent. We point out that our results are consistent with the findings of Gabányi et al. (2021) who reported that only 2 per cent of their *WISE*-selected IR-bright DOGs are detected in the FIRST. For our sample sources, the lower detection rate ($<$ 1.0 per cent) found in the FIRST can be because that our *Spitzer*-selected DOGs are much fainter in the FIR than the *WISE*-selected DOGs. This is further vindicated by the fact that, in our sample itself, we find that the radio-detected DOGs are somewhat brighter at 24 μm than those not detected in the radio. In our sample, the radio-detected DOGs have 24 μm fluxes in the range of 0.41 mJy to 3.2 mJy with a median value of 0.6 mJy, while, the radio undetected DOGs have 24 μm fluxes distributed over a similar range (0.4 mJy to 3.3 mJy) but have a lower median value of 0.52 mJy.

3.4.2 Flux densities

We examine the flux density distributions of our sample sources in different radio observations.

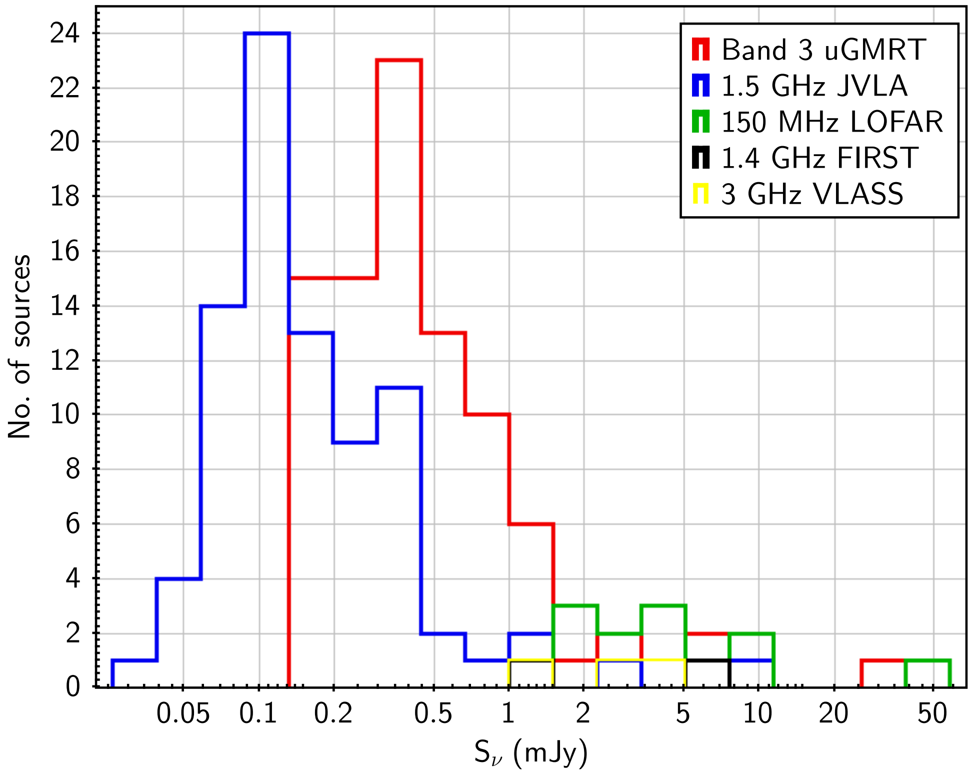

Figure 3.4: The flux density distributions of radio-detected sources in different observations. The band-3 uGMRT (red) and 1.5 GHz VLA (blue) surveys detect much fainter sources having flux densities down to 0.137 mJy and 0.035 mJy respectively, as compared to LOFAR (green), FIRST (black) and VLASS (yellow) surveys.

Figure 3.4 shows the flux density distributions of our radio-detected DOGs at 400 MHz, 1.5 GHz and 150 MHz. Table 3.3 lists the range and median values of flux density distributions. We find that 400 MHz flux densities of 91/321 radio-detected DOGs are distributed in the range of 0.137 mJy to 26.88 mJy with a median value of 0.37 mJy. The 1.5 GHz flux densities are found in the range of 0.035 mJy to 9.33 mJy, with a median value of 0.13 mJy. Unlike uGMRT and VLA observations, the LOFAR detections are limited only to relatively bright 11 sources with 150 MHz flux densities in the range of 1.56 mJy to 40 mJy with a median value of 3.75 mJy. We note that the flux density distributions at different frequencies may not offer a direct comparison, although both 400 MHz and 1.5 GHz flux density distributions show that the radio emission in our sample DOGs are generally faint at the level of sub-mJy that remained mostly undetected in the FIRST and VLASS surveys.

Table 3.3: The range and median values of various parameters.

Parameter (unit)	N_{sources}	Range	Median
Optical properties			
m_r	321	22.63 - 26.97	25.21
redshift (z)	131	0.034 - 2.99	1.19
IR properties			
$S_{24\ \mu\text{m}}$ (mJy)	321	0.4 - 3.3	0.55
$\log(\nu L_{24\ \mu\text{m}})$ ($L_{\odot}$)	131	7.9 - 12.37	11.19
Radio properties			
$S_{400\ \text{MHz uGMRT}}$ (mJy)	91	0.137 - 26.88	0.37
$S_{1.5\ \text{GHz, VLA}}$ (mJy)	83	0.035 - 9.33	0.13
$S_{150\ \text{MHz, LOFAR}}$ (mJy)	11	1.56 - 40.0	3.75
$\alpha_{400\ \text{MHz}}^{1.5\ \text{GHz}}$	65	-1.89 - 0.02	-0.91
$\log(L_{400\ \text{MHz}})$ (W Hz^{-1})	44	21.36 - 25.98	24.45
$\log(L_{1.5\ \text{GHz}})$ (W Hz^{-1})	39	20.95 - 25.52	23.95

It is worth mentioning that using stacking of FIRST image cutouts, Gabányi et al. (2021) reported the median 1.4 GHz flux density to be nearly 0.16 mJy in their sample of IR-bright PL-DOGs. Our 1.5 GHz VLA observations detect all the sources with flux density above 0.16 mJy. Hence, we emphasize that our deep uGMRT and VLA observations allow the direct detection of radio emission in DOGs that was only anticipated from the stacking of the FIRST images.

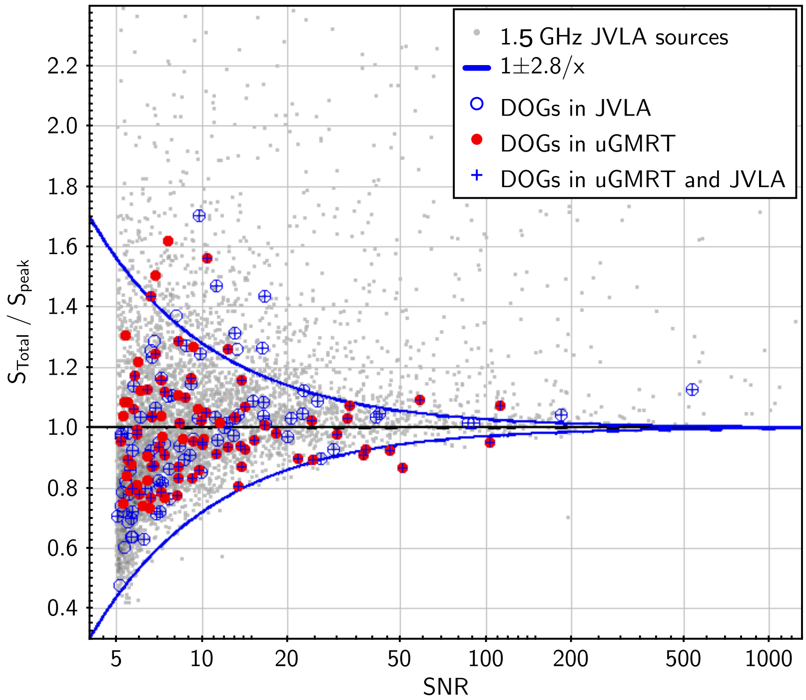

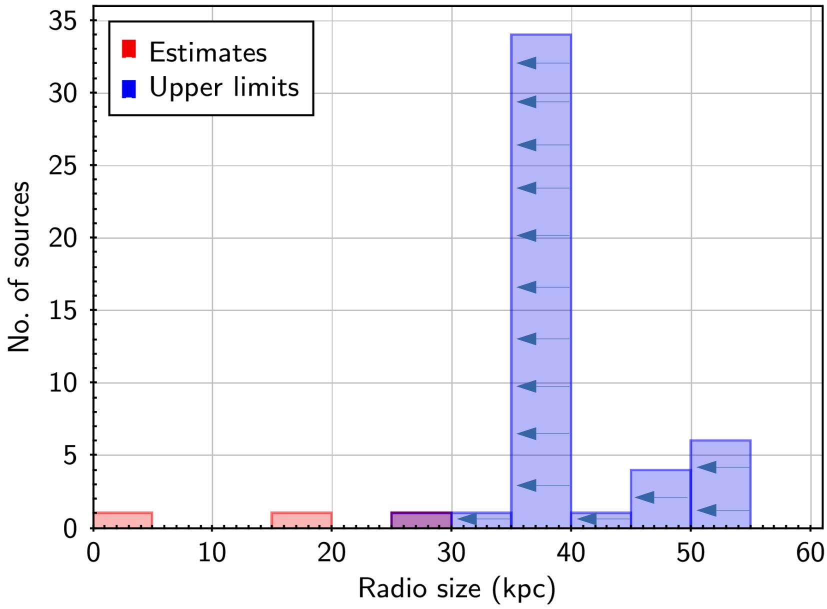

Figure 3.5: *Top panel*: The ratio of total-to-peak flux density versus SNR plot. Sources falling within the envelope of blue curves are unresolved point sources. The sources detected in both uGMRT and VLA observations appear twice as the values based on both observations are shown. An offset on the ratio of total-to-peak flux density seen in the uGMRT observations is adjusted to 1. The y-axis is restricted to 2.4 for highlighting the trend shown by the faint point sources. *Bottom panel*: The histogram of physical sizes of 50 radio-detected DOGs having redshift estimates. Most of our sources are unresolved point sources.

3.4.3 Radio sizes and morphologies

The size and morphology of radio emission are important parameters for unveiling the nature of a radio source. A typical double-lobe radio morphology can be considered as an unambiguous signature of AGN-jet activity. The radio size of AGN-jet system can also infer the evolutionary stage of radio source (An & Baan, 2012). For our sample sources, the source extraction algorithm provides the source size measurements by fitting one or more two-dimensional elliptical Gaussians to the radio emission. However, the presence of noise peaks around a source can affect the fitted size, particularly in the case of faint sources. To account for the errors introduced by noise peaks, we use the diagnostic plot of the total-to-peak flux density ratio versus signal-to-noise ratio (SNR) (see Figure 3.5 (*Left panel*)). This method is commonly used in the studies involving a large faint radio source population (see Singh & Chand, 2018; Ishwara-Chandra et al., 2020). We note that the unresolved point sources are expected to have $S_{\rm total}/S_{\rm peak} = 1.0$. Although, Figure 3.5 (*Left panel*) shows an increasingly large dispersion around $S_{\rm total}/S_{\rm peak} = 1.0$ line for fainter sources that suffer higher fractional error caused by the negative and positive noise peaks present around them. To account for the errors, we plot a curve defined as $y = 1 - \frac{2.8}{x}$ that envelopes nearly all the sources unexpectedly falling below $S_{\rm total}/S_{\rm peak} = 1.0$ line. The reflection of this curve around $S_{\rm total}/S_{\rm peak} = 1.0$ line defined as $y = 1 + \frac{2.8}{x}$ is plotted to account for the errors introduced by positive noise peaks. All the sources falling within the upper and lower curves $y = 1 \pm \frac{2.8}{x}$ can be assumed as unresolved point sources, while extended sources lie outside the upper envelope curve.

From the total-to-peak flux density ratio versus SNR diagnostic plot, we find that all but seven of our radio sources are unresolved point sources (see Figure 3.5 (*Left panel*)). We visually inspected all seven sources and find that only five sources appear marginally resolved in the 400 MHz uGMRT or 1.5 GHz VLA images. We fitted resolved sources with two dimensional Gaussian using the JMFIT task in the Astronomical Image Processing System (AIPS[4]) that provides deconvolved sizes along with other parameters such as peak flux densities, integrated flux densities, and convolved sizes. We measure the radio sizes by considering the geometric mean of the deconvolved major axis and minor axis. Notably, deconvolved sizes of marginally resolved sources are of only a few arcsec. Thus, we find that the radio-detected DOGs in our sample exhibit mostly (104/109 $\sim$ 95.4%) unresolved or marginally resolved radio emission in the 400 MHz uGMRT and 1.5 GHz VLA observations. Hence, we conclude that, in general, radio emission in DOGs is likely to be compact such that it appears unresolved in the 400 MHz uGMRT and 1.5 GHz VLA observations having resolution of $6''.0$ and $4''.5$, respectively. Our results are consistent with the findings of Gabányi et al. (2021) who reported that the IR-bright DOGs in their sample mostly exhibit unresolved radio emission in the 1.4 GHz FIRST observations with $5''.0$ resolution. Further, five of our sample sources classified as resolved are only marginally extended and do not reveal radio structures. Thus, we find that the morphological details of our sample sources remained unclear due to the fact that only unresolved or slightly resolved emission is seen in our 400 MHz uGMRT and 1.5 GHz VLA images.

We also attempted to constrain the physical sizes of the radio emission in our sample sources. Among 109 radio-detected sources only 50 sources (47 unresolved and three resolved sources) have available redshift estimates. For unresolved sources, we place an upper limit of $4''.5$ on their angular sizes using the VLA observations, whenever available, otherwise $6''.0$ upper limit is used from the uGMRT observations. We use deconvolved radio sizes for slightly resolved

[4]http://www.aips.nrao.edu/index.shtml

sources. Figure 3.5 (*Right panel*) shows the distribution of physical radio sizes or the upper limits placed on them for our sample sources. We find that the upper limits on physical sizes for 47/50 sources are distributed in the range of 29.4 kpc to 50.7 kpc with a median value of 37.5 kpc. The three marginally resolved sources have radio sizes of 2.7 kpc, 17.8 kpc and 26.8 kpc. From Figure 3.5 (*Right panel*) it is evident that the physical radio sizes in our sample DOGs are mostly smaller than 40 kpc and the radio-emitting structures are expected to reside within the host galaxy. We note that recently Patil et al. (2020) studied IR-bright radio-bright DOGs using 10 GHz VLA observations of sub-arcsec resolution and found that nearly 93/155 (60%) of their sample sources exhibit compact sizes of $< 0''.2$ that corresponds to 1.7 kpc at $z = 2.0$. Thus, we infer that, similar to radio-bright DOGs, our radio-faint ($S_{1.4\ \rm GHz} < 1.0$ mJy) DOGs powered by the AGN (see Section 3.5) can possess radio jets of a few kpc.

3.4.4 Radio spectral characteristics

We examined the radio spectral indices of our sample sources using their total flux densities measured at 400 MHz and 1.5 GHz. Only 65/109 radio-detected sources have detections at both frequencies. We obtained an upper limit on the spectral indices of 26 sources detected at 400 MHz but not at 1.5 GHz. The 18 sources detected at 1.5 GHz but not at 400 MHz have only lower limits on their spectral indices. Figure 3.6 (*Left panel*) shows the histogram of two-point spectral index measured between 400 MHz and 1.5 GHz ($\alpha_{400\ \rm MHz}^{1.5\ \rm GHz}$). We find that the distribution of $\alpha_{400\ \rm MHz}^{1.5\ \rm GHz}$ spans in the range of -1.89 to $+0.02$ with a median value of -0.91. The typical uncertainty in the spectral index of an individual source is $<$ 10 per cent. Notably, the median value is different than that ($\alpha = -0.7$) usually seen for the general radio source population. Figure 3.6 (*Left panel*) shows that the spectral index ($\alpha_{400\ \rm MHz}^{1.5\ \rm GHz}$) distribution for our sample sources is bimodal, *i.e.*, one set of sources show steep spectral index ($\alpha_{400\ \mathrm{MHz}}^{1.5\ \mathrm{GHz}} < -0.9$), while another set of sources shows a relatively flat spectral index ($\alpha_{400\ \mathrm{MHz}}^{1.5\ \mathrm{GHz}} > -0.8$). The distributions of upper and lower limits on $\alpha_{400\ \mathrm{MHz}}^{1.5\ \mathrm{GHz}}$ also reinforce the bimodal trend.

To gain more insights into the nature of our sample sources we plot spectral indices versus physical radio sizes (see Figure 3.6, *Right panel*). It is clear that the steep spectrum sources are mostly compact, and hence, these can be classified as the Compact-Steep-Spectrum (CSS) sources. The CSS sources are known to exhibit the jet-lobe structure of a few kpc to a few tens of kpc with a steep spectrum ($\alpha < -1.0$) and represent radio galaxies in their early phase of evolution (O'Dea & Saikia, 2021). Our remaining sample sources with non-steep spectral index are also compact (see Figure 3.6, *Right panel*). Given the small sizes but non-steep spectral indices, these sources can possibly constitute Peaked-Spectrum (PS) sources that are believed to represent the earliest phase of the evolution of radio galaxy with sizes $<$ 1.0 kpc. The PS sources exhibit a peak in their radio spectrum, and based on the peak frequency (ν_{p}), they can be classified as the GHz-Peaked-Spectrum (GPS, 1.0 GHz $\leq \nu_{\mathrm{p}} \leq$ 5.0 GHz) sources, the High-Frequency-Peakers (HFP, $\nu_{\mathrm{p}} >$ 5.0 GHz) and the MHz-Peaked-Spectrum (MPS, $\nu_{\mathrm{p}} <$ 1.0 GHz) (see O'Dea & Saikia, 2021). In Figure 3.6 (*Right panel*), we classify compact non-steep spectrum sources as the PS candidates considering that the two-point spectrum is insufficient to confirm the presence of peak in the radio spectrum. We note that the multi-frequency broadband radio SEDs are required to determine ν_{p} to confirm their nature. To examine the spectral behaviour at lower frequencies, we used 150 MHz flux densities, whenever available. Figure 3.7 shows a plot of $\alpha_{400\ \mathrm{MHz}}^{1.5\ \mathrm{GHz}}$ versus $\alpha_{150\ \mathrm{MHz}}^{400\ \mathrm{MHz}}$ in which only 65 sources with detection in at least two frequencies (400 MHz and 1.5 GHz) are considered. There are only 11/65 sources detected at all three frequencies (150 MHz, 400 MHz and 1.5

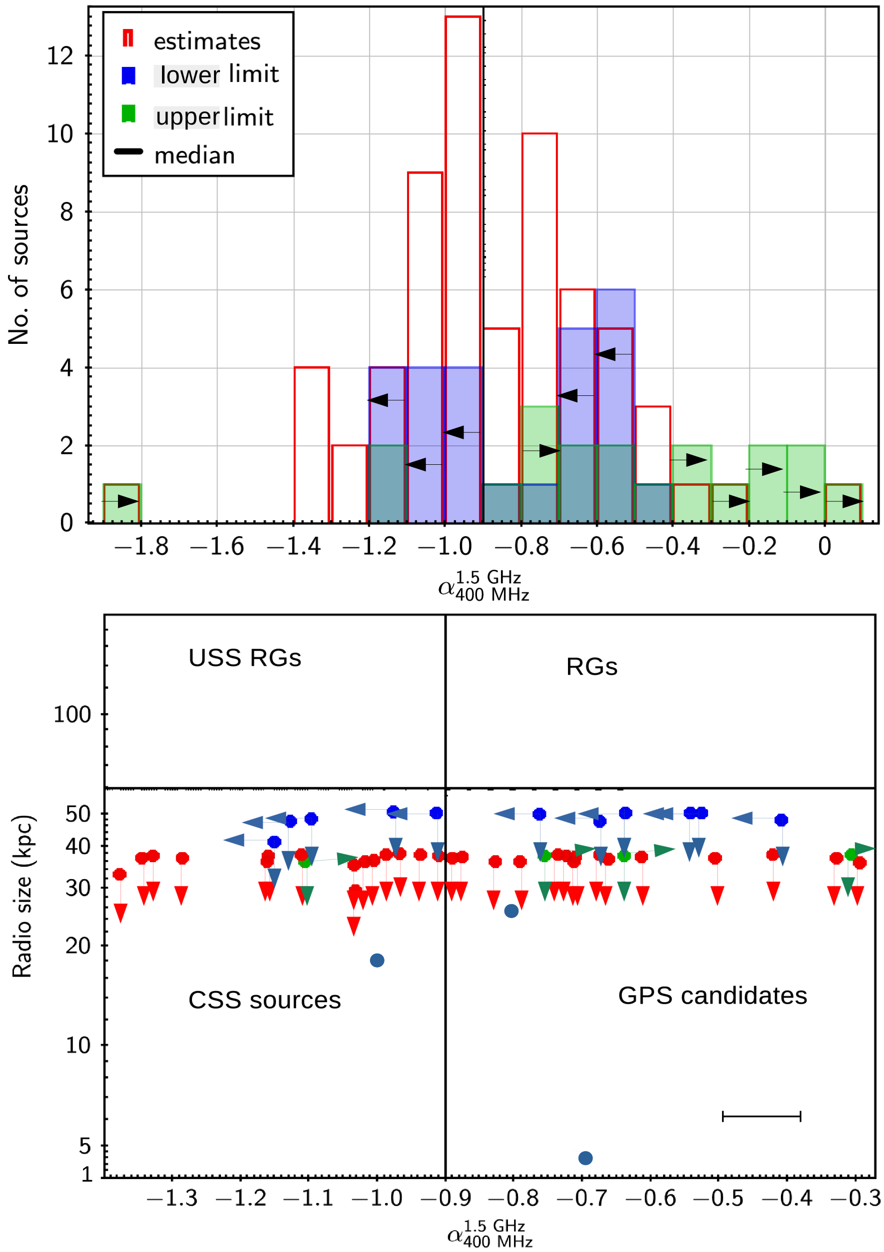

Figure 3.6: *Top panel* : The histogram of spectral index between 400 MHz and 1.5 GHz. The spectral index distribution is bimodal showing either steep or flat spectral indices.. *Bottom panel* : The radio sizes versus spectral indices plot. The plot indicates that most of our radio-detected DOGs are either Compact-Steep-Spectrum (CSS) or GHz-Peaked-Spectrum (GPS) sources. Sources with radio sizes and upper limits derived from the 400 MHz uGMRT and 1.5 GHz VLA observations are indicated by blue and red points, respectively.

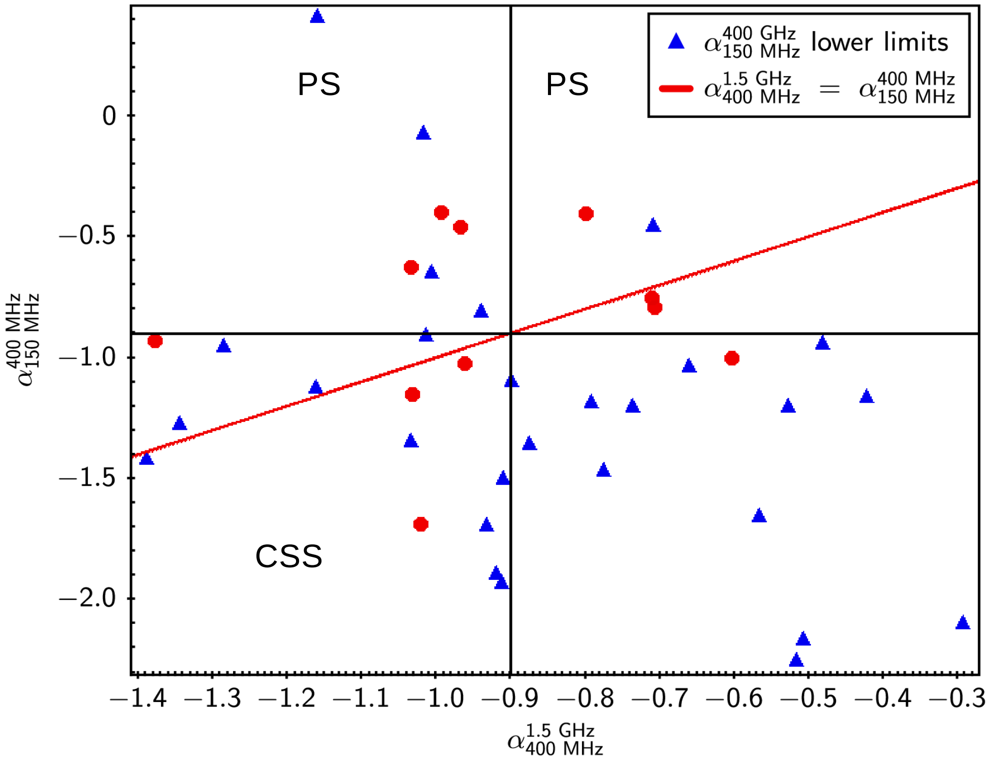

Figure 3.7: The 400 MHz - 1.5 GHz spectral index versus 150 MHz - 400 MHz spectral index plot. The plot indicates that most of the sources in our radio-detected DOG sample are either Peaked-Spectrum (PS) sources or Compact-Steep-Spectrum (CSS) sources

GHz) and have estimates of $\alpha_{400\ \mathrm{MHz}}^{1.5\ \mathrm{GHz}}$ as well as $\alpha_{150\ \mathrm{MHz}}^{400\ \mathrm{MHz}}$. The majority (54/65) of our sources have only loose constraints on $\alpha_{150\ \mathrm{MHz}}^{400\ \mathrm{MHz}}$ lower limits due to a large mismatch between the sensitivities of uGMRT and LOFAR observations. From Figure 3.7, it is evident that the sources with no detection in the 150 MHz LOFAR observations can plausibly be PS sources that have 150 MHz flux densities much lower than the LOFAR detection limit. In fact, the sources classified as CSS on the basis of $\alpha_{400\ \mathrm{MHz}}^{1.5\ \mathrm{GHz}}$ can also be PS sources. A PS source at $z \geq 1.2$ (median redshift in our sample) with ν_{p} = 400 MHz in the observed frame will have ν_{p} $\geq$ 880 MHz in the rest frame. Thus, our study demonstrates that the DOGs in our sample are likely to host CSS and PS sources of small sizes, and we need deeper multi-frequency observations of high resolution (sub-arcsec or better) to ascertain this possibility.

3.4.5 Radio luminosities

We examined the radio luminosity distributions of our sample sources. We note that the radio luminosity estimates are limited only to 44/91 uGMRT detected sources and 39/83 VLA detected sources that have available redshifts. For the remaining sources, we place a lower limit on their radio luminosities by assuming a conservative lower limit of $z > 1.0$ on their redshifts based on the empirical [3.6] - z relationship, similar to the widely used K-z relationship (Willott et al., 2003). Figure 3.8 shows the radio luminosity distributions at 400 MHz and 1.5 GHz. We find that the 400 MHz radio luminosities are distributed in the range of 2.3 $\times$ 10^{21} W Hz^{-1} to 9.46 $\times$ 10^{25} W Hz^{-1} with a median value of 2.81 $\times$ 10^{24} W Hz^{-1}. We find that the majority (39/44) of our sources have 400 MHz radio luminosity higher than 10^{24} W Hz^{-1}. The lower limits on 400 MHz radio luminosities are found to be distributed across 5.7 $\times$ 10^{23} W Hz^{-1} to 3.7 $\times$ 10^{25} W Hz^{-1} with a median value of 1.6 $\times$ 10^{24} W Hz^{-1}. Thus, the radio-detected

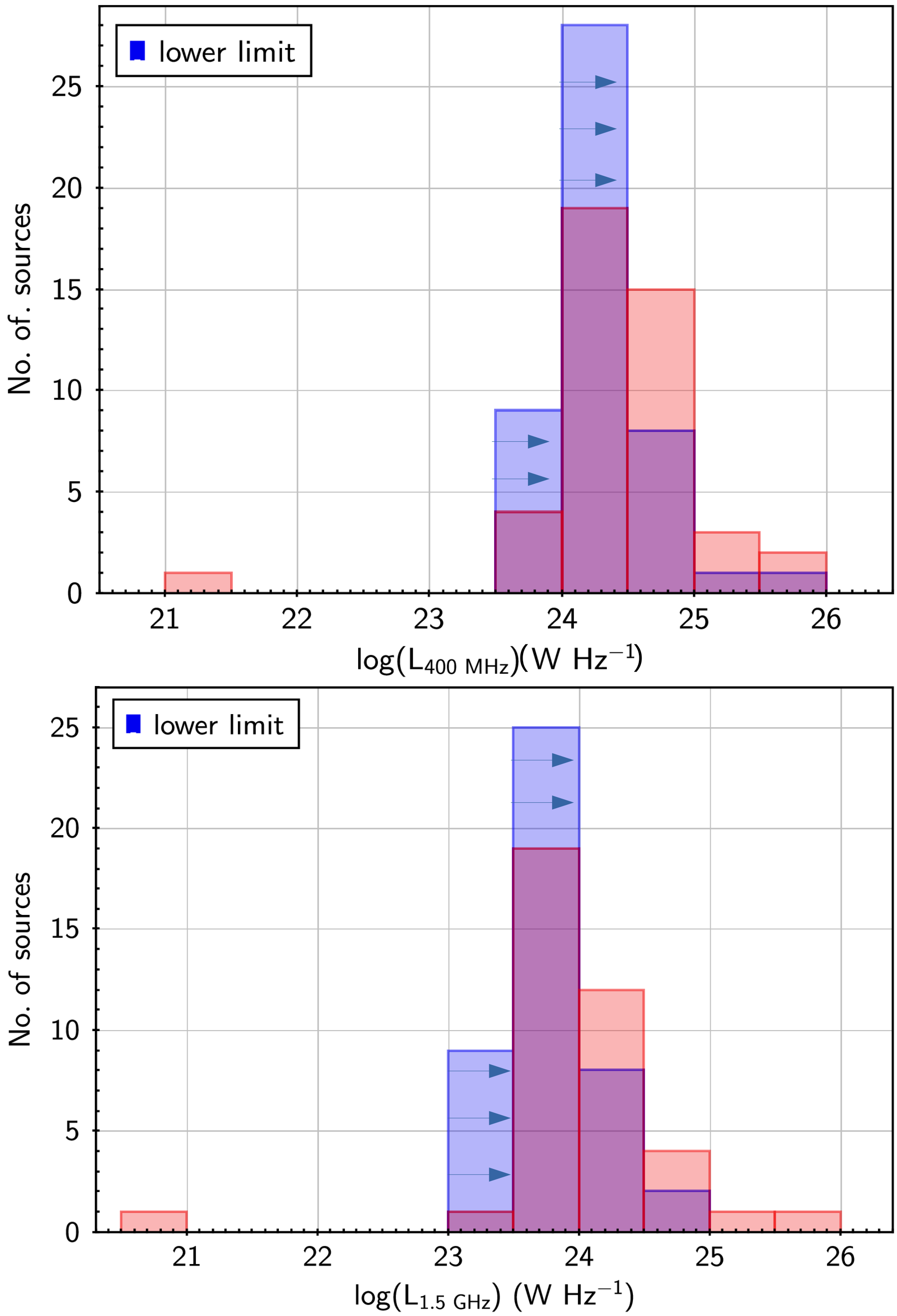

Figure 3.8: *Top panel* : The histogram of 400 MHz luminosity of our sample sources. *Bottom panel*: The histogram of 1.5 GHz luminosity of our sample sources. The lower limits on the radio luminosities are derived assuming the lower limit on their redshifts ($z > 1.0$).

sources with $z > 1$ are likely to be powerful radio sources. We note that the 1.5 GHz radio luminosity distribution spans over 9.1 $\times$ 10^{20} W Hz^{-1} to 3.3 $\times$ 10^{25} W Hz^{-1} with a median value of 8.9 $\times$ 10^{23} W Hz^{-1}. The lower limits on 1.5 GHz luminosities are distributed over 2.4 $\times$ 10^{23} W Hz^{-1} to 7.5 $\times$ 10^{24} W Hz^{-1} with a median value of 5.0 $\times$ 10^{23} W Hz^{-1}. We find that both 400 MHz and 1.5 GHz radio luminosity distributions exhibit a similar trend (see Figure 3.8).

We note that the high radio luminosity $> 10^{24}$ W Hz^{-1} found in most of our sources can be considered as a signature of AGN originated radio emission. The relationship between radio luminosity and star formation rate $L_{1.4\ \rm GHz}$ (W Hz^{-1}) = 4.6 $\times$ 10^{21} [SFR ($M_{\odot}$ yr^{-1})], assuming the radio emission arising only from star-formation (Condon et al., 2002), infers an extremely high star-formation rate of $> 100 M_{\odot}$ yr^{-1} required to produce the radio luminosity even for sources lying at the lower end of the luminosity distribution. Further, spectral characteristics, *i.e.*, CSS or potentially PS sources confirm the AGN originated radio emission. In Section 3.5 we show that the MIR colour-colour diagnostic plot (see Figure 3.9) also confirms that our sample sources, including the radio-detected ones, are AGN dominated. We point out that the FIRST and NVSS selected radio-bright ($S_{1.4\ \rm GHz}$ > 7 mJy) DOGs reported in Patil et al. (2020) have 1.4 GHz radio luminosities in the range of 10^{25} W Hz^{-1} to 3.2 $\times$ 10^{27} W Hz^{-1} with a median value of 2.0 $\times$ 10^{26} W Hz^{-1}. Thus, in comparison to the radio-bright DOGs, our radio-faint DOGs ($S_{1.5\ \rm GHz}$ > 0.07 mJy) at the similar redshifts ($z_{\rm median}$ = 1.2) are nearly two dex less luminous, which can be understood due to their faintness in radio by a similar factor. Therefore, our deep 400 MHz uGMRT and 1.5 GHz VLA observations unveil a population of less luminous radio-AGN in DOGs that were remained unexplored in the shallow radio surveys of the previous generation.

3.5 Prevalence of AGN in DOGs

Our radio observations have suggested that the radio-detected DOGs mostly contain AGN. To examine the prevalence of AGN in DOGs, we also study the MIR properties of our sample sources.

3.5.1 MIR colour-colour diagnostic

The MIR colours based on the *Spitzer* IRAC observations have been used to identify the AGN population by exploiting the power-law spectral characteristics of AGN-heated dust emission in the MIR wavelengths (Lacy et al., 2004; Stern et al., 2005; Donley et al., 2012). In fact, MIR colour criteria have proven efficient in identifying obscured-AGN that can remain elusive in the optical and X-ray wavelengths (see Fiore et al., 2009). In Figure 3.9, we show MIR colour-colour plot $\log(S_{5.8}/S_{3.6})$ versus $\log(S_{8.0}/S_{4.5})$; where $S_{3.6}$, $S_{4.5}$, $S_{5.8}$, and $S_{8.0}$ are fluxes at 3.6 μm, 4.5 μm, 5.8 μm and 8.0 μm bands, respectively. We find that only 268/321 of our MIPS-selected DOGs have IRAC coverage and fluxes available in the first two IRAC bands. There are only 75/268 sources with fluxes available in all four IRAC bands. For sources lacking the detections in 5.8 μm or 8.0 μm bands, we used the upper limits of 27.5 μJy and 32.5 μJy on their fluxes, respectively.

Using the MIR colour-colour plot, we find that all but two of our DOGs (73/75 $\sim$ 97%) with detections in four IRAC bands fall within the AGN selection wedge proposed by Lacy et al. (2004). Also, most of our DOGs are lying on or close to the power-law locus suggesting their MIR emission is mainly arising from AGN. Sources with only upper limits on 5.8 μm or 8.0 μm fluxes also mostly fall within the AGN selection wedge (see Figure 3.9). These sources are likely to remain within the AGN selection wedge if their fluxes are a few times lower than the 5σ detection limits. Hence, from the MIR colour-colour diagnostic plot, it is evident

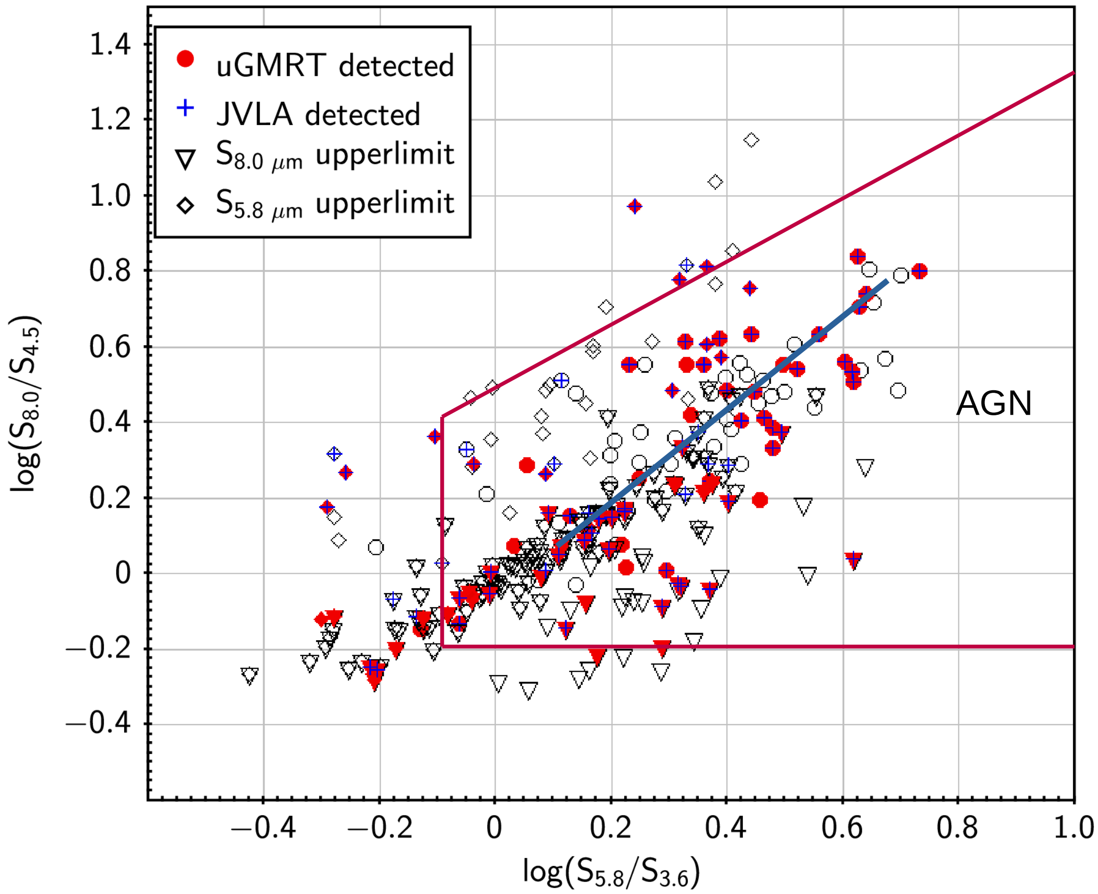

Figure 3.9: The MIR colour-colour diagnostic plot. The AGN selection wedge proposed by Lacy et al. (2004) is shown with the red solid lines depicting the boundaries of region defined as $(\log(S_{5.8}/S_{3.6}) > -0.1) \wedge (\log(S_{8.0}/S_{4.5}) > -0.2)$ $\wedge$ $(\log(S_{8.0}/S_{4.5}) \leq 0.8\log(S_{5.8}/S_{3.6}) + 0.5)$; where $\wedge$ is 'AND' operator. The blue diagonal line represents the locus of AGN showing power-law MIR emission with spectral index ranging over -0.5 to -3.0.

that the vast majority of our sample DOGs are likely to contain AGN. In our sub-sample of 75 DOGs having MIR colour estimates, we find the radio detections in 37 sources, and all but one radio-detected sources fall within the AGN wedge. Hence, we can conclude that, a vast majority of radio-detected DOGs contain AGN, which is evident from the MIR colour-colour diagnostics and their radio characteristics. Further, the MIR colour-colour plot also reveals a population of AGN-dominated DOGs with no radio emission. These sources can be radio-weak AGN that fall below the detection limit of our uGMRT and VLA observations (see Section 3.6).

3.5.2 X-ray emission in DOGs

X-ray observations can allow us to measure the amount of obscuration in AGN. Although, heavily obscured AGN known as the Compton-thick AGN (CT-AGN) with absorbing column density (N_{H}) $\geq$ 1.5 $\times$ 10^{24} cm^{-2} are often missed in the *XMM-N* observations with energy coverage limited to 10 keV (Ricci et al., 2015). The CT-AGN at higher redshifts can still be detected in the *XMM-N* observations owing to the shift of rest-frame high-energy (E >10 keV) spectrum into the 0.5−10 keV band. We examine the X-ray detection of our sample DOGs by using the X-ray point-source catalogue obtained from the 1.3 Ms *XMM*-Newton observations (Chen et al., 2018) that were meant to cover the *Spitzer* Extragalactic Representative Volume Survey (SERVS) region and are found to overlap with the region covered by our uGMRT observations. We find that all but four of our sample sources fall within the *XMM*-SERVS coverage and only 24/317 (7.6%) sources are detected in the X-ray. The 0.5−10 keV X-ray fluxes for our 24 sources are found in the range of 3.57 $\times$ 10^{-15} erg s^{-1} cm^{-2} to 3.68 $\times$ 10^{-14} erg s^{-1} cm^{-2} with a median value of 1.8 $\times$ 10^{-14} erg s^{-1} cm^{-2} (see Table 3.4). We note that the measurement of absorbing column density (N_{H}) requires X-ray spectral modelling, which may not be feasible for our very faint sources. Also, the detailed X-ray spectral modelling of X-ray detected DOGs is beyond the scope of this paper. To place constraints on N_H, we use the hardness ratio (HR) parameter defined as H-S/H+S, where H and S are fluxes in the hard band (2.0-10 keV) and soft band (0.5-2.0 keV), respectively.

We use the N_H−HR relationship plot (from Riguccini et al., 2019) that predicts N_H from HR, assuming a power−law X-ray spectrum with photon index $\Gamma = 1.9$ and accounts for the effects of N_H and redshift (z) over a wide range of values. Figure 3.10 shows the HR versus 0.5-10 keV flux plot for our sample sources. We find that the HR values of our sources are distributed in the range of -0.11 to 0.91, with a median value of 0.76. In fact, all but one sources have HR >0.5. From the N_H−HR relationship plot, we find that our sources are likely to have N_H higher than a few times of 10^{23} cm^{-2}, hence, inferring them to be heavily obscured. It is fairly possible that due to high obscuration and high redshift a significant population of AGN dominated DOGs may remain elusive in the existing X-ray observations. We note that all our X-ray detected sources have high 0.5−10 keV X-ray luminosity in the range of 2.29×10^{43} erg s^{-1} to 2.29×10^{45} erg s^{-1} with a median value of 2.0×10^{44} erg s^{-1}. The observed X-ray luminosities of our sample sources are similar to those found for dust−obscured quasars (see Lansbury et al., 2020). Hence, the low X-ray detection rate 24/317 (7.6%) in our sample DOGs even in the deep *XMM*-SERVS survey can be understood if less luminous as well as heavily obscured AGN are missed. It is worth pointing out that the X-ray detection rate (7.6%) in our sample DOGs is much lower than the radio detection rate (109/321 = 34%). Therefore, our study demonstrates the importance of deep radio observations in unveiling the AGN population in DOGs that remained mostly undetected in the deep *XMM-N* X-ray survey.

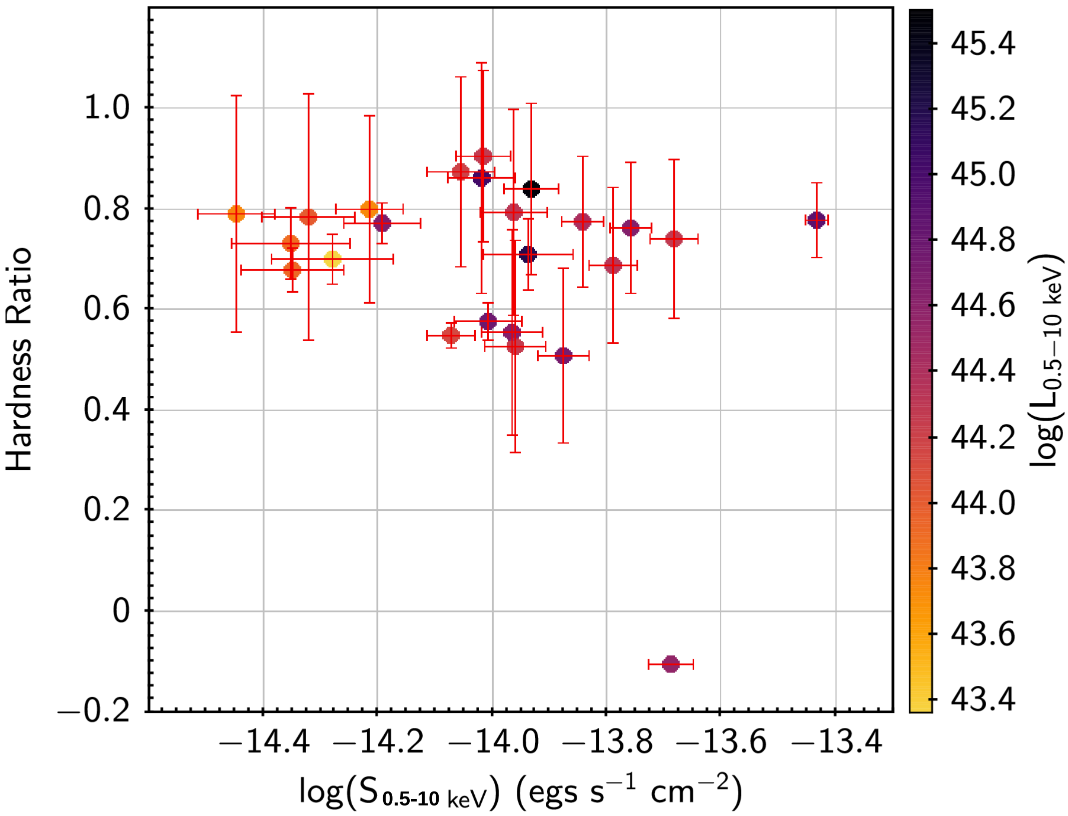

Figure 3.10: The hardness ratio versus 0.5-10 keV X-ray flux plot meant to infer the spectral behaviour and obscuration in DOGs. The 0.5−10 keV X-ray luminosities are indicated with a colour bar.

Table 3.4: The X-ray detected DOGs sample in uGMRT band-3 FoV.

RA	DEC	$S_{24\ \mu m}$ (mJy)	m_r	z	T_{exp} (ks)	HR	$F_{0.5-10\ keV}$ (10^{-14} erg cm^2 s^{-1})	log$L_{0.5-10\ keV}$ (erg s^{-1})
02 : 23 : 30	−04 : 34 : 41	0.67 ± 0.02	24.47 ± 0.02	2.30 ± 0.30 (p)	95.4	0.51 ± 0.09	1.33 ± 0.14	44.73 ± 0.11
02 : 23 : 40	−04 : 17 : 35	0.46 ± 0.03	26.00 ± 0.13	1.57 ± 0.34 (p)	197.2	0.79 ± 0.04	0.36 ± 0.06	43.76 ± 0.17
02 : 24 : 14	−04 : 40 : 11	0.43 ± 0.02	26.12 ± 0.07	2.76 ± 0.22 (p)	85.9	0.58 ± 0.05	0.99 ± 0.13	44.80 ± 0.13
02 : 24 : 32	−04 : 50 : 23	0.50 ± 0.03	25.13 ± 0.05	1.68 ± 0.19 (p)	75.9	0.79 ± 0.05	1.09 ± 0.15	44.31 ± 0.14
02 : 24 : 59	−04 : 14 : 13	3.24 ± 0.03	22.72 ± 0.01	1.90 ± 0.57 (p)	68.2	0.76 ± 0.04	1.74 ± 0.14	44.65 ± 0.08
02 : 25 : 12	−04 : 19 : 11	0.81 ± 0.03	24.17 ± 0.02	1.76 ± 0.10 (p)	91.2	0.78 ± 0.02	3.68 ± 0.17	44.89 ± 0.05
02 : 25 : 14	−04 : 34 : 19	2.38 ± 0.04	23.09 ± 0.01	3.54 ± 0.14 (p)	71.3	0.86 ± 0.02	0.96 ± 0.13	45.04 ± 0.14
02 : 25 : 21	−04 : 08 : 44	1.25 ± 0.02	24.90 ± 0.03	1.60 ± 0.26 (p)	63.9	0.55 ± 0.04	0.85 ± 0.08	44.15 ± 0.09
02 : 25 : 23	−04 : 58 : 17	1.06 ± 0.03	24.35 ± 0.03	1.76 ± 0.23 (p)	101.4	0.78 ± 0.04	0.48 ± 0.09	44.01 ± 0.19
02 : 25 : 26	−04 : 22 : 31	1.11 ± 0.03	23.81 ± 0.01	1.68 ± 0.12 (p)	79.9	0.68 ± 0.06	0.45 ± 0.09	43.93 ± 0.20
02 : 25 : 54	−05 : 31 : 39	0.66 ± 0.02	24.51 ± 0.03	0.93 ± 0.09 (p)	67.9	0.70 ± 0.07	0.52 ± 0.13	43.36 ± 0.25
02 : 26 : 01	−04 : 45 : 52	0.71 ± 0.03	24.29 ± 0.02	1.24 ± 0.08 (p)	100.5	0.8 ± 0.03	0.61 ± 0.08	43.73 ± 0.13
02 : 26 : 06	−04 : 44 : 16	1.26 ± 0.03	24.63 ± 0.03	1.71 ± 0.19 (p)	81.5	0.91 ± 0.03	0.97 ± 0.11	44.28 ± 0.11
02 : 26 : 20	−04 : 45 : 36	0.80 ± 0.02	24.30 ± 0.03	1.2706 ± 0.0001 (s)	78.3	0.77 ± 0.06	0.64 ± 0.10	43.78 ± 0.16
02 : 26 : 22	−05 : 04 : 21	1.03 ± 0.03	24.65 ± 0.02	3.77 ± 0.30 (p)	56.1	0.71 ± 0.00	1.15 ± 0.21	45.19 ± 0.18
02 : 26 : 24	−04 : 13 : 43	0.65 ± 0.03	25.10 ± 0.04	1.65 ± 0.07 (p)	86.1	-0.11 ± 0.05	2.05 ± 0.18	44.57 ± 0.09
02 : 26 : 33	−04 : 43 : 06	0.76 ± 0.02	24.43 ± 0.04	2.33 ± 0.65 (p)	99.7	0.55 ± 0.09	1.08 ± 0.13	44.66 ± 0.12
02 : 26 : 42	−04 : 02 : 05	0.58 ± 0.02	24.76 ± 0.04	5.12 ± 0.14 (p)	93.6	0.84 ± 0.03	1.17 ± 0.13	45.51 ± 0.11
02 : 26 : 47	−05 : 31 : 12	1.11 ± 0.03	24.67 ± 0.15	1.26 ± 0.11 (p)	70.9	0.74 ± 0.05	2.08 ± 0.20	44.28 ± 0.10
02 : 26 : 52	−04 : 04 : 15	0.45 ± 0.03	25.63 ± 0.10	1.60 ± 0.38 (p)	93.1	0.53 ± 0.10	1.09 ± 0.13	44.26 ± 0.12
02 : 27 : 16	−04 : 32 : 42	0.89 ± 0.03	24.59 ± 0.01	1.45 ± 0.19 (p)	75.7	0.69 ± 0.05	1.63 ± 0.16	44.33 ± 0.10
02 : 27 : 29	−04 : 48 : 58	0.62 ± 0.03	25.09 ± 0.04	1.65 ± 0.10 (p)	114.7	0.77 ± 0.03	1.44 ± 0.12	44.41 ± 0.08
02 : 27 : 50	−04 : 49 : 31	0.43 ± 0.03	25.77 ± 0.09	1.62 ± 0.11 (p)	74.6	0.73 ± 0.00	0.44 ± 0.11	43.88 ± 0.25
02 : 27 : 58	−05 : 10 : 29	0.51 ± 0.03	24.70 ± 0.04	1.65 ± 0.08 (p)	80.6	0.87 ± 0.02	0.88 ± 0.12	44.20 ± 0.14

Notes- The spectroscopic and photometric redshifts are indicated, within brackets, by ‘s’ and ‘p’, respectively.

To obtain better constraints on the absorbing column density we need good quality spectra with suffcient counts. To explore X-ray spectral properties of DOGs we identify another a sample of 34 DOG in the XMM-SERVS region. This work in presented in Chapter 4.

3.6 Stacking Analysis

Stacking is a useful tool to probe the existence of faint radio emission in sources with flux densities falling below the detection level of a given survey (White et al., 2007). The noise-rms in stacked image decreases by a factor of $\sqrt{N}$, where N is the number of image cutouts used for stacking, and all cutouts are assumed to be of the same depth. We used the stacking method to examine the existence of radio emission in the radio-undetected DOGs in our sample. We preferred median stacking over mean stacking as, unlike the mean, the median is less affected by extreme outliers. To obtain the deepest stacked image, we avoided the image cutouts of high noise-rms, *i.e.*, > 40 μJy beam^{-1} and > 20 μJy beam^{-1} in the 400 MHz uGMRT and 1.5 GHz VLA images, respectively. We note that among 230/321 DOGs with no detected counterparts in the 400 MHz uGMRT observations, a large fraction of sources fall in the peripheral region having relatively high noise-rms (> 40 μJy beam^{-1}), and only 116 sources lying mostly in the central region have noise-rms < 40 μJy beam^{-1}. The 1.5 GHz VLA mosaiced image of several pointings has nearly constant noise-rms, and 206/238 DOGs with no 1.5 GHz detected counterparts have noise-rms < 20 μJy beam^{-1}. We stacked $1' \times 1'$ radio image cutouts centred at the optical positions of our radio-undetected DOGs and computed the pixel-by-pixel median value.

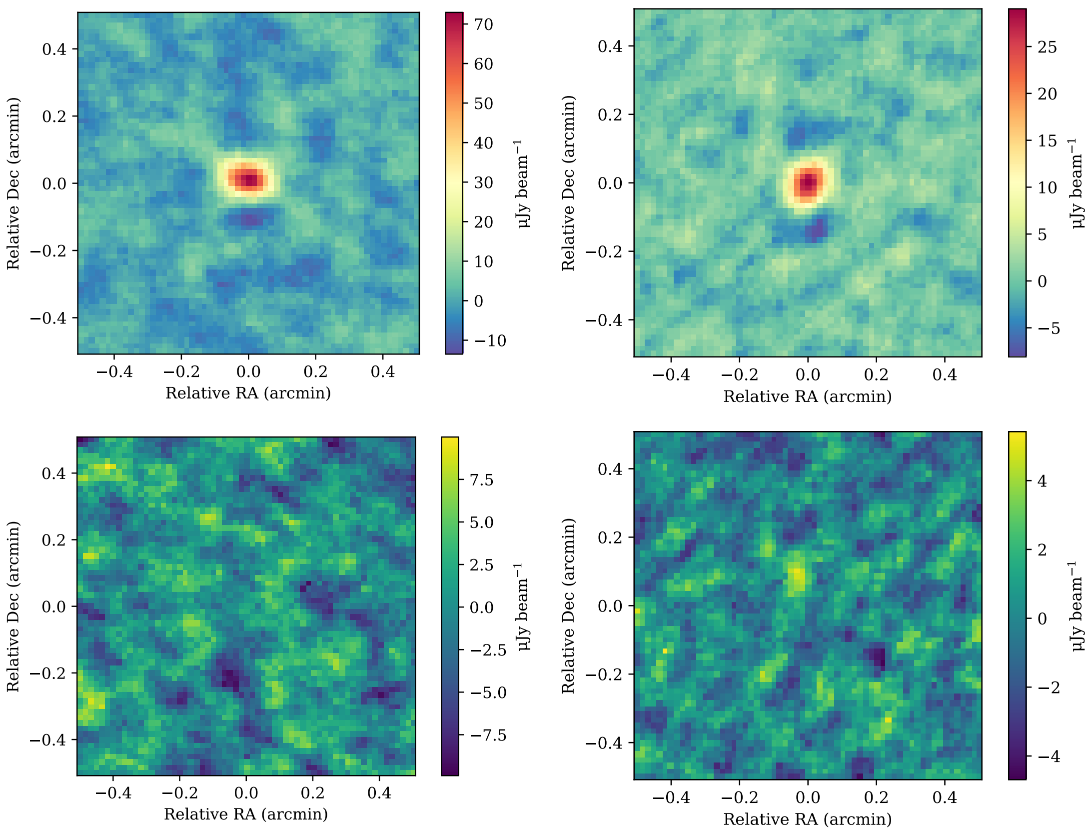

Figure 3.11: The median-stacked images of DOGs with no detected radio counterparts. *Upper left panel*: The 400 MHz uGMRT stacked image with cutouts centred at the DOGs positions. *Upper right panel*: The 1.5 GHz VLA stacked image with cutouts centred at the DOGs positions. *Lower left panel*: The 400 MHz uGMRT stacked image with cutouts centred at random positions. *Lower right panel*: The 1.5 GHz VLA stacked image with cutouts centred at random positions.

Table 3.5: The details of stacked 400 MHz uGMRT and 1.5 GHz VLA images.

Observations	$N_{cutouts}$	S_{peak}	noise-rms	SNR	Size	PA	Positions
		(μJy beam^{-1})	(μJy beam^{-1})		($'' \times ''$)	(deg)	
400 MHz uGMRT	116	72.9	3.4	21.4	7.7 $\times$ 5.2	82	DOGs
	116	10.8	3.1	3.5			random
1.5 GHz VLA	206	29.0	1.5	19.3	6.2 $\times$ 5.1	137	DOGs
	206	5.2	1.4	3.7			random

Notes - The cutoff on noise-rms < 40 μJy beam^{-1} and < 20 μJy beam^{-1} is applied for the 400 MHz uGMRT and 1.5 GHz image cutouts, respectively. The off-centered strongest signal (brightest pixel) is considered in the median-stacked images for random positions.

In Table 3.5, we list our stacking results. We note that the 400 MHz uGMRT median-stacked image shows a clear detection with the brightest central pixel value corresponding to the flux density of 72.9 μJy beam^{-1} and SNR 21.4 (see Figure 3.11, *upper left panel*). The noise-rms of 400 MHz median-stacked image is only 3.4 μJy beam^{-1}, which is, as expected, nearly $\sqrt{N}$ times lower than the median noise-rms (30 μJy beam^{-1}) of our uGMRT observations. Hence, stacking analysis allows us to probe radio emission at a level which is nearly ten times fainter than that is directly detected in our uGMRT observations. Further, to ensure the reliability of detection in our stacked image, we performed stacking of radio image cutouts centred at the positions randomly shifted by $\mathbf{1' - 2'}$ *w.r.t.*, DOGs positions. We find that the median-stacked image with random positions yields no detection of any emission significantly higher than the noise-rms of 3.1 μJy beam^{-1} (see Figure 3.11, *lower left panel*). In fact, the brightest pixel lying far away from the centre in $1' \times 1'$ stacked image, corresponds to the flux density of 10.8 μJy beam^{-1} with SNR 3.5. Hence, we find that the radio emission detected in our uGMRT median-stacked image, centred at the positions of radio-undetected DOGs, is genuine.

A similar exercise is performed to obtain the median-stacked image at 1.5 GHz with the VLA image cutouts (see Figure 3.11, *upper right panel*). We find a clear detection with flux density 29.0 μJy beam^{-1} and SNR 19.3 above the noise-rms of 1.5 μJy beam^{-1} (see Table 3.5). The 1.5 GHz stacked image at random positions shows only noise with no significant emission (see Figure 3.11, *lower right panel*). We note that, similar to 400 MHz uGMRT stacked image, the 1.5 GHz stacked image (noise-rms $\sim$ 1.5 μJy beam^{-1}) is also nearly ten times deeper than the VLA image (noise-rms $\sim$ 16 μJy beam^{-1}). Thus, using stacking analysis we demonstrate that our sample DOGs with no directly detected counterparts in the 400 MHz uGMRT and 1.5 GHz VLA observations, possess faint radio emission with peak flux density of 72.9 μJy beam^{-1}, 29 μJy beam^{-1} at 400 MHz and 1.5 GHz, respectively. It is worth noting that both 400 MHz uGMRT and 1.5 GHz VLA median-stacked images show nearly an unresolved point source emission (see Figure 3.11, *upper panel*). The central emission components detected in the stacked images are fitted with a single Gaussian and gives sizes of $7''.7 \times 5''.2$ and $6''.2 \times 5''.1$, that are similar to the synthesized beam sizes of uGMRT ($6''.7 \times 5''.3$) and 1.5 GHz VLA ($4''.5 \times 4''.5$) observations. Thus, we find that, similar to our radio-detected DOGs, radio-undetected DOGs are likely to possess compact radio emission smaller than $6''.0$ at much fainter levels.

Further, to understand the nature of DOGs with feeble radio emission but no directly detected radio counterparts in our 400 MHz uGMRT and 1.5 GHz VLA observations, we compare their redshift distributions and average radio luminosities with the radio-detected DOGs. We note that only 50/109 (45.9%) radio-detected DOGs have estimated redshifts distributed across 0.034 to 2.64 with a median value of 1.22, while, only 81/212 (38.2%) radio-undetected DOGs have redshifts in the range of 0.693 to 2.99 with a median value of 1.19. Although, the median redshifts of both sub-populations appear similar, but a lower fraction of sources with available redshifts indicates that the radio-undetected DOGs possibly reside at higher redshifts than the radio-detected ones. Further, for radio-undetected sources, we find an average $L_{1.5\ \mathrm{GHz}} = 2.25\ \times\ 10^{23}$ W Hz^{-1} using $S_{1.5\ \mathrm{GHz}} = 0.029$ mJy beam^{-1} derived from the median-stacked image and median redshift of 1.19. We note that the average 1.5 GHz luminosity can only be a lower limit considering that a large fraction of potentially high-z sources lack redshift estimates. Moreover, the average radio luminosity of otherwise radio-undetected DOGs infers them to be powered by a low-luminosity AGN or high star-formation rate ($\sim\ 100 M_{\odot}$ yr^{-1}) or both. We emphasize that more sensitive radio observations are required to unveil their nature via direct detections of such individual sources. Since a large fraction of our DOGs lack redshift estimates it is also important to conducted deeper spec$-z$ and photo$-z$ surveys. In the next section, we discuss the importance of planned and upcoming deeper radio continuum surveys.

3.7 Importance of the deeper radio continuum surveys from the SKA and its pathfinders

We note that deep radio continuum surveys are planned with the upcoming largest radio telescope array SKA operating at various frequencies, *i.e.*, 50 MHz - 350 MHz, and 350 MHz - 15.3 GHz frequency domains covered with the SKA1-low and the SKA1-mid, respectively. As per the baseline design performance, SKA1-mid is expected to achieve noise-rms of 4.4 μJy beam^{-1} in one hour observing time with an angular resolution of $0''.7$ in the 0.35-1.05 GHz band centred at 770 MHz (see SKA factsheet[5]). We also note that, prior to the SKA surveys, deep radio continuum surveys although of smaller sky-area coverage, have already been conducted with the SKA pathfinder telescopes, such as the MeerKAT in South Africa and the Australian SKA pathfinders (ASKAP). The MeerKAT International GHz Tiered Extragalactic Exploration (MIGHTEE) survey achieved 2.0 μJy beam^{-1} noise-rms at 950 MHz - 1.7 GHz band (central frequency 1284 MHz) with a total sky coverage of 20 deg^2 in various deep fields (see Heywood et al., 2022). The Evolutionary Map of the Universe (EMU) survey conducted with the ASKAP at 944 MHz offers continuum images with noise-rms of 25-30 μJy beam^{-1} and resolution of 11$''$ - 18$''$ over a large area of 270 deg^2 (Norris et al., 2021).

We emphasize that, in comparison to our 400 MHz uGMRT (noise-rms = 30 μJy beam^{-1}) and 1.5 GHz VLA (noise-rms = 16 μJy beam^{-1}) observations, the MIGHTEE survey provides deeper radio images. Also, the EMU survey with its large sky-area coverage (270 deg^2) and depth similar to the 1.5 GHz VLA observations, would allow us to explore a much larger source population. As expected, a much deeper SKA1-mid survey with sub-arcsec angular resolution would be more useful in revealing compact radio structures in DOGs. For instance, most of the DOGs in our sample appeared unresolved in our 400 MHz uGMRT and 1.5 GHz VLA observations with the angular resolution of 4$''$.5 - 6$''$.0, but, deep SKA-mid observations of sub-arcsec resolution can show jet-lobe structure piercing through the dense environments of their host galaxies at z = 1-2. Also, SKA observations spanning across a wide range of frequencies would enable us to measure $\nu_{\rm p}$ and confirm the evolutionary stage of radio sources hosted in DOGs which are inferred to host CSS or PS sources. With stacking, we confirmed the existence of faint radio emission (72.9 μJy beam^{-1} at 400 MHz and

[5] https://www.skatelescope.org/wp-content/uploads/2018/08/16231-factsheet-telescopes-v71.pdf

29 μJy beam^{-1} at 1.5 GHz) in otherwise radio-undetected sources in our 400 MHz uGMRT and 1.5 GHz VLA observations. We note that the deeper radio surveys from the MIGHTEE and SKA would directly detect faint radio emission in DOGs that remained undetected in the current radio observations.

In addition to the SKA, the upcoming next generation VLA (ngVLA; Kirkpatrick et al., 2018) is expected to provide unprecedented sensitive and high spatial resolution radio observations at frequencies $1.2 - 116$ GHz which will be more than an order of magnitude higher than the VLA and the Atacama Large Millimeter/submilimeter Array (ALMA; Wootten & Thompson, 2009). With an array of 244 antennas each having diameter of 18 m, the core of the ngVLA will be located near the current VLA location on the plains of San Agustin, New Mexico which will provide a large collecting area with a baseline as long as $\sim$ 1000 km[6]. The current reference design suggests that the ngVLA would offer an unprecedented sensitive observations down to 1 μJy beam^{-1} with sub-arcsec angular resolution ($0''.3$ with a 36 km baseline) at 8 GHz in an estimated integration time of 200 hrs for a proposed wide survey covering 10 square-degree of the Stripe 82 field (Kirkpatrick et al., 2018). Thus, deep and wide radio surveys with high angular resolutions from SKA, ngVLA would not only be able to detect hidden AGN in radio-bright DOGs but also in radio-faint DOGs ($L_{1.5\ \rm GHz} < 10^{24}$ GHz) as well. Therefore, our study presents a demonstrated science case for the deeper radio continuum surveys from the upcoming next generation radio telescopes *e.g.*, ngVLA, SKA and its pathfinders.

Further, we emphasize that Very Long Baseline Interferometric (VLBI) observations providing milli-arcsecond (mas) resolution can also enable us to detect radio structures at parsec-scales. It is worth mentioning that Frey et al. (2016)

[6] https://ngvla.nrao.edu/

performed VLBI observations using the European VLBI Network (EVN[7]) at 1.7 GHz for four Hot DOGs at $z \sim 1.7$ - 2.6. All four sources appearing unresolved in the FIRST observations have a total 1.4 GHz flux density in the range of 1.4 mJy - 3.6 mJy. The EVN observations revealed extended radio emission with their projected linear sizes of hundreds to thousands of parsec. Notably, in two of their sample sources, Frey et al. (2016) found that the flux density of the VLBI-detected component is much lower than the total flux density observed in the FIRST, suggesting that 70-90 per cent of the radio emission originates from angular scales larger than that probed by the EVN. Recently, Fan et al. (2020) performed VLBI observations of a hyper-luminous dust-obscured quasar W2246-0526 at $z = 4.6$ using EVN plus enhanced Multi-Element Radio Linked Interferometer Network (e-MERLIN[8]) and the Very Long Baseline Array (VLBA[9]), and detected only an unresolved nuclear component ($<$ 32 pc) at 1.66 GHz in the EVN plus e-MERLIN observations, while this source remained undetected in the VLBA observations. Also, flux density of the core component (75 $\pm$ 9 μJy) detected in the EVN plus e-MERLIN observations accounts for only about 10 per cent of that detected in the FIRST. Therefore, considering the fact that VLBI detection requires compact mas-scale core emission of nearly 0.1 mJy, and up to 90 per cent flux density may arise from the region larger than mas-scales, we can expect that only relatively bright DOGs (*e.g.*, $S_{1.4~\rm GHz}~\geq$ 1.0 mJy) can possibly be regarded as good candidates for the VLBI observations. Hence, we emphasize that the relatively radio-bright DOGs reported in our study may also be used for VLBI observations to probe the early evolutionary stage of radio jets residing in dusty environments.

[7]https://www.evlbi.org/

[8]https://www.e-merlin.ac.uk/index.html

[9]https://science.nrao.edu/facilities/vlba

3.8 Summary and conclusions

Using sensitive 400 MHz uGMRT (5σ = 0.15 mJy beam^{-1}) and 1.5 GHz VLA (5σ = 0.08 mJy beam^{-1}) observations, we investigated the radio emission characteristics of 321 DOGs selected with the main criterion of flux ratio of 24 μm to r band optical ($S_{24\ \mu\mathrm{m}}/S_r$) $\geq$ 1000. The combination of deep 24 μm *Spitzer* and HSC-SSP optical data allows us to select IR-faint ($S_{24\ \mu\mathrm{m}} \geq$ 0.4 mJy) DOGs at higher redshift ($z_{\mathrm{median}} \geq$ 1.2). The main conclusions of our study are outlined below.

1. Our 400 MHz uGMRT observations detect only 91/321 (28.4 per cent) of our sample sources, and yield the highest detection rate, in comparison to the 1.5 GHz VLA and 150 MHz LOFAR observations. With the combination of 400 MHz uGMRT and 1.5 GHz VLA observations, the radio detection rate increases to 109/321 (34 per cent), if detection at one frequency (400 MHz uGMRT or 1.5 GHz VLA) is considered. We note that the radio detection rates in the uGMRT and VLA observations are much higher than that (< 1.0 per cent) obtained with the FIRST and VLASS. The higher detection rates in the uGMRT and VLA can be attributed to their better sensitivities and the radio emission of sub-mJy level in our sample DOGs.

2. We find that our sample DOGs mostly have radio emission at sub-mJy level with 400 MHz flux densities distributed in the range of 0.137 mJy to 26.9 mJy with a median value of 0.37 mJy. The flux densities at 1.5 GHz are found in the range of 0.035 mJy to 9.33 mJy with a median value of 0.13 mJy. Notably, 79/83 (95 per cent) VLA detected sources have 1.5 GHz flux density less than 1.0 mJy.

3. In our uGMRT and VLA observations, all except five sources appear unre-

solved with angular sizes $< 4''.5$. Five sources are only marginally resolved and do not reveal any morphological details. The distribution of upper limits on the radio sizes suggests that most of our sources are expected to possess compact radio emission ($<$ 40 kpc at $z = 1.2$) confined within their hosts.

4. The distribution of two-point spectral index ($\alpha_{400\ \mathrm{MHz}}^{1.5\ \mathrm{GHz}}$) appears bimodal with most sources having either steep ($\alpha_{400\ \mathrm{MHz}}^{1.5\ \mathrm{GHz}} < -0.9$) or flat ($\alpha_{400\ \mathrm{MHz}}^{1.5\ \mathrm{GHz}} > -0.8$) spectral index. The spectral index and upper limits derived at the lower-frequencies using 150 MHz LOFAR observations suggest that our sources are potentially CSS or PS sources. Thus, considering their compact radio sizes and spectral characteristics, we infer that most of our radio sources in DOGs are likely to be CSS or PS representing the young radio sources residing in obscured environments. Our results are consistent with the findings of Patil et al. (2020), who reported the existence of young compact radio-jets in radio-bright DOGs.

5. We find that both 400 MHz and 1.5 GHz radio luminosity distributions span in the range of 10^{21} W Hz^{-1} to 10^{26} W Hz^{-1} with a median value of nearly 10^{24} W Hz^{-1}. In fact, all but one of our sample sources have 1.5 GHz luminosities higher than 10^{23} W Hz^{-1}, suggesting them to be mainly powered by AGN.

6. The MIR colour-colour diagnostic plot also confirms that the most of our radio-detected sources contain AGN. Further, many radio-undetected sources too fall within the MIR AGN selection wedge, revealing a population of AGN that remained undetected in our deep 400 MHz uGMRT and 1.5 GHz VLA observations.

7. The deep *XMM*-SERVS survey could detect only 24/317 (7.9 per cent) of

our sample sources. The absorbing column densities (N_H) estimated from the hardness ratios suggest that all our X-ray detected sources are heavily obscured with $N_H > 10^{23}$ cm^{-2}. The observed 0.5−10 keV X-ray luminosities distributed in the range of 2.29×10^{43} erg s^{-1} to 2.29×10^{45} erg s^{-1} with a median value of 2.0×10^{44} erg s^{-1}, are similar to the luminous quasars. We infer that the *XMM*-SERVS survey possibly detects only X-ray luminous AGN, while less luminous and/or heavily obscured AGN are likely to remain undetected.

8. The large difference in the detection rates found at the radio (34 per cent) and X-ray (7.9 per cent) wavelengths for our sample DOGs suggests the limitations of X-ray surveys. The deep radio observations are found more effective in unveiling the AGN population residing in obscured environments.

9. We find that the median-stacked images at 400 MHz uGMRT and 1.5 GHz VLA show a clear detection of radio emission in otherwise radio-undetected DOGs, suggesting them to possess faint radio emission that remained undetected in our observations. The average 1.5 GHz radio luminosity of the radio-undetected DOGs infers them to be powered by either low-luminosity AGN or high star-formation rate of $100 M_\odot$ yr^{-1} or both.

10. Our stacked images yield a clear detection of radio emission with SNR $\simeq$ 20 and noise-rms of 3.4 μJy beam^{-1} at 400 MHz and 1.5 μJy beam^{-1} at 1.5 GHz. Therefore, our stacking analysis demonstrates that the planned deeper radio surveys from the SKA and its pathfinder would enable us to detect the radio source population that remained undetected in the current 400 MHz uGMRT and 1.5 GHz VLA observations.

Chapter 4

X-ray spectral properties of dust-obscured galaxies in the XMM-SERVS deep field †

4.1 Introduction

AGN in the local universe are known to be obscured by circumnuclear material distributed in the form of a torus (Bianchi et al., 2012; Ricci et al., 2017b; Zhao et al., 2021) as envisaged by the unification model (Antonucci & Miller, 1985; Urry & Padovani, 1995). Depending on the orientation of the obscuring torus, AGN can be broadly classified into type 1 (pole-on view) and type 2 (edge-on view). As expected, type 2 AGN exhibit higher line-of-sight column densities ($N_{\rm H} \sim 10^{22} - 10^{24}$ cm^{-2} or even higher) at X-ray wavelengths (Singh et al., 2011) and they constitute most of the obscured population of AGN in the local universe ($z \leq 0.05$). Hard X-ray (> 10 keV) spectral studies have also revealed

† **Abhijit Kayal** and Veeresh Singh, "X-ray spectral properties of dust-obscured galaxies in the XMM-SERVS region of XMM-LSS field" (*Submitted* in MNRAS)

the presence of heavily obscured AGN, *i.e.*, CT-AGN with $N_{\rm H} \geq 1.5 \times 10^{25}$ cm^{-2} but their fraction is likely to be small ($\sim$ 5$-$10 per cent) among local type 2 AGN (Comastri, 2004; Burlon et al., 2011; Torres-Albà et al., 2021). Although, a much higher fraction of obscured AGN, most of them being CT-AGN, is inferred to be present at higher ($z \sim 0.5-1.5$) redshifts (Akylas et al., 2012; Ananna et al., 2019). The modelling of the X-ray background (XRB) spectrum peaking at 20$-$30 keV requires 10 to 40 per cent of CT-AGN (Gilli et al., 2007; Treister et al., 2009a). The SMBH mass function derived from the AGN luminosity function can also be reconciled with a significant population of CT-AGN at $z \sim 1-2$, the epoch during which AGN activity peaked (Marconi et al., 2004). Although, obscured AGN population at high$-z$ is poorly explored and the exact fraction of CT-AGN at higher redshifts is still a subject of debate. Therefore, it is important to detect and constrain the population of obscured AGN at higher redshifts.

DOGs containing large reservoirs of gas and dust, are arguably thought to be potential hosts of obscured AGN (Narayanan et al., 2010; Suleiman et al., 2022). DOGs are defined to be bright in far-IR but faint in optical with the flux ratio of 24 μm far-IR band to R band optical $(\frac{f_{24\ \mu m}}{f_{\rm R}}) \geq 1000$ and they represent the population of optically-faint high-redshift ($z \sim 1.5-2.5$) galaxies (see Section 3.3.1) with their total 8$-$1000 μm IR luminosities ($10^{11} - 10^{14}\ L\odot$) similar to the local LIRGs and ULIRGs (Sanders & Mirabel, 1996; Melbourne et al., 2012). The high IR luminosity of DOGs is explained by invoking gas-rich major merger leading to an intensely star-forming dusty merged system (Hopkins et al., 2008; Yutani et al., 2022). The large gas reservoir is also likely to fuel as well as obscure the accreting SMBH. In fact, it is believed that the SF DOGs can evolve into AGN-dominated DOGs which can eventually turn into quasars or red ellipticals (Granato et al., 2004; Hopkins et al., 2006; Alexander & Hickox, 2012). The obscured AGN are commonly detected in the extreme population of

AGN-dominated DOGs characterized by relatively hot dust emission, also known as the 'Hot DOGs' which are HLIRGs ($L_{\rm IR} \geq 10^{13}\ L_{\odot}$; Tsai et al., 2015; Farrah et al., 2017). However, the presence of obscured AGN in less extreme AGN-SF composite DOGs cannot be ruled out as their SEDs can be well-fitted with or without AGN component (Bussmann et al., 2009; Lanzuisi et al., 2009; Teng & Veilleux, 2010).

X-ray observations can provide an efficient means to identify obscured AGN in DOGs. There have been several attempts to exploit the X-ray observations of DOGs. Although, most of the previous studies have been limited either to highly luminous Hot DOGs (Stern et al., 2014; Ricci et al., 2017b) or hampered with poor quality X-ray spectra (Martínez-Sansigre et al., 2007; Vito et al., 2018; Zou et al., 2020). The high-quality X-ray observations of DOGs are limited only to a few relatively nearby sources (Zappacosta et al., 2018; Assef et al., 2020; Toba et al., 2020). The flat X-ray spectrum of the stacked emission of undetected DOGs, which falls below the detection limit of the X-ray surveys, is considered as an indication of a large fraction of CT-AGN in them (Fiore et al., 2008, 2009; Treister et al., 2009b). Although, the flat X-ray spectrum can also be produced from a low-luminosity AGN having a moderate obscuration (see Georgantopoulos et al., 2008) or due to a significant population of non-AGN DOGs among the X-ray undetected DOGs (Pope et al., 2008). Therefore, deep and large-area X-ray surveys are required to examine the prevalence of obscured AGN in DOGs. We note that the X-ray observations from *XMM-Newton* and *Chandra* limited upto 10 KeV energy range pose a challenge to detect heavily obscured AGN in nearby galaxies as soft X-ray photons are mostly absorbed, and consequently, it becomes difficult to accurately determine photoelectric absorption cut-off and the line-of-sight column density. However, for high$-z$ galaxies, X-ray spectra are redshifted towards lower energies and *XMM-Newton* and *Chandra* observations are useful for constraining absorbing column density and spectral characteristics (Lanzuisi et al., 2015; Koss et al., 2016). In this paper, we present X-ray spectral characteristics of DOGs in the XMM-*Spitzer* Extragalactic Representative Volume Survey (XMM-SERVS) extra-galactic field. The deep *XMM-Newton* observations available in this field allow us to obtain reasonably good quality spectra for a large sample of DOGs.

This Chapter is structured as follows. In Section 4.2, we describe our DOGs sample, their selection criteria, redshifts and multiwavelength data. In Section 4.3, we discuss the X-ray observations and the data reduction. In Section 4.4, we describe the X-ray spectral modelling and the best-fitted parameters. Section 4.5, is devoted to the results and discussion on the evolutionary scenario of DOGs. In Section 4.6, we present the conclusions of our study.
We adopt cosmological parameters H_0 = 70 km s^{-1} Mpc^{-1}, $\Omega_{\rm M}$ = 0.27, Ω_Λ = 0.73.

4.2 The sample, selection criteria and redshifts

In the 5.3 deg^2 area of the XMM-SERVS deep field region (34°.2 $\leq$ RA (J2000) $\leq$ 37°.125; and -5°.72 $\leq$ DEC (J2000) $\leq$ -3°.87) we identified 34 DOGs with sufficiently good X-ray spectral quality. Table 4.1 lists the sample sources and other parameters, *i.e.*, source name including RA and DEC information, 24 μm flux, $r-$band magnitude, flux ratio of 24 μm to $r-$band, redshift, and details of the X-ray observations. In this section, we describe our search for DOGs and multiwavelength data available in the XMM-SERVS field.

4.2.1 The sample of DOGs and multiwavelength data in the XMM-SERVS field

The XMM-SERVS provides the *XMM-Newton* survey of the SERVS field which covers nearly 5.3 deg^2 in the XMM-LSS region (Chen et al., 2018). The SERVS, a deep near-IR photometric survey, was performed with the post-cryogenic Spitzer in 3.6 μm and 4.5 μm Infrared Array Camera (IRAC) bands (Mauduit et al., 2012). The XMM-SERVS region is also covered with other multiwavelength surveys that include UV observations from the GALEX Deep Imaging Survey[1], optical photometric observations in u, g, r, i, z and four narrow-band filters from the HSC-SSP (Aihara et al., 2018),Y, J, H, $K_{\rm s}$ bands photometric observations from the VISTA Deep Extragalactic Observations Survey (VIDEO; Jarvis et al., 2013), mid-IR (3.6 μm, 4.5 μm, 5.8 μm and 8.0 μm from IRAC and 24 μm, 70 μm and 160 μm from the MIPS) observations from the SWIRE (Lonsdale et al., 2003); far-IR (100 μm, 160 μm from PACS and 250 μm, 350 μm and 500 μm from SPIRE) observations from the *Herschel* Multi-tiered Extragalactic Survey (HerMES; Oliver et al., 2012), and radio surveys at various frequencies (see Singh et al., 2014b; Heywood et al., 2020).

To identify DOGs in the XMM-SERVS region, we utilised 24 μm SWIRE and wide HSC-SSP optical data and followed the method described in Kayal et al. (2022). We began with the 24 μm source catalogue (signal-to-noise ratio (SNR) $\geq$ 5) and identified their optical counterparts. Since the positional uncertainty of the 24 μm sources ($2''.0$) is relatively larger than that for the optical sources ($0''.05$), we used the positions of 3.6 μm IRAC counterparts of the 24 μm sources, from the SWIRE band-merged catalogue[2] to increase the reliability of the positional cross-matching. The optical and band-merged 3.6 μm $-$ 24 μm source catalogues

[1] http://www.galex.caltech.edu/researcher/techdoc-ch2.html

[2] https://irsa.ipac.caltech.edu/data/SPITZER/SWIRE/overview.html

were cross-matched using a radius of $1''.0$ and the nearest match was considered as a true counterpart. We found optical and 3.6 μm counterparts for all our 24 μm sources owing to a much higher sensitivity in the optical and 3.6 μm band (7.3 μJy beam^{-1} at 5σ) than that for the 24 μm band (0.3 mJy beam^{-1} at 5σ).

To select DOGs, we used the conventional criterion of the flux ratio of 24 μm to the $r-$band optical ($\frac{f_{24\ \mu m}}{f_{\rm r}}$) $\geq$ 1000, which corresponds to the colour cut of R - [24] $\geq$ 7.5, where magnitudes are in AB system (see Dey et al., 2008; Fiore et al., 2008; Toba et al., 2015). Using the aforementioned criterion, we found a total of 1239 DOGs within the 5.3 deg^2 of the XMM-SERVS region. To study the X-ray properties of DOGs, we searched their X-ray counterparts using the XMM-SERVS X-ray point source catalogue (Chen et al., 2018). The availability of the band-merged catalogue, containing optical (from CFHTLS and HSC-SSP) and near-IR counterparts (from VIDEO and SERVS) of X-ray point sources (see Chen et al., 2018) allows us to identify the X-ray counterparts of the DOGs by simply cross-matching the optical positions within the tolerance radius of $1''.0$ in the two catalogues. In the above exercise, we found only 89/1239 (7.2 per cent) DOGs with X-ray counterparts. As expected, the fraction of the X-ray identified DOGs is similar to that reported in the previous studies (e.g., Kayal et al., 2022) that used data of similar depth.

Our sample represents a fainter population of DOGs having 24 μm flux ($S_{24\ \mu m}$) in the range of 0.39 mJy to 8.11 mJy with a median value of 0.65 mJy. As expected, our DOGs are also faint in optical wavelengths with m_r distributed across 22.64 to 25.94, with a median value of 24.68. The faintness of DOGs can be attributed to their high redshifts ($0.586 \leq z \leq 4.65$, median value 1.75). Therefore, unlike previous studies limited to relatively bright DOGs (Lanzuisi et al., 2009), our sample allows us to probe a fainter population residing at higher redshifts.

4.2.2 Spectroscopic and photometric redshifts of DOGs

Redshift estimates of DOGs are required for their X-ray spectral fittings and luminosity measurements. We obtain redshift estimates of our DOGs using various redshift measurement campaigns performed in the XMM-SERVS region. We gleaned spectroscopic redshifts from the HSC-SSP PDR-3 redshift catalogue that includes spectroscopic redshifts from different campaigns, *i.e.*, PRIMUS (Coil et al., 2011), VIPERS (Garilli et al., 2014), VVDS (Le Fèvre et al., 2013), SDSS-BOSS (Dawson et al., 2013; Menzel et al., 2016). We have also used Chen et al. (2018) catalogue, which lists spectroscopic redshifts for X-ray sources, whenever available, using the aforementioned redshift surveys as well as UKIDSS Ultra-Deep Survey (UDSz; Bradshaw et al., 2013; McLure et al., 2013), 3D-HST Survey (Skelton et al., 2014; Momcheva et al., 2016) and other publicly available spectroscopic redshift catalogues[3]. From these data, we find spectroscopic redshifts for only seven X-ray detected DOGs (see Table 4.1).

For the remaining sources, we obtain photometric redshifts. We note that there have been several efforts to estimate photometric redshifts in the XMM-SERVS region, *e.g.*, CFHTLS based photo$-z$ estimates (Ilbert et al., 2006; Coupon et al., 2009), HSC-SSP based photo$-z$ estimates (Tanaka et al., 2018; Schuldt et al., 2021). We prefer to use more accurate photo$-z$ estimates derived from the multi-band photometry spanning across optical to near-IR. Nyland et al. (2023) estimated photometric redshifts using the Tractor image-modeling software based de-blended multi-band forced photometry across 13 optical near-IR bands (u' band from the CFHTLS, g, r, i, z and y bands from the HSC-SSP, Z, Y, J, H, and Ks bands from the VIDEO and 3.6 μm and 4.5 μm bands from the *Spitzer*/DeepDrill). The photo$-z$ estimates based on the forced photome-

[3]https://www.nottingham.ac.uk/astronomy/UDS/data/data.html

try are more accurate and supersede previous estimates based on the traditional position-matched multi-band photometry (e.g., Chen et al., 2018; Ni et al., 2021; Zou et al., 2021, 2022). Previous test bed study on the Tractor based photo$-z$ estimate limited to 1.0 deg^2 in the XMM-SERVS, showed accurate photometric redshifts with normalized median absolute deviation (NMAD), $\sigma_{\rm NMAD} \leq 0.08$ and an outlier fraction of only ≤1.5 per cent (see Nyland et al., 2017).

We note that the photo$-z$ reported in Nyland et al. (2023) are limited only to the VIDEO/*Spitzer* DeepDrill region of 4.5 deg^2, which does not fully cover the XMM-SERVS field of 5.3 deg^2. We find that only 70/89 of our DOGs falling within the VIDEO region have photo$-z$ estimates from Nyland et al. (2023). For the remaining 19/89 DOGs, we considered photo$-z$ estimates from Desprez et al. (2023), who have used multiband photometric data (u, $u^{\star}$ from the CFHT-MegaCam, g, r, i, z, and y from the HSC-SSP, and Y, J, H, and Ks data from the VIDEO, whenever available). The photo$-z$ for sources falling outside the VIDEO region are based on only seven-band optical data. The photo$-z$ estimates are precise with $\sigma_{\rm NMAD} \leq 0.04$ down to $m_i = 25$, and an outlier fraction of ≤6 per cent. We point out that Desprez et al. (2023) have reported two different versions of the photo$-z$ catalogue, *i.e.*, one version uses the HSC pipeline for the photometric extraction and Phosphoros code for the redshift estimation, while the second version uses Source Extractor for the photometry and Le PHARE code (Arnouts et al., 1999; Ilbert et al., 2006) for the redshift measurements. We use the second version of the photo−z catalogue due to its slightly better performance. Among the 19 DOGs, we find photo$-z$ for 18 sources from Desprez et al. (2023). Thus, in total, we find redshift estimates for 88/89 sources, *i.e.*, spec$-z$ for 07 sources and photo$-z$ for 81 sources (see Table 4.1). To obtain useful X-ray spectra, we restricted our sample to sources with 0.5−10 keV X-ray counts ≥ 200 total counts. The total counts are based on Chen et al. (2018) catalogue. The limit placed on the total counts allows us to obtain reliable constraints on the continuum spectral shape and absorption column density. The cutoff on the total counts yields only 34/89 sources. Therefore, our study presents the X-ray spectral analysis of only 34 DOGs.

4.3 The X-ray observations and data reduction

To study the X-ray spectral properties of our DOGs, we used archival *XMM-Newton* observations, which were performed mainly under the XMM-SERVS project. Using a total of 155 pointings, XMM-SERVS observations provide a nearly uniform coverage of 5.3 deg^2 sky-area (Chen et al., 2018). The XMM-SERVS project used a total of 2.7 Ms of flare-filtered exposure time which includes 1.3 Ms observations carried out in AO-15 and all the available archival *XMM-Newton* data from other surveys, *e.g.*, XMM-LSS survey (Pacaud et al., 2006; Pierre et al., 2016), *XMM-Newton* Medium Deep Survey (XMDS, Chiappetti et al., 2005), Subaru *XMM-Newton* Deep Survey (SXDS, Ueda et al., 2008) and XMM-XXL-North field (Pierre et al., 2016). The combination of different epochs of archival data makes XMM-SERVS survey the deepest X-ray survey in the XMM-LSS region. The depth of XMM-SERVS survey is comparable to some of the pencil beam surveys such as SXDS covering only 1.14 deg^2 (Ueda et al., 2008) and XMM-COSMOS covering only 2.0 deg^2 (Cappelluti et al., 2009). The XMM-SERVS detected a total of 5242 X-ray sources with flux limits of 1.7×10^{-15} erg cm^{-2} s^{-1}, 1.3×10^{-14} erg cm^2 s^{-1} and 6.5×10^{-15} erg cm^{-2} s^{-1} in the soft band (0.5$-$2.0 keV), hard band (2.0$-$10 keV) and full band (0.5$-$10 keV), respectively (Chen et al., 2018).

Table 4.1: The sample of X-ray detected DOGs in the XMM-SERVS field

Source Name (1)	$S_{24\ \mu m}$ (mJy) (2)	m_r (mag) (3)	$S_{24\ \mu m}/S_r$ (4)	Redshift (5)	Ref. (6)	XID (7)	ObsID (8)	ObsDate (YYYY-MM-DD:Thh:mm:ss) (9)	$T_{\rm obs}$ (ks) (10)
J02:16:57-04:02:02	0.806±0.026	24.96±0.10	2141.7	$1.155^{+0.146}_{-0.122}$	D23	XMM00059	0404967501	2007-01-09T18:45:25.0	18.9
							0404967901	2007-01-10T14:40:38.0	14.9
							0553911601	2008-07-03T19:15:54.0	13.5
							0742430301	2015-02-06T19:24:58.0	100.0
J02:17:05-04:56:54	0.601±0.023	25.64±0.03	3005.0	$1.732^{+0.284}_{-0.098}$	N23	XMM00131	0112370101	2000-07-31T21:49:26.0	61.4
							0112371001	2000-08-02T20:24:27.0	66.0
							0112370601	2002-08-12T05:43:17.0	47.9
J02:17:06-05:25:47	0.648±0.022	24.53±0.02	1159.3	$1.843^{+0.121}_{-1.143}$	N23	XMM00136	0112370701	2002-08-08T15:05:39.0	49.6
							0404966501	2006-08-09T07:21:12.0	11.9
J02:17:15-04:01:17	0.708±0.028	25.12±0.09	2187.2	$2.188^{+0.401}_{-1.822}$	D23	XMM00191	0404967401	2007-01-08T14:06:49.0	15.0
							0404967501	2007-01-09T18:45:25.0	18.9
							0404967901	2007-01-10T14:40:38.0	14.9
							0553911601	2008-07-03T19:15:54.0	13.5
							0742430301	2015-02-06T19:24:58.0	100.0
J02:17:16-04:30:09	0.923±0.027	24.06±0.01	1074.4	0.5862±0.0079 (s)	PR	XMM00205	0112371701	2000-08-08T04:37:14.0	39.6
							0112372001	2003-01-07T04:18:37.0	28.0
							0404967001	2007-01-08T00:52:16.0	14.9
J02:17:22-04:36:55	1.282±0.024	25.71±0.06	6788.8	$4.648^{+0.091}_{-0.251}$	N23	XMM00250	0112371701	2000-08-08T04:37:14.0	39.6
							0112372001	2003-01-07T04:18:37.0	28.0
							0404967001	2007-01-08T00:52:16.0	14.9
J02:17:24-04:18:44	0.412±0.027	25.94±0.05	2706.8	$2.948^{+0.080}_{-1.000}$	N23	XMM00267	0404967001	2007-01-08T00:52:16.0	14.9
							0404967401	2007-01-08T14:06:49.0	15.0
							0404967501	2007-01-09T18:45:25.0	18.9
							0553911601	2008-07-03T19:15:54.0	13.5
							0742430301	2015-02-06T19:24:58.0	100.0
							0785100101	2016-07-01T15:53:31.0	22.5
J02:17:33-04:06:13	0.436±0.026	24.85±0.03	1045.5	$1.287^{+0.033}_{-0.033}$	D23	XMM00359	0404967401	2007-01-08T14:06:49.0	15.0
							0404967501	2007-01-09T18:45:25.0	18.9
							0553911601	2008-07-03T19:15:54.0	13.5
							0742430301	2015-02-06T19:24:58.0	100.0
J02:17:36-04:59:11	0.391±0.026	25.80±0.04	2255.6	$3.067^{+0.165}_{-0.547}$	N23	XMM00393	0112370101	2000-07-31T21:49:26.0	61.4
							0112371001	2000-08-02T20:24:27.0	66.0
J02:17:36-05:01:07	0.544±0.027	24.71±0.02	1144.4	1.421 (s)	UDSz	XMM00395	0112370101	2000-07-31T21:49:26.0	61.4
							0112371001	2000-08-02T20:24:27.0	66.0

Notes : Column 1 - source name based on its RA (J2000) and DEC (J2000); Column (2) - 24 μm flux; Column (3) - r band magnitude; Column (4) - flux ratio of 24 μm band to r band; Column (5) - redshift of source, 's' within brackets indicates spectroscopic redshift; Column (6) - Reference for the redshift (N23 - Nyland et al. (2023); D23 - Desprez et al. (2023), PR - PRIMUS, VI - VIPERS); Column (7) - XID corresponding to Chen et al. (2018) X-ray catalogue; Column (8) - observation IDs from *XMM-Newton* and *Chandra* observations, 'Ch' within brackets indicates *Chandra* observations; Column (9) - observation dates for the corresponding observation IDs; Column (10) - observation time in ks.

Table 4.1: Continue.

Source Name	$S_{24\ \mu m}$ (mJy)	m_r (mag)	$S_{24\ \mu m}/S_r$	Redshift	Ref.	XID	ObsID	ObsDate (YYYY-MM-DD:Thh:mm:ss)	$T_{\rm obs}$ (ks)
(1)	(2)	(3)	(4)	(5)	(6)	(7)	(8)	(9)	(10)
J02:17:40-04:32:43	0.391±0.024	24.99±0.02	1071.9	$1.732^{+0.338}_{-0.108}$	N23	XMM00421	0112371701	2000-08-08T04:37:14.0	39.6
							0112372001	2003-01-07T04:18:37.0	28.0
							0404967001	2007-01-08T00:52:16.0	14.9
							0785100101	2016-07-01T15:53:31.0	22.5
J02:17:49-05:23:07	8.104±0.024	22.63±0.01	2534.3	0.8420±0.0092 (s)	PR	XMM00497	0112370701	2002-08-08T15:05:39.0	49.6
							0112370801	2002-08-09T05:29:19.0	50.8
							0404966401	2006-07-31T02:38:25.0	11.9
							0553911301	2008-08-10T10:08:41.0	13.7
J02:18:37-04:29:50	0.579±0.027	24.68±0.01	1193.1	$1.473^{+0.115}_{-0.345}$	N23	XMM00860	0112370401	2000-08-06T05:12:57.0	46.8
							0112371501	2000-08-06T20:08:34.0	11.8
							0404966901	2007-01-07T18:38:27.0	19.9
							0553911501	2009-01-01T17:29:55.0	15.0
							0785100101	2016-07-01T15:53:31.0	22.5
							0785100301	2016-07-02T20:09:16.0	26.1
							0793580101	2017-01-02T14:22:49.0	28.0
J02:19:01-04:24:41	0.438±0.023	25.40±0.03	1756.8	$1.759^{+0.241}_{-0.091}$	N23	XMM01034	0112370401	2000-08-06T05:12:57.0	46.8
							0112371501	2000-08-06T20:08:34.0	11.8
							0404966901	2007-01-07T18:38:27.0	19.9
							0553911501	2009-01-01T17:29:55.0	15.0
							0785100101	2016-07-01T15:53:31.0	22.5
							0785100301	2016-07-02T20:09:16.0	26.1
							0793580101	2017-01-02T14:22:49.0	28.0
J02:19:31-04:49:41	1.040±0.027	24.29±0.01	1501.2	0.7953±0.0089 (s)	PR	XMM01279	0112370301	2000-08-04T20:16:28.0	66.0
							0112370401	2000-08-06T05:12:57.0	46.8
							0112371501	2000-08-06T20:08:34.0	11.8
							0785100801	2016-07-05T01:04:36.0	23.0
							0793580301	2017-01-01T10:04:38.0	9.0
							0793580101	2017-01-02T14:22:49.0	28.0
							0780452301	2017-02-09T11:06:48.0	24.1
J02:19:56-05:05:01	1.217±0.024	25.06±0.02	3548.3	$1.652^{+3.768}_{-0.0269}$	N23	XMM01464	0112370301	2000-08-04T20:16:28.0	66.0
							0404966601	2007-01-06T14:04:02.0	13.9
							0785100801	2016-07-05T01:04:36.0	23.0
							0780452401	2017-02-09T18:08:28.0	23.0
							14348 (Ch)	2011-10-03T09:28:05	63.7
							13374 (Ch)	2011-10-07T05:41:46	75.7
J02:20:32-04:50:02	4.436±0.040	22.68±0.01	1454.4	1.084±0.0011 (s)	VI	XMM01723	0037982001	2002-08-14T13:52:03.0	17.8
							0785100501	2016-07-03T10:23:26.0	22.0
							0785100801	2016-07-05T01:04:36.0	23.0
							0785101201	2016-07-06T03:57:56.0	25.9
							0793580301	2017-01-01T10:04:38.0	9.0
							0793580801	2017-01-16T20:33:01.0	18.0
J02:20:33-05:08:55	1.346±0.028	24.20±0.01	1775.1	$2.048^{+0.383}_{-0.076}$	N23	XMM01731	0147111301	2003-07-24T09:02:34.0	12.9
							0404966601	2007-01-06T14:04:02.0	13.9
							0785101101	2016-07-05T21:22:56.0	22.5
							0793580701	2017-01-03T08:02:49.0	16.0
							0780452401	2017-02-09T18:08:28.0	23.0
							14348 (ch)	2011-10-03T09:28:05	63.7
							13374 (ch)	2011-10-07T05:41:46	75.7

Table 4.1: Continue.

Source Name (1)	$S_{24\ \mu m}$ (mJy) (2)	m_r (mag) (3)	$S_{24\ \mu m}/S_r$ (4)	Redshift (5)	Ref. (6)	XID (7)	ObsID (8)	ObsDate (YYYY-MM-DD:Thh:mm:ss) (9)	$T_{\rm obs}$ (ks) (10)
J02:20:34-05:06:58	0.833±0.022	24.74±0.01	1808.1	$2.870^{+0.136}_{-0.258}$	N23	XMM01740	0147111301	2003-07-24T09:02:34.0	12.9
							0404966601	2007-01-06T14:04:02.0	13.9
							0785100801	2016-07-05T01:04:36.0	23.0
							0785101101	2016-07-05T21:22:56.0	22.5
							0793580701	2017-01-03T08:02:49.0	16.0
							0793580801	2017-01-16T20:33:01.0	18.0
							14348 (Ch)	2011-10-03T09:28:05	63.7
							13374 (Ch)	2011-10-07T05:41:46	75.7
J02:21:30-04:02:03	1.013±0.022	25.84±0.10	6070.7	$1.096^{+0.387}_{-0.335}$	D23	XMM02186	0037982501	2003-01-25T01:19:09.0	14.1
							0037982401	2003-01-25T05:51:41.0	18.9
							0037982201	2003-01-28T19:15:43.0	16.4
							0404960601	2006-07-07T03:36:58.0	11.9
							0785101501	2016-07-07T14:16:31.0	22.0
							0793581001	2017-01-04T20:54:08.0	9.0
J02:21:50-05:23:58	0.647±0.024	24.45±0.02	1077.9	$1.900^{+0.153}_{-0.166}$	N23	XMM02347	0147111501	2003-07-24T17:12:34.0	11.0
							0404960401	2006-07-06T19:43:38.0	11.9
							0785101001	2016-07-05T14:47:56.0	22.5
							0785101101	2016-07-05T21:22:56.0	22.5
							0785101601	2016-07-07T20:55:41.0	22.0
							0793580701	2017-01-03T08:02:49.0	16.0
							0793581101	2017-01-04T23:56:38.0	9.0
J02:22:32-04:49:09	0.682±0.021	24.39±0.02	1080.9	$1.815^{+1.106}_{-0.099}$	N23	XMM02660	0109520501	2001-07-03T22:44:36.0	24.8
							0112680801	2002-01-31T20:21:47.0	15.6
							0785101701	2016-07-08T03:22:21.0	27.4
							0785101801	2016-07-29T05:19:31.0	22.0
							0780450201	2016-08-13T23:26:35.0	17.0
							0793581201	2017-01-01T12:54:38.0	35.0
J02:23:30-04:34:42	0.668±0.022	24.47±0.02	1132.8	$2.300^{+0.319}_{-0.289}$	N23	XMM03098	0109520601	2002-01-31T13:04:39.0	23.6
							0112680501	2002-07-25T16:24:58.0	23.6
							0780450301	2016-08-14T04:29:55.0	17.0
							0780450601	2016-08-14T14:36:35.0	17.0
							0780452201	2017-01-07T17:07:14.0	18.0
J02:23:38-04:05:13	1.684±0.027	24.39±0.04	2660.3	$3.275^{+0.292}_{-0.162}$	N23	XMM03153	0109520101	2002-01-29T08:46:18.0	26.6
							0210490101	2005-01-01T19:07:51.0	107.5
J02:24:01-04:05:28	0.919±0.029	25.41±0.08	3687.1	$1.678^{+0.148}_{-0.053}$	N23	XMM03342	0109520101	2002-01-29T08:46:18.0	26.6
							0112680301	2003-01-19T04:19:09.0	23.4
							0210490101	2005-01-01T19:07:51.0	107.5
							6390 (Ch)	2005-09-13T21:44:12	11.9
							7182 (Ch)	2005-10-12T03:55:24	22.9
							6394 (Ch)	2005-10-12T22:57:34	17.5
							7184 (Ch)	2005-10-14T19:16:55	22.7
							7183 (Ch)	2005-10-15T14:18:10	19.9
							7185 (Ch)	2005-11-21T09:59:42	32.9

Table 4.1: Continue.

Source Name (1)	$S_{24\ \mu m}$ (mJy) (2)	m_r (mag) (3)	$S_{24\ \mu m}/S_r$ (4)	Redshift (5)	Ref. (6)	XID (7)	ObsID (8)	ObsDate (YYYY-MM-DD:Thh:mm:ss) (9)	$T_{\rm obs}$ (ks) (10)
J02:24:59-04:14:14	3.239±0.029	22.71±0.01	1092.0	$1.900^{+1.025}_{-0.118}$	N23	XMM03798	0112680301	2003-01-19T04:19:09.0	23.4
							0210490101	2005-01-01T19:07:51.0	107.5
							0780450701	2016-08-14T19:39:55.0	17.9
							0780451101	2017-01-07T10:58:53.0	20.9
J02:25:12-04:19:11	0.805±0.025	24.16±0.01	1031.1	$1.759^{-0.065}_{-0.141}$	N23	XMM03900	0112681001	2002-01-30T16:49:27.0	41.8
							0112680301	2003-01-19T04:19:09.0	23.4
							0780450701	2016-08-14T19:39:55.0	17.9
							0780451101	2017-01-07T10:58:53.0	20.9
J02:25:14-04:34:21	2.376±0.040	23.09±0.01	1131.5	$3.538^{+0.069}_{-0.212}$	N23	XMM03916	0112681001	2002-01-30T16:49:27.0	41.8
							0780450601	2016-08-14T14:36:35.0	17.0
							0780450701	2016-08-14T19:39:55.0	17.9
							0780451001	2017-01-07T04:50:33.0	20.9
							6864 (Ch)	2006-11-12T05:00:26	29.7
J02:26:06-04:44:19	1.259±0.028	24.62±0.03	2460.1	$1.732^{+0.295}_{-0.082}$	N23	XMM04259	0109520301	2002-02-02T11:26:13.0	22.6
							0780451001	2017-01-07T04:50:33.0	20.9
							0780451301	2017-01-08T18:27:03.0	20.0
							0780451401	2017-01-09T00:20:23.0	20.0
							0780452601	2017-02-10T05:38:28.0	16.0
							9368 (Ch)	2007-11-23T16:55:22	75.0
							18264 (Ch)	2016-09-27T19:47:17	22.8
J02:26:24-04:13:43	0.647±0.027	25.10±0.04	1957.8	$1.652^{+0.075}_{-0.074}$	N23	XMM04404	0112680101	2002-01-28T23:39:09.0	30.2
							0112680201	2002-07-14T02:10:42.0	21.6
							0780451501	2017-01-09T06:13:43.0	20.0
							0780451601	2017-01-09T12:07:03.0	36.4
							0780451701	2017-01-10T19:11:08.0	20.0
J02:26:33-04:43:07	0.756±0.024	24.42±0.03	1228.2	$2.333^{+0.748}_{-0.557}$	N23	XMM04475	0109520201	2002-01-29T16:53:38.0	25.6
							0109520301	2002-02-02T11:26:13.0	22.6
							0112681301	2002-07-26T08:26:58.0	40.4
							0780451301	2017-01-08T18:27:03.0	20.0
							0780451401	2017-01-09T00:20:23.0	20.0
							0780452101	2017-01-13T09:20:32.0	20.0
							0780452601	2017-02-10T05:38:28.0	16.0
							9368 (Ch)	2007-11-23T16:55:22	75.0
J02:26:47-05:31:13	1.112±0.025	24.67±0.15	2256.0	$1.070^{+0.231}_{-0.185}$	D23	XMM04583	0404964801	2006-07-07T11:42:54.0	11.9
							0404964901	2006-07-07T15:39:35.0	11.7
							0404969201	2006-07-26T20:57:30.0	7.9
							0553910401	2008-08-06T22:19:42.0	11.9
							0785102401	2016-08-12T12:23:12.0	22.0
							0785102501	2016-08-12T18:49:52.0	22.0
							0793581601	2017-01-05T08:26:38.0	9.0
J02:27:16-04:32:42	0.887±0.028	24.59±0.01	1683.1	$1.759^{+0.325}_{-0.055}$	N23	XMM04804	0112680401	2002-02-02T18:26:41.0	24.9
							0112681301	2002-07-26T08:26:58.0	40.4
							0780451801	2017-01-11T01:04:28.0	20.0
							0780452101	2017-01-13T09:20:32.0	20.0
J02:27:29-04:48:58	0.620±0.027	25.08±0.04	1854.3	$1.652^{+0.123}_{-0.078}$	N23	XMM04899	0109520201	2002-01-29T16:53:38.0	25.6
							0780451901	2017-01-11T06:57:48.0	20.0
							0780452101	2017-01-13T09:20:32.0	20.0

Table 4.2: The best-fit spectral parameters of X-ray detected DOGs

Source Name	$T_{\rm exp}^{\rm Eff}$ (ks)	$C_{0.5-10\ \rm keV}$ (cts)	Model	$N_{\rm H}$ (10^{22} cm^{-2})	$E_{\rm Fe}$ (keV)	$EW_{\rm Fe}$ (keV)	Cstat (dof)	$F_{2-10\ \rm keV}$	log$L_{2-10\ \rm keV}^{\rm obs}$ (erg s^{-1})	log$L_{2-10\ \rm keV}^{\rm int}$ (erg s^{-1})
(1)	(2)	(3)	(4)	(5)	(6)	(7)	(8)	(9)	(10)	(11)
J02:16:57-04:02:02	70.8	695	abs*PL+R+L	$1.36^{+0.46}_{-0.40}$	2.94	0.11	588.4 (655)	$6.87^{+1.36}_{-1.44}$	$44.5^{+0.03}_{-0.04}$	$44.54^{+0.04}_{-0.04}$
J02:17:05-04:56:54	86.5	535	abs*PL+R	$1.25^{+0.86}_{-0.73}$			525.9 (529)	$3.66^{+0.95}_{-0.98}$	$44.62^{+0.04}_{-0.05}$	$44.66^{+0.05}_{-0.05}$
J02:17:06-05:25:47	46.5	176	abs*PL+R	$0.76^{+1.29}_{\rm peg}$			168.0 (208)	$1.70^{+0.56}_{-0.55}$	$44.29^{+0.06}_{-0.09}$	$44.31^{+0.08}_{-0.09}$
J02:17:15-04:01:17	70.8	385	abs*PL+R	$48.45^{+21.68}_{-15.24}$			478.5 (489)	$7.24^{+1.06}_{-1.11}$	$44.76^{+0.07}_{-0.06}$	$45.29^{+0.08}_{-0.09}$
J02:17:16-04:30:09	58.2	125	abs*PL	$2.94^{+1.30}_{-0.98}$			185.2 (189)	$1.43^{+0.31}_{-0.33}$	$43.24^{+0.07}_{-0.08}$	$43.35^{+0.07}_{-0.08}$
J02:17:22-04:36:55	53.8	173	abs*PL	$26.45^{+12.39}_{-10.17}$			218.9 (217)	$1.10^{+0.24}_{-0.25}$	$44.89^{+0.06}_{-0.07}$	$45.43^{+0.06}_{-0.07}$
J02:17:24-04:18:44	79.7	1037	abs*PL+R+L	$4.04^{+1.33}_{-1.28}$	1.48	0.06	653.8 (696)	$4.52^{+0.71}_{-0.72}$	$45.27^{+0.03}_{-0.03}$	$45.39^{+0.03}_{-0.03}$
J02:17:33-04:06:13	46.0	160	abs*PL+R	$0.01^{+0.42}_{\rm peg}$			250.4 (292)	$0.91^{+0.88}_{-0.29}$	$43.87^{+0.10}_{-0.09}$	$43.87^{+0.07}_{-0.08}$
J02:17:36-04:59:11	70.5	130	abs*PL	$8.49^{+5.48}_{-3.61}$			234.5 (229)	$0.89^{+0.22}_{-0.23}$	$44.63^{+0.07}_{-0.08}$	$44.90^{+0.07}_{-0.08}$
J02:17:36-05:01:07	80.9	305	abs*PL+R	$0.65^{+0.67}_{-0.61}$			329.4 (368)	$1.51^{+0.54}_{-0.52}$	$44.03^{+0.06}_{-0.07}$	$44.06^{+0.06}_{-0.06}$
J02:17:40-04:32:43	60.0	242	abs*PL+R	$0.34^{+0.73}_{\rm peg}$			280.8 (311)	$1.30^{+0.77}_{-0.34}$	$44.32^{+0.07}_{-0.08}$	$44.33^{+0.06}_{-0.06}$
J02:17:49-05:23:07	64.4	742	abs*PL+R+L	$13.91^{+3.63}_{-2.79}$	3.18	0.17	617.7 (655)	$14.24^{+1.54}_{-1.49}$	$44.38^{+0.03}_{-0.03}$	$44.61^{+0.05}_{-0.06}$
J02:18:37-04:29:50	79.5	129	abs*PL+R	$3.02^{+1.73}_{-1.43}$			226.5 (233)	$1.03^{+0.61}_{-0.26}$	$43.98^{+0.1}_{-0.1}$	$44.08^{+0.08}_{-0.09}$
J02:19:01-04:24:41	62.4	146	abs*PL+R	$0.48^{+1.30}_{\rm peg}$			220.1 (231)	$1.19^{+0.44}_{-0.45}$	$44.09^{+0.06}_{-0.11}$	$44.11^{+0.08}_{-0.09}$
J02:19:31-04:49:41	76.1	565	abs*PL+R+L	$0.81^{+0.32}_{-0.27}$	3.84	0.18	483.9 (613)	$5.16^{+1.17}_{-1.08}$	$44.01^{+0.04}_{-0.05}$	$44.03^{+0.04}_{-0.04}$
J02:19:56-05:05:01	85.9	341	abs*PL+R	$1.14^{+0.48}_{-0.51}$			403.3 (477)	$1.28^{+0.39}_{-0.09}$	$44.33^{+0.06}_{-0.04}$	$44.38^{+0.04}_{-0.05}$
J02:20:32-04:50:02	52.7	101	abs*PL+L	$7.80^{+7.10}_{-3.68}$	3.08	0.24	206.2 (172)	$1.43^{+0.42}_{-0.43}$	$43.80^{+0.09}_{-0.13}$	$44.02^{+0.10}_{-0.12}$
J02:20:33-05:08:55	51.9	137	abs*PL+R	$4.92^{+2.81}_{-2.62}$			239.4 (238)	$1.71^{+1.11}_{-0.48}$	$44.47^{+0.10}_{-0.10}$	$44.63^{+0.08}_{-0.10}$
J02:20:34-05:06:58	60.8	47	abs*PL+R	$5.02^{+10.85}_{-5.02}$			109.7 (126)	$0.69^{+0.8}_{-0.3}$	$44.33^{+0.18}_{-0.23}$	$44.47^{+0.16}_{-0.21}$
J02:21:30-04:02:03	33.7	109	abs*PL+L	$0.79^{+0.66}_{-0.51}$	3.16	0.75	108.9 (153)	$1.47^{+0.37}_{-0.34}$	$43.97^{+0.09}_{-0.11}$	$44.00^{+0.08}_{-0.08}$
J02:21:50-05:23:58	65.9	163	abs*PL+R	$2.15^{+2.21}_{-1.83}$			256.7 (263)	$1.72^{+0.52}_{-0.58}$	$44.24^{+0.06}_{-0.10}$	$44.30^{+0.10}_{-0.12}$
J02:22:32-04:49:09	65.6	226	abs*PL+R+L	$4.91^{+2.37}_{-2.05}$	1.48	0.2	234.1 (285)	$2.73^{+0.90}_{-0.81}$	$44.51^{+0.06}_{-0.06}$	$44.64^{+0.07}_{-0.08}$
J02:23:30-04:34:42	66.0	166	abs*PL	$0.93^{+1.60}_{\rm peg}$			209.9 (238)	$0.71^{+0.14}_{-0.15}$	$44.43^{+0.07}_{-0.07}$	$44.49^{+0.07}_{-0.07}$
J02:23:38-04:05:13	104.7	375	abs*PL+R	$3.06^{+2.34}_{-2.14}$			356.7 (376)	$1.33^{+0.35}_{-0.28}$	$44.88^{+0.05}_{-0.05}$	$44.98^{+0.05}_{-0.05}$
J02:24:01-04:05:28	62.8	61	abs*PL	$0.73^{+1.83}_{\rm peg}$			141.2 (131)	$0.47^{+0.18}_{-0.18}$	$43.92^{+0.11}_{-0.13}$	$43.97^{+0.11}_{-0.13}$
J02:24:59-04:14:14	55.6	170	abs*PL	$3.71^{+1.59}_{-1.24}$			222.6 (249)	$1.30^{+0.25}_{-0.25}$	$44.41^{+0.06}_{-0.07}$	$44.56^{+0.06}_{-0.07}$
J02:25:12-04:19:11	72.0	661	abs*PL+R	$2.99^{+1.6}_{-1.26}$			554.5 (636)	$6.61^{+1.19}_{-1.15}$	$44.76^{+0.03}_{-0.04}$	$44.84^{+0.05}_{-0.05}$
J02:25:14-04:34:21	40.2	67	abs*PL+R+L	$114.96^{+125.02}_{-36.42}$	1.49	0.27	167.7 (164)	$1.80^{+0.81}_{-0.56}$	$44.31^{+0.32}_{-0.13}$	$45.42^{+0.13}_{-0.15}$
J02:26:06-04:44:19	51.9	103	abs*PL+R	$15.86^{+8.63}_{-6.32}$			192.1 (212)	$1.46^{+0.83}_{-0.24}$	$44.15^{+0.17}_{-0.12}$	$44.52^{+0.09}_{-0.10}$
J02:26:24-04:13:43	47.0	238	abs*PL+R	$0.01^{+0.31}_{\rm peg}$			316.6 (387)	$2.96^{+1.08}_{-0.99}$	$44.43^{+0.05}_{-0.09}$	$44.43^{+0.07}_{-0.08}$
J02:26:33-04:43:07	101.9	110	abs*PL+L	$1.28^{+3.87}_{\rm peg}$	1.88	0.33	289.9 (300)	$0.43^{+0.17}_{-0.15}$	$44.26^{+0.09}_{-0.14}$	$44.31^{+0.10}_{-0.12}$
J02:26:47-05:31:13	67.8	255	abs*PL+R	$3.15^{+1.23}_{-1.11}$			411.4 (461)	$3.39^{+1.43}_{-0.88}$	$44.13^{+0.07}_{-0.08}$	$44.23^{+0.06}_{-0.07}$
J02:27:16-04:32:42	60.2	151	abs*PL+R+L	$4.24^{+2.35}_{-2.0}$	1.04	0.16	218.3 (232)	$1.21^{+0.64}_{-0.19}$	$44.28^{+0.1}_{-0.07}$	$44.42^{+0.07}_{-0.08}$
J02:27:29-04:48:58	49.7	257	abs*PL+R	$7.31^{+4.39}_{-4.82}$			291.9 (327)	$2.39^{+0.66}_{-0.60}$	$44.31^{+0.05}_{-0.07}$	$44.48^{+0.08}_{-0.08}$

Note: $F_{2-10\ \rm keV}$ are in units of 10^{-14} erg cm^{-2} s^{-1}.

4.3.1 *XMM-Newton* data reduction

For each X-ray detected DOG, we downloaded all the available data from the *XMM-Newton* Science Archive[4]. The details of the X-ray observations are listed in Table 4.1. We reduced the *XMM-Newton* pn and MOS data using Science Analysis System (SAS) v21.0.0. The Observation Data Files (ODFs) were processed using `EPICPROC`, (`EPPROC` and `EMPROC` for pn and MOS, respectively) tasks to create pn, MOS1, and MOS2, event files for each observation ID. From each event file, we created good time intervals (GTI) event file using the `EVSELECT` task. The flaring background time intervals were identified from the single-event light curves of high (10−12 keV) and low (0.3−10 keV) energies and the time intervals exceeding count rates 3σ above the mean value were removed. The GTI files were calibrated using the most recent calibration files. Further, we filtered the event files at the energy ranges that overlap with the instrumental background lines, *i.e.*, Cu lines at 7.2−7.6 and 7.8−8.2 keV for pn.

For each observation ID, we extracted spectrum from each detector using a circular region of 15″ centred on the source position. The background spectrum was extracted from a neighbouring source-free region. In case of a source with multiple observations, we co-added the source as well as background spectra from individual observation IDs. We note that despite moderately deep XMM-SERVS observations with median pn exposure time of 46 ks per pointing, our DOGs tend to suffer from poor photon statistics. Therefore, to increase the spectral quality, we combine spectra from pn, MOS1 and MOS2 using the `EPICSPECCOMBINE` task. To combine the spectra from all three detectors, we ensure a common energy range (0.5−10 keV). The response and auxiliary files were computed by averaging the individual files of each detector.

[4] https://nxsa.esac.esa.int/nxsa-web/search

4.3.2 *Chandra* Data reduction

In order to improve the spectral quality, we also checked the availability of *Chandra* observations of our sample sources using *Chandra* Source Catalog Release 2.0 (CSA 2.0[5]). Three of our sample sources have *Chandra* archival data with total counts > 10. We reduced *Chandra*/ACIS data using Chandra Interactive Analysis of Observations (CIAO) software version 4.15 (CALDB version 4.10.4). For data reduction, we followed the standard procedure, which includes the removal of hot pixels, cosmic afterglows and background flaring time intervals. The cleaned event files were calibrated using the most recent calibration files. From each individual observation, we have extracted source spectrum using `SPECEXTRACT` task and considered $1''.5$ extraction region centred on the X-ray source. The background spectrum was extracted from a source-free circular region of radius $3''.0$ selected in the same CCD chip. The `SPECEXTRACT` task also generates auxiliary and response matrix files. In case of sources having multiple *Chandra*/ACIS observations, we added all individual spectra of a source. We created combined source spectrum, background spectrum, response, and auxiliary matrices using CIAO task `COMBINE_SPECTRA`.

4.4 X-ray spectral analysis

We performed X-ray spectral fittings of our sources using XSPEC v12.13.0c Arnaud (1996). In order to get reliable goodness-of-fit statistics with low-count spectra, we preferred to use Cash statistics (Cash, 1979) instead of χ^2 statistics. To fit the spectra, we began with a baseline model characterized by a simple absorbed power law which is defined as TBABS × ZTBABS × POWERLAW. The absorption from our Milky Way Galaxy is accounted for by the first absorption

[5] https://cxc.cfa.harvard.edu/csc/

component (`tbabs`) in which $N_{\rm H}$ is fixed to the Galactic value obtained from the NASA's HEASARC $N_{\rm H}$ calculator[6]. The galactic absorption in the direction of the XMM-SERVS field is found in the range of $1.86 - 2.45 \times 10^{20}$ cm^{-2}. The second absorption component accounts for the photoelectric absorption at source redshift. To obtain a better constraint on the absorbing column density, we fix the photon index (Γ) to 2.0, considering the fact that AGN generally exhibit a steep photon index in the range of 1.9 to 2.0 (Singh et al., 2011). In fact, it has been a common practice to fix the photon index to a typical value while dealing with low-count X-ray spectra (see Tozzi et al., 2006; Corral et al., 2016; Zou et al., 2020). We note that, our baseline model does not account for reflection, and therefore, we add a reflection component, whenever required. Similarly, commonly observed Fe K_{α} line emission is added using an unresolved Gaussian, whenever apparent. To model the reflection component, we used `pexrav`, a phenomenological model, which considers reflection from a neutral medium. We avoid using torus-based or more complex models due to low counts in spectra. We find that the continuum spectra can also be fitted well with the `plcbs` model, which, in addition to absorption, accounts for the Compton scattering of X-ray photons in obscured sources with column densities upto 5×10^{24} cm^{-2}. Although, both (simple absorbed power law as well as `plcbs`) models give similar values of column densities and fit statistics. Given the preference for a simpler model, we use absorbed power law rather than `plcbs`. The effect of scattering is not significant due to lower column densities (see Section 4.5.1).

In Table 4.2, we list the best-fitted spectral parameters. Figure 4.1 shows the best-fitted X-ray spectra of all our sample sources. We found that, the X-ray spectra of our sample sources are well-fitted with a simple absorbed power law plus reflection component. 28/34 sources show the presence of reflection

[6] https://heasarc.gsfc.nasa.gov/cgi-bin/Tools/w3nh/w3nh.pl

Table 4.3: The comparison of various parameters in different samples of X-ray detected DOGs

Reference	No. of DOGs	Redshift (z)	$S_{24\ \mu m}$ (mJy)	$m_{\rm r}$ (mag)	$N_{\rm H}$ (10^{22} cm^{-2})	$logL^{\rm int}_{2-10\ \rm keV}$ (erg s^{-1})
1	34	0.586−4.65 (1.75)	0.39−8.11 (0.65)	22.64−25.94 (24.68)	0.01−114.96 (3.01)	43.35−45.27 (44.32)
2	14	1.22−5.22 (2.29)	0.08−1.08 (0.24)	24.51−27.01 (26.34)	0.80−900.0 (17.0)	41.50−44.82 (43.57)
3	10	2.085−2.658 (2.503)	1.92−19.16 (7.50)	20.76−22.37 (22.07)	1.00−8.00 (1.95)	44.10−45.60 (45.10)
4	6	0.282−1.023 (0.775)	9.02−16.19 (16.07)	18.22−21.56 (21.29)	4.10−67.20 (18.10)	43.30−45.30 (44.20)

Note: Reference - 1 - This work; 2 - Corral et al. (2016); 3 - Lansbury et al. (2020); 4 - Zou et al. (2020). The median value of parameters is given within brackets.

component rising toward high energies. Fe Kα emission line is detected in 10/34 sources. We found only narrow unresolved (<100 eV) Fe Kα lines with equivalent widths in the range of 0.06 keV to 0.75 keV. The energy of Fe Kα in the observed frame is consistent with the source redshift within errors, except for two sources, XMM02660 and XMM04804. The detection of the Fe Kα line in remaining sources is likely to be hindered due to low counts in spectra.

4.5 Results and Discussion

4.5.1 The column densities in DOGs

One of the main objectives of our study is to constrain absorption column densities in DOGs and estimate the fraction of CT-AGN. Our spectral analysis demonstrates that most of our sample DOGs are moderately obscured with column densities in the range of 1.0×10^{20} cm^{-2} to 1.15×10^{24} cm^{-2} with a median value of 3.01×10^{22} cm^{-2} (see Table 4.3). There is only one DOG (J02:25:14-04:34:21) which can be classified as a CT-AGN candidate. Notably, J02:25:14-04:34:21, a

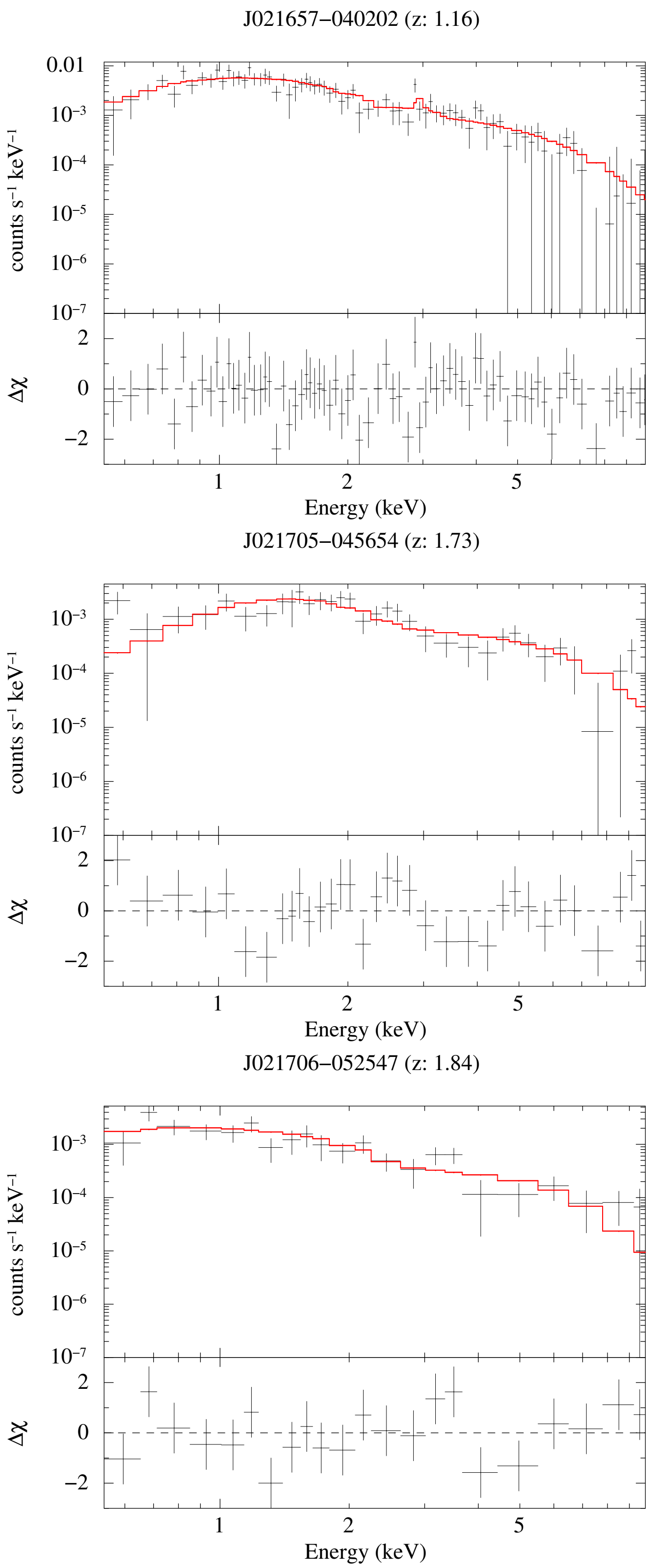

Figure 4.1: The best-fitted $0.5-10$ keV *XMM-Newton* spectra of X-ray detected DOGs. The X-ray spectra are rebinned for visual purpose with 10 counts per bin with 3σ significance. The top panels show spectra as well as fitted model (in red colour) and the bottom panels show residuals.

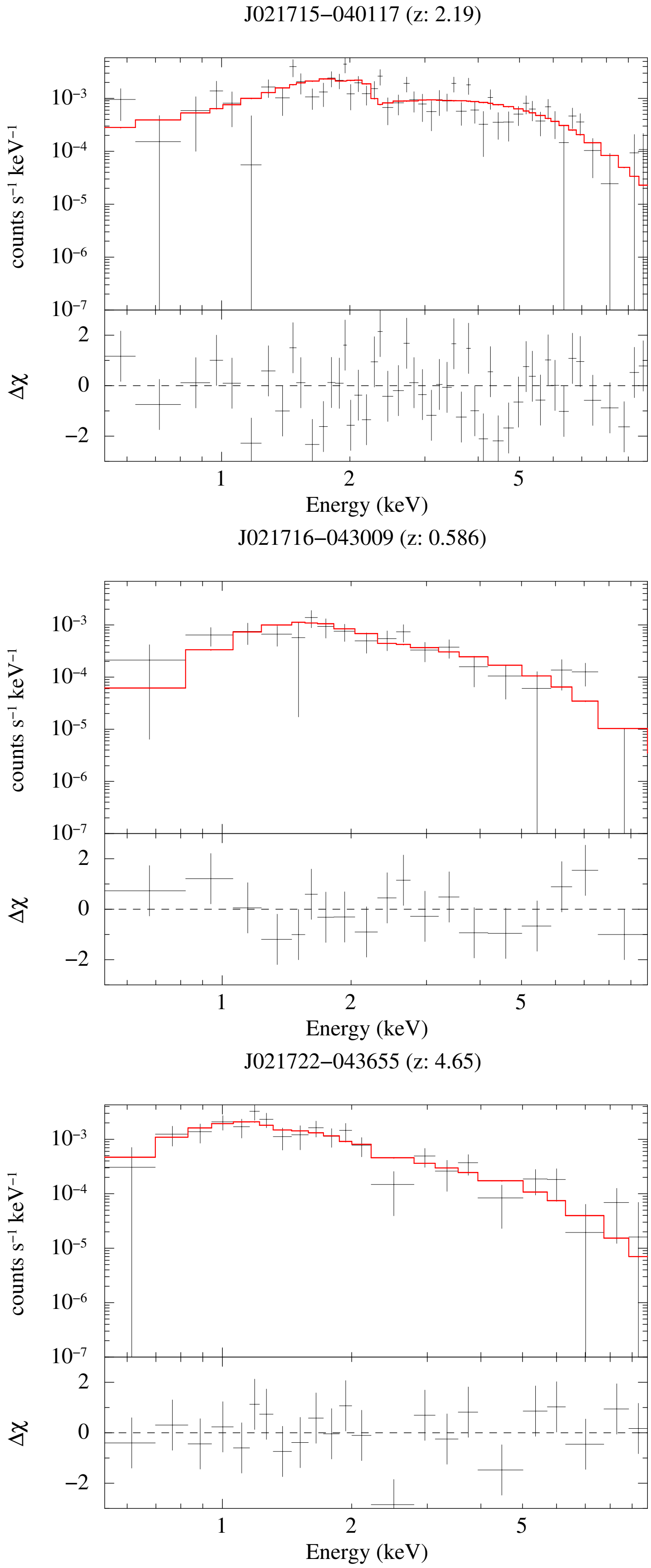

Figure 4.1: Continued.

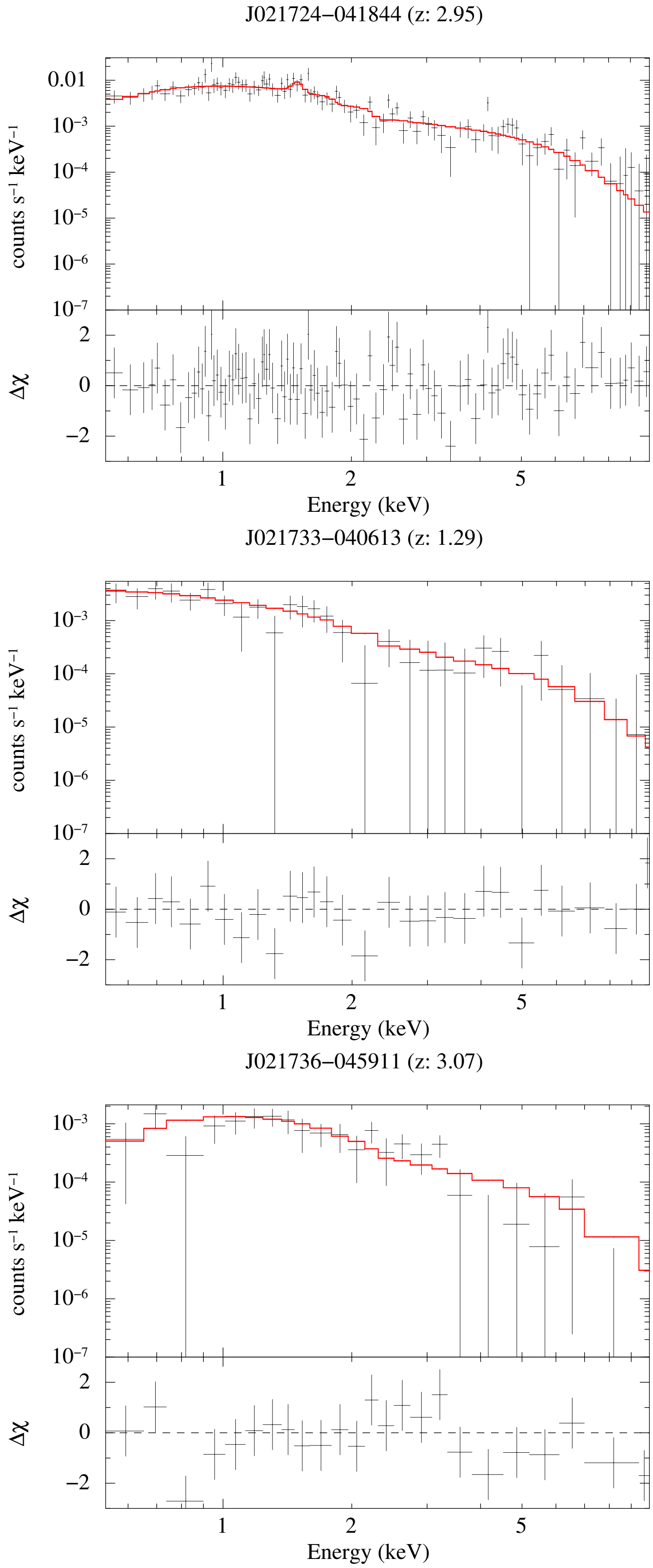

Figure 4.1: Continued.

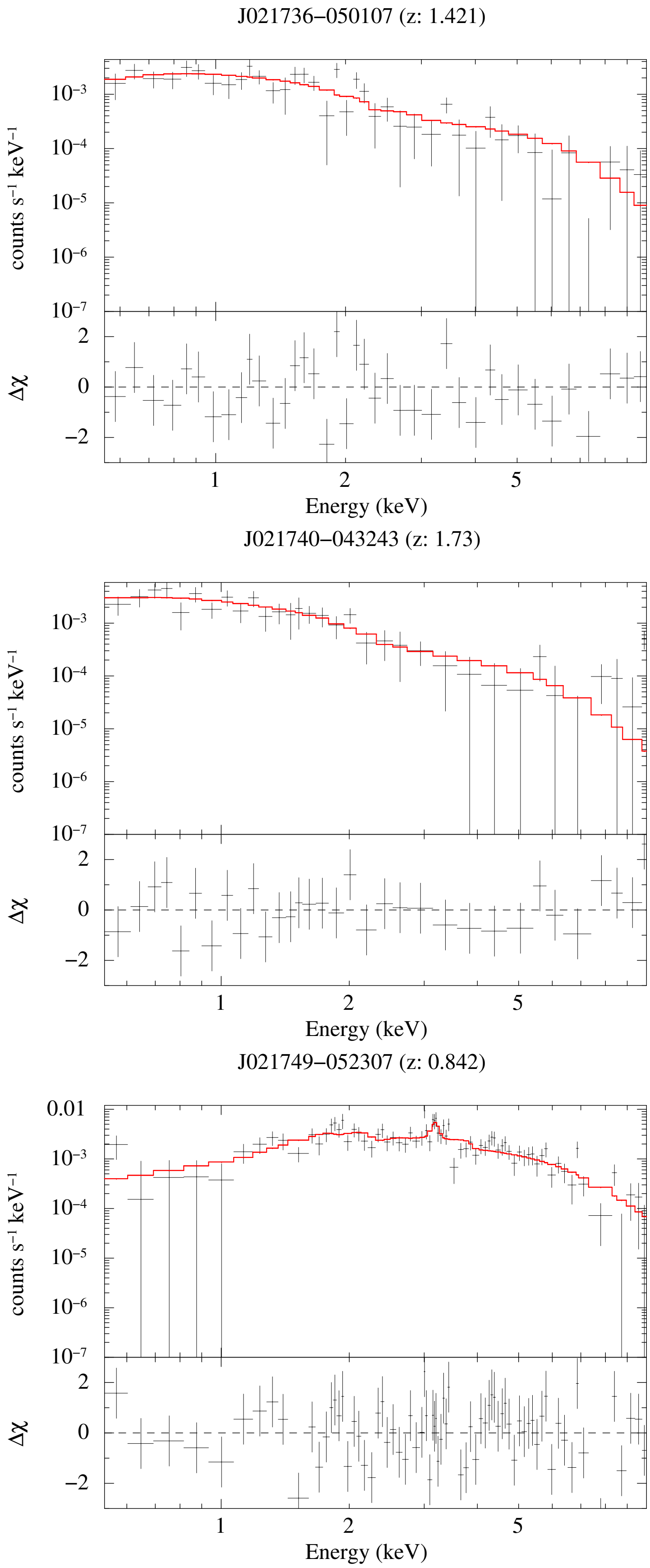

Figure 4.1: Continued.

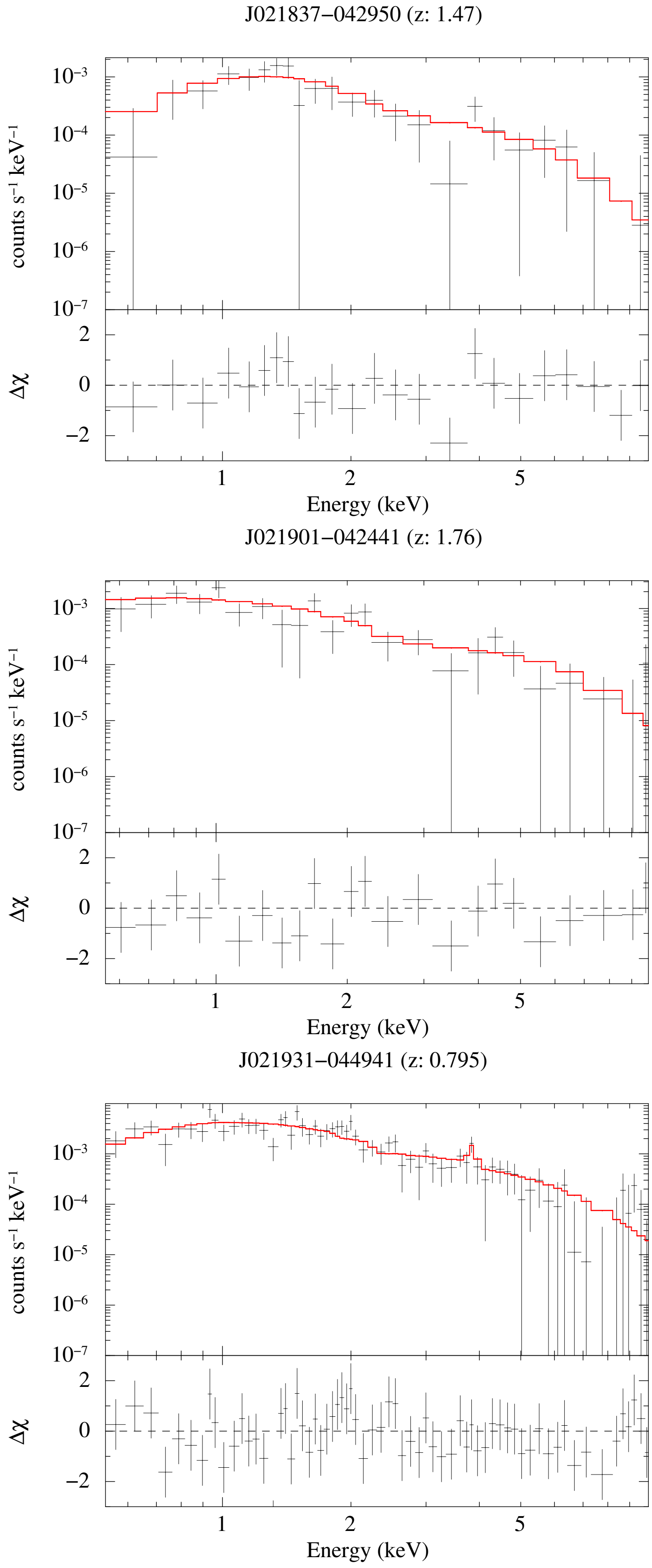

Figure 4.1: Continued.

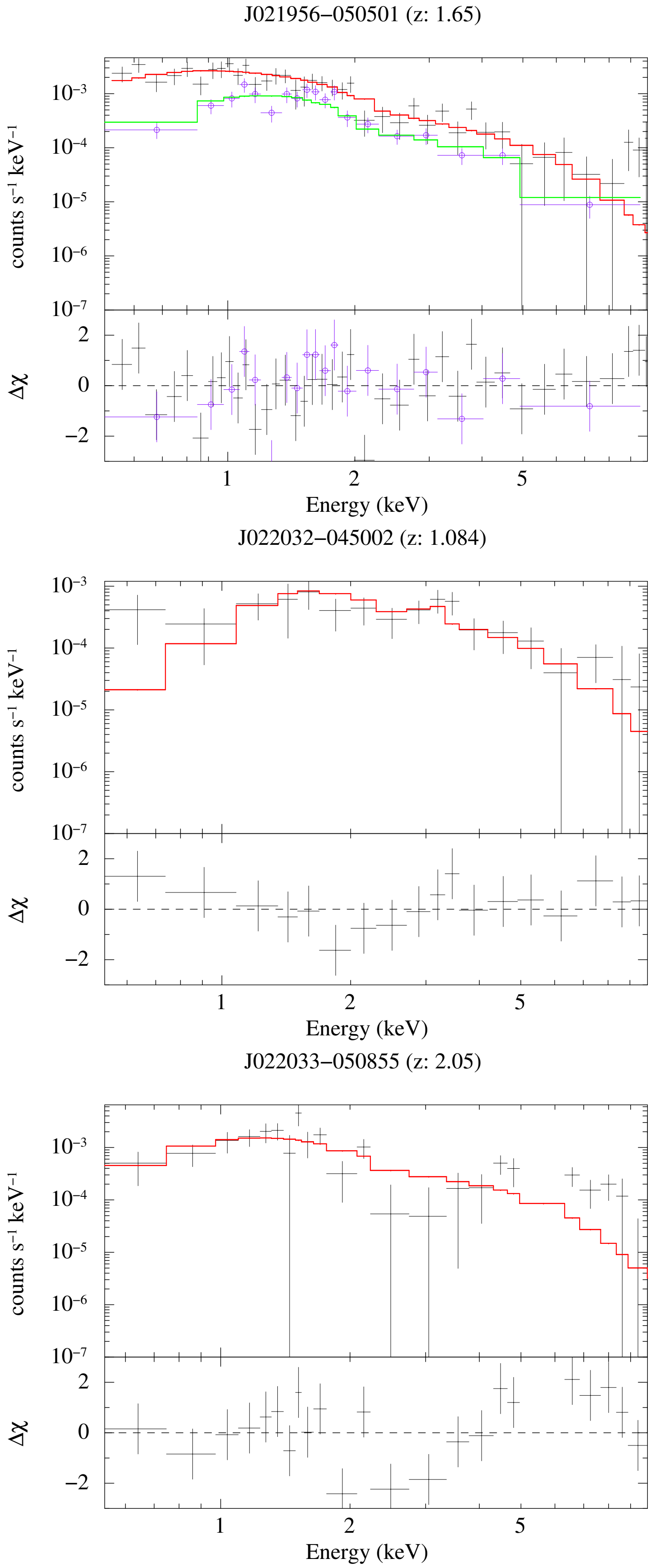

Figure 4.1: Continued. The *Chandra* spectra are shown in purple colour and the corresponding fitted models are shown in green colour.

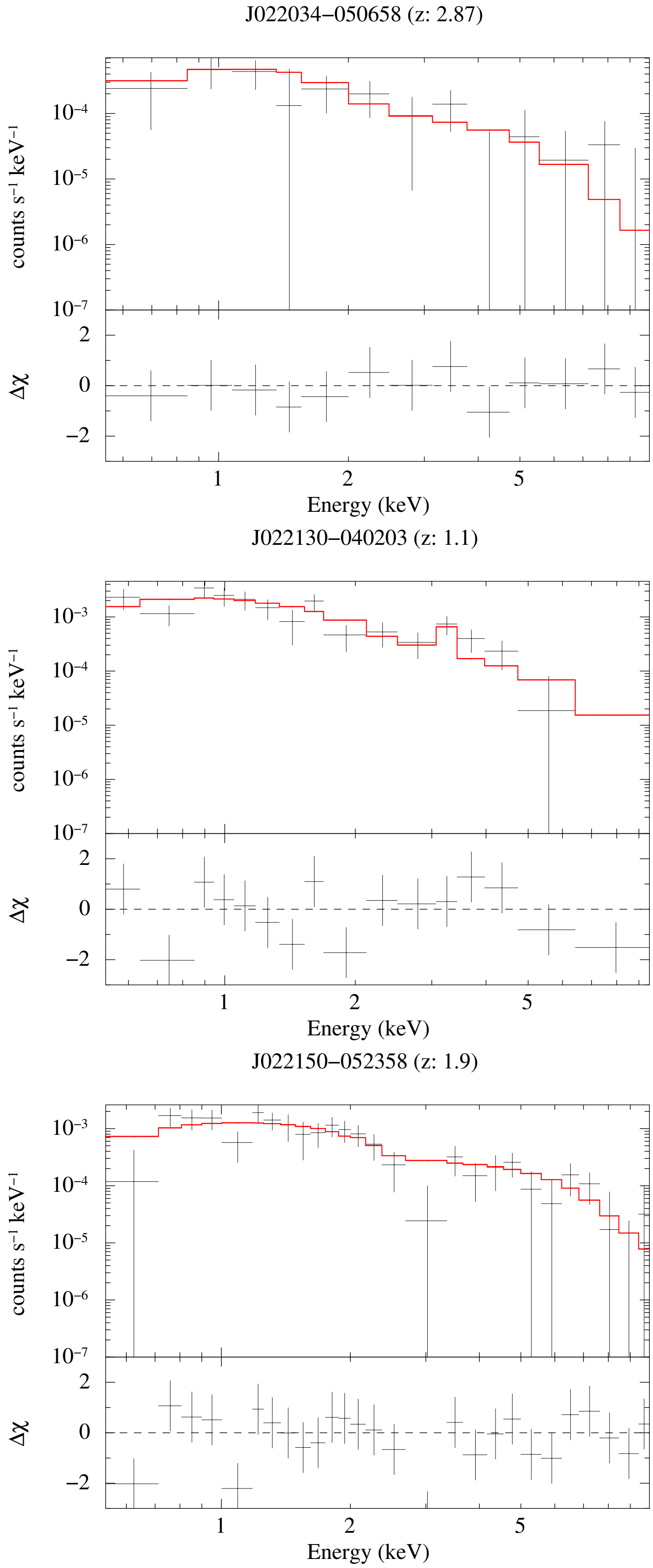

Figure 4.1: Continued.

J022232−044909 (z: 1.82)

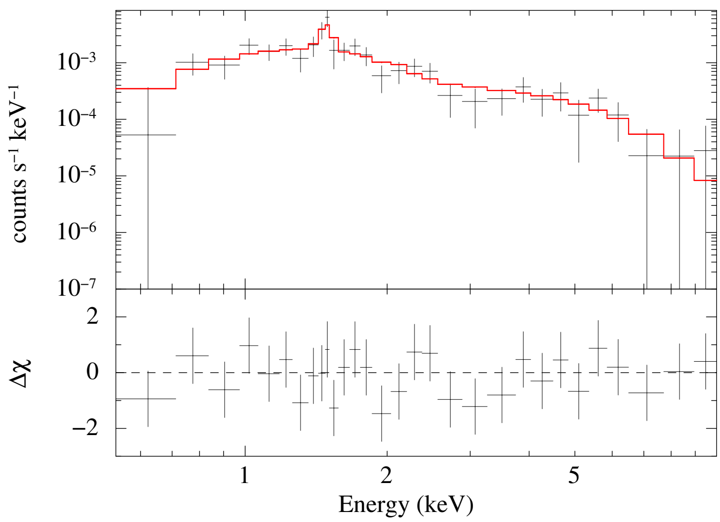

J022330−043442 (z: 2.3)

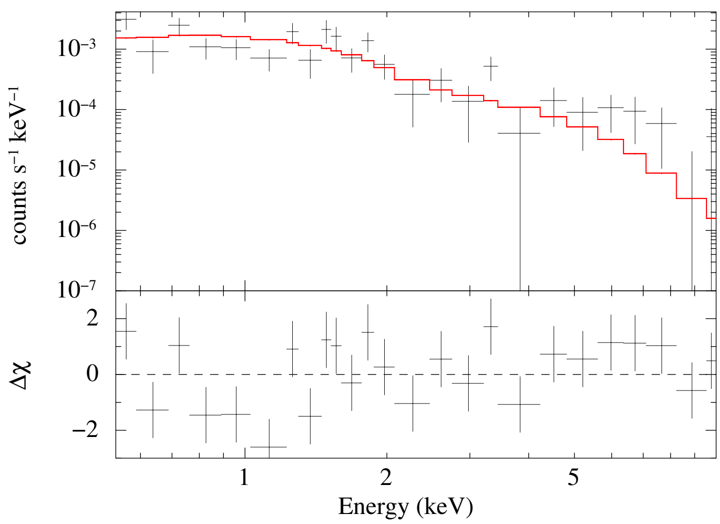

J022338−040513 (z: 3.28)

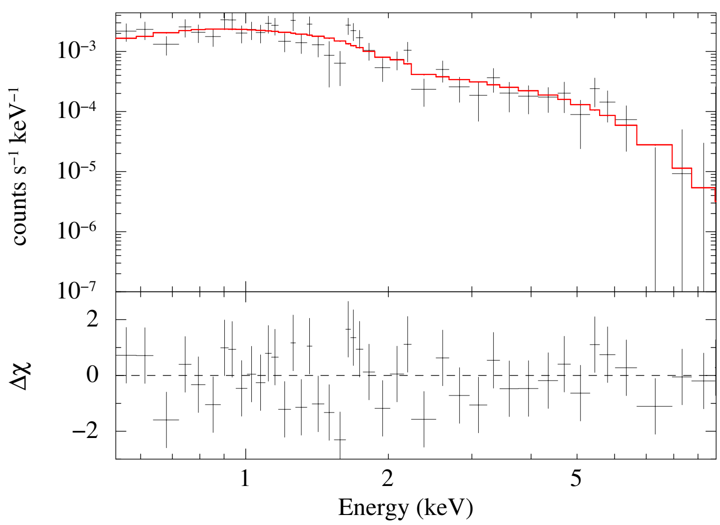

Figure 4.1: Continued.

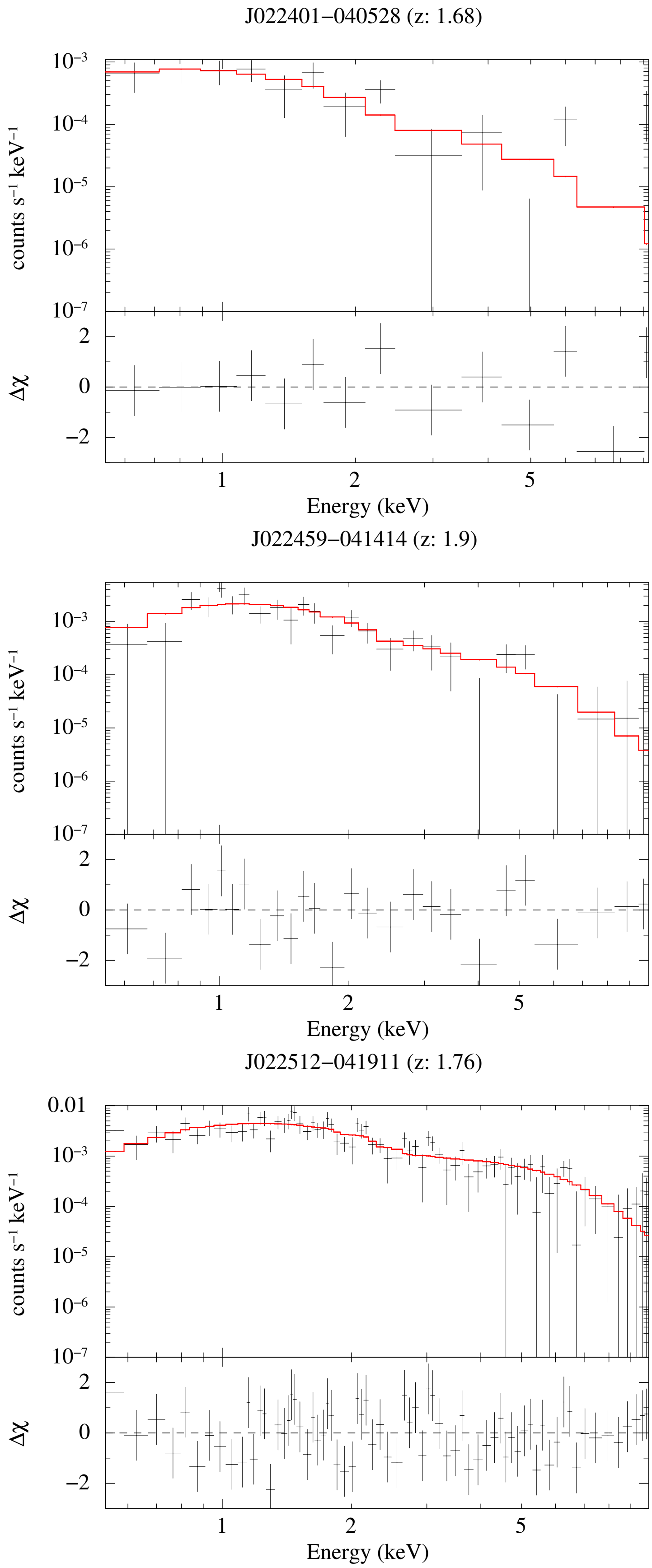

Figure 4.1: Continued.

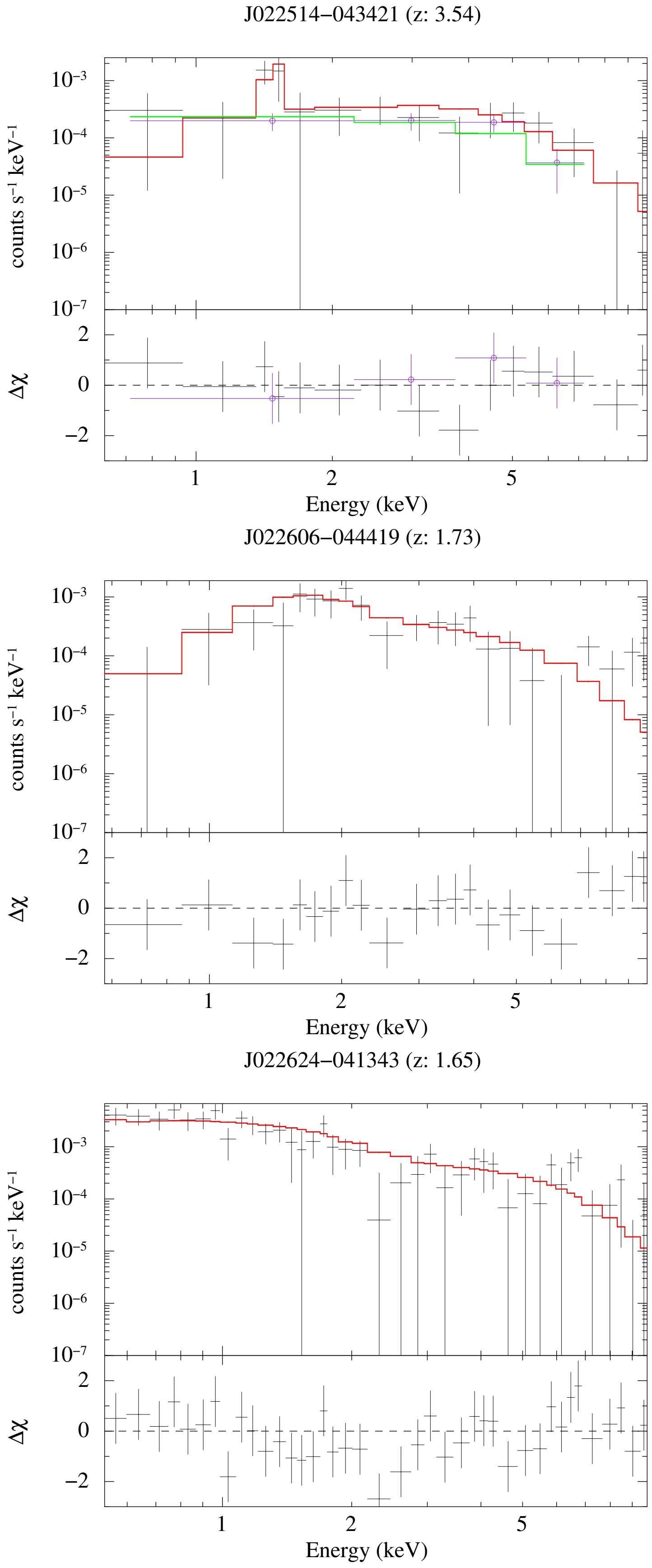

Figure 4.1: Continued.

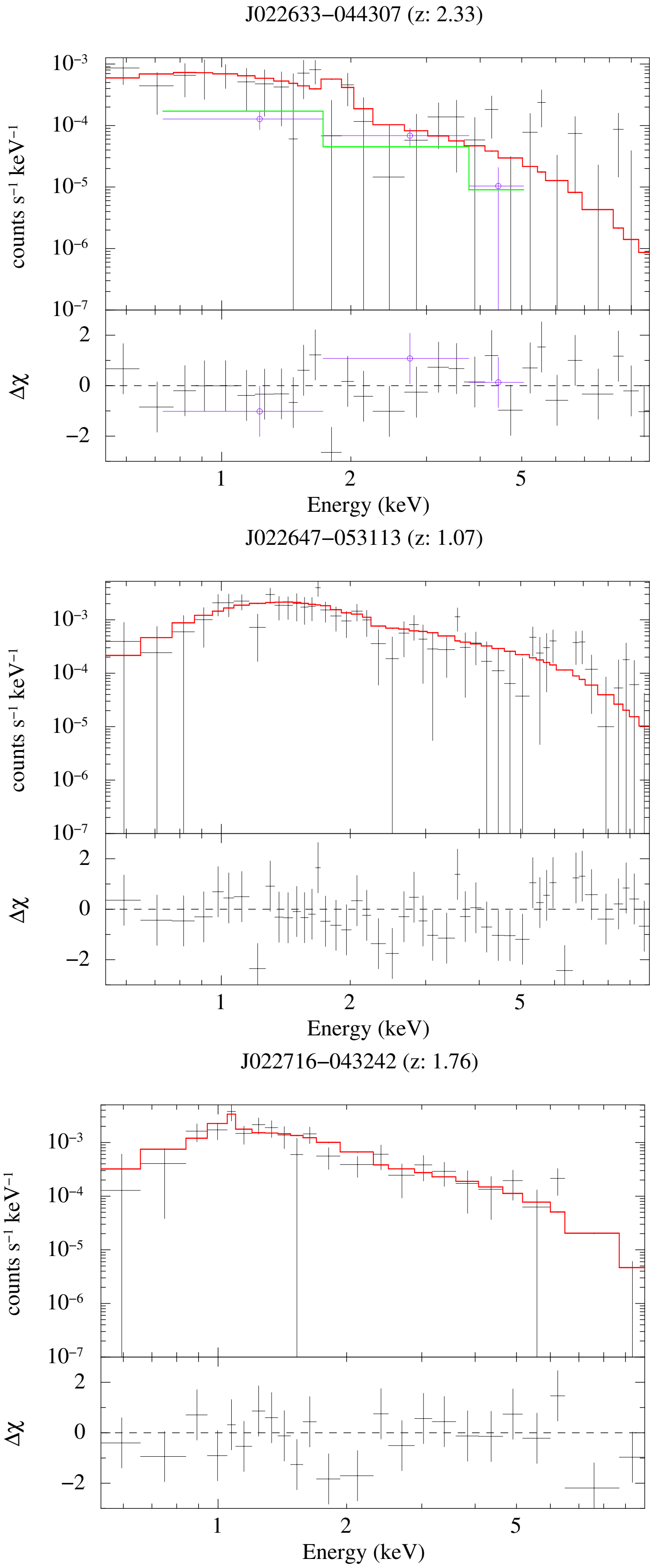

Figure 4.1: Continued.

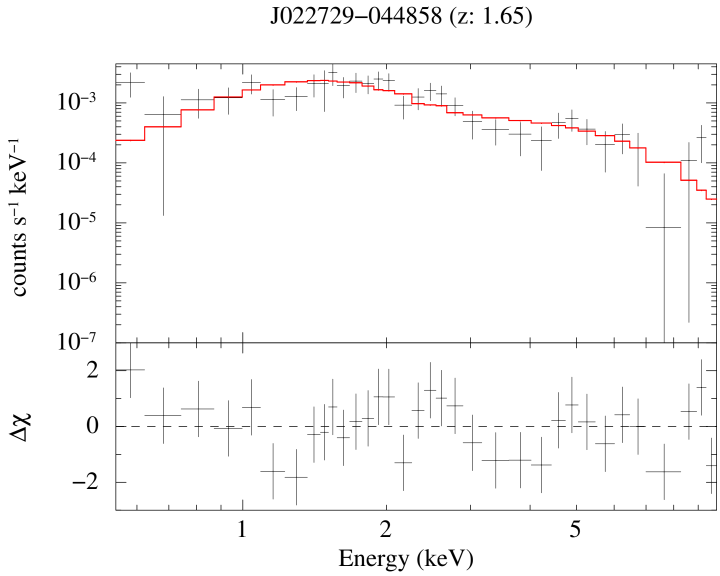

Figure 4.1: Continued.

CT-AGN candidate, has both *XMM-Newton* as well as *Chandra* observations. In addition to the one CT-AGN candidate, three more sources with $N_{\rm H} > 10^{23}$ cm^{-2} can be classified as heavily obscured AGN. Therefore, we find that only 04/34 (11.7 per cent) of our sample DOGs are heavily obscured and the remaining DOGs show either moderate (10^{22} cm^{-2} $\leq N_{\rm H} \leq 10^{23}$ cm^{-2}) or low absorption ($N_{\rm H} <$ 10^{22} cm^{-2}) . In Table 4.3, we show the comparison of $N_{\rm H}$ and other parameters (*i.e.,* redshift, 24 μm flux, optical $r-$band magnitude, and absorption corrected 2.0$-$10 keV X-ray luminosity) of our DOGs with other samples of DOGs reported in the literature (e.g., Corral et al., 2016; Lansbury et al., 2020; Zou et al., 2020). It is apparent that the $N_{\rm H}$ distribution for our sample is broadly consistent with those found in the literature.

Despite apparently similar $N_{\rm H}$ distributions found in different DOGs sample, we caution that differences in spectral quality and inherent biases ought to be accounted for. For instance, Corral et al. (2016) derived $N_{\rm H}$ for a sample of 14 DOGs in CDFS using spectra from deep 6 Ms *Chandra* observations and seven of their sample sources also have 3 Ms *XMM-Newton* data. Corral et al. (2016) demonstrated that, for the same set of sources, better quality spectra often render significantly higher $N_{\rm H}$ than that derived from their low counts spectra presented in Georgantopoulos et al. (2011). It is worth pointing out that, unlike our DOGs, a majority ($9/14 \simeq 64$ per cent) of DOGs in their sample showed high obscuration ($N_{\rm H} > 10^{23}$ cm^{-2}). Also, the fraction of CT-AGN (20−30 per cent) reported in their sample is higher than that found in our study. The higher fraction of heavily obscured DOGs found in Corral et al. (2016) sample can also be attributed to the inherent sample biases as their sample sources are fainter (both in MIR and optical bands) than ours and can indeed be more obscured. Further, we point out that somewhat lower $N_{\rm H}$ estimates reported by Zou et al. (2020) and Lansbury et al. (2020) are based on low counts X-ray spectra. To perform X-ray spectral study of 12 relatively nearby ($0.3 < z < 1.0$) bright DOGs with broad optical emission lines Zou et al. (2020) used snapshot *Chandra* observations with only 3 ks exposure time for each source and found $N_{\rm H}$ in the range of 4.1×10^{22} cm^{-2} to 6.7×10^{23} cm^{-2} (see Table 4.3). Using *XMM-Newton* observations of relatively low exposure (nearly 10− 30 ks exposure time) Lansbury et al. (2020) found $N_{\rm H}$ in the range of $1{-}8 \times 10^{22}$ cm^{-2} for the sample of ten luminous, heavily dust-reddened quasars. Therefore, considering lower $N_{\rm H}$ derived from the low-quality spectra, we caution that the $N_{\rm H}$ estimates and the fraction of CT-AGN need to be examined with sufficiently high-quality spectra.

4.5.2 The absorption corrected X-ray luminosities

The absorption corrected 2.0−10 keV X-ray luminosities in the observed frame for our sample sources span across 2.24×10^{43} to 1.86×10^{45} erg s^{-1} with a median value of 2.09×10^{44} erg s^{-1}. As expected, X-ray luminosities of our DOGs are similar to other DOGs and high−redshift reddened quasars reported in the literature (see Table 4.3). The high X-ray luminosities of our DOGs suggest the presence of luminous AGN in them. To further explore the nature of our DOGs, we utilised $L^{\rm int}_{2-10~\rm keV}$ versus $N_{\rm H}$ plot (see Figure 4.2). We find that, our DOGs show a trend of increasing $N_{\rm H}$ with an increase in X-ray luminosity. The highly luminous AGN enshrouded with high column densities ($N_{\rm H} > 10^{23}$ cm^{-2}) can be explained if they are Hot DOGs. From $L_{\rm X-ray} - L_{\rm IR}$ correlation (Zou et al., 2020), one can expect high IR luminosities ($L_{6~\mu m} > 10^{44}$ erg s^{-1}) for sources with high X-ray luminosities ($L_{2-10~\rm keV} > 10^{44}$ erg s^{-1}). Our DOGs with relatively low X-ray luminosity are expected to be less luminous in IR. Therefore, the trend observed in the $L^{\rm int}_{2-10~\rm keV}$ versus $N_{\rm H}$ plot can be explained if our sample DOGs constitute a heterogeneous population. Also, a significant variation in $N_{\rm H}$ for sources with similar X-ray luminosities can be understood, if they belong to different evolutionary phases. In the early phase, DOGs are likely to be more obscured, while, in the later phase, dominant feedback processes can blow out surrounding material leading to a less obscured AGN. We note that, in the same X-ray luminosity bin, DOGs reported by Corral et al. (2016) show systematically higher $N_{\rm H}$ than our DOGs. As discussed in Section 4.5.1 we note that inherent sample biases and/or spectral quality may influence $N_{\rm H}$ estimation. In the next section, we discuss the evolutionary scenario of our DOGs.

4.5.3 The $N_{\rm H}$ versus Eddington ratios plot : Evolutionary scenario of DOGs

Accreting black holes are known to launch powerful outflows, which are related to accretion rate (interpreted in terms of Eddington ratio; $\lambda_{\rm Edd}$) and the presence of surrounding material (Fabian et al., 2008; Thompson et al., 2015). To gain better insights into the nature of DOGs, we exploited $N_{\rm H}$ versus Eddington ratio ($\lambda_{\rm Edd}$) diagnostic plot. Since our DOGs host dominant AGN, surrounding material

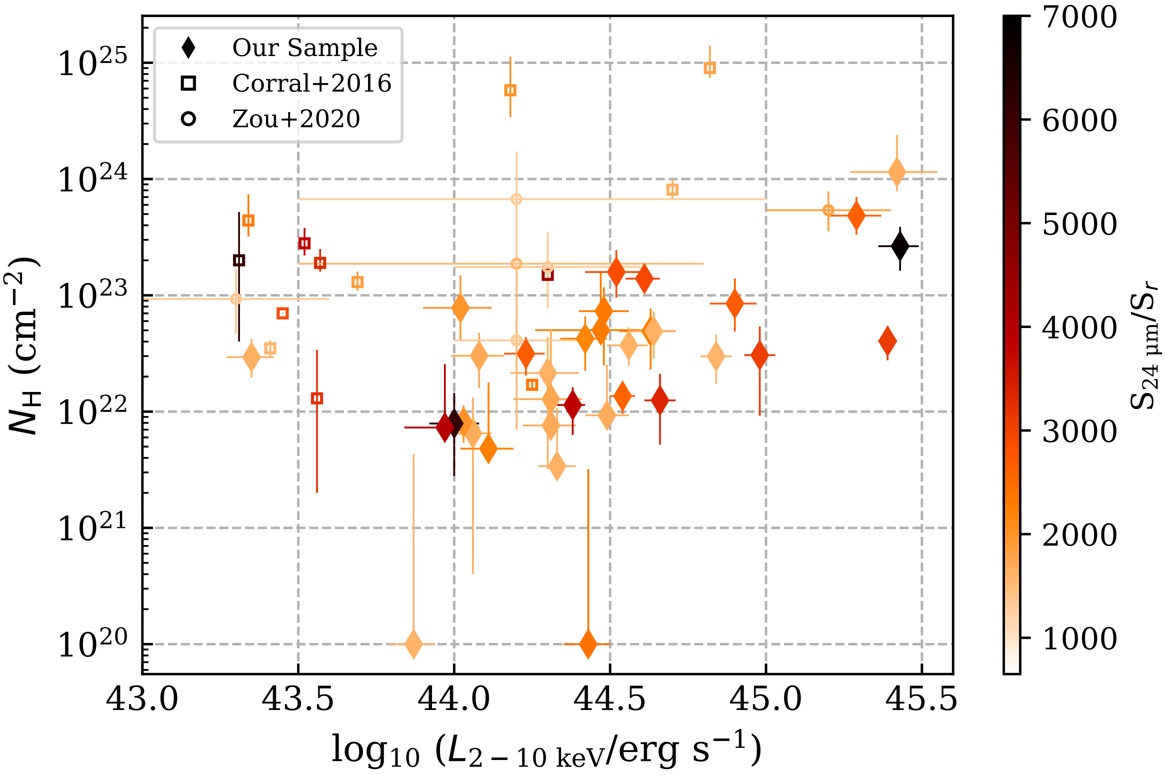

Figure 4.2: The N_{H} versus 2.0−10 keV luminosity plot for our sample DOGs. This plot helps us to examine the dependence of N_{H} onto 2.0−10 keV X-ray luminosity.

causing absorption is likely to be affected by the radiative feedback. In Figure 4.3 we show $N_{\rm H}$ versus $\lambda_{\rm Edd}$ plot for our DOGs as well as other DOGs from the literature. For our sample sources, we estimated $\lambda_{\rm Edd} = \frac{L_{\rm bol}}{1.26\times10^{38}\ M_{\rm BH}}$; where $L_{\rm bol}$ is measured in the units of erg s^{-1} and $M_{\rm BH}$ in the units of $M_{\odot}$. We obtained $L_{\rm bol}$ estimates from $L_{2-10\ \rm keV}$ using the correlation reported by Duras et al. (2020). Since black hole masses of our DOGs are not available, we assume $M_{\rm BH} = 10^{8.5}$ M$\odot$, which is an average value for DOGs reported by Zou et al. (2020). To account for the deviation of the actual value of $M_{\rm BH}$ from the average value, we consider $10^{8}\ M_{\odot} - 10^{9}\ M_{\odot}$ range for $M_{\rm BH}$. The large error bars introduced in $\lambda_{\rm Edd}$ correspond to the range of $M_{\rm BH}$.

In the $N_{\rm H}$ versus $\lambda_{\rm Edd}$ plot, we show tracks and mark different regions (*i.e.*, blowout region having short-lived obscuration, long-lived obscuration, and obscuration related to host-galaxy dust lanes). The solid and dotted tracks represent the effective column density ($N_{\rm H}$) around AGN with $\lambda_{\rm Edd}$ assuming single scattering (Fabian et al., 2009) and radiation trapping (Ishibashi et al., 2018), respectively. The circumnuclear material is expected to undergo a fast blowout phase if column densities are lower, *i.e.*, the blowout region. If column densities are much higher and falling above tracks, obscuration is likely to sustain against outflows which in turn results in long-lived obscuration. Low column densities ($N_{\rm H} < 10^{22}$ cm^{-2}) in DOGs can be accounted for by the obscuration from the host galaxy dust lanes.

From Figure 4.3, it is evident that all of our DOGs, irrespective of their obscuration level, lie in the blowout region. Thus, our DOGs are likely to evolve into unobscured quasars. In fact, a substantial fraction of DOGs with $N_{\rm H} < 10^{22}$ cm^{-2} overlaps with the dust-reddened quasars reported by Lansbury et al. (2020). A few of our DOGs showing super Eddington accretion rates and high obscuration ($N_{\rm H} > 10^{23}$ cm^{-2}) can be Hot DOGs which are known to exhibit

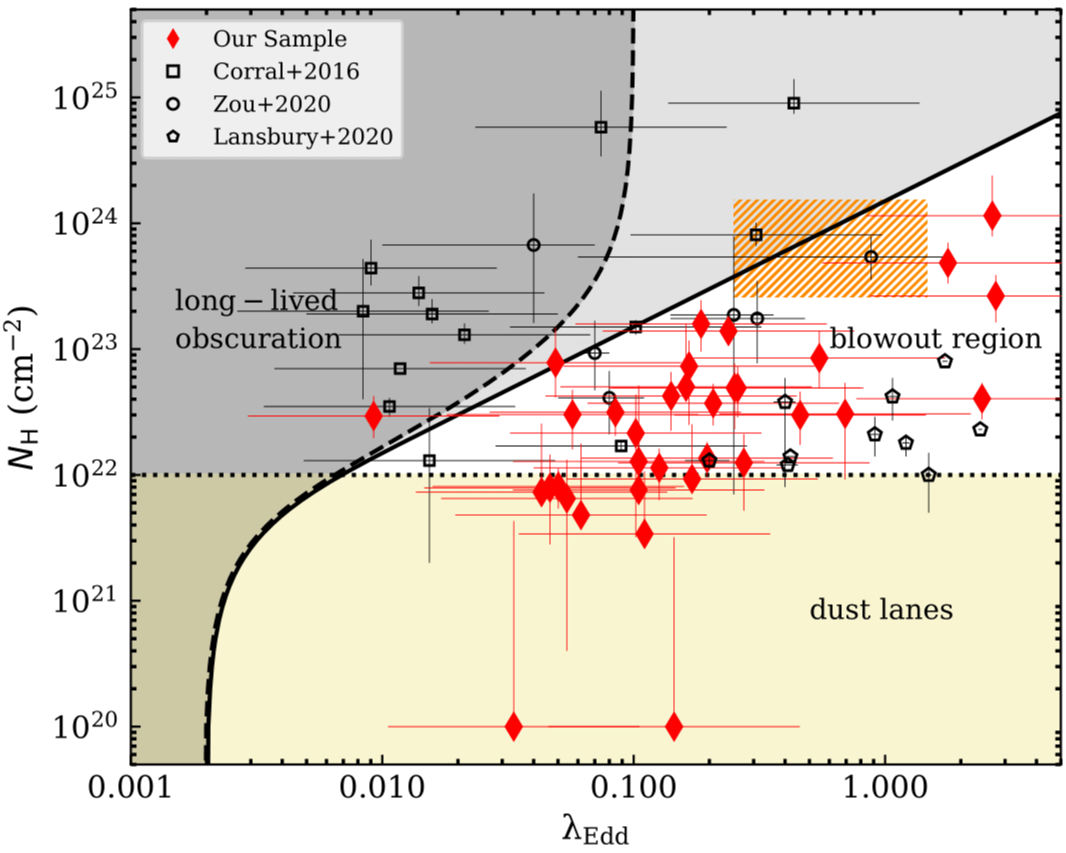

Figure 4.3: The $N_{\rm H}$ versus Eddington ratio plot for our sample DOGs. The grey-shaded region represents observed region for long-lived obscured sources. The solid line, representing the boundary between long-lived obscured sources region and short-lived obscuration (blowout) region, is based on the single-scattering limit and the dashed line shows the radiation-trapping limit (Ishibashi et al. 2018). The yellow shaded region with low absorption represents obscuration possibly caused by the host galaxy. The orange shaded region shows the possible regions for the WISE Hot DOGs from Vito et al. (2018); Wu et al. (2018).

higher obscuration than reddened quasars (Vito et al., 2018). Hot DOGs supposedly belong to an early phase of evolution during which accretion is at it's peak, but the feedback has not yet blown out the surrounding reservoir of gas and dust. In contrast, reddened quasars belong to a later phase during which feedback is dominantly ongoing. Further, reddened quasars can show different levels of X-ray obscuration depending upon their evolutionary stages (Goulding et al., 2018). In other words, reddened quasars can represent a heterogeneous population belonging to an early evolutionary phase just after the Hot DOGs as well as a late phase during which radiative feedback has swept away surrounding material. From the $N_{\rm H}$ versus $\lambda_{\rm Edd}$ plot, we conclude that, barring a few, the majority of our DOGs belong to the middle to late evolutionary phase, during which AGN feedback is likely to be dominant.

4.6 Conclusions

In this work, we study the X-ray spectral properties of 34 DOGs using deep *XMM-Newton* observations in the XMM-SERVS. To achieve better-quality spectra, we combined all the archival *XMM-Newton* pn and MOS observations, and utilised *Chandra*/ACIS observations, whenever available. Our conclusions are outlined as below.

1. We find that the 0.5−10 keV X-ray spectra of our DOGs can be characterized with a simple absorbed power law plus a reflection component. In 10/34 sources, we detect a narrow Fe Kα emission line. The detection of the Fe Kα line in the remaining sources is likely to be hindered due to low counts in the spectra.

2. Most of our DOGs show a moderate level of obscuration with absorbing column density in the range of 1.0×10^{20} cm^{-2} to 1.14×10^{24} cm^{-2} with a median value of 3.0×10^{22} cm^{-2}. The fraction of heavily obscured DOGs ($N_{\rm H} > 10^{23}$ cm^{-2}) is only 11.7 per cent. The X-ray absorption column densities of our DOGs are broadly consistent with those reported in the literature. Although, we caution that spectral quality and inherent biases need to be accounted for while comparing column densities from different samples.

3. The absorption corrected 2.0−10 keV X-ray luminosities of our DOGs are in the range of 2.24×10^{43} to 1.86×10^{45} erg s^{-1} with a median value of 2.09 $\times$ 10^{44} erg s^{-1}. The high X-ray luminosities suggest the presence of luminous AGN. The $N_{\rm H}$ versus $L^{\rm int}_{2-10\ keV}$ plot shows that high luminosity sources tend to possess higher obscuration, which infers their similarity with Hot DOGs.

4. Based on $N_{\rm H}$ versus $\lambda_{\rm Edd}$ diagnostic plot, we find that all but four DOGs show similarity with the reddened quasars. Four DOGs with super Eddington accretion and high obscuration, are likely to be Hot DOGs which belong to an early evolutionary phase during which accretion as well as star-formation rate peak. In the $N_{\rm H}$ versus $\lambda_{\rm Edd}$ diagnostic plot, all of our DOGs belong to the blowout region suggesting for a short-lived obscuration.

Overall, we find that our DOGs are likely to represent a heterogeneous population belonging to the different evolutionary phases.

Chapter 5

Multi-epoch hard X-ray view of the heavily obscured AGN in the Circinus Galaxy[†]

5.1 Introduction

The widely accepted unification model of AGN invokes a gaseous and dusty axisymmetric toroidal structure popularly known as 'torus' around the accreting SMBHs (e.g., Antonucci & Miller, 1985; Urry & Padovani, 1995; Ramos Almeida & Ricci, 2017). The evidence for the presence of the obscuring torus has come from a variety of observations that include the detection of broad emission lines in spectro-polarimetric observations of type 2 Seyferts (Moran, 2007), biconical shapes of narrow-line regions (NLRs) in type 2 Seyferts (Schmitt et al., 2003),

[†] **Abhijit Kayal**, Veeresh Singh, Claudio Ricci, N. P. S. Mithun, Santosh Vadawale, Gulab Dewangan and Poshak Gandhi, 2023, "Multi-epoch hard X-ray view of Compton-thick AGN Circinus Galaxy" *MNRAS*, Volume 522, Issue 3, pp.4098-4115, https://doi.org/10.1093/mnras/stad1216

and systematically higher X-ray absorbing column density in type 2 Seyferts (Singh et al., 2011; Ricci et al., 2017b). To explain the observed differences between two sub-classes of Seyfert galaxies, most of the early studies assumed a doughnut-shaped uniform-density obscuring medium (see Netzer, 2015). Albeit, X-ray monitoring campaigns of nearby AGN (*e.g.*, NGC 1365; Risaliti et al., 2005, NGC 4151; Puccetti et al., 2007, and NGC 7582 Rivers et al., 2015) finding the change in absorbing column density on timescales of days to several hours, favoured a clumpy obscuring medium. The discrete clouds forming the obscuring medium possibly exist at scales ranging from sub-parsec to a few hundred parsec (Bianchi et al., 2012; Torricelli-Ciamponi et al., 2014). Also, the column density of clumpy absorbing medium is likely to increase towards the equatorial plane (see Nenkova et al., 2008). However, despite a large number of studies, the location, geometry, and physical state of the obscuring material are still widely debated (e.g., Hönig, 2019; Saha et al., 2022).

The high-resolution infrared (IR) observations from the Very Large Telescope Interferometer (VLTI) have revealed that, contrary to the prevalent paradigm of the classical torus, the dust around AGN is not distributed in one single toroidal structure (Hönig et al., 2012; Tristram et al., 2014; Leftley et al., 2018). In fact, a two-component structure composed of an equatorial thin disk and a polar-extended cone-like feature, is implied from the modelling of IR interferometry data (see Figure 5.1). However, IR observations probe only the dusty phase of the obscuring matter around the AGN and may not yield a complete picture of circumnuclear material. The X-ray observations of AGN can provide insights into the geometry and distribution of circumnuclear material owing to the fact that X-ray emission emanating from the inner regions of the accreting system carries imprints of absorption and scattering caused by the gaseous phase of circumnuclear material (Risaliti et al., 2005; Morgan et al., 2012).

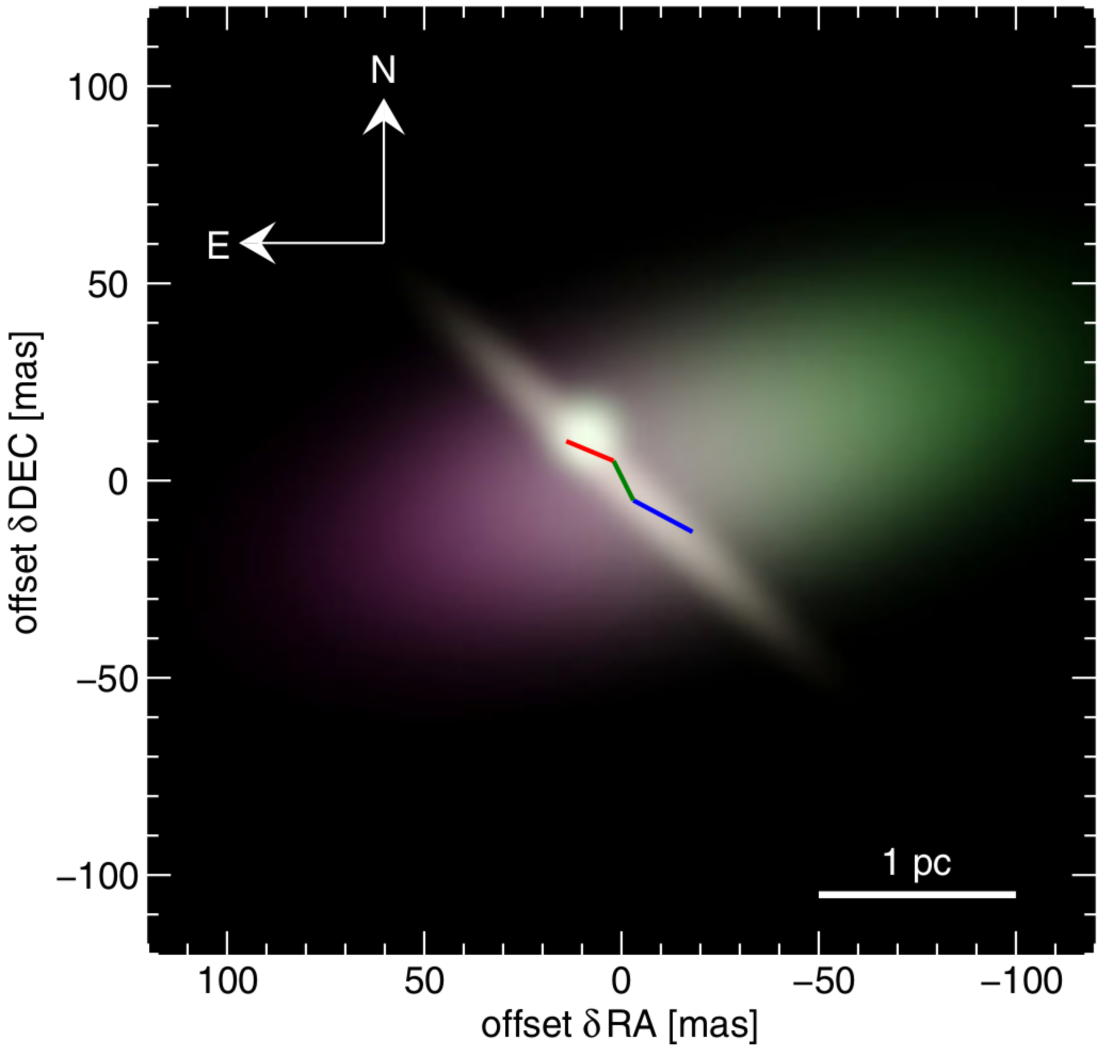

Figure 5.1: The three-component model image of the mid-infrared emission from the nucleus of the Circinus galaxy adapted from Tristram et al. (2014). The emission at 13.0 μm, 10.5 μm and 8.0 μm is depicted by logarithmically-scaled false colours in red, green and blue, respectively. Two distinct dust emitting regions can be clearly seen in the image, where the compact elongated structure resembles to an equatorial thin disk while another nearly perpendicular extended structure resembles to a polar extended feature. The trace of the water maser disk is plotted with the blue and red color lines.

The multi-epoch X-ray observations have revealed a significant change in the line-of-sight column density ($N_{\rm H,\ LOS}$) even in Compton-thick ($N_{\rm H,\ LOS} > 1.5 \times 10^{24}$ cm^{-2}) AGN (CT$-$AGN) (*e.g.*, MRK 3; Guainazzi et al., 2016, NGC 1068; Zaino et al., 2020, NGC 1358; Marchesi et al., 2022). The timescale for a significant variability in $N_{\rm H,\ LOS}$ depends on the distances, velocities and filling factors of the obscuring clouds around the SMBH. The type 2 AGN, in which line-of-sight passes through the obscuring torus, can be suitable targets to probe changes in $N_{\rm H,\ LOS}$. However, only a small number of such sources have been studied, hitherto, due to the unavailability of multi-epoch hard X-ray observations on timescales ranging from a few days to years. The hard X-ray ($>$ 10 keV) observations are crucial to probe any variation in covering factor and to break well-known line-of-sight column density and photon index ($N_{\rm H,\ LOS} - \Gamma$) degeneracy (see Puccetti et al., 2014; Marchesi et al., 2019). Also, hard X-ray observations are useful in mitigating the influences of off-nuclear X-ray sources. With the availability of multi-epoch hard X-ray observations on timescales ranging from days to years, Circinus galaxy (hereafter 'Circinus') is a suitable target for investigating changes associated with the AGN and reprocessing circumnuclear material. Due to its proximity (redshift (z) $\sim 0.00145 \pm 0.00001$ and luminosity distance, D$_L$ = 4.2 Mpc (Freeman et al., 1977)) and brightness, Circinus offers an advantage for performing an in-depth study of circumnuclear reprocessing material.

In this chapter, we investigate changes associated with the circumnuclear X-ray reprocessing material such as $N_{\rm H,\ LOS}$, average column density and covering factor in Circinus, for the first time, using multi-epoch hard X-ray observations from the *BeppoSAX*, *Suzaku*, *NuSTAR*, and *AstroSat* taken at ten different epochs across the period of 22 years from 1998 to 2020. The hard X-ray observations of the last three epochs *i.e.*, 2016 August 23, 2020 January 28 and 2020 November 26, are presented here for the first time. The chapter is organized as follows. In

Section 5.2, we provide a brief description of previous studies performed on Circinus with the main focus on the results obtained from hard X-ray observations. In Section 5.3, we give the details of X-ray observations and data reduction. In Section 5.4, we present the X-ray spectral modelling of off-nuclear sources and contamination model. In Section 5.5, we describe multi-epoch broadband X-ray modelling. Section 5.6 is devoted to the discussion of plausible geometry, changes in line-of-sight column density and the location of obscuring clouds. In Section 5.7, we summarise the results of our study.

In our study, we assume a flat Λ-cold dark matter cosmology with $H_0 = 70$ km s^{-1} Mpc^{-1}, $\Omega_\Lambda = 0.73$, and $\Omega_m = 0.27$, the same as those used in XSPEC 12.11.1c (Arnaud, 1996). With these cosmological parameters, $1''.0$ corresponds to 29 parsec at the distance of Circinus. We used Galactic neutral column density of $N_{\rm H}^{\rm gal} = 5.6 \times 10^{21}$ cm^{-2} (Kalberla et al., 2005) toward the direction of Circinus. The errors quoted on the spectral parameters are of 90 per cent confidence, unless stated otherwise.

5.2 Previous studies on Circinus

Based on the optical spectroscopic observations Circinus is classified as a Seyfert type 2 AGN with starburst activity (Freeman et al., 1977; For et al., 2012). The mass of SMBH ($M_{\rm BH}$) in the Circinus is estimated to be 1.7×10^6 M$\odot$ (Koss et al., 2017) using the relation between black hole mass and stellar velocity dispersion (Kormendy & Ho, 2013). The bolometric luminosity is estimated to be $L_{\rm bol} = 4 \times 10^{43}$ erg s^{-1} from the MIR nuclear spectrum (Moorwood et al., 1996). The estimates of black hole mass and bolometric luminosity suggest Eddington ratio ($L/L_{\rm Edd}$) of 0.2. The high resolution VLTI mid-infrared interferometric instrument (MIDI) observations revealed that the parsec-scale MIR emission around

AGN in the Circinus is composed of two distinct components : (i) a disc-like component coinciding with the disc observed in maser emission, and (ii) a component extending in a polar direction, along the ionisation cone seen in the optical (Tristram et al., 2007, 2014). The polar component is found to be responsible for upto $\sim 80\%$ of the MIR emission on parsec-scales (Tristram et al., 2014).

Circinus is widely studied in the X-ray wavelengths and is classified as a Compton-Thick (CT) AGN ($N_{\rm H} \geq 1.5 \times 10^{24}$ cm^{-2}). The X-ray observations below 10 keV from the *ASCA*, *Chandra*, and *XMM-Newton* showed only a reflection dominated spectrum with prominent Fe Kα emission line (see Matt et al., 1996; Guainazzi et al., 1999). Early observations at hard X-ray from the *BeppoSAX* showed a high absorbing column density of $\rm N_H \sim 4 \times 10^{24}$ cm^{-2} confirming Circinus to be a CT-AGN. Interestingly, two *BeppoSAX* observations performed almost three years apart during 1998 and 2001 reported a dramatic flux ($\sim$ 50 percent) and spectral variation (Bianchi et al., 2002). The observed variability was ascribed to an extremely variable Ultra Luminous X-ray (ULX) source named Circinus Galaxy X1(CGX1; Bauer et al., 2001) that contaminated *BeppoSAX* spectrum obtained with $2'.0$ extraction region. However, an intrinsic variation to AGN or line-of-sight column density could not be completely ruled out. Using $3 - 70$ keV *Suzaku* observations Yang et al. (2009) reported the presence of a direct AGN component transmitted through a column density of $\simeq 4 \times 10^{24}$ cm^{-2}. Later on, using *Chandra* and *XMM-Newton* observations of higher spatial resolution Arévalo et al. (2014) accounted for the contribution from the off-nuclear contaminating X-ray sources, and reported that the hard X-ray spectrum is Compton-scattered by an optically-thick torus having equatorial column density $6 - 10 \times 10^{24}$ cm^{-2} with a relatively steeper photon index of $\Gamma = 2.2 - 2.4$. Notably, *NuSTAR* observations did not support the detection of transmitted AGN component which was earlier suggested with the *Suzaku* observations. More recently, Andonie et al. (2022) showed that the 3−70 keV *NuSTAR* spectrum of Circinus can be fitted with a model considering the reprocessing components consisted of accretion disc, BLR, a flared disc and a hollow cone in the polar direction.

5.3 X-ray observations and Data reduction

For our study, we utilised all the available hard X-ray observations ($E > 10$ keV) taken from the *NuSTAR*, *AstroSat*, *Suzaku* and *BeppoSAX* during 1998 to 2020. Circinus is observed with the *NuSTAR* at six different epochs, twice with the *BeppoSAX*, and once each with the *AstroSat* and *Suzaku*. To constrain the soft X-ray part of the spectra and contamination from the off-nuclear X-ray sources, we utilised *Chandra* and *XMM-Newton* observations. The *XMM-Newton* observations taken on 2013 February 03 and 2016 August 23 were performed quasi−simultaneously with the *NuSTAR* observations of corresponding epochs. The start and end times of each *XMM-Newton* and *NuSTAR* pair of observations are within 12 hours. We list the basic details of all the X-ray observations in Table 5.1. In the following subsections, we describe our observations and data reduction procedures.

5.3.1 NuSTAR

Circinus has been observed with the Nuclear Spectroscopic Telescope Array (*NuSTAR*; Harrison et al., 2013) with its two co-aligned units having focal plane modules FPMA and FPMB. There are a total of six *NuSTAR* observations of Circinus during 2013 to 2020. We note that all the *NuSTAR* observations, except one taken on 2013 January 25 have targeted an ULX binary named ULX5 (see Mondal et al., 2021) residing 4′ to the south−west of the AGN, thus imaged Circinus at off-axis.

Table 5.1: The summary of X-ray observations

Epoch	Instrument	Date & start time	ObsID	Energy band (keV)	Detector	$T_{\rm exp}$ (ks)	Count-rate (cts s^{-1})	Off-axis (′)
(1)	(2)	(3)	(4)	(5)	(6)	(7)	(8)	(9)
1	*NuSTAR*	2020-11-26T05:51:09	80601502001	3−79	FPMA	106.1	0.86±0.01	2.65
				3−79	FPMB	105.2	0.82±0.01	2.65
2	*AstroSat*	2020-01-28T21:34:57	A07_100T02_9000003470 A07_100T02_9000003476	0.3−7.0	SXT	57.5	0.13±0.01	0.06
				3−80	LAXPC	85.4	6.72±0.10	0.06
				22−70	CZTI	71.0	0.56±0.06	...
	XMM Newton	2018-09-18T13:48:49	0824450301	0.5−10	pn	85.5	1.09±0.004	6.04
3	*NuSTAR*	2016-08-23T06:41:08	90201034002	3−79	FPMA	49.8	0.57±0.01	5.76
				3−79	FPMB	49.7	0.55±0.01	5.76
	XMM Newton	2016-08-23T16:53:33	0792382701	0.5−10	pn	16.2	1.72±0.01	5.78
4	*NuSTAR*	2013-02-05T05:06:07	30002038006	3−79	FPMA	36.2	0.82±0.005	3.05
				3−79	FPMB	36.1	0.85±0.005	3.05
5	*NuSTAR*	2013-02-03T03:01:07	30002038004	3−79	FPMA	40.3	0.84±0.01	2.91
				3−79	FPMB	40.2	0.86±0.01	2.91
	XMM Newton	2013-02-03T07:24:11	0701981001	0.5−10	pn	36.2	1.89±0.01	3.69
6	*NuSTAR*	2013-02-02T01:01:07	30002038002	3−79	FPMA	18.3	0.92±0.01	2.85
				3−79	FPMB	18.3	0.92±0.01	2.85
7	*NuSTAR*	2013-01-25T03:51:07	60002039002	3−79	FPMA	53.9	1.12±0.005	2.73
				3−79	FPMB	53.8	1.05±0.004	2.73
	Chandra	2010-12-17T18:10:27	12823	0.5−10	ACIS-S	152.4	0.063±0.001	0.21
8	*Suzaku*	2006-07-21T12:29:57	701036010	0.5−10	XIS-0	108.0	0.54±0.002	0.93
				0.5−10	XIS-1	108.0	0.53±0.002	0.76
				0.5−10	XIS-2	108.0	0.53±0.002	0.97
				0.5−10	XIS-3	108.0	0.52±0.002	1.09
				10−70	HXD-PIN	88.3	0.40±0.003	3.91
				50−120	HXD-GSO	88.3	0.14±0.012	3.91
9	*BeppoSAX*	2001-01-07T06:36:41	5114000100	2.0−10	MECS	51.7	0.18±0.002	1.77
				15−100	PDS	37.9	1.72±0.03	...
	XMM-Newton	2001-08-06T08:54:51	0111240101	0.5−10	pn	103.0	2.45±0.01	1.71
10	*BeppoSAX*	1998-03-13T06:32:49	5004700200	2.0−10	MECS	71.5	0.14±0.001	1.88
				15−100	PDS	63.3	1.83±0.03	...

Notes: $T_{\rm exp}$ is the net exposure time after removal of bad time−intervals. The net count rate in the total energy band is estimated after the removal of bad time−intervals and subtraction of background. The parameters of *AstroSat* observations are combination of observations taken under the two different observation IDs. Epochs are listed in chronological order based on the availability of hard X-ray (> 10 keV) observations.

The *NuSTAR* with $12'.5 \times 12'.5$ field-of-view (FOV) and angular resolutions of $18''$ Full Width at Half Maximum (FWHM) offers a clear detection of Circinus, along with the ULX5.

The *NuSTAR* data were reduced using the standard pipeline (`NUPIPELINE`) provided in the *NuSTAR* Data Analysis Software (`NUSTARDAS`, v2.1.2) within the HEASoft package (v6.30), in combination with the calibration database (v20220706). The unfiltered level 1 event lists were screened to reduce the internal background at high energies via standard depth corrections and removal of South Atlantic Anomaly (SAA) passages. The latest calibration files were used to create level 2 event files. We extracted the source spectra and lightcurves of AGN by using an aperture with a radius $100''$ for both FPMA and FPMB. The background spectra were extracted from a source-free region in the same chip using a circular aperture of the same size. We note that the 2016 *NuSTAR* observations show Circinus at a large off-axis angle of $5'.7$ with an elongated PSF. Hence, to include all the source emission with minimum contamination from the background, we extracted the source spectrum from an elliptical region (major axis = $90''$, minor axis = $50''$ and PA = $44°$). The net exposure times and count rates for both FPMA and FPMB of our observations are listed in Table 5.1. To apply χ^2 statistics, we binned our spectra to have a minimum of $50-100$ counts per bin.

5.3.2 XMM-Newton

To study the broadband spectral properties of Circinus, we used *XMM-Newton* observations taken simultaneously with the *NuSTAR* observations on 2013 February 03 and 2016 August 23, respectively (see Table 5.1). Both of these observations were aimed at ULX5. The AGN located nearly $4'$ away is well detected due to sufficiently high angular resolution ($6''.0$) and large FOV ($30'$) of EPIC pn/MOS cameras. To check variability in off-nuclear sources, we used *XMM-Newton* observations taken on four different epochs *i.e.*, 2018 September 18, 2016 August 23, 2013 February 03 and 2001 August 06. In all the epochs, EPIC pn observations were taken in the full window mode with the medium filter, except for 2016 when the thin filter was used.

We reduced the data using Science Analysis System (SAS v19.0.0) following the standard procedure. We considered only single and double events with quality flag set equal to 0. We obtained calibrated event files by using the latest calibration files. The good time interval event files were generated by removing time intervals of flaring background with count rates exceeding 0.8 ct s^{-1} for pn in the $10-12$ keV band. The net exposure times for pn in the $0.5-10$ keV energy band are found to be 85.5 ks, 16.2 ks, 36.2 ks and 103.0 ks for 2018, 2016, 2013 and 2001 observations, respectively (see Table 5.1). We generated response matrices and ancillary response files using the RMFGEN and ARFGEN tasks, respectively. The spectra were binned to have a minimum of 30 counts per bin.

We point out that the EPIC pn image, with an angular resolution of $6''.0$, enables us to spatially resolve AGN and neighbouring off-nuclear X-ray sources CGX1 and CGX2. We extracted CGX1 and CGX2 spectra using circular apertures of radii $7''.5$ and $11''$, respectively. To perform joint *XMM-Newton* and *NuSTAR* spectral fit, we extracted *XMM-Newton* pn spectrum using $100''$ radius to match the extraction region of the *NuSTAR* spectrum. The background spectra were extracted using a polygon region covering an area devoid of any source emission in the same chip.

5.3.3 AstroSat

We (PI: A. Kayal) observed Circinus using *AstroSat* during 2020 January 28 to 2020 February 01. The Soft X-ray Telescope (SXT) onboard *AstroSat* was kept as the prime instrument for these observations.

5.3.3.1 SXT

The SXT (see Section 2.7.3 for instrumental details) observations of Circinus were performed in photon counting (PC) mode. We used SXTPIPELINE (version 1.4b[1]) to generate cleaned and calibrated level 2 event files for each orbit. The SXT data reduction pipeline includes standard processes such as event extraction, screening criteria (*e.g.*, eliminating bad pixels, SAA passage, and events with grades >12), and calibration. The cleaned and calibrated level 2 event files for each orbit were then merged using SXTPYJULIAMERGER_V02 that removed any overlap between the consecutive orbits. The merged level 2 event file gives an effective exposure time of 57.49 ks. The scientific data products, *e.g.*, images, light curves and spectra were extracted using the XSELECT task within the HEASOFT package. We extracted the source spectrum using a circular region of radius $13'$ with encircled energy fraction of 92.3%. For spectral analysis, we used SXT spectrum in the energy range 3−7 keV, along with the relevant response files and background spectrum provided by the SXT instrument team. Considering calibration uncertainties in the response we added a systematic uncertainty of 3 per cent to the SXT data (Jithesh et al., 2019; Swain et al., 2023). Also, we accounted for the gain variation (Singh et al., 2017) by using the gain fit task in the XSPEC with the slope fixed at one.

5.3.3.2 LAXPC

We used data from the LAXPC20 unit only (see Section 2.7.3 for instrumental details). The LAXPC30 unit is suspected to have undergone a gas leakage resulting in a continuous gain shift and LAXPC10 is unstable (see Antia et al.,

[1] https://www.tifr.res.in/~astrosat_sxt/sxtpipeline.html

2017). The data from LAXPC were processed and analysed using the latest version (August 15, 2022) of the LAXPC pipeline package `laxpcSoft`, provided by the LAXPC POC[2]. The level 2 event file was generated by combining the level 1 event files from all orbits and removing any overlap between two consecutive orbits. We obtain a net exposure time of 85.4 ks by considering only good time intervals and selecting events from only the top layer of the LAXPC20 unit. We applied gain shift utility to account for the shift in gain values of the background spectrum during the time of observations. We obtained a gain offset of −0.4 keV, a value similar to the one reported in previous studies (Antia et al., 2021) The spectrum and lightcurve were extracted from the level 2 file by applying appropriate response functions and gain variations. Due to the completely background−dominated spectrum at higher energies, we used the LAXPC spectrum only in the 4−20 keV energy band. We also added systematic uncertainty of 3.0 per cent to account for calibration uncertainties in the response (Antia et al., 2021).

5.3.3.3 CZTI

The Cadmium Zinc Telluride Imager (CZTI, Bhalerao et al., 2017) onboard *AstroSat* is a hard X-ray coded mask instrument operating in the 22−200 keV energy range. It contains four identical but independent quadrants, with each quadrant consists of sixteen CZT detector modules. We reduced data using CZTI data analysis pipeline[3] version 3.0. From the raw event list, we generated cleaned event files by applying the recommended GTI selection criteria. We generated background subtracted spectra for each quadrant by using the CZTBINDATA task. The spectra of all four quadrants from two sets of observations (A07_100T02_9000003470 and

[2] `https://www.tifr.res.in/astrosat{_}laxpc/software.html`
[3] `http://astrosat-ssc.iucaa.in/cztiData`

A07_100T02_9000003476) were added together by using the CZTADDSPEC task. The combination of two observations provided a net exposure time of 71.04 ks. The source counts were detected above 5σ in the $22-70$ keV energy range. Hence, we used the $22-70$ keV CZTI spectrum after grouping it into broader energy bins.

5.3.4 Suzaku

The Circinus was observed with the *Suzaku* (Mitsuda et al., 2007) on 2006 July 21 for nearly 140 ks. There are four X-ray Imaging Spectrometer (XIS, Koyama et al., 2007) CCDs located in the focal planes of the respective foil mirrors X-ray telescopes, and a non-imaging collimated Hard X-ray Detector (HXD) onboard *Suzaku*. The four XIS CCDs, *i.e.*, XIS0, XIS1, XIS2, and XIS3 are sensitive in $0.4-10$ keV energy band with a spectral resolution of 130 eV at 6 keV and field-of-view (FoV) of $17'.8 \times 17'.8$. The half$-$power diameter of X-ray telescope is nearly $2'.0$. The three XIS units have front-illuminated CCDs, while XIS1 with back-illuminated CCDs provides better quantum efficiency in the sub-keV energy range. The HXD uses 16 phoswich counter detectors with each unit consisting of a GSO scintillation counter and PIN silicon diodes. The PIN detector is sensitive in the energy range of $12-60$ keV, while GSO is sensitive above 40 keV.

We reduced the XIS and HXD data using the HEASOFT software package (version 6.30) and following the steps given in Suzaku Data Reduction Guide[4]. From cleaned calibrated event files, we extracted XIS spectra using a circular extraction region with a radius of $2'.5$ centered at the Circinus. The background spectra were extracted from a source-free region. The HXD spectra were generated using the HXDPINXBPI script. The HXD being a collimating instrument, requires background estimation from the non-X-ray instrumental background (NXB) and cosmic X-ray background (CXB). We utilised the response and NXB files pro-

[4]https://heasarc.gsfc.nasa.gov/docs/suzaku/analysis/abc/

vided by the Suzaku team. To apply χ^2 minimisation, we binned PIN and GSO spectra such that each bin has a minimum signal-to-noise ratio of 3. The binned spectra of PIN and GSO have energy ranges of 10−70 keV and 50−120 keV, respectively. The count rates for PIN and GSO are 0.40 ± 0.003 ct s^{-1} and 0.14 ± 0.012 ct s^{-1}, respectively. We note that, due to relatively coarse angular resolution, both XIS as well as HXD spectra of Circinus are contaminated by the neighbouring off-nuclear sources.

5.3.5 BeppoSAX

The X-ray satellite *BeppoSAX* (Boella et al., 1997) carried four co−aligned instruments, namely a Low Energy Concentrator Spectrometer (LECS), three Medium Energy Concentrator Spectrometers (MECS), a High−Pressure Gas Scintillation Proportional Counter (HPGSPC), and a Phoswich Detector System (PDS). With imaging capabilities, LECS and MECS operated in 0.1−10 keV and 1.3−10 keV energy ranges, respectively. Both LECS and MECS have an energy resolution of 8% and an angular resolution of nearly $1'.2$ arcmin at 6 keV. The HPGSPC and PDS are collimating instruments having large FOV of $1^\circ.5 \times 1^\circ.5$ and cover 4−120 keV and 15−200 keV energy ranges, respectively. Since PDS is more sensitive than HPGSPC in the overlapping energy range, we preferred to use PDS data. Also, considering better sensitivity of MECS than LECS in the overlapping band we used MECS spectrum. Thus, our broadband spectral analysis is based on MECS and PDS spectra. We obtained MECS and PDS spectral products from the SSDC multi-mission interactive archive[5]. The corresponding response and background files were taken from the CALDB directory.

[5]https://www.ssdc.asi.it/mmia/index.php?mission=saxnfi

5.3.6 *Chandra* ACIS-S

The high spatial resolution ($0''.5$) of *Chandra* ACIS-S enable us to resolve and assess the contribution of off-nuclear sources (see Section 5.4). With that in mind, we have used *Chandra* ACIS-S observations of Circinus taken on 17 December 2010. With 152 ks exposure time these are the deepest imaging observations performed with the *Chandra*. Technical details of *Chandra* ACIS-S are provided in Section 2.7.1. We reduced *Chandra* data using the CIAO software[6] (v4.14) and the latest available calibration files from CALDB v4.9.8. In data processing we removed the $0''.5$ pixel randomization, and corrected for charge transfer inefficiency (CTI), excluded bad pixels and time intervals of high background. With 3.2 s frame time no source except AGN suffers from pile up. Using calibrated and cleaned event file we extracted spectra of off-nuclear sources.

5.4 Assessment of contamination from off-nuclear sources

We point out that *Chandra* ACIS and *XMM-Newton* pn images offering higher angular resolutions of $0''.5$ and $6''.0$, respectively, show off-nuclear X-ray sources CGX1 and CGX2 located close to the AGN (see Figure 5.2). CGX1 is located north−east to the AGN at a distance of $15''$, while CGX2 is detected at a distance of $25''$ towards the south of AGN. The *NuSTAR* images with an angular resolution of $18''$ (FWHM) are unable to spatially resolve CGX1 and CGX2. Therefore, the *NuSTAR* spectrum includes contributions from these two neighbouring off-nuclear X-ray sources in addition to that from AGN. We note that the deep *Chandra* ACIS image taken in 2010 December shows several faint off-nuclear sources in

[6] https://cxc.harvard.edu/ciao/

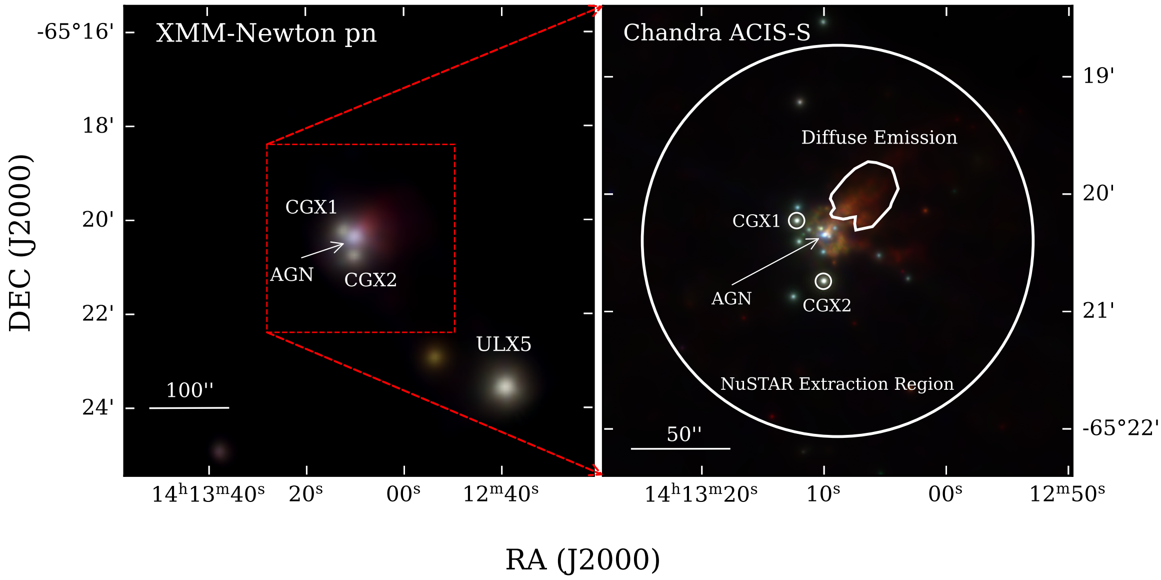

Figure 5.2: *Left panel* : The *XMM-Newton* pn image of Circinus in which the AGN and the off-nuclear contaminating sources CGX1, CGX2 and ULX5 are marked. *Right panel* : The zoom-in view of the central region as seen in the sensitive *Chandra* ACIS-S image of higher resolution with $\sim$ 152 ks exposure time which are among the deepest imaging observations performed with Chandra. Three different colours in this RGB image represents three different energy bands *i.e.*, 0.3−1.5 keV (Red), 1.5−2.5 keV (Green) and 2.5−8.0 keV (Blue). The large circle shows NuSTAR extraction region of radius 100″. The off-nuclear contaminating sources CGX1, CGX2 and extraction regions for extended diffuse emission are marked. The circle of 100″ radius depicts the extraction region of *NuSTAR* spectrum.

addition to CGX1 and CGX2. Although, Arévalo et al. (2014) demonstrated that the cumulative contribution from the faint sources is insignificant in comparison to the CGX1 and CGX2, which is further vindicated by the fact that *XMM-Newton* pn images of different epochs detect only relatively bright CGX1 and CGX2. Hence, we account for the contaminations from CGX1 and CGX2 while analysing *NuSTAR* spectra. We recall that *XMM-Newton* and *NuSTAR* images show ULX5 (Walton et al., 2013) as a bright X-ray source located $4'.5$ away south-west to the AGN. The *BeppoSAX*, *Suzaku* and *AstroSat* observations with a fairly coarse angular resolution of collimating instruments are unable to resolve AGN and neighbouring sources CGX1, CGX2 as well as ULX5. Except for *Suzaku* XISs spectra, the soft X-ray spectra from *BeppoSAX* MECS and *AstroSat* SXT include the contribution from ULX5. Therefore, while modelling the broadband spectra of these instruments, we account for the contamination from ULX5 too, in addition to CGX1 and CGX2.

To assess and remove the contribution of contaminating off-nuclear X-ray sources, we followed a procedure similar to that presented by Arévalo et al. (2014). Using *Chandra* ACIS and *XMM-Newton* pn observations, we model 0.5−10 keV X-ray spectra of individual contaminants, *i.e.*, CGX1, CGX2, ULX5 and extended emission. For each contaminating source, we attempt to achieve a baseline model that can provide a reasonably good fit to the spectra of all epochs. With the knowledge of the spectral shape and parameters of contaminants, we formulate a contamination model that accounts for the contribution of all contaminants. In the following subsections, we discuss spectral modelling of contaminating sources and formulation of the contamination model.

5.4.1 CGX1

CGX1 is an X-ray binary classified as an ULX with $L_{0.3-8.0\ \mathrm{keV}}$ in the range of 4.0×10^{39} erg s^{-1} to 3.0×10^{40} erg s^{-1} (Bauer et al., 2001; Esposito et al., 2015; Qiu et al., 2019). The *Chandra* ACIS and *XMM-Newton* pn/MOS images detect CGX1 at RA = $14^h\ 13^m\ 12.21^s$, DEC = $-65° \ 20' \ 13''.7$ (J2000), which is $15''$ away from the AGN toward the northeast. The *Chandra* ACIS observations of higher angular resolution ($0''.5$) offer a clean detection of CGX1 with no contamination from the AGN and the diffuse emission. We extracted the *Chandra* ACIS spectrum of CGX1 using a circular aperture of $2''.4$ radius. Unlike *Chandra*, *XMM-Newton* pn spectra of CGX1 are extracted using a larger circular region of $7''.5$ radius due to its larger PSF of $6''.0$. Also, background determination in the *XMM-Newton* pn images is a little tricky due to the contamination from AGN and diffuse X-ray emission present around it. Following Arévalo et al. (2014), we extracted the background spectra for CGX1 using an annular region around it, which excludes masked circular regions around the neighbouring CGX2 and AGN. The inner and outer radii of the annular region were set as $7''.5$ and $30''$, respectively.

The *XMM-Newton* pn spectra begin to show rising background contamination above 6.0 keV (see Qiu et al., 2019). Therefore, we fit *XMM-Newton* pn spectra only in the 0.5−6.0 keV energy band. However, due to its higher angular resolution ($0''.5$) *Chandra* ACIS observations are not contaminated by the diffuse emission, and we consider full 0.5−10 keV energy band, while fitting the *Chandra* spectrum. We find that the 0.5−10 keV *Chandra* spectrum can be best fitted with a simple absorbed power-law model with photon index (Γ) of 1.8. The absorption consists of two components, *i.e.*, galactic column density fixed to 5.6 $\times\ 10^{21}$ cm^{-2} and intrinsic absorption due to the interstellar material (ISM) of the

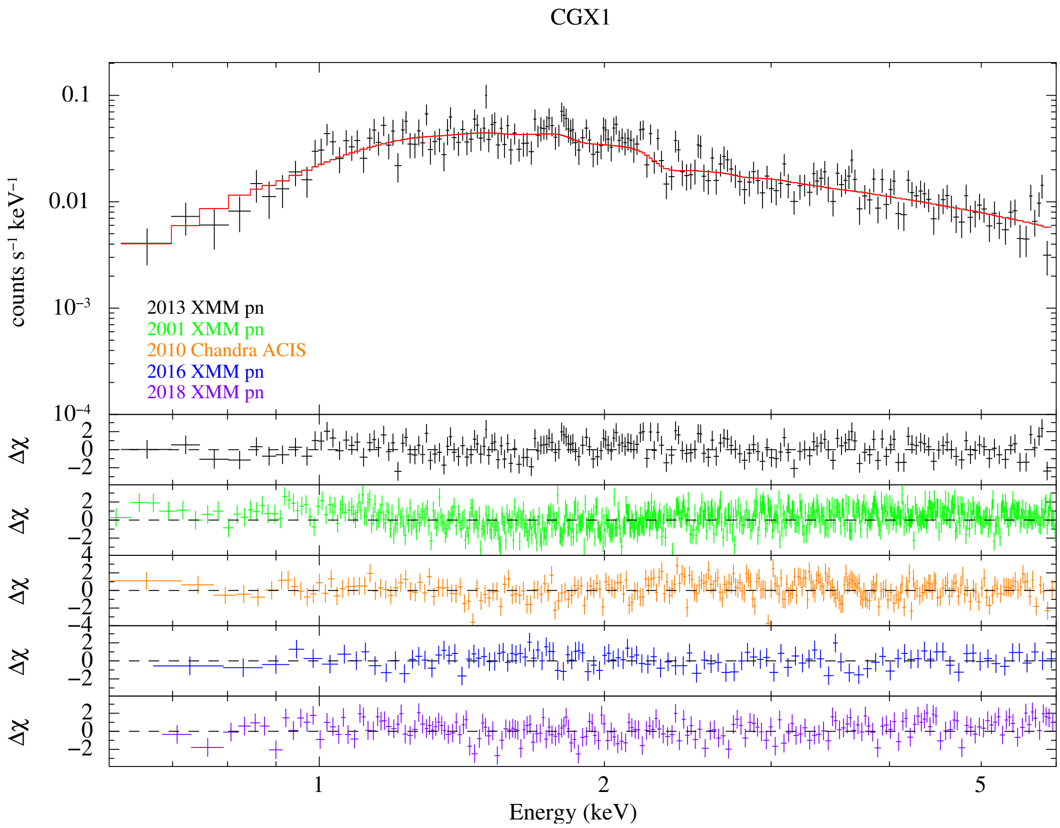

Figure 5.3: The 0.5 - 6.0 keV *XMM-Newton* pn/MOS spectra of CGX1 modelled with a simple absorbed power-law. All multi-epoch spectra are fitted with the same model with all the parameters frozen except power-law normalization. The *XMM-Newton* pn spectrum is shown for 2013 epoch in the top panels, while residuals are shown for 2001 (in green), 2013 (in black), 2016 (in blue) and 2018 (in violet) in the bottom panels. The orange residual is shown for *Chandra* ACIS spectrum.

host galaxy. Notably, *XMM-Newton* pn spectra for all four epochs can also be fitted with an absorbed power law (see Table 5.2). To attain a baseline model, we fixed the photon index to 1.8 while fitting the *XMM-Newton* spectra of different epochs. The absorbing column density and normalisations were left to vary. We find that absorbing column density is similar, in the range of $0.32^{+0.04}_{-0.04} \times 10^{22}$ cm^{-2} to $0.42^{+0.06}_{-0.06} \times 10^{22}$ cm^{-2}, during 2013, 2016 and 2018, while it is relatively high ($0.69^{+0.03}_{-0.03} \times 10^{22}$ cm^{-2}) in 2001 epoch. Our spectral fits of CGX1 are consistent with the fact that the change in flux is due to variable absorption rather than the intrinsic change in the source itself (Qiu et al., 2019). We point out that the fitting of the 2001 spectrum can be improved by adding an ionised absorber (ABSORI). However, to maintain a common baseline model across all the epochs, we prefer to use only neutral absorbing material. Also, an equally good fit can be obtained by other models, *e.g.*, multi-colour accretion disk (DISKBB), Comptonization model (COMPTT). Figure 5.3 shows the fitted spectra and residuals for all five different epochs. In Table 5.2, we list the best-fitted parameters for different epochs.

5.4.2 CGX2

CGX2 is known to be a young supernova remnant and X-ray emission is interpreted as the thermal X-ray emission arising from a shock-heated plasma produced by the interaction of outflowing supernova ejecta with the circum-stellar material (CSM) (Quirola-Vásquez et al., 2019). The CGX2 is located at RA = $14^{\mathrm{h}}\ 13^{\mathrm{m}}\ 10^{\mathrm{s}}.01$, DEC = $-65^{\circ}\ 20'\ 44''.4$, $25''$ south of AGN. In *Chandra* ACIS image of 2010, CGX2 is neatly separated from the diffuse emission around AGN. We extracted source spectrum by considering a circular extraction region of $2''.4$ radius centred at CGX2. The background spectrum was extracted from an annular region centered at CGX2 with inner and outer radii of $5''.0$ and $7''.0$, respectively.

The *XMM-Newton* pn spectra of different epochs were extracted using a circular extraction region of 10″ radius. The background spectra were extracted in a manner similar to that for CGX1, *i.e.*, an annulus centred at CGX2 with the exclusion of masked regions around CGX1 and AGN.

We find that the 0.5−10 keV *Chandra* ACIS and *XMM-Newton* pn/MOS spectra can be best fitted with a combination of two VPSHOCK models. The VPSHOCK model characterises X-ray emission arising from a constant temperature shock-heated plasma (Borkowski et al., 2001). The best fit of the *XMM-Newton* pn spectrum for the 2013 epoch (Figure 5.4) is obtained with a model consisting of two VPSHOCK components with plasma temperatures (kT) of $2.98^{+1.81}_{-0.87}$ keV and $7.89^{+0.75}_{-0.69}$ keV (see Table 5.2). The two plasma components can be interpreted as the forward and reverse shock emission. The two plasma emission components are absorbed with a column density ($N_{\rm H}$) in the range of $0.23^{+0.08}_{-0.08}$ − $0.70^{+0.08}_{-0.08}$ $\times$ 10^{22} cm^{-2} in addition to the galactic column density of 5.6 $\times$ 10^{21} cm^{-2}. For simplicity, we assumed that both plasma components suffer from the same amount of absorption, and hence $N_{\rm H}$ of both components were tied together. We find that the *XMM-Newton* pn/MOS and *Chandra* spectra of other epochs can be fitted reasonably well with the same model (see Table 5.2, Figure 5.4). To maintain the same baseline model with minimum free parameters, we fixed plasma temperatures to 3.0 keV and 8.0 keV, values similar to that obtained from the 2013 epoch *XMM-Newton* pn spectrum. We note that, in addition to the plasma temperature, the VPSHOCK model includes ionisation timescale $\tau = n_e t$, where n_e is the electron density and t is the time since the plasma was shocked, individual atomic abundances for various elements such as He, C, N, O, Ne, Mg, Si, S, Ar, Ca, Fe, Ni. The *Chandra* and *XMM-Newton* spectra show the presence of various emission lines, including strong Fe lines. In our best fits, most of the emission lines except Fe lines can be accounted for by using abundances fixed

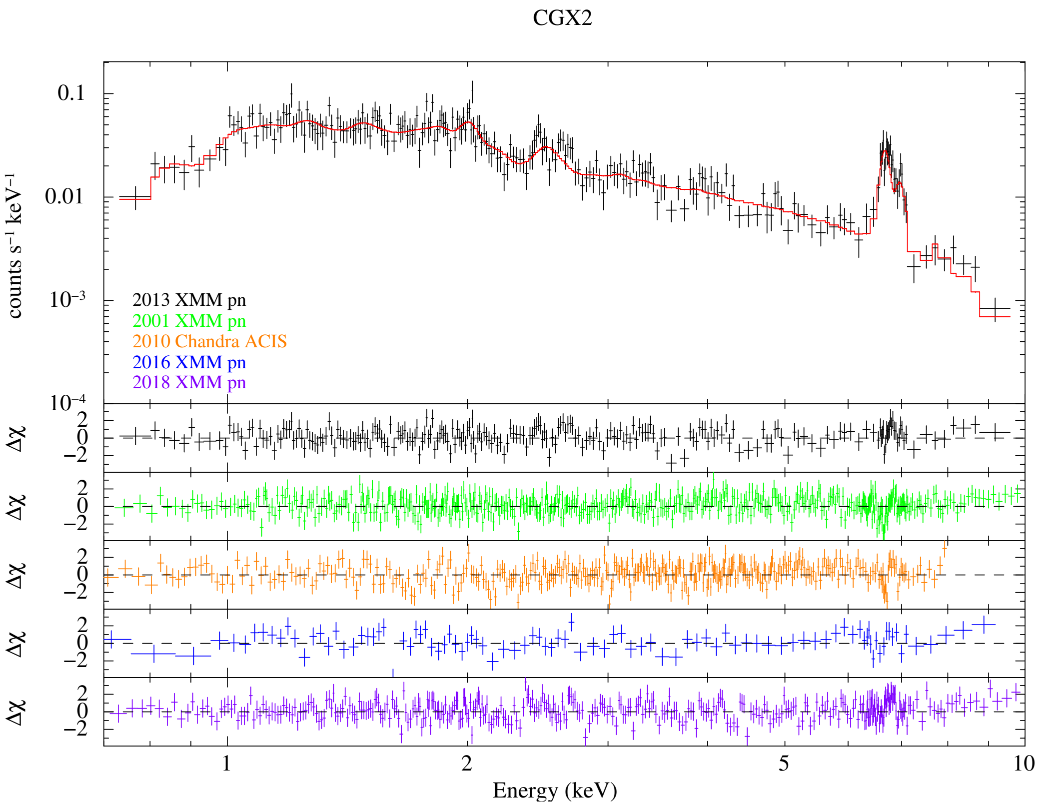

Figure 5.4: The 0.5 - 10.0 keV *XMM-Newton* pn/MOS spectra of CGX2 fitted with a model characterised by the thermal emission from shocked heated material. All multi-epoch spectra are fitted with the same model with all the parameters frozen except power-law normalization. The *XMM-Newton* pn spectrum is shown for 2013 epoch in the top panels, while residuals are shown for 2001 (in green), 2013 (in black), 2016 (in blue) and 2018 (in violet) in the bottom panels. The orange residual is shown for *Chandra* ACIS spectrum.

to Solar values. As expected, our fitted parameters are broadly consistent with those reported by Quirola-Vásquez et al. (2019), who characterised the continuum emission with the same model but convolved it with the SHELLBLUR model. The SHELLBLUR model accounts for asymmetry in emission line profiles, clearly seen in the *Chandra* grating spectra.

5.4.3 ULX5

The ULX5 located at RA = $14^{\rm h}$ $12^{\rm m}$ 39^{s}, DEC = -65° 23′ 34″ at the distance of 4′.5 away from AGN is clearly detected in the *XMM-Newton* pn and *NuSTAR* images. ULX5 lying in the outskirts of Circinus galaxy is known to be a variable source with L_X ∼ in the range of 4.5 × 10^{39} to 1.8 × 10^{40} erg s^{-1} (see Walton et al., 2013; Mondal et al., 2021). We extracted *XMM-Newton* pn spectra using a circular aperture of 30″ radius. The background spectra were extracted using a source-free region in the same chip. We find that 0.5−10 keV multi-epoch *XMM-Newton* pn/MOS spectra can be best fitted with the DISKBB model characterising emission from an accretion disk assumed to be consisting of multiple blackbody components. The spectral modelling of different epochs yields the temperature of the accretion disk in the range of 1.0 to 2.0 keV (see Table 5.2). The 0.5−10 keV flux and accreting disc temperature suggest ULX5 in a high state in the 2013 and 2018 epochs, while it appears to be in a low state during the 2001 and 2016 epochs. Figure 5.5 shows multi-epoch spectral fits and residuals.

5.4.4 Diffuse soft X-ray emission

The *Chandra* ACIS image shows extended diffuse X-ray emission around AGN with an apparent elongation towards the north−west direction (see Figure 5.2). We extracted the spectrum using a polygon region such that it includes most of the extended emission and excludes AGN and X-ray point sources. We find that

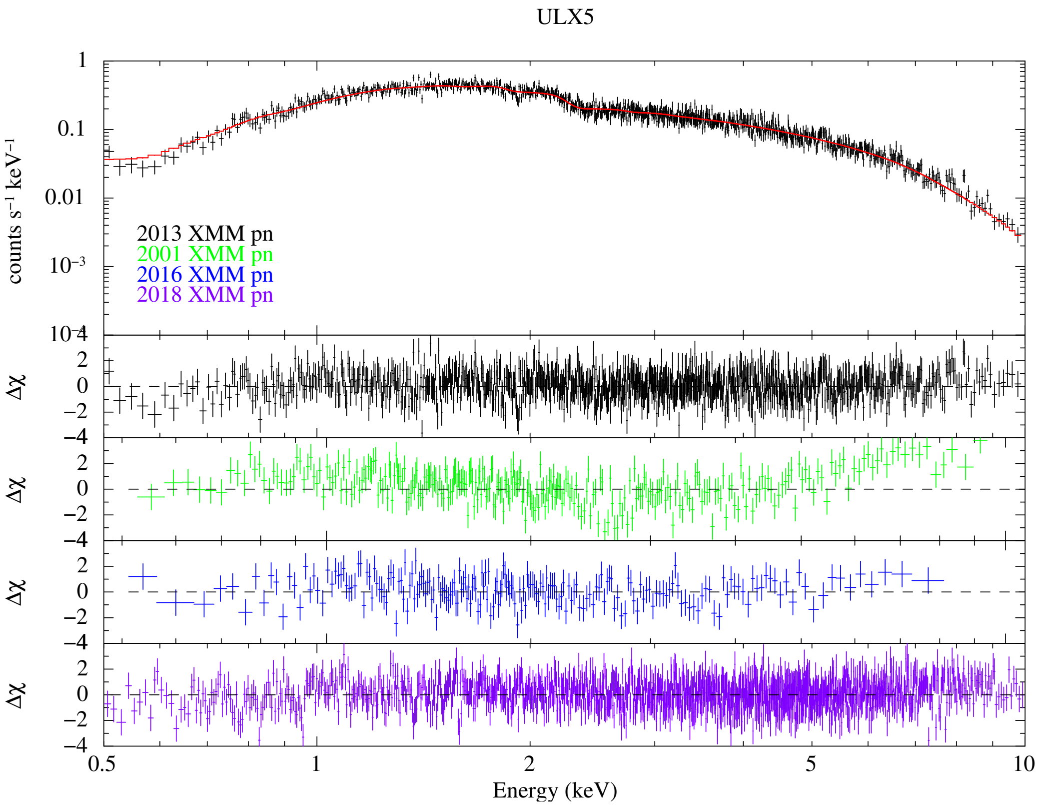

Figure 5.5: The 0.5-10 keV *XMM-Newton* pn/MOS spectra of ULX5 fitted with DISKBB model. The *XMM-Newton* pn spectrum is shown for 2013 epoch in the top panels, while residuals are shown for 2001 (in green), 2013 (in black), 2016 (in blue) and 2018 (in violet) in the bottom panels.

the 0.7−8.0 keV *Chandra* X-ray spectrum can be fitted with a model consisting of a soft component represented by the APEC model characterising the emission from hot gas, and a hard component representing the scattered emission from AGN (see Figure 5.6). The hard component can be described by the scattered power-law component in the MYTorus model. Our best-fitted model gives a plasma temperature of 0.82 keV and a steep power-law (Γ = 2.06) emission Compton-scattered from a nearly edge-on torus ($\theta_{\rm incl}$ = 76°) with the line-of-sight column density of 10^{25} cm^{-2}, which allows no directly transmitted component in the *Chandra* energy band (see Table 5.2). We obtain the best fit (reduced χ^2 = 1.15) by keeping the elements abundance in APEC model as a free parameter and by adding a few unresolved Gaussian emission lines at 0.74 keV, 1.3 keV and 1.8 keV. The elements abundance is only 0.2 times of the Solar value.

Our *Chandra* X-ray spectrum is similar to that reported in Arévalo et al. (2014), who analysed 0.7−8.0 keV *Chandra* spectra of different regions, *i.e.*, ionisation cone, circumnuclear region, central annulus, large-scale extended emission, and found similar spectra for all the regions. Mingo et al. (2012) highlighted the morphological correspondence between radio lobes and diffuse extended X-ray emission at kpc-scales and favoured a scenario in which extended diffuse X-ray emission is mainly arising from the shock-heated gas produced via the interaction of the radio jet with the surrounding gas. They found that the soft X-ray spectrum can be fitted well with the APEC model yielding gas temperature (kT) of 0.74 keV and a low elements abundance of 0.15 $Z_\odot$. We note that our spectral parameters are consistent with the previous studies (e.g., Mingo et al., 2012; Arévalo et al., 2014).

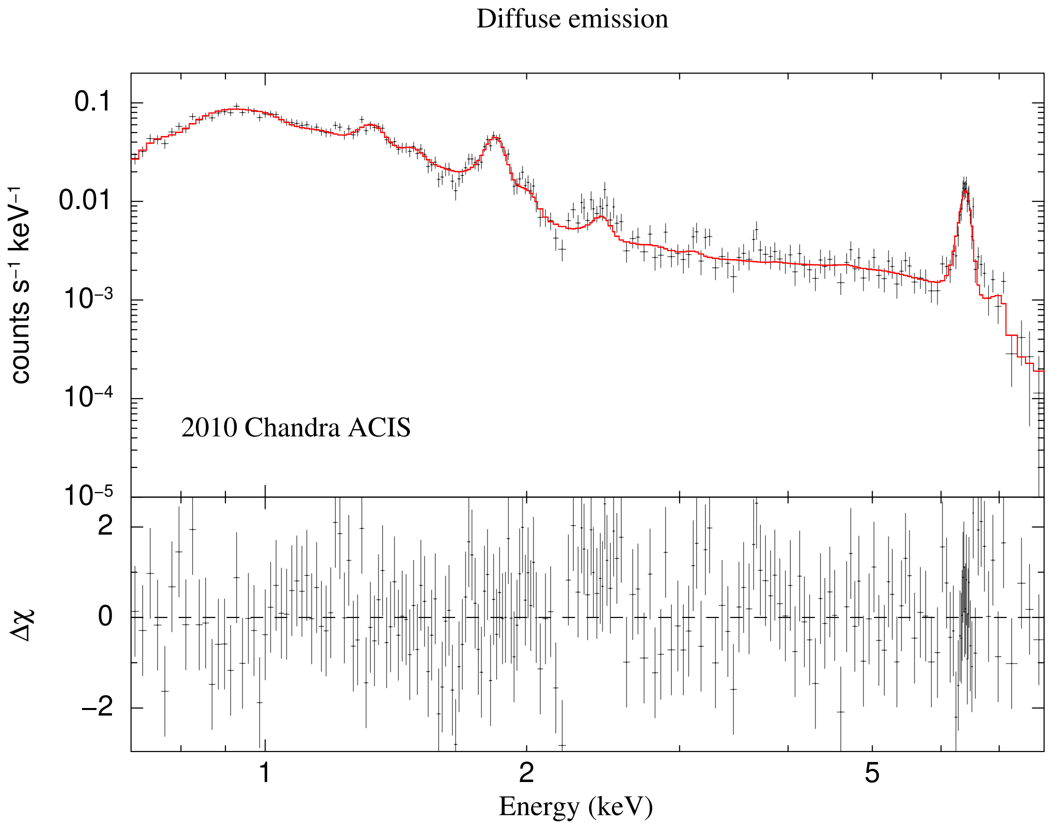

Figure 5.6: The 0.7-8.0 keV *Chandra* spectrum of diffuse X-ray emission fitted with a model consisting of a soft component represented by APEC component and a hard component represented by Compton reflection plus emission lines.

5.4.5 Contamination model

To account for the contributions from all contaminating sources while performing broadband spectral fittings, we formulate a contamination model. We define contamination model as the sum of the models characterising contaminants (CGX1, CGX2 and extended X-ray emission), *i.e.*, TBABS × (TBABS × PO + TBABS × VPSHOCK + TBABS × VPSHOCK + APEC + LINES). We note that the hard component of diffuse extended X-ray emission is a Compton-scattered AGN component which would be included in the physically motivated models considering the scattered emission from AGN. Hence, we do not add a scattered power law component to our contamination model. In the case of *BeppoSAX*, *Suzaku* and *AstroSat* spectral modelling, we include the contribution from ULX5, and hence, the contamination model is defined as TBABS × (TBABS × PO + TBABS × VPSHOCK + TBABS × VPSHOCK + APEC + LINES + TBABS × DISKBB). We note that, for epochs with no simultaneous *XMM-Newton* observations, we consider the fact that the multi-epoch spectra of a contaminant can be fitted with the same model and variability seen across different epochs can be accounted for by a varying normalisation (see Table 5.2). Thus, while modelling broadband spectra, we fixed spectral shapes and parameters of contaminants but varied their normalisations within a range observed from their multi-epoch spectral fittings. The contribution from extended diffuse X-ray emission is likely to remain constant. Hence, we keep all the spectral parameters of the soft component of diffuse emission fixed.

5.5 Broadband X-ray spectral modelling

We modelled the broadband X-ray spectra of Circinus for all ten epochs. The broadband spectra are based on the *BeppoSAX* MECS plus PDS observations

Table 5.2: The best fitted spectral parameters and fluxes of CGX1, CGX2 and ULX5 during different epochs

Parameters (1)	Unit (2)	2001 (3)	2010 (4)	2013 (5)	2016 (6)	2018 (7)
CGX1 [Model: TBABS × TBABS × PO]						
$N_{\rm H}^{\rm gal}$	10^{22} cm^{-2}	0.56^{f}	0.56^{f}	0.56^{f}	0.56^{f}	0.56^{f}
$N_{\rm H}$	10^{22} cm^{-2}	$0.69^{+0.03}_{-0.03}$	$0.51^{+0.05}_{-0.05}$	$0.32^{+0.04}_{-0.04}$	$0.42^{+0.06}_{-0.06}$	$0.35^{+0.05}_{-0.05}$
Γ		1.8^{f}	$1.80^{+0.06}_{-0.06}$	1.8^{f}	1.8^{f}	1.8^{f}
$Norm_{\Gamma}$	10^{-4}	$1.10^{+0.22}_{-0.22}$	$2.48^{+0.21}_{-0.19}$	$3.96^{+0.16}_{-0.16}$	$5.98^{+0.30}_{-0.30}$	$1.87^{+0.08}_{-0.08}$
$F_{0.5-10.0\ \rm keV}$	10^{-12} erg cm^{-2} s^{-1}	$3.86^{+0.06}_{-0.06}$	$0.97^{+0.03}_{-0.03}$	$1.50^{+0.05}_{-0.05}$	$2.21^{+0.10}_{-0.10}$	$0.70^{+0.26}_{-0.28}$
$\chi^2_{\rm r}$ (dof)		1.28 (647)	1.09 (299)	1.06 (191)	0.69 (116)	1.11 (202)
CGX2 [Model: TBABS × (TBABS × VPSHOCK + TBABS × VPSHOCK)]						
$N_{\rm H}^{\rm gal}$	10^{22} cm^{-2}	0.56^{f}	0.56^{f}	0.56^{f}	0.56^{f}	0.56^{f}
$N_{\rm H}$	10^{22} cm^{-2}	$0.70^{+0.08}_{-0.08}$	$0.44^{+0.04}_{-0.04}$	$0.30^{+0.10}_{-0.09}$	$0.35^{+0.18}_{-0.19}$	$0.23^{+0.08}_{-0.08}$
$kT^{\rm R}$	keV	8.0^{f}	8.0^{f}	$7.89^{+0.75}_{-0.69}$	8.0^{f}	8.0^{f}
$kT^{\rm F}$	keV	3.0^{f}	3.0^{f}	$2.98^{+1.81}_{-0.87}$	3.0^{f}	3.0^{f}
$\tau_{\rm u}^{\rm R}$	10^{13} s cm^{-3}	5.0^{f}	5.0^{f}	$5.0^{\rm peg}_{-4.58}$	5.0^{f}	5.0^{f}
$\tau_{\rm u}^{\rm F}$	10^{11} s cm^{-3}	5.5^{f}	5.5^{f}	$5.5^{+7.01}_{-2.47}$	5.5^{f}	5.5^{f}
$Norm^{\rm R}$	10^{-4}	$6.81^{+0.40}_{-0.41}$	$7.13^{+0.33}_{-0.34}$	$5.98^{+0.65}_{-0.91}$	$4.88^{+0.65}_{-0.70}$	$4.16^{+0.25}_{-0.26}$
$Norm^{\rm F}$	10^{-4}	$3.34^{+0.70}_{-0.68}$	$2.96^{+0.47}_{-0.46}$	$2.15^{+0.86}_{-0.77}$	$0.99^{+1.03}_{-0.90}$	$0.64^{+0.37}_{-0.33}$
$F_{0.5-10\ \rm keV}$	10^{-12} erg cm^{-2} s^{-1}	$1.49^{+0.04}_{-0.04}$	$1.59^{+0.03}_{-0.03}$	$1.34^{+0.04}_{-0.04}$	$1.00^{+0.08}_{-0.08}$	$0.85^{+0.03}_{-0.03}$
$\chi^2_{\rm r}$ (dof)		0.96 (472)	1.23 (338)	0.95 (264)	1.26 (87)	1.13 (358)
ULX5 [Model: TBABS × DISKBB]						
$N_{\rm H}^{\rm gal}$	10^{22} cm^{-2}	0.56^{f}		0.56^{f}	0.56^{f}	0.56^{f}
$T_{\rm in}$	keV	$1.17^{+0.03}_{-0.03}$		$1.85^{+0.02}_{-0.02}$	$1.08^{+0.03}_{-0.03}$	$1.78^{+0.01}_{-0.01}$
$Norm_{\rm diskbb}$	10^{-2}	$2.37^{+0.27}_{-0.24}$		$3.26^{+0.16}_{-0.15}$	$8.88^{+0.10}_{-0.10}$	$3.53^{+0.11}_{-0.10}$
$F_{0.5-10.0\ \rm keV}$	10^{-12} erg cm^{-2} s^{-1}	$0.63^{+0.01}_{-0.02}$		$6.07^{+0.07}_{-0.08}$	$1.66^{+0.04}_{-0.06}$	$5.88^{+0.04}_{-0.05}$
$\chi^2_{\rm r}$ (dof)		1.75 (288)		0.97 (896)	1.06 (205)	1.13 (1198)
Diffuse emission [Model: TBABS × APEC + MYTORUS]						
$N_{\rm H}^{\rm gal}$	10^{22} cm^{-2}		0.56^{f}			
kT	keV		$0.82^{+0.02}_{-0.02}$			
Z	$Z_{\odot}$		$0.19^{+0.02}_{-0.02}$			
$Norm_{\rm apec}$	10^{-3}		$1.13^{+0.10}_{-0.09}$			
$N_{\rm H}$	10^{24} cm^{-2}		$10.00^{\rm peg}_{-4.08}$			
Γ			2.00^{f}			
$\theta_{\rm Incl}$	degrees		80.0^{f}			
$A_{\rm S}$	10^{-2}		$6.31^{\rm peg}_{-0.39}$			
$F_{0.5-10\ \rm keV}$	10^{-13} erg cm^{-2} s^{-1}		$8.85^{+0.15}_{-0.16}$			
$\chi^2_{\rm r}$ (dof)			1.15 (200)			

Notes - 2010 epoch observations are from *Chandra* ACIS-S while remaining are from *XMM-Newton* EPIC pn. $N_{\rm H}^{\rm gal}$ and $N_{\rm H}$ represent the Galactic and line-of-sight column density at the source redshift, respectively. Γ is photon index of power law emission. kT denotes plasma temperature. $\tau_{\rm u}$ represents the upper limit on the ionisation timescale in VPSHOCK model. 'R' and 'F' denote reverse and forward shock components, respectively. $A_{\rm S}$ is the normalisation of scattered component in MYTORUS model. ^{f} denotes the fixed value of a parameter.

of 1998 March 13 and 2001 January 07 epoch, *Suzaku* XISs plus PIN and GSO observations of 2006 July 21 epoch, *NuSTAR* observations of 2013 January 25, 2013 February 02, 2013 February 05, and 2020 November 26, *XMM-Newton* plus *NuSTAR* observations of 2013 February 03 and 2016 August 23, and *AstroSat* observations of 2020 January 28 (see Table 5.1). We avoid soft X-ray data points below 3.0 keV to mitigate the effects of off-nuclear contaminating sources. The exclusion of X-ray data below 3.0 keV also brings uniformity in terms of spectral coverage for all the multi-epoch spectra, considering that only *NuSTAR* spectra covering 3.0−79 keV energy band are available for four epochs (see Table 5.1). Thus, broadband spectra are limited to 3.0−79 keV whenever *NuSTAR* observations are used, even when simultaneous *XMM-Newton* observations are available. The *BeppoSAX*, *Suzaku* and *AstroSat* spectra cover nearly 3.0−100 keV energy range.

We fitted the spectra of all ten epochs together, considering that the joint fit is useful for reducing the uncertainties in the spectral parameters and for breaking degeneracies between different parameters (Baloković et al., 2021; Saha et al., 2022). The joint fit of multi-epoch spectra can be considered equivalent to the spectrum integrated over a long period of time. Therefore, we can easily identify spectral parameters that remain constant over a long timescale. A parameter variable across different epochs can also be identified by allowing it to vary across epochs. Therefore, with the multi-epoch joint spectral modelling we aim to place better constraints on geometrical parameters such as torus average column density, covering factor and inclination angle. We also aim to probe the viability of variable line-of-sight column density ($N_{\rm H,LOS}$). To minimise the model-dependent effects, we explore three different physically-motivated models. The details of the spectral fittings with these models are given below in the following subsections.

5.5.1 Joint spectral modelling with MYTorus model

The MYTorus model considers reprocessing material distributed in a toroidal geometry with a circular cross-section and uniform density (Murphy & Yaqoob, 2009). The opening angle of the torus ($\theta_{\rm tor}$) is fixed to 60°, which gives a covering factor of (cos $\theta_{\rm tor}$) 0.5. The inclination angle of the torus ($\theta_{\rm incl}$), *i.e.*, the angle between the torus symmetric axis and the line-of-sight, is a free parameter, and it can have any value in the range of 0° (a face-on torus) to 90° (an edge-on torus). The MYTorus model considers different spectral components, *i.e.*, AGN intrinsic emission transmitted through obscuring material, the scattered emission from the reprocessing material toward the line-of-sight, and the fluorescent emission lines, in a self-consistent manner. The three components are denoted as MYTZ (transmitted component), MYTS (Compton-scattered continuum), and MYTL (fluorescent emission lines). The MYTZ, an energy-dependent multiplicative factor applied to the intrinsic continuum, accounts for the line-of-sight obscuration. In principle, the intrinsic continuum can have any spectral shape. We assumed a power law spectral shape which is consistent with the inherent assumption of the MYTorus model that the scattered continuum and fluorescent emission-line components are reprocessed emission of a power law continuum. The scattered component can have cutoff energy in the range of 100 keV to 500 keV. The MYTL component fits fluorescent emission lines Fe Kα and Fe Kβ at 6.4 keV and 7.06 keV, respectively.

To fit the joint spectra of different epochs, we begin with the MYTorus model plus the contamination model. The MYTorus model is aimed at fitting the AGN spectral components, while the contamination model accounts for the contribution from the contaminant sources (see Section 5.4.5). We considered the transmitted component (MYTZ) and the Compton-scattered component (MYTS). In XSPEC notation the model can be expressed as $c_1 \times$ TBABS (MYTZ $\times$ CUTOFFPL $+ c_2 \times$ MYTS $+$ LINES $+$ CONTAMINATION MODEL). First, we used the MYTorus model in the coupled configuration by tying together various parameters (*i.e.*, photon index, column density and normalisations) of all three components. This configuration assumes that the scattered and emission line components result from the reprocessing of intrinsic power law emission from a uniform torus. While performing the fit, we kept the photon index (Γ), column density ($N_{\rm H}$), inclination angle ($\theta_{\rm incl}$) and normalisations as free parameters. We note that the MYTorus model introduces a cutoff on the scattered component by using different tables with termination energies fixed to 100 keV, 160 keV, 200 keV, 300 keV, 400 keV and 500 keV. We begin with the termination energy of the scattered component fixed to 500 keV, the highest value. To have consistency between the scattered and the transmitted components, we used a cutoff power law for the transmitted component with cutoff energy ($E_{\rm cut}$) fixed to the termination energy of the scattered component. Also, we notice that the *NuSTAR* spectra show Ni absorption edge at 8.3 keV, which is not included in the MYTorus scattered component. Therefore, while fitting the *NuSTAR* spectra, we added Ni edge using the ZEDGE model and kept its optical depth and normalisation as free parameters. We also account for the cross-normalisation between different instruments by using a multiplicative factor in the cumulative model. While fitting the joint spectrum from two or more instruments, we fixed the cross-normalisation factor to 1 for one instrument and left it to vary for other instruments. In Table 5.3, we list the cross-normalisation factors for different instruments and find them to be consistent with the values reported in the literature (e.g., Madsen et al., 2016).

To fit the multi-epoch spectra, we first assumed no variability across epochs for any of the parameters. So, all the spectral parameters of different epochs were tied together with an assumption of no intra-epoch variability in all the parameters (see case (i) in Table 5.3). We find that the MYTorus model in the coupled configuration reproduces Compton hump peaking at 30 keV, but it leaves significant residuals in the soft band. The 6.4 keV emission line also shows residuals for the *XMM-Newton* data points, which can be understood due to the fact that the spectral resolution of the *XMM-Newton* (150 eV) is nearly 2.5 times better than that for *NuSTAR* which has 400 eV spectral resolution at 6.4 keV. The addition of an unresolved emission line only to the *XMM-Newton* data provides an improved fit. In the case of *BeppoSAX*, *Suzaku*, and *AstroSat* spectral fittings, we added unresolved emission lines to the MECS, XISs and SXT spectra. We noticed that the significant residuals seen mainly in the soft band can be accounted by adding narrow Gaussians for the unresolved emission lines detected at various energies ranging from 3.0 keV to 7.45 keV. In general, energies and normalisations of these emission lines are consistent with the previous studies (Sambruna et al., 2001; Massaro et al., 2006; Arévalo et al., 2014), which identify them as Ar, Ca, Cr, Fe and Ni lines of different ionisations with several of them being He-like and H-like ions. Except for Fe lines, all other emission lines are less prominent with the equivalent widths in the range of 20 eV to 150 eV and normalisations of the order of 10^{-4} to 10^{-6}.

Table 5.3: The joint fit spectral parameters using MYTORUS model

Parameters	1998-03-13 (*Beppo*) (1)	2001-01-07 (*Beppo*) (2)	2006-07-21 (*Suzaku*) (3)	2013-01-25 (*Nu*) (4)	2013-02-02 (*Nu*) (5)	2013-02-03 ($X+Nu$) (6)	2013-02-05 (*Nu*) (7)	2016-08-23 ($X+Nu$) (8)	2020-01-28 (*AstroSat*) (9)	2020-11-26 (*Nu*) (10)
					Model: MYTORUS + lines + contamination					
					case (i) : all parameters varied but tied across epochs					
Γ					$2.28^{+0.01}_{-0.02}$					
$N_{\mathrm{H,\ LOS}}$					$6.10^{+0.20}_{-0.17}$					
θ_{incl}					$76.9^{+0.5}_{-0.5}$					
A_{Z} (10^{-9})					$1.32^{+0.11}_{-0.12}$					
A_{S}					$1.22^{+0.10}_{-0.11}$					
E_{cut}					160^{f}					
χ_r(dof)					1.123 (8107)					
C_{XMM}						1.0^{f}		$0.96^{+0.01}_{-0.01}$		
C_{NuA}				$1.30^{+0.01}_{-0.01}$	$1.23^{+0.02}_{-0.02}$	$1.23^{+0.01}_{-0.01}$	$1.19^{+0.01}_{-0.01}$	$1.34^{+0.02}_{-0.02}$		$1.20^{+0.01}_{-0.01}$
C_{NuB}				$1.35^{+0.01}_{-0.01}$	$1.27^{+0.02}_{-0.02}$	$1.26^{+0.01}_{-0.01}$	$1.22^{+0.01}_{-0.01}$	$1.40^{+0.02}_{-0.02}$		$1.21^{+0.01}_{-0.01}$
C_{XIS0}	$0.81^{+0.01}_{-0.01}$ (ME)	$0.77^{+0.01}_{-0.01}$ (ME)	$0.94^{+0.01}_{-0.01}$						$0.72^{+0.04}_{-0.04}$ (S)	
C_{XIS1}			$0.96^{+0.01}_{-0.01}$							
C_{XIS2}			$0.91^{+0.01}_{-0.01}$							
C_{XIS3}			$0.91^{+0.01}_{-0.01}$							
C_{PIN}	$1.18^{+0.03}_{-0.03}$ (P)	$1.03^{+0.03}_{-0.03}$ (P)	$1.45^{+0.02}_{-0.02}$						$0.91^{+0.05}_{-0.05}$ (LX)	
C_{GSO}			$1.56^{+0.26}_{-0.26}$						$1.52^{+0.25}_{-0.25}$ (CZ)	
					case (ii) : only normalisation untied across epochs					
Γ					$2.27^{+0.02}_{-0.02}$					
$N_{\mathrm{H,\ LOS}}$					$6.03^{+0.18}_{-0.18}$					
θ_{incl}					$76.7^{+0.5}_{-0.5}$					
A_{Z} (10^{-9})	$1.32^{+0.18}_{-0.16}$	$1.22^{+0.22}_{-0.20}$	$1.32^{+0.12}_{-0.12}$	$1.25^{+0.13}_{-0.12}$	$1.27^{+0.14}_{-0.13}$	$1.28^{+0.12}_{-0.11}$	$1.29^{+0.14}_{-0.12}$	$1.36^{+0.14}_{-0.13}$	$1.45^{+0.42}_{-0.31}$	$1.29^{+0.13}_{-0.12}$
A_{S}	$1.23^{+0.17}_{-0.15}$	$1.05^{+0.19}_{-0.17}$	$1.23^{+0.12}_{-0.11}$	$1.10^{+0.11}_{-0.10}$	$1.14^{+0.12}_{-0.11}$	$1.16^{+0.11}_{-0.10}$	$1.17^{+0.12}_{-0.11}$	$1.30^{+0.13}_{-0.12}$	$1.48^{+0.43}_{-0.32}$	$1.17^{+0.12}_{-0.11}$
E_{cut}					160^{f}					
χ_r(dof)					1.116 (8089)					

Notes - *Beppo* : *BeppoSAX*; $X+Nu$: *XMM-Newton* plus *NuSTAR*; *Nu* : *NuSTAR*. C_{XMM}, C_{NuA}, C_{NuB}, C_{XIS0}, C_{XIS1}, C_{XIS2}, C_{XIS3}, C_{PIN}, C_{GSO} represent cross-normalisation factors for *XMM-Newton*, *NuSTAR* FPMA, *NuSTAR* FPMB, *Suzaku* XIS0, XIS1, XIS2, XIS3, PIN and GSO, respectively. The cross-normalisation factors for *BeppoSAX* MECS, PDS, *AstroSat* SXT, LAXPC and CZTI are indicated with 'ME', 'P', 'S', 'LX' and 'CZ', The units of column densities, inclination angle (θ_{incl}) and normalisations are 10^{24} cm^{-2}, degrees and erg cm^2 s^{-1} keV^{-1}, respectively. ^{f} Fixed value of a parameter.

Table 5.3: Continued.

Parameters	1998-03-13	2001-01-07	2006-07-21	2013-01-25	2013-02-02	2013-02-03	2013-02-05	2016-08-23	2020-01-28	2020-11-26
	(*Beppo*)	(*Beppo*)	(*Suzaku*)	(*Nu*)	(*Nu*)	(*X + Nu*)	(*Nu*)	(*X + Nu*)	(*AstroSat*)	(*Nu*)
	(1)	(2)	(3)	(4)	(5)	(6)	(7)	(8)	(9)	(10)
Model: MYTorus + lines + contamination										
case (iii) : only $N_{\rm H,\ LOS}$ untied across epochs										
Γ	$2.28^{+0.01}_{-0.01}$									
$N_{\rm H,\ LOS}$	$6.00^{+1.35}_{-1.34}$	$6.28^{+1.09}_{-1.17}$	$4.43^{+0.22}_{-0.32}$	$6.47^{+0.20}_{-0.19}$	$6.33^{+0.25}_{-0.20}$	$6.39^{+0.21}_{-0.20}$	$6.09^{+0.20}_{-0.20}$	$5.28^{+0.47}_{-0.18}$	$4.86^{+1.15}_{-0.84}$	$6.14^{+0.47}_{-0.16}$
$\theta_{\rm incl}$	$77.2^{+0.8}_{-0.5}$									
$A_{\rm Z}$ (10^{-9})	$1.36^{+0.20}_{-0.11}$									
$A_{\rm S}$	$1.29^{+0.20}_{-0.10}$									
$E_{\rm cut}$	160^{f}									
χ_r(dof)	1.101 (8098)									
case (iv) : $N_{\rm H,\ LOS}$ and normalisations untied across epochs										
Γ	$2.28^{+0.01}_{-0.01}$									
$N_{\rm H,\ LOS}$	$6.17^{+1.36}_{-1.43}$	$6.23^{+1.17}_{-1.22}$	$4.48^{+0.22}_{-0.34}$	$6.43^{+0.21}_{-0.32}$	$6.37^{+0.32}_{-0.32}$	$6.39^{+0.22}_{-0.33}$	$5.97^{+0.28}_{-0.36}$	$5.14^{+0.38}_{-0.22}$	$5.32^{+2.80}_{-1.84}$	$6.18^{+0.19}_{-0.40}$
$\theta_{\rm incl}$	$77.1^{+0.6}_{-0.7}$									
$A_{\rm Z}$ (10^{-9})	$1.37^{+0.13}_{-0.12}$	$1.27^{+0.20}_{-0.18}$	$1.35^{+0.03}_{-0.03}$	$1.33^{+0.04}_{-0.04}$	$1.35^{+0.08}_{-0.08}$	$1.34^{+0.03}_{-0.03}$	$1.32^{+0.07}_{-0.07}$	$1.32^{+0.07}_{-0.05}$	$1.43^{+0.62}_{-0.52}$	$1.35^{+0.04}_{-0.04}$
$A_{\rm S}$	$1.31^{+0.18}_{-0.18}$	$1.14^{+0.16}_{-0.20}$	$1.28^{+0.12}_{-0.15}$	$1.25^{+0.14}_{-0.14}$	$1.28^{+0.16}_{-0.16}$	$1.27^{+0.13}_{-0.13}$	$1.23^{+0.14}_{-0.15}$	$1.22^{+0.18}_{-0.14}$	$1.44^{+0.67}_{-0.59}$	$1.28^{+0.14}_{-0.19}$
$E_{\rm cut}$	160^{f}									
χ_r(dof)	1.102 (8080)									

We note that keeping all the parameters tied across epochs gives an acceptable fit with χ^2_r (dof) = 1.123 (8107) (see case (i) in Table 5.3). However, as expected, the fit statistics improve slightly with χ^2_r (dof) = 1.116 (8089) if normalisations are varied across epochs. The fit statistics show further improvement if $N_{\rm H,LOS}$ is considered as a varying parameter across epochs (see case (iii) in Table 5.3). We note that, an equally good fit is obtained if normalisations across epochs are tied but $N_{\rm H,LOS}$ is kept variable (see case (iv) in Table 5.3). Therefore, our joint spectral fitting favours the variability in $N_{\rm H,LOS}$ across epochs. It is worth noting that, the fit statistics show no significant improvement if other parameters such as photon index (Γ), inclination angle ($\theta_{\rm incl}$) are kept variable across epochs. Thus, our spectral modelling with the MYTorus model shows that, in all epochs, AGN emission can be characterised with a steep power law spectrum ($\Gamma = 2.28^{+0.01}_{-0.01}$) piercing through a Compton-thick line-of-sight column density ($N_{\rm H,LOS}$ in the range of $4.48^{+0.22}_{-0.34} \times 10^{24}$ cm^{-2} to $6.43^{+0.21}_{-0.32} \times 10^{24}$ cm^{-2}) in a nearly edge-on ($\theta_{\rm incl} = 77°$) torus. Further, we find that the transmitted component vanishes with its normalisation nearly 10^9 times lower than that of the scattered component. The absence of the transmitted component can be ascribed to a heavily Compton-thick line-of-sight column density wherein hard X-ray spectrum (> 10 keV) is fully accounted for by the scattered component. We note that our results are consistent with Arévalo et al. (2014), who modelled 2.0−79 keV combined spectra of *XMM-Newton*, *NuSTAR* spectra and *Swift*/BAT and reported a Compton scattered dominated steep power law ($\Gamma = 2.2 - 2.4$) spectrum from an obscured AGN with torus equatorial column density of $N_{\rm H} = 6{-}10 \times 10^{24}$ cm^{-2}.

To examine the possibility of a patchy torus in which transmitted and scattered components encounter different column densities, we performed spectral fitting by untying the column densities of transmitted and scattered components.

We obtained nearly the same fit statistics with nearly the same parameters except for the column densities (see case (ii) in Table 5.3). We find that the globally averaged column density ($N_{\rm H,avg} = 5.70^{+0.30}_{-0.30} \times 10^{24}$ cm^{-2} $-$ 10^{25} cm^{-2}) implied from the scattered component is significantly lower than the line-of-sight column density ($N_{\rm H,\ LOS} \geq 10^{25}$ cm^{-2}). In fact, $N_{\rm H,\ LOS}$ is encountering the upper limit allowed in the MYTorus model, and an actual value can be even higher. A significantly higher line-of-sight column density than the global average column density indicates a patchy torus around the AGN. However, we note that the line-of-sight column density, attaining the upper limit of its value allowed by the model, remains unconstrained. To overcome this issue, we attempted to fit our multi-epoch spectra using other models described below.

5.5.2 Joint spectral modelling with borus02 model

The borus02 model (Baloković et al., 2018) assumes uniform-density reprocessing matter having a spherical geometry with two conical polar cut-outs. The borus02 model consists of a Compton-scattered continuum and fluorescent emission lines. The intrinsic continuum is accounted separately by a cutoff power law multiplied by a line-of-sight absorbing column density (tbabs) and the Compton scattering losses (cabs) occurred along the line-of-sight. Unlike the MYTorus model, this model considers covering factor (f_c) that can vary in the range of 0.1 to 1.0, corresponding to the torus opening angle ($\theta_{\rm tor}$) in 0° to 84° range. The torus inclination angle ($\theta_{\rm incl}$) varies in the range of 0° to 90°. The borus02 model can account for a patchy environment by allowing a line-of-sight column density ($N_{\rm H,\ LOS}$) to be different than the average column density of the torus ($N_{\rm H,\ tor}$).

We fitted the joint spectra of all ten epochs using the borus02 model that can be expressed as c_1 × tbabs (ztbabs × cabs × cutoffpl + borus02 + lines + contamination model), where borus02 represents a reprocessed component. The intrinsic cutoff power law includes line-of-sight absorption and losses that occurred due to Compton-scattering. While fitting the spectra of each epoch, we allowed all the parameters (*e.g.*, column density, spectral index, inclination angle and opening angle of the torus) to vary. Similar to the MYTorus model, we see residuals at soft energies (< 10 keV) that can be accounted for by adding narrow Gaussians for the emission lines at various energies between 3.0 to 7.5 keV.

Table 5.4: The joint fit spectral parameters using BORUS02 model

Parameters	1998-03-13 (*Beppo*) (1)	2001-01-07 (*Beppo*) (2)	2006-07-21 (*Suzaku*) (3)	2013-01-25 (*Nu*) (4)	2013-02-02 (*Nu*) (5)	2013-02-03 ($X+Nu$) (6)	2013-02-05 (*Nu*) (7)	2016-08-23 ($X+Nu$) (8)	2020-01-28 (*AstroSat*) (9)	2020-11-26 (*Nu*) (10)
					Model: BORUS02 + lines + contamination					
					case (i) : all parameters varied but tied across epochs					
Γ					$2.39^{+0.04}_{-0.01}$					
$N_{\rm H,\ LOS}$					$6.10^{+0.33}_{-0.04}$					
$N_{\rm H,\ tor}$					$14.05^{+0.98}_{-0.82}$					
$\theta_{\rm tor}$					$73.8^{+0.1}_{-0.1}$					
$\theta_{\rm incl}$					$80.8^{+0.1}_{-0.1}$					
$f_{\rm cov}$					$0.28^{+0.01}_{-0.01}$					
$A_{\rm Z} = A_{\rm S}$					$13.58^{+1.27}_{-1.36}$					
$E_{\rm cut}$					$108.3^{+1.2}_{-2.1}$					
χ_r(dof)					1.138 (8105)					
$C_{\rm XMM}$						1.0^f		$0.94^{+0.01}_{-0.01}$		
$C_{\rm NuA}$				$1.29^{+0.01}_{-0.01}$	$1.27^{+0.01}_{-0.01}$	$1.24^{+0.01}_{-0.01}$	$1.20^{+0.01}_{-0.01}$	$1.34^{+0.01}_{-0.01}$		$1.21^{+0.01}_{-0.01}$
$C_{\rm NuB}$				$1.34^{+0.01}_{-0.01}$	$1.31^{+0.01}_{-0.01}$	$1.26^{+0.01}_{-0.01}$	$1.23^{+0.01}_{-0.01}$	$1.40^{+0.01}_{-0.01}$		$1.22^{+0.01}_{-0.01}$
$C_{\rm XIS0}$	$0.84^{+0.01}_{-0.01}$ (ME)	$0.77^{+0.01}_{-0.01}$ (ME)	$0.97^{+0.01}_{-0.01}$						$0.69^{+0.05}_{-0.05}$ (S)	
$C_{\rm XIS1}$			$0.99^{+0.01}_{-0.01}$							
$C_{\rm XIS2}$			$0.93^{+0.01}_{-0.01}$							
$C_{\rm XIS3}$			$0.93^{+0.01}_{-0.01}$							
$C_{\rm PIN}$	$1.20^{+0.02}_{-0.02}$ (P)	$1.04^{+0.02}_{-0.02}$ (P)	$1.45^{+0.02}_{-0.02}$						$0.88^{+0.05}_{-0.05}$ (LX)	
$C_{\rm GSO}$			$1.52^{+0.24}_{-0.24}$						$1.55^{+0.22}_{-0.22}$ (CZ)	
					case (ii) : only normalisation is untied across epochs					
Γ					$2.39^{+0.05}_{-0.02}$					
$N_{\rm H,\ LOS}$					$6.16^{+0.23}_{-0.16}$					
$N_{\rm H,\ tor}$					$14.05^{+0.91}_{-0.77}$					
$\theta_{\rm tor}$					$73.7^{+0.2}_{-0.1}$					
$\theta_{\rm incl}$					$80.8^{+0.1}_{-0.1}$					
$f_{\rm cov}$					$0.28^{+0.01}_{-0.01}$					
$A_{\rm Z} = A_{\rm S}$	$14.09^{+2.13}_{-1.41}$	$13.19^{+1.51}_{-1.00}$	$14.17^{+2.36}_{-1.57}$	$13.26^{+0.33}_{-1.40}$	$13.21^{+1.49}_{-1.49}$	$13.92^{+1.35}_{-1.35}$	$13.52^{+1.47}_{-1.47}$	$15.02^{+0.62}_{-1.57}$	$17.97^{+2.31}_{-2.00}$	$13.65^{+0.30}_{-1.75}$
$E_{\rm cut}$					$105.7^{+2.7}_{-2.2}$					
χ_r(dof)					1.134 (8096)					

Notes - The abbreviation for spectral parameters and their units are same as mentioned in Table 5.3.

Table 5.4: Continued.

Parameters	1998-03-13 (*Beppo*) (1)	2001-01-07 (*Beppo*) (2)	2006-07-21 (*Suzaku*) (3)	2013-01-25 (*Nu*) (4)	2013-02-02 (*Nu*) (5)	2013-02-03 ($X+Nu$) (6)	2013-02-05 (*Nu*) (7)	2016-08-23 ($X+Nu$) (8)	2020-01-28 (*AstroSat*) (9)	2020-11-26 (*Nu*) (10)
Model: BORUS02 + lines + contamination										
case (iii) : only $N_{\rm H,\ LOS}$ is untied across epochs										
Γ	$2.40^{+0.02}_{-0.01}$									
$N_{\rm H,\ LOS}$	$5.85^{+1.76}_{-0.81}$	$5.22^{+0.90}_{-0.68}$	$4.19^{+0.16}_{-0.14}$	$6.24^{+0.18}_{-0.15}$	$6.32^{+0.19}_{-0.16}$	$6.30^{+0.26}_{-0.21}$	$6.15^{+0.20}_{-0.16}$	$5.84^{+0.17}_{-0.14}$	$5.37^{+2.66}_{-0.72}$	$6.22^{+0.13}_{-0.12}$
$N_{\rm H,\ tor}$	$14.05^{+0.98}_{-1.01}$									
$\theta_{\rm tor}$	$73.7^{+0.2}_{-0.1}$									
$\theta_{\rm incl}$	$80.8^{+0.2}_{-0.1}$									
$f_{\rm cov}$	$0.28^{+0.01}_{-0.01}$									
$A_{\rm Z} = A_{\rm S}$	$14.26^{+0.26}_{-1.01}$									
$E_{\rm cut}$	$110.5^{+2.9}_{-2.0}$									
χ_r(dof)	1.117 (8096)									
case (iv) : $N_{\rm H,\ LOS}$ and normalisations untied across epochs										
Γ	$2.40^{+0.04}_{-0.02}$									
$N_{\rm H,\ LOS}$	$5.87^{+1.18}_{-1.00}$	$5.15^{+1.00}_{-0.68}$	$4.19^{+0.42}_{-0.30}$	$6.24^{+0.22}_{-0.18}$	$6.39^{+0.28}_{-0.25}$	$6.38^{+0.32}_{-0.22}$	$6.13^{+0.31}_{-0.21}$	$5.89^{+0.28}_{-0.21}$	$5.69^{+0.40}_{-0.29}$	$6.28^{+0.27}_{-0.20}$
$N_{\rm H,\ tor}$	$14.05^{+0.86}_{-0.93}$									
$\theta_{\rm tor}$	$73.7^{+0.1}_{-0.1}$									
$\theta_{\rm incl}$	$80.8^{+0.1}_{-0.1}$									
$f_{\rm cov}$	$0.28^{+0.01}_{-0.02}$									
$A_{\rm Z} = A_{\rm S}$	$14.88^{+1.51}_{-1.44}$	$13.59^{+1.19}_{-1.13}$	$14.82^{+2.01}_{-1.71}$	$14.05^{+0.71}_{-0.74}$	$14.62^{+1.40}_{-1.58}$	$14.81^{+1.11}_{-0.77}$	$13.88^{+1.27}_{-1.63}$	$14.60^{+1.34}_{-1.62}$	$16.93^{+3.31}_{-2.84}$	$14.68^{+0.43}_{-0.96}$
$E_{\rm cut}$	$109.4^{+4.8}_{-2.2}$									
χ_r(dof)	1.117 (8087)									

We find that the BORUS02 model provides an acceptable fit to the multi-epoch spectra with reduced $\chi^2 = 1.138$ for 8105 dof (see case (i) in Table 5.4). We note that, untying normalisations across epochs renders a slight improvement in the fit statistics with reduced $\chi^2 = 1.134$ for 8096 dof. Although, keeping variable $N_{\rm H,LOS}$ across epochs gives further improvement in the fit statistics with reduced $\chi^2 = 1.117$ for 8096 dof (see case (iii) in Table 5.4). Notably, we obtain nearly the same fit statistics and parameters if both normalisations and $N_{\rm H,LOS}$ are kept variable across epochs (see case (iv) in Table 5.4). Also, untying other parameters (*e.g.*, photon index, $\theta_{\rm tor}$, $\theta_{\rm incl}$) across epochs gives no significant improvement in the fit statistics. Thus, the best fit of multi-epoch joint spectra suggests for a variable line-of-sight column density.

We note that, similar to the MYTORUS model, the BORUS02 model too shows that the multi-epoch spectra of AGN can be characterised by a steep power law ($\Gamma = 2.40^{+0.04}_{-0.02}$) emission piercing through Compton-thick line-of-sight column density of $4.19^{+0.42}_{-0.30} - 6.39^{+0.28}_{-0.25} \times 10^{24}$ cm^{-2} with a nearly edge-on torus ($\theta_{\rm incl} \simeq 80.8^{+0.1}_{-0.1}$). However, unlike the MYTORUS model, BORUS02 model allows us to constrain the globally averaged column density ($N_{\rm H,tor} = 14.05^{+0.86}_{-0.93} \times 10^{24}$ cm^{-2}), torus opening angle ($\theta_{\rm tor}$) $\simeq 73^{\circ}.7$ and covering factor ($f_{\rm cov} = 0.28^{+0.01}_{-0.02}$) (see Table 5.4). In a nutshell, circumnuclear material in Circinus can be well described as a thin torus with an opening angle of $73^{\circ}.7$ (average), an inclination angle of 80° and a relatively low covering factor of 0.28.

5.5.3 Joint spectral modelling with UXCLUMPY model

The UXCLUMPY model (Buchner et al., 2019) considers clumpy structure of the reprocessing matter consists of small (angle subtended at the black hole in the range $0'.1 - 1^{\circ}$) spherical clouds each having constant density. The clouds are distributed in an axis-symmetric geometry with a decreasing number towards the pole from the equatorial plane following a Gaussian function $N = N_0 \exp\{-(\beta/\sigma)^m\}$, where N denotes the number of clouds seen along the line-of-sight, N_0 is the number of clouds at the equatorial plane, β is the inclination angle towards the pole from the equatorial plane, σ is the angular width of the distribution (the torus scale height) and varies in the range $6° - 90°$. In addition to an axisymmetric clumpy torus, this model considers a Compton-thick reflector near the corona, which can be interpreted as part of the dust-free broad-line region or a warped disk. The clumpy reprocessing material considered in this model results in leakage of soft photons along Compton-thick sight lines. Similar to the other models, the UXClumpy model considers transmitted component, Compton-scattered component and fluorescent emission lines in a self-consistent manner.

We note that both the MYTorus and borus02 models consider reprocessor of uniform density, however, circumnuclear material can be clumpy (Nenkova et al., 2008). Therefore, the UXCLUMPY model assuming clumpy reprocessing material consists of small clouds provides a more realistic structure. Also, unlike previous models, the UXCLUMPY model considers line-of-sight column density that can vary in the range of 10^{20} cm^{-2} to 10^{26} cm^{-2}. We fitted the joint spectra of all ten epochs using a model defined as const*tbabs*(UXCLUMPY_cutoff)+ line + contamination, where the UXCLUMPY_cutoff represents UXCLUMPY model with a high energy cut-off in the range of 60 keV to 400 keV. The constant parameter and tbabs account for the cross-normalisation factor, and galactic column density, respectively. While performing the fit, we kept all the parameters of the UXCLUMPY model free. We noticed that often torus inclination angle becomes very low, resulting in an unstable fit. Therefore, we fixed the torus inclination angle to 80° based on the value obtained from the MYTorus and borus02 model.

Table 5.5: The joint fit spectral parameters using UXCLUMPY model

Parameters	1998-03-13 (*Beppo*) (1)	2001-01-07 (*Beppo*) (2)	2006-07-21 (*Suzaku*) (3)	2013-01-25 (*Nu*) (4)	2013-02-02 (*Nu*) (5)	2013-02-03 ($X+Nu$) (6)	2013-02-05 (*Nu*) (7)	2016-08-23 ($X+Nu$) (8)	2020-01-28 (*AstroSat*) (9)	2020-11-26 (*Nu*) (10)
Model: UXCLUMPY + lines + contamination										
case (i) : all parameters varied but tied across epochs										
Γ					$2.05^{+0.01}_{-0.02}$					
$N_{\mathrm{H,\ LOS}}$					$8.91^{+0.14}_{-0.08}$					
θ_{incl}					80^{f}					
σ_{tor}					$7.0^{+0.4}_{\mathrm{peg}}$					
CTKCover					$0.32^{+0.01}_{-0.01}$					
$A_{\mathrm{Z}} = A_{\mathrm{S}}$					$0.80^{+0.01}_{-0.03}$					
E_{cut}					$400^{\mathrm{peg}}_{-37.4}$					
χ_r(dof)					1.165 (8106)					
C_{XMM}						1.0^{f}		$0.97^{+0.02}_{-0.01}$		
C_{NuA}				$1.19^{+0.01}_{-0.01}$	$1.16^{+0.01}_{-0.02}$	$1.16^{+0.01}_{-0.01}$	$1.11^{+0.01}_{-0.01}$	$1.25^{+0.02}_{-0.02}$		$1.11^{+0.01}_{-0.01}$
C_{NuB}				$1.24^{+0.01}_{-0.01}$	$1.20^{+0.01}_{-0.03}$	$1.19^{+0.01}_{-0.01}$	$1.14^{+0.01}_{-0.01}$	$1.30^{+0.02}_{-0.02}$		$1.12^{+0.01}_{-0.01}$
C_{XIS0}	$0.87^{+0.02}_{-0.02}$ (ME)	$0.80^{+0.02}_{-0.02}$ (ME)	$1.04^{+0.01}_{-0.01}$						$0.73^{+0.05}_{-0.05}$ (S)	
C_{XIS1}			$1.08^{+0.01}_{-0.01}$							
C_{XIS2}			$1.00^{+0.01}_{-0.01}$							
C_{XIS3}			$1.00^{+0.01}_{-0.01}$							
C_{PIN}	$1.10^{+0.02}_{-0.02}$ (P)	$0.96^{+0.02}_{-0.04}$ (P)	$1.34^{+0.02}_{-0.02}$						$0.84^{+0.06}_{-0.06}$ (LX)	
C_{GSO}			$1.48^{+0.24}_{-0.24}$						$1.44^{+0.24}_{-0.24}$ (CZ)	
case (ii) : only normalisation is untied across epochs										
Γ					$2.05^{+0.01}_{-0.02}$					
$N_{\mathrm{H,\ LOS}}$					$8.95^{+0.19}_{-0.10}$					
θ_{incl}					80^{f}					
σ_{tor}					$7.0^{+0.4}_{\mathrm{peg}}$					
CTKCover					$0.32^{+0.02}_{-0.001}$					
$A_{\mathrm{Z}} = A_{\mathrm{S}}$	$0.77^{+0.01}_{-0.03}$	$0.63^{+0.01}_{-0.02}$	$0.83^{+0.01}_{-0.03}$	$0.79^{+0.03}_{-0.02}$	$0.79^{+0.01}_{-0.02}$	$0.79^{+0.02}_{-0.03}$	$0.80^{+0.02}_{-0.02}$	$0.82^{+0.02}_{-0.03}$	$0.91^{+0.06}_{-0.06}$	$0.80^{+0.02}_{-0.02}$
E_{cut}					$400^{\mathrm{peg}}_{-22.0}$					
χ_r(dof)					1.164 (8097)					

Notes - The abbreviation for spectral parameters and their units are the same as mentioned in Table 5.3.

Table 5.5: Continued.

Parameters	1998-03-13	2001-01-07	2006-07-21	2013-01-25	2013-02-02	2013-02-03	2013-02-05	2016-08-23	2020-01-28	2020-11-26
	(*Beppo*)	(*Beppo*)	(*Suzaku*)	(*Nu*)	(*Nu*)	($X+Nu$)	(*Nu*)	($X+Nu$)	(*AstroSat*)	(*Nu*)
	(1)	(2)	(3)	(4)	(5)	(6)	(7)	(8)	(9)	(10)
Model: UXCLUMPY + lines + contamination										
case (iii) : only $N_{\rm H,\ LOS}$ is untied across epochs										
Γ	$2.06^{+0.01}_{-0.01}$									
$N_{\rm H,\ LOS}$	$7.84^{+0.24}_{-0.21}$	$12.01^{+0.30}_{-0.26}$	$6.97^{+0.07}_{-0.05}$	$8.84^{+0.19}_{-0.11}$	$8.95^{+0.43}_{-0.29}$	$8.99^{+0.30}_{-0.25}$	$8.59^{+0.29}_{-0.28}$	$6.54^{+0.14}_{-0.13}$	$4.46^{+1.42}_{-0.94}$	$8.84^{+0.09}_{-0.08}$
$\theta_{\rm incl}$	80^{f}									
$\sigma_{\rm tor}$	$7.0^{+0.2}_{\rm peg}$									
CTKCover	$0.31^{+0.005}_{-0.001}$									
$A_{\rm Z}=A_{\rm S}$	$0.80^{+0.01}_{-0.002}$									
$E_{\rm cut}$	$400^{\rm peg}_{-14.3}$									
χ_r(dof)	1.159 (8097)									
case (iv) : $N_{\rm H,\ LOS}$ and normalisations untied across epochs										
Γ	$2.08^{+0.01}_{-0.01}$									
$N_{\rm H,\ LOS}$	$6.42^{+0.38}_{-0.36}$	$4.70^{+0.46}_{-0.44}$	$4.32^{+0.04}_{-0.03}$	$8.63^{+0.18}_{-0.14}$	$8.93^{+0.24}_{-0.31}$	$9.26^{+0.75}_{-0.53}$	$8.36^{+0.81}_{-0.67}$	$5.38^{+0.21}_{-0.21}$	$4.13^{+2.23}_{-1.07}$	$8.84^{+0.16}_{-0.15}$
$\theta_{\rm incl}$	80^{f}									
$\sigma_{\rm tor}$	$7.1^{+0.6}_{\rm peg}$									
CTKCover	$0.33^{+0.01}_{-0.01}$									
$A_{\rm Z}=A_{\rm S}$	$0.77^{+0.02}_{-0.02}$	$0.61^{+0.02}_{-0.02}$	$0.82^{+0.04}_{-0.01}$	$0.87^{+0.02}_{-0.01}$	$0.88^{+0.02}_{-0.01}$	$0.86^{+0.02}_{-0.01}$	$0.87^{+0.02}_{-0.01}$	$0.69^{+0.02}_{-0.01}$	$0.70^{+0.27}_{-0.07}$	$0.88^{+0.01}_{-0.01}$
$E_{\rm cut}$	$400^{\rm peg}_{-17.8}$									
χ_r(dof)	1.152 (8088)									

Similar to our previous spectral modellings, we attempted to fit the multi-epoch spectra with the UXCLUMPY model using different scenarios. The spectral fitted parameters based on the UXCLUMPY model are listed in Table 5.5. We plot the best−fitted joint spectra and residuals in Figure 5.7. We find that the best fit is achieved when both $N_{\rm H,LOS}$ and normalisations are varied across epochs (see case (iv) in Table 5.5). We also tried varying other parameters (*e.g.*, photon index, $\sigma_{\rm tor}$, and `CTKCover`) but found no further significant improvement in the fit statistics. It is worth noting that similar to the MYTorus and borus02 models, UXCLUMPY too reveals a steep spectrum ($\Gamma = 2.08^{+0.01}_{-0.01}$) AGN obscured with Compton-thick column densities. Although, line-of-sight column density ($N_{\rm H,\ LOS}$) changes from $4.13^{+2.23}_{-1.07} \times 10^{24}$ cm^{-2} to $9.26^{+0.75}_{-0.53} \times 10^{24}$ cm^{-2} across various epochs. A significant change in $N_{\rm H,\ LOS}$ from one to other epochs at various timescales is consistent with a clumpy obscuring material wherein the obscuring clouds can move in or out of the line-of-sight. A detailed discussion on the implications of variable $N_{\rm H,\ LOS}$ is given in Section 5.6.

We note that the angular dispersion of clouds in the torus ($\sigma_{\rm tor}$) is nearly 7° (with lower limit pegging to the hard limit of 6°). Therefore, $\sigma_{\rm tor}$ parameter indicates a thin torus. However, our spectral modelling always requires an inner ring of Compton-thick material to fully account for the scattered components. The covering factor of the inner Compton-thick reflector (`CTKCover`) is $0.33^{+0.01}_{-0.01}$. Both `CTKCover` and $\sigma_{\rm tor}$ parameters provide constraints on the geometry of the circumnuclear material. The implications of these parameters are discussed in Section 5.6. We point out that our spectral parameters from the UXCLUMPY model are broadly consistent with those obtained by Buchner et al. (2019), although we find a somewhat steeper photon index and require no warm mirror component, which is a scattered component arriving to the observer without encountering heavy absorption from the torus. One of the main differences in our spectral fitting is the inclusion of the contamination model.

5.6 Discussion

5.6.1 Constraints on the geometry and covering factor

With the modelling of multi-epoch spectra of Circinus, we find the evidence for reprocessing material distributed in the form of torus around AGN. The best-fitted models favour a nearly edge-on torus with an inclination angle of $77° - 81°$, which is consistent with the findings at other wavelengths. For instance, IR interferometric observations revealed a circumnuclear dusty disc component with inclination angle of $> 75°$ (see Tristram et al., 2014; Isbell et al., 2022). In sub-millimeter wavelengths, both continuum as well as CO(3-2), [C I](1-0) emission line maps obtained with the Atacama Large Millimeter/Submillimeter Array (ALMA) showed a circumnuclear disk having the size of a few tens of parsec and inclination angle of $> 70°$. Also, H_2O maser disc is found to be edge-on with an inclination angle close to 90° (Greenhill et al., 2003). Therefore, a multi-phase circumnuclear material is plausibly distributed in the form of a torus that transforms into a disc at inner regions around AGN.

Further, we attempted to place constraints on the covering factor of reprocessing material. The MYTorus model yielding a good fit for the multi-epoch spectra assumes a fixed value of covering factor ($f_{\rm cov}$) of 0.5. However, in a realistic scenario, the covering factor can be variable. Therefore, we applied the BORUS02 model, which considers $f_{\rm cov}$ as a free parameter. We showed that our multi-epoch spectra could be jointly fitted with the BORUS02 model resulting covering factor of nearly 0.28 (see Table 5.4). The confidence contours between the covering factor ($f_{\rm cov}$) and average column density ($N_{\rm H,\ tor}$) show that both the parameters derived from the multi-epoch joint fit are well constrained (see

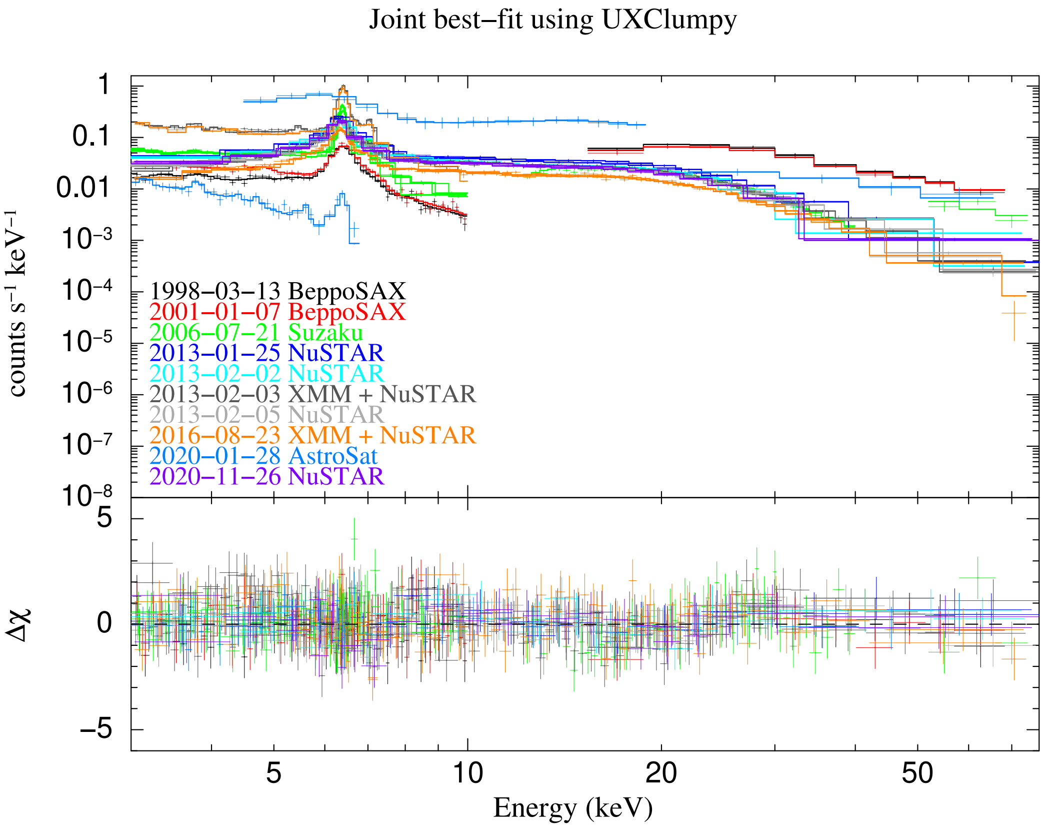

Figure 5.7: The multi-epoch spectra jointly fitted with UXCLUMPY model. Residuals seen around 6−7 keV can be attributed to Fe Kα and Kβ emission lines detected with different instruments of differing energy resolution. For a better display of residuals all the spectra are rebinned with a minimum of 50 to 200 counts per bin.

Figure 5.8). Also, since keeping the covering factor a variable parameter across epochs does not improve the spectral fit, and hence, we conclude that the overall geometry of the torus remains nearly the same across all epochs.

We recall that the BORUS02 model allows us to estimate the covering factor, but it considers a uniform reprocessing material. Keeping this limitation in mind, we used the UXCLUMPY model, which considers clumpy reprocessing material with clouds having a gaussian distribution along the direction perpendicular to the torus equatorial plane. This model also considers an inner ring of Compton-thick material to explain Compton hump, if needed. We find that our spectra are well fitted with the UXCLUMPY model, which gives angular dispersion of nearly 7°. Thus, a low value of angular dispersion infers a thin torus. It is worth mentioning that a direct comparison of covering factors obtained in the BORUS02 and the UXCLUMPY models is not possible as they assume different geometries for the reprocessing material. Although, both models infer that the torus is likely to be thin with a relatively low covering factor. Further, we point out that an inner ring of Compton-thick reflector is needed in the UXCLUMPY model to well describe the spectra of all epochs. The covering factor of the inner ring (`CTKCover`) is found to be 0.33. The presence of an inner ring inferred from the UXCLUMPY model may be interpreted as the wind launch site (Krolik & Begelman, 1988), a puffed-up inner rim of accretion disk or a warped disk which tends to hide AGN when the torus or accretion disk is viewed edge-on, as in the case of Circinus. In a recent work, Andonie et al. (2022) suggested that the inner ring can plausibly depict the accretion disc and the BLR region.

In the literature, there have been several attempts to probe the circumnuclear material in Circinus. For instance, recently Ursini et al. (2023) performed Imaging X-ray Polarimetry Explorer (IXPE) observations and reported a significantly polarised (28±7 per cent degree of polarization and a polarization angle of 18°±5°) 2.0 − 6.0 keV soft X-ray AGN emission mostly due to a neutral reflector. The observed polarization properties were explained by considering the reprocessing of X-ray emission from an edge−on uniform-density torus having the ratio of inner to outer radius 0.1−0.5 and a half-opening angle of 45° − 55°, which infers a covering factor of nearly 0.5, a value consistent with the MYTorus model. However, considering IR Interferometric observations of Circinus providing a direct evidence of clumpy circumnuclear environment (see Tristram et al., 2014; Stalevski et al., 2019; Isbell et al., 2022), we favour the geometrical parameters inferred from the models assuming clumpy circumnuclear material. We point out that, Uematsu et al. (2021) modelled 3 − 100 keV broad-band X-ray spectrum of Circinus with a clumpy torus model and suggested a Compton-thick but geometrically thin torus with an angular width (σ) = $10.3^{+0.7}_{-0.3}$ degrees, which is consistent with our findings. Further, covering factor can be related to the accretion rate or AGN intrinsic luminosity with a trend of decreasing covering factor with the increase in accretion rate and AGN luminosity (see Buchner & Bauer, 2017; Ricci et al., 2017c). The low covering factor of 0.28 found in the Circinus can be understood due to its high accretion rate, *i.e.,* $L/L_{\rm Edd} = 0.2$. Circinus hosts a luminous AGN. The absorption-corrected intrinsic 2 − 10 keV AGN luminosity in different epochs is found to be in the range of $2.0 - 3.7 \times 10^{42}$ erg s^{-1}, which is also consistent with the value inferred from the infrared-X-ray correlation (see, Gandhi et al., 2009; Asmus et al., 2015).

5.6.2 Variability in line-of-sight column density

We investigated the presence of variability in the line-of-column density, which can provide clear evidence for the clumpy torus. From our spectral modelling, it is evident that measured $N_{\rm H,\ LOS}$ is model dependent. Therefore, for our analysis, we prefer to use $N_{\rm H,LOS}$ measured from the UXCLUMPY model owing to the

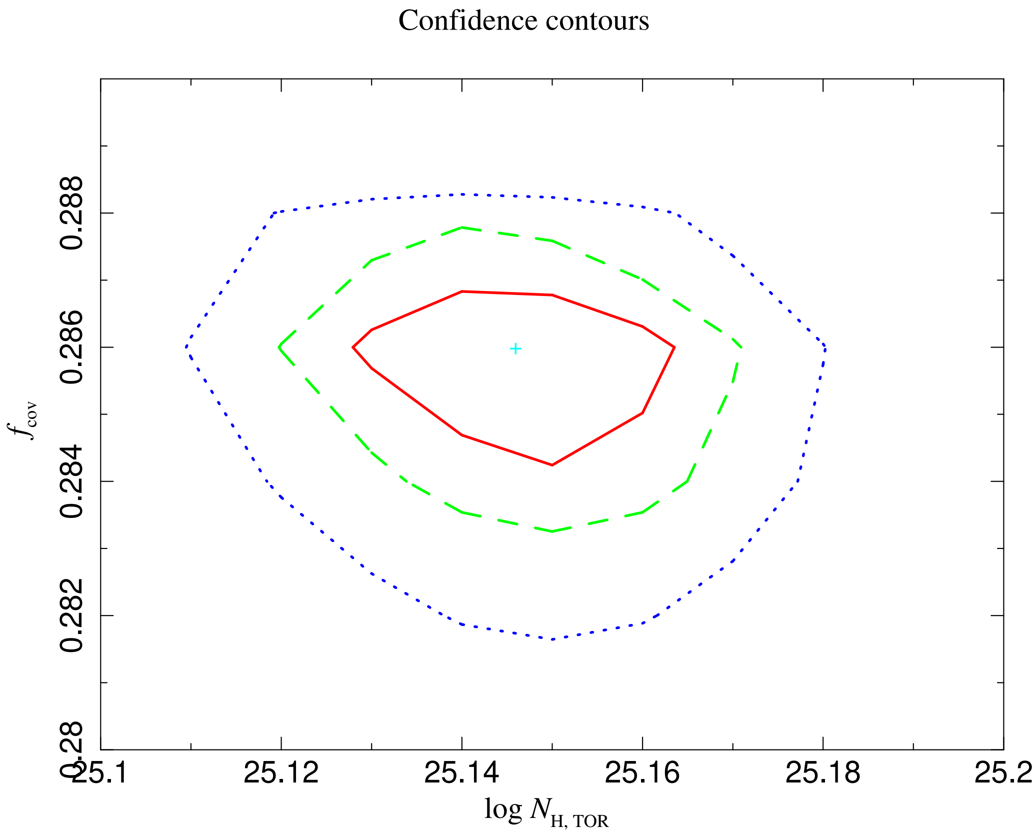

Figure 5.8: Confidence contours based on the joint spectral fit using BORUS02 model. The confidence contours from inward to outward represent 1σ, 2σ and 3σ significant level.

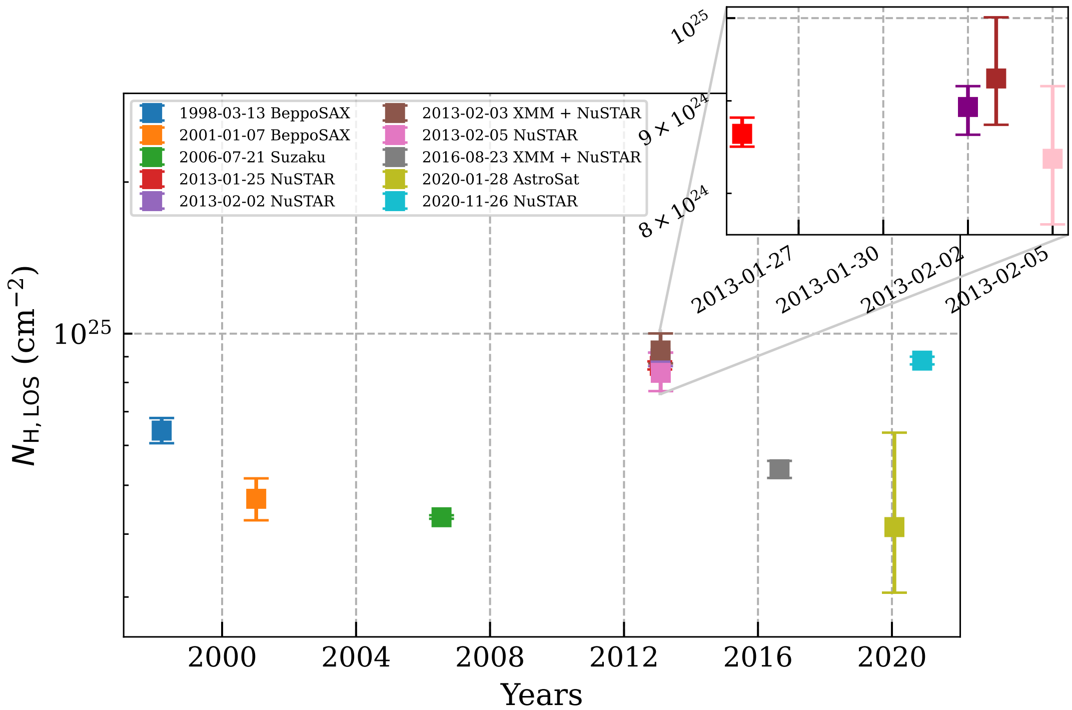

Figure 5.9: The plot showing line-of-sight column density ($N_{\mathrm{H,LOS}}$) variability across different epochs. The estimates of $N_{\mathrm{H,LOS}}$ are based on the best fit (case-iv) of joint spectral modelling using the UXClumpy model.

fact that both MYTORUS and BORUS02 models assume a uniform-density torus. In Figure 5.9, we plot the line-of-sight column density ($N_{\rm H,LOS}$) for all ten epochs using the best-fitted values obtained from the UXCLUMPY model. We find that, $N_{\rm H,LOS}$ exhibits a significant variability on years timescales. For instance, $N_{\rm H,LOS}$ changes from $6.42^{+0.38}_{-0.36} \times 10^{24}$ cm^{-2} $4.70^{+0.46}_{-0.44} \times 10^{24}$ cm^{-2} between 1998 March 13 to 2001 January 07, *i.e.*, a nearly 27 per cent decrease in 3 years timescale. From 2006 July 21 to 2013 January 25, $N_{\rm H,LOS}$ becomes nearly double, which is 100 per cent increase in 6.5 years. The $N_{\rm H,LOS}$ variation on months timescales is also evident. We find that $N_{\rm H,LOS}$ changes from $4.13^{+2.23}_{-1.07} \times 10^{24}$ cm^{-2} to $8.84^{+0.16}_{-0.15} \times 10^{24}$ cm^{-2} between 2020 January 28 and 2020 November 26. The *NuSTAR* observations separated by one day to couple of weeks in 2013 allow us to probe $N_{\rm H,LOS}$ variability on shorter timescales. One of the noticeable variations can be seen between 2013 February 03 and 2013 February 05 where $N_{\rm H,LOS}$ changes from $9.26^{+0.75}_{-0.53} \times 10^{24}$ cm^{-2} to $8.36^{+0.81}_{-0.67} \times 10^{24}$ cm^{-2} in two days timescales. However, uncertainties on $N_{\rm H,LOS}$ makes this variation only tentative. On the shortest timescales of one day from 2013 February 02 to 2013 February 03, we find only a marginal change ($\Delta N_{\rm H,LOS} = 0.33 \times 10^{24}$ cm^{-2}) in the line-of-sight column density. The significance level of change in $N_{\rm H,LOS}$ is low due to relatively large uncertainties. Although, we find a clear evidence of change in $N_{\rm H,LOS}$ on months to year timescales. We note the our results on $N_{\rm H,LOS}$ variation should be treated with caution as the influence of the variability in off-nuclear contaminating sources, albeit accounted by using contamination model, cannot be completely ruled out. We also point out that several studies in the literature have demonstrated the change in the line-of-sight column density on timescales ranging from hours to months as clouds of the clumpy material pass in and out of the observer's line of sight (see Risaliti et al., 2010; Ricci et al., 2016). The cloud moving close to AGN would eclipse the central AGN more frequently than those far away from it. Therefore, similar to other nearby CT-AGN (*e.g.*, MRK 3; Guainazzi et al., 2016, NGC 1068; Zaino et al., 2020), our study demonstrates the plausible variability in $N_{\rm H,LOS}$ in Circinus on various timescales ranging from days to months to years.

5.6.3 Location of obscuring clouds

To know the location of obscuring cloud, we follow the method proposed by Risaliti et al. (2002, 2005) according to which the distance between obscuring clouds and SMBH can be estimated using the equation given below.

$$D_{\rm cl-BH} = 600\ t_{100}^2 n_{10}^2 N_{\rm H,24}^{-2} R_{\rm S}$$

where $D_{\rm cl-BH}$ is the distance between obscuring cloud and black hole, t_{100} is time over which $N_{\rm H,LOS}$ variability observed, n_{10} is the cloud density in units of 10^{10} cm^{-3} and $N_{\rm H,24}$ is the change in the line-of-sight column density in units of 10^{24} cm^{-2}, and $R_{\rm S}$ is Schwarzschild radius. We caution that the aforementioned equation assumes that the change in $N_{\rm H,LOS}$ is caused due to a single cloud crossing the line-of-sight. It also assumes that the cloud is located sufficiently close to the AGN resulting into a large coverage of the X-ray emitting AGN. Thus, $N_{\rm H,LOS}$ variations are expected to occur only on timescales of a few days or even shorter. Hence, to estimate the location of obscuring cloud, we use $N_{\rm H,LOS}$ variations observed only on the short timescales of a few days to couple of weeks. For the sake of consistency with the assumption of the adopted method (see Risaliti et al., 2002, 2005), we used $N_{\rm H,LOS}$ derived from the UXCLUMPY model. We estimate cloud density as $n = |N_{\rm H,obs1} - N_{\rm H,obs1}|/d_{\rm corona}$ with an assumption that the change in $N_{\rm H,LOS}$ is due to a single cloud, where $N_{\rm H,obs1}$ and $N_{\rm H,obs2}$ are the line-of-sight column densities at two different epochs, and $d_{\rm corona}$ is the size of the corona.

Table 5.6: The estimate of distance between obscuring cloud and SMBH

Observation range	$t_{100\ \mathrm{ks}}$ (100 ks)	$\Delta N_{\mathrm{H,LOS,24}}$ (10^{24} cm^{-2})	$n_{10,\ \mathrm{3Rs}}$ (10^{10} cm^{-3})	$n_{10,\ \mathrm{15Rs}}$ (10^{10} cm^{-3})	$D_{\mathrm{cl-BH,\ 3Rs}}$ (pc)	$D_{\mathrm{cl-BH,\ 15Rs}}$ (pc)
2013-01-25 to 2013-02-02	6.81	0.30	19.87	3.97	19.93	0.79
2013-02-02 to 2013-02-03	0.94	0.33	21.85	4.36	0.38	0.015
2013-02-03 to 2013-02-05	1.80	0.90	59.60	11.90	1.40	0.056

Notes - $D_{\mathrm{cl-BH,\ 3Rs}}$ and $D_{\mathrm{cl-BH,\ 15Rs}}$ are the estimates of distance between obscuring cloud and SMBH using coronal size set equal to $3R_{\mathrm{S}}$ and $15R_{\mathrm{S}}$, respectively.

In general, X-ray corona size (d_{corona}) is found to be in the range of $3R_{\mathrm{S}}$ $-$ $15R_{\mathrm{S}}$ (see McHardy et al., 2005; Fabian et al., 2015; Kamraj et al., 2018). Considering $M_{\mathrm{BH}} = 1.7 \times 10^{6}\ M_{\odot}$ (Koss et al., 2017) for Circinus, we obtained R_{S} ($2GM_{\mathrm{BH}}/c^{2}$) = 5.04 $\times$ 10^{11} cm.

Using variability in $N_{\mathrm{H,LOS}}$ measured across various timescales, we list the estimated distance between obscuring cloud and SMBH in Table 5.6 for two extreme values ($3R_{\mathrm{S}}$ and $15R_{\mathrm{S}}$) of corona size. As expected, we find that the change in $N_{\mathrm{H,LOS}}$ on the shortest timescales is associated with the obscuring clouds located closest to the AGN. For instance, $N_{\mathrm{H,LOS}}$ variability on a one-day timescale between the *NuSTAR* observations taken on 2013 February 02 and 2013 February 03, provide 0.015 $-$ 0.38 parsec distance range for obscuring cloud. Hence, the material responsible for the $N_{\mathrm{H,LOS}}$ variability on a one-day timescale is likely to be associated with the inner part of the torus. It is worth mentioning that IR interferometric observations of Circinus have revealed dust emission from putative torus with a projected size of 0.2$\times$1.1 pc disk-like geometry (see Tristram et al., 2014). Therefore, our constraints on the location of obscuring material based on the hard X-ray observations are consistent with the IR interferometric observations. Also, our estimate on the location of clouds in Circinus is similar to those reported in other nearby AGN, *e.g.*, NGC 1068 (Zaino et al., 2020) and

NGC 1358 (Marchesi et al., 2022). The $N_{\rm H,LOS}$ variability on a one-week timescale seen between 2013 January 25 and 2013 February 02 suggests the location of clouds at a distance of 0.79 to 19.93 parsec, which may be associated with the outer part of the obscuring torus. We note that $N_{\rm H,LOS}$ variability on a few years timescales is unable to place a reliable constraint on the location of obscuring material. Also, we caution that the location of the obscuring material inferred in our analysis is only a characteristic due to the significant errors associated with $N_{\rm H,LOS}$.

5.7 Summary

In this study, we present multi-epoch broadband X-ray spectral modelling of a nearby Compton-thick AGN in Circinus using all the available hard X-ray observations taken during ten different epochs in 22 years from 1998 to 2020. Six out of ten epochs of observations are from the *NuSTAR*, while the remaining four epochs of observations are from *BeppoSAX* (for two epochs), *Suzaku* and *AstroSat*. The *Chandra* and *XMM-Newton* imaging observations of higher spatial resolution reveal the existence of off-nuclear sources that contaminate hard X-ray spectra. Therefore, prior to the broadband spectral modelling, we account for the spectral shape and contribution of contaminating sources.

With an aim to constrain the geometry and structure of reprocessing material around AGN and its evolution, we performed broadband X-ray spectral modelling of all ten epochs using physically-motivated models, *i.e.*, MYTorus, borus02 and UXCLUMPY. We find that AGN is heavily obscured by Compton-thick column densities during all the epochs. MYTorus model reveals a purely reflection-dominated spectrum with a vanishing transmitted component. The obscuring torus is found to be nearly edge-on with an inclination angle of 77°.

The BORUS02 model infers a thin torus with an opening angle of nearly 73°, an inclination angle of 80°.8 and a low covering factor of 0.28. Interestingly, the UXCLUMPY model also suggests a thin torus with angular dispersion of obscuring cloud only 7° with an inner ring of Compton-thick material having a covering factor in the range of 0.33. Therefore, it does seem that the overall structure at parsece scale is likely to remain unchanged. One of the important results of our study is the tentative evidence of variable line-of-sight column density at all timescales ranging from one day to one week to a few years. The variable line-of-sight column density supports the presence of eclipsing clouds associated with the reprocessing material at sub-parsec scales.

Chapter 6

Summary and future work

Here, I present the summary of the thesis work, which is mainly focused at unveiling population of AGN in DOGs and understanding their nature, evolution stage including a detailed study of circumnuclear environments around the CT-AGN in the Circinus galaxy.

6.1 Radio-AGN hosted in DOGs

Radio observations being insensitive to the dust-obscuration, have been exploited to unveil the population of AGN residing in galaxies with large dust content. In this paper, we investigate the radio characteristics of 321 DOGs ($S_{24\ \mu m}/S_{r\ band}$ $\geq$1000) by using mainly deep band-3 (250$-$550 MHz) observations from the upgraded Giant Metrewave Radio Telescope (uGMRT) and 1.5 GHz Jansky Very Large Array (VLA) observations. We find that, for our sample of DOGs, deep (median noise-rms = 30 μJy beam^{-1}) 400 MHz band-3 uGMRT observations yield the highest detection rate (28 per cent) among those obtained with the VLA, and the LOw Frequency ARray (LOFAR) radio observations and the *XMM-Newton* X-ray observations. The radio characteristics of our sample sources, *i.e.*, linear extent (<40 kpc at z <1.2), bimodal spectral index ($\alpha_{400\ \mathrm{MHz}}^{1.5\ \mathrm{GHz}}$) distribution and the radio luminosities ($L_{1.5\ \mathrm{GHz}}$ >5.0 × 10^{23} W Hz^{-1}), suggest them to be mainly consist of Compact−Steep−Spectrum (CSS) or Peaked-Spectrum (PS) sources representing an early phase of the AGN-jet activity in dust-obscured environments. With stacking, we find the existence of faint radio emission ($S_{400\ \mathrm{MHz}}$ = 72.9 μJy beam^{-1} and $S_{1.5\ \mathrm{GHz}}$ = 29 μJy beam^{-1} with signal-to-noise ratio ∼ 20) in otherwise radio-undetected DOGs. Our study revealing the faint emission at a few tens of μJy level in high−z DOGs can be used as a test-bed for the deeper radio continuum surveys planned with the Square-Kilometer Array (SKA) and its pathfinders.

6.2 X-ray spectral properties of AGN hosted in DOGs

With an aim to explore the population of high−z obscured AGN and their evolutionary scenario, we performed X-ray spectral modelling of 34 DOGs (0.59 ≤ z ≤ 4.65) using all the existing *XMM-Newton* data, and *Chandra*/ACIS data, whenever available in the *XMM-SERVS* extragalactic field. We find that the X-ray spectra of our DOGs can be well described with an absorbed power law and reflection component. The column densities derived from the spectral modellings show that all but four of our DOGs are moderately obscured ($N_{\mathrm{H}} < 10^{23}$ cm^{-2}) and the fraction of heavily obscured DOGs is limited only to 11.7%. The absorption corrected 2.0−10 keV X-ray luminosities are high (in the range of 2.24 × 10^{43} to 1.86 × 10^{45} erg s^{-1} with a median value of 2.09 × 10^{44} erg s^{-1}) and suggest for the presence of luminous AGN. The N_{H} versus Eddington ratio diagnostic plot infers that our DOGs represent a heterogeneous population containing Hot DOGs as well as reddened quasars. Only a few of our DOGs are likely to belong to an early phase (Hot DOGs) during which accretion and obscuration peak, while the remaining DOGs possibly belong to a late phase during which radiative feedback from dominant AGN blows away obscuring material.

6.3 Multi-epoch hard study of the CT-AGN in the Circinus Galaxy

We presented the multi-epoch broadband X-ray spectral modelling of a nearby Compton-thick AGN in the Circinus galaxy. We utilise all the available hard X-ray (> 10 keV) observations taken from different telescopes, *i.e.*, *BeppoSAX*, *Suzaku*, *NuSTAR* and *AstroSat*, at ten different epochs across 22 years from 1998 to 2020. The 3.0−79 keV broadband X-ray spectral modelling using physically-motivated models, namely MYTorus, borus02 and UXCLUMPY, infers the presence of a torus with a low covering factor of 0.28, an inclination angle of $77^\circ - 81^\circ$ and Compton-thick line-of-sight column densities ($N_{\rm LOS} = 4.13 - 9.26 \times 10^{24}$ cm^{-2}) in all the epochs. The joint multi-epoch spectral modelling suggests that the overall structure of the torus is likely to remain unchanged. However, we find tentative evidence for the variable line-of-sight column density on timescales ranging from one day to one week to a few years, suggesting a clumpy circumnuclear material located at sub-parsec to tens of parsec scales.

6.4 Future work

In our work, we have demonstrated the importance of deep radio observations acquired from the uGMRT that yielded the highest detection rates (28 per cent) in comparison to the less deep FIRST and VLASS observations. Also, stacking results demonstrated the presence of AGN-originated radio emission in DOGs that are yet to be detected with the current observations. We note that there are ongoing efforts to carry out deep continuum radio surveys in various extra-galactic fields, including the *XMM-LSS* . For instance, MeerKAT International GHz Tiered Extragalactic Exploration (MIGHTEE; Heywood et al., 2020) survey aims to achieve 2.0 μJy beam^{-1} noise-rms at 950 MHz -1.7 GHz band (central frequency 1284 MHz) with a total sky coverage of 20 deg^2 in various deep fields. We are part of these radio survey campaigns and plan to utilise much deeper radio surveys to unveil AGN hosted in the dust-obscured galaxies that are either at higher redshifts and/or possess much fainter emission. Further, we plan to perform new radio observations that can yield a sub-arcsec angular resolution, which in turn can reveal compact radio structures and confirm the presence of young radio AGN in DOGs. We note that most of our sample sources appeared unresolved in our 400 MHz uGMRT and 1.5 GHz VLA observations with the angular resolution of $4''.5 - 6''.0$, but, deep high-frequency ($>$ 1.5 GHz) VLA A-configuration observations providing sub-arcsec resolution can potentially reveal jet-lobe structures piercing through the dense environments of their host galaxies at $z > 1.0$. With more radio observations across a wide range of frequencies, we aim to investigate their radio spectra that would enable us to confirm the evolutionary stage, *e.g.*, GPS, HFP or CSS sources.

Bibliography

Abramowicz, M. A., Czerny, B., Lasota, J. P., & Szuszkiewicz, E. 1988, Astrophys. J., 332, 646, doi: 10.1086/166683 [Cited on page 3.]

Agrawal, P. C. 2006, Adv. Sp. Res., 38, 2989, doi: 10.1016/j.asr.2006.03.038 [Cited on page 35.]

Agrawal, P. C., Yadav, J. S., Antia, H. M., et al. 2017, J. Astrophys. Astron., 38, 30, doi: 10.1007/s12036-017-9451-z [Cited on page 35.]

Aihara, H., Arimoto, N., Armstrong, R., et al. 2018, PASJ, 70, S4, doi: 10.1093/pasj/psx066 [Cited on page 91.]

Aihara, H., Alsayyad, Y., Ando, M., et al. 2022, Publ. Astron. Soc. Japan, 74, 247, doi: 10.1093/pasj/psab122 [Cited 2 times on pages 43 and 44.]

Akylas, A., Georgakakis, A., Georgantopoulos, I., Brightman, M., & Nandra, K. 2012, A&A, 546, A98, doi: 10.1051/0004-6361/201219387 [Cited on page 88.]

Alexander, D. M., & Hickox, R. C. 2012, New Astron. Rev., 56, 93, doi: 10.1016/j.newar.2011.11.003 [Cited 3 times on pages 10, 12, and 88.]

Alonso-Herrero, A., García-Burillo, S., Pereira-Santaella, M., et al. 2019, Astron. Astrophys., 628, doi: 10.1051/0004-6361/201935431 [Cited on page 8.]

An, T., & Baan, W. A. 2012, Astrophys. J., 760, 77, doi: 10.1088/0004-637X/760/1/77 [Cited on page 61.]

Ananna, T. T., Treister, E., Urry, C. M., et al. 2019, ApJ, 871, 240, doi: 10.3847/1538-4357/aafb77 [Cited on page 88.]

Andonie, C., Ricci, C., Paltani, S., et al. 2022, Mon. Not. R. Astron. Soc., 511, 5768, doi: 10.1093/mnras/stac403 [Cited 2 times on pages 131 and 171.]

Antia, H. M., Yadav, J. S., Agrawal, P. C., et al. 2017, Astrophys. J. Suppl. Ser., 231, 10, doi: 10.3847/1538-4365/aa7a0e [Cited on page 135.]

Antia, H. M., Agrawal, P. C., Dedhia, D., et al. 2021, Journal of Astrophysics and Astronomy, 42, 32, doi: 10.1007/s12036-021-09712-8 [Cited on page 136.]

Antonucci, R. 1993, Annu. Rev. Astron. Astrophys., 31, 473, doi: 10.1146/annurev.aa.31.090193.002353 [Cited on page 8.]

Antonucci, R. R. J., & Miller, J. S. 1985, Astrophys. J., 297, 621, doi: 10.1086/163559 [Cited 4 times on pages 8, 10, 87, and 125.]

Arévalo, P., Bauer, F. E., Puccetti, S., et al. 2014, Astrophys. J., 791, 81, doi: 10.1088/0004-637X/791/2/81 [Cited 6 times on pages 130, 141, 142, 149, 156, and 159.]

Arnaud, K., Smith, R., & Siemiginowska, A. 2011, hxra [Cited 3 times on pages 31, 32, and 33.]

Arnaud, K. A. 1996, Astron. Data Anal. Softw. Syst. V, A.S.P. Conf. Ser., 101, 17 [Cited 3 times on pages 33, 102, and 129.]

Arnouts, S., Cristiani, S., Moscardini, L., et al. 1999, MNRAS, 310, 540, doi: 10.1046/j.1365-8711.1999.02978.x [Cited on page 94.]

Asmus, D., Gandhi, P., Hönig, S. F., Smette, A., & Duschl, W. J. 2015, Mon. Not. R. Astron. Soc., 454, 766, doi: 10.1093/mnras/stv1950 [Cited on page 172.]

Assef, R. J., Brightman, M., Walton, D. J., et al. 2020, ApJ, 897, 112, doi: 10.3847/1538-4357/ab9814 [Cited on page 89.]

Bahcall, J. N., Kozlovsky, B.-Z., & Salpeter, E. E. 1972, Astrophys. J., 171, 467, doi: 10.1086/151300 [Cited on page 6.]

Ballantyne, D. R. 2008, Astrophys. J., 685, 787, doi: 10.1086/591048 [Cited on page 10.]

Baloković, M., Cabral, S. E., Brenneman, L., & Urry, C. M. 2021, Astrophys. J., 916, 90, doi: 10.3847/1538-4357/abff4d [Cited on page 153.]

Baloković, M., Brightman, M., Harrison, F. A., et al. 2018, Astrophys. J., 854, 42, doi: 10.3847/1538-4357/aaa7eb [Cited on page 160.]

Barthel, P., Tytler, D., & Thomson, B. 1990, A&ApS, 82, 339 [Cited on page 6.]

Bauer, F. E., Brandt, W. N., Sambruna, R. M., et al. 2001, Astron. J., 122, 182, doi: 10.1086/321123 [Cited 2 times on pages 130 and 142.]

Becker, R. H., White, R. L., & Helfand, D. J. 1995, Astrophys. J., 450, 559, doi: 10.1086/176166 [Cited on page 43.]

Begelman, M. C., & Cioffi, D. F. 1989, Astrophys. J., 345, L21, doi: 10.1086/185542 [Cited on page 9.]

Bennert, N., Jungwiert, B., Komossa, S., Haas, M., & Chini, R. 2006, Astron. Astrophys., 446, 919, doi: 10.1051/0004-6361:20053571 [Cited on page 7.]

Bhalerao, V., Bhattacharya, D., Vibhute, A., et al. 2017, J. Astrophys. Astron., 38, doi: 10.1007/s12036-017-9447-8 [Cited 3 times on pages 30, 35, and 136.]

Bhatnagar, S., & Cornwell, T. J. 2004, Astron. Astrophys., 426, 747, doi: 10.1051/0004-6361:20040354 [Cited on page 24.]

Bianchi, S., Mainieri, V., & Padovani, P. 2022, in Handbook of X-ray and Gamma-ray Astrophysics, 4 [Cited on page 11.]

Bianchi, S., Maiolino, R., & Risaliti, G. 2012, Adv. Astron., 2012, 782030, doi: 10.1155/2012/782030 [Cited 2 times on pages 87 and 126.]

Bianchi, S., Matt, G., Fiore, F., et al. 2002, Astron. Astrophys., 396, 793, doi: 10.1051/0004-6361:20021414 [Cited on page 130.]

Blandford, R., Meier, D., & Readhead, A. 2019, Annu. Rev. Astron. Astrophys., 57, 467, doi: 10.1146/annurev-astro-081817-051948 [Cited on page 10.]

Blandford, R. D., & Payne, D. G. 1982, Mon. Not. R. Astron. Soc., 199, 883, doi: 10.1093/mnras/199.4.883 [Cited on page 10.]

Blandford, R. D., & Rees, M. J. 1974, Mon. Not. R. Astron. Soc., 169, 395, doi: 10.1093/mnras/169.3.395 [Cited on page 9.]

Blandford, R. D., & Znajek, R. L. 1977, Mon. Not. R. Astron. Soc., 179, 433, doi: 10.1093/mnras/179.3.433 [Cited on page 10.]

Bloom, S. D., & Marscher, A. P. 1996, Astrophys. J., 461, 657, doi: 10.1086/177092 [Cited on page 10.]

Boella, G., Butler, R. C., Perola, G. C., et al. 1997, Astron. Astrophys. Suppl. Ser., 122, 299, doi: 10.1051/aas:1997136 [Cited on page 138.]

Borkowski, K. J., Lyerly, W. J., & Reynolds, S. P. 2001, Astrophys. J., 548, 820, doi: 10.1086/319011 [Cited on page 145.]

Bradshaw, E. J., Almaini, O., Hartley, W. G., et al. 2013, MNRAS, 433, 194, doi: 10.1093/mnras/stt715 [Cited on page 93.]

Browne, I. W. A., Wilkinson, P. N., Patnaik, A. R., & Wrobel, J. M. 1998, MNRAS, 293, 257, doi: 10.1046/j.1365-8711.1998.01072.x [Cited on page 22.]

Buchner, J., & Bauer, F. E. 2017, Mon. Not. R. Astron. Soc., 465, 4348, doi: 10.1093/mnras/stw2955 [Cited on page 172.]

Buchner, J., Brightman, M., Nandra, K., Nikutta, R., & Bauer, F. E. 2019, Astron. Astrophys., 629, A16, doi: 10.1051/0004-6361/201834771 [Cited 2 times on pages 164 and 168.]

Burlon, D., Ajello, M., Greiner, J., et al. 2011, ApJ, 728, 58, doi: 10.1088/0004-637X/728/1/58 [Cited on page 88.]

Bussmann, R. S., Dey, A., Borys, C., et al. 2009, ApJ, 705, 184, doi: 10.1088/0004-637X/705/1/184 [Cited on page 89.]

Cappelluti, N., Brusa, M., Hasinger, G., et al. 2009, A&A, 497, 635, doi: 10.1051/0004-6361/200810794 [Cited on page 95.]

Cash, W. 1979, ApJ, 228, 939, doi: 10.1086/156922 [Cited on page 102.]

Chartas, G., Kochanek, C. S., Dai, X., Poindexter, S., & Garmire, G. 2009, Astrophys. J., 693, 174, doi: 10.1088/0004-637X/693/1/174 [Cited on page 5.]

Chartas, G., Rhea, C., Kochanek, C., et al. 2016, Astron. Nachrichten, 337, 356, doi: 10.1002/asna.201612313 [Cited on page 5.]

Chen, C. T., Brandt, W. N., Luo, B., et al. 2018, Mon. Not. R. Astron. Soc., 478, 2132, doi: 10.1093/mnras/sty1036 [Cited 7 times on pages 72, 91, 92, 93, 94, 95, and 96.]

Chiappetti, L., Tajer, M., Trinchieri, G., et al. 2005, Astron. Astrophys., 439, 413, doi: 10.1051/0004-6361:20042583 [Cited on page 95.]

Coil, A. L., Blanton, M. R., Burles, S. M., et al. 2011, ApJ, 741, 8, doi: 10.1088/0004-637X/741/1/8 [Cited on page 93.]

Comastri, A. 2004, in Astrophysics and Space Science Library, Vol. 308, Supermassive Black Holes in the Distant Universe, ed. A. J. Barger, 245 [Cited 2 times on pages 13 and 88.]

Combes, F., García-Burillo, S., Audibert, A., et al. 2019, Astron. Astrophys., 623, doi: 10.1051/0004-6361/201834560 [Cited on page 8.]

Condon, J. J. 1992, ARA&A, 30, 575, doi: 10.1146/annurev.aa.30.090192.003043 [Cited on page 39.]

Condon, J. J., Cotton, W. D., & Broderick, J. J. 2002, Astron. J., 124, 675, doi: 10.1086/341650 [Cited on page 69.]

Condon, J. J., Cotton, W. D., Greisen, E. W., et al. 1998, Astron. J., 115, 1693, doi: 10.1086/300337 [Cited on page 40.]

Cooke, K. C., Kartaltepe, J. S., Tyler, K. D., et al. 2019, Astrophys. J., 881, 150, doi: 10.3847/1538-4357/ab30c9 [Cited on page 12.]

Cool, R. J., Moustakas, J., Blanton, M. R., et al. 2013, Astrophys. J., 767, doi: 10.1088/0004-637X/767/2/118 [Cited on page 52.]

Cornwell, T. 1982, Synth. Mapping, Proc. NRAO-VLA Work. held 21-25 June 1982 Socorro, NM. Ed. by A.R. Thompson L.R. D'Addario. Green Bank Natl. Radio Astron. Obs. p.. 13, 1982, 13 [Cited on page 24.]

Cornwell, T. J. 2008, IEEE J. Sel. Top. Signal Process., 2, 793, doi: 10.1109/JSTSP.2008.2006388 [Cited on page 24.]

Corral, A., Georgantopoulos, I., Comastri, A., et al. 2016, A&A, 592, A109, doi: 10.1051/0004-6361/201527624 [Cited 5 times on pages 103, 104, 116, 117, and 118.]

Coupon, J., Ilbert, O., Kilbinger, M., et al. 2009, Astron. Astrophys., 500, 981, doi: 10.1051/0004-6361/200811413 [Cited on page 93.]

Davidson, K., & Netzer, H. 1979, Rev. Mod. Phys., 51, 715, doi: 10.1103/RevModPhys.51.715 [Cited on page 6.]

Davies, R. I., Mueller Sanchez, F., Genzel, R., et al. 2007, Astrophys. J., 671, 1388, doi: 10.1086/523032 [Cited on page 10.]

Davis, S. W., & Laor, A. 2011, Astrophys. J., 728, doi: 10.1088/0004-637X/728/2/98 [Cited on page 3.]

Dawson, K. S., Schlegel, D. J., Ahn, C. P., et al. 2013, Astron. J., 145, doi: 10.1088/0004-6256/145/1/10 [Cited on page 93.]

De Marco, B., & Ponti, G. 2019, Astron. Nachrichten, 340, 290, doi: 10.1002/asna.201913612 [Cited on page 5.]

Della Ceca, R., Carrera, F. J., Caccianiga, A., et al. 2015, MNRAS, 447, 3227, doi: 10.1093/mnras/stu2665 [Cited on page 12.]

den Herder, J. W., Brinkman, A. C., Kahn, S. M., et al. 2001, A&A, 365, L7, doi: 10.1051/0004-6361:20000058 [Cited on page 34.]

Dermer, C. D., & Schlickeiser, R. 1993, Astrophys. J., 416, 458, doi: 10.1086/173251 [Cited on page 10.]

Desprez, G., Picouet, V., Moutard, T., et al. 2023, A&A, 670, A82, doi: 10.1051/0004-6361/202243363 [Cited 2 times on pages 94 and 96.]

Dey, A., Soifer, B. T., Desai, V., et al. 2008, Astrophys. J., 677, 943, doi: 10.1086/529516 [Cited 3 times on pages 39, 45, and 92.]

Donley, J. L., Koekemoer, A. M., Brusa, M., et al. 2012, Astrophys. J., 748, doi: 10.1088/0004-637X/748/2/142 [Cited 2 times on pages 38 and 70.]

Duras, F., Bongiorno, A., Ricci, F., et al. 2020, A&A, 636, A73, doi: 10.1051/0004-6361/201936817 [Cited on page 120.]

Eardley, D. M., & Press, W. H. 1975, Annu. Rev. Astron. Astrophys., 13, 381, doi: 10.1146/annurev.aa.13.090175.002121 [Cited on page 3.]

Efstathiou, A., & Rowan-Robinson, M. 1995, Mon. Not. R. Astron. Soc., 273, 649, doi: 10.1093/mnras/273.3.649 [Cited on page 8.]

Elitzur, M., & Shlosman, I. 2006, Astrophys. J., 648, L101, doi: 10.1086/508158 [Cited on page 8.]

Esposito, P., Israel, G. L., Milisavljevic, D., et al. 2015, Mon. Not. R. Astron. Soc., 452, 1112, doi: 10.1093/mnras/stv1379 [Cited on page 142.]

Fabian, A. C., Lohfink, A., Kara, E., et al. 2015, Mon. Not. R. Astron. Soc., 451, 4375, doi: 10.1093/MNRAS/STV1218 [Cited on page 177.]

Fabian, A. C., Vasudevan, R. V., & Gandhi, P. 2008, MNRAS, 385, L43, doi: 10.1111/j.1745-3933.2008.00430.x [Cited on page 118.]

Fabian, A. C., Zoghbi, A., Ross, R. R., et al. 2009, Nature, 459, 540, doi: 10.1038/nature08007 [Cited 2 times on pages 5 and 120.]

Fan, L., Chen, W., An, T., et al. 2020, Astrophys. J., 905, L32, doi: 10.3847/2041-8213/abcebf [Cited on page 83.]

Farrah, D., Lonsdale, C. J., Weedman, D. W., et al. 2008, Astrophys. J., 677, 957, doi: 10.1086/529485 [Cited on page 39.]

Farrah, D., Petty, S., Connolly, B., et al. 2017, Astrophys. J., 844, 106, doi: 10.3847/1538-4357/aa78f2 [Cited 3 times on pages 38, 39, and 89.]

Fiore, F., Grazian, A., Santini, P., et al. 2008, Astrophys. J., 672, 94, doi: 10.1086/523348 [Cited 3 times on pages 45, 89, and 92.]

Fiore, F., Puccetti, S., Brusa, M., et al. 2009, Astrophys. J., 693, 447, doi: 10.1088/0004-637X/693/1/447 [Cited 2 times on pages 70 and 89.]

Fomalont, E. B., & Perley, R. A. 1999, Synth. imaging radio II, 180, 79 [Cited 2 times on pages 19 and 20.]

For, B. Q., Koribalski, B. S., & Jarrett, T. H. 2012, Mon. Not. R. Astron. Soc., 425, 1934, doi: 10.1111/j.1365-2966.2012.21416.x [Cited on page 129.]

Freeman, K. C., Karlsson, B., Lynga, G., et al. 1977, Astron. Astrophys., 55, 445 [Cited 2 times on pages 128 and 129.]

Frey, S., Paragi, Z., Gabányi, K. É., & An, T. 2016, Mon. Not. R. Astron. Soc., 455, 2058, doi: 10.1093/mnras/stv2399 [Cited 2 times on pages 82 and 83.]

Fridman, P. A., & Baan, W. A. 2001, A&A, 378, 327, doi: 10.1051/0004-6361:20011166 [Cited on page 20.]

Frieden, B. R. 1972, J. Opt. Soc. Am., 62, 511, doi: 10.1364/JOSA.62.000511 [Cited on page 24.]

Fritz, J., Franceschini, A., & Hatziminaoglou, E. 2006, Mon. Not. R. Astron. Soc., 366, 767, doi: 10.1111/j.1365-2966.2006.09866.x [Cited on page 8.]

Gabányi, K., Frey, S., & Perger, K. 2021, Mon. Not. R. Astron. Soc., 506, 3641, doi: 10.1093/mnras/stab1923 [Cited 5 times on pages 14, 40, 57, 59, and 62.]

Gandhi, P., Horst, H., Smette, A., et al. 2009, Astron. Astrophys., 502, 457, doi: 10.1051/0004-6361/200811368 [Cited on page 172.]

Garilli, B., Guzzo, L., Scodeggio, M., et al. 2014, Astron. Astrophys., 562, doi: 10.1051/0004-6361/201322790 [Cited 2 times on pages 52 and 93.]

Garmire, G. P., Bautz, M. W., Ford, P. G., Nousek, J. A., & Ricker, Jr., G. R. 2003, X-Ray Gamma-Ray Telesc. Instruments Astron., 4851, 28, doi: 10.1117/12.461599 [Cited 2 times on pages 29 and 34.]

Gaskell, C. M. 2009, New Astron. Rev., 53, 140, doi: 10.1016/j.newar.2009.09.006 [Cited on page 6.]

Georgantopoulos, I., Georgakakis, A., Rowan-Robinson, M., & Rovilos, E. 2008, A&A, 484, 671, doi: 10.1051/0004-6361:20078790 [Cited on page 89.]

Georgantopoulos, I., Rovilos, E., Xilouris, E. M., Comastri, A., & Akylas, A. 2011, A&A, 526, A86, doi: 10.1051/0004-6361/201014417 [Cited on page 117.]

Ghisellini, G. 2013, Lect. Notes Phys., 873, 1, doi: 10.1007/978-3-319-00612-3 [Cited on page 6.]

Gilli, R., Comastri, A., & Hasinger, G. 2007, Astron. Astrophys., 463, 79, doi: 10.1051/0004-6361:20066334 [Cited on page 88.]

Goulding, A. D., Zakamska, N. L., Alexandroff, R. M., et al. 2018, ApJ, 856, 4, doi: 10.3847/1538-4357/aab040 [Cited on page 122.]

Granato, G. L., De Zotti, G., Silva, L., Bressan, A., & Danese, L. 2004, ApJ, 600, 580, doi: 10.1086/379875 [Cited on page 88.]

Greene, J. E., Ho, L. C., & Barth, A. J. 2008, Astrophys. J., 688, 159, doi: 10.1086/592078 [Cited on page 2.]

Greenhill, L. J., Kondratko, P. T., Lovell, J. E. J., et al. 2003, Astrophys. J., 582, L11, doi: 10.1086/367602 [Cited on page 169.]

Griffin, M. J., Abergel, A., Abreu, A., et al. 2010, Astron. Astrophys., 518, L3, doi: 10.1051/0004-6361/201014519 [Cited on page 38.]

Guainazzi, M., Matt, G., & Perola, G. C. 2005, Astron. Astrophys., 444, 119, doi: 10.1051/0004-6361:20053643 [Cited on page 10.]

Guainazzi, M., Matt, G., Antonelli, L. A., et al. 1999, Mon. Not. R. Astron. Soc., 310, 10, doi: 10.1046/j.1365-8711.1999.02803.x [Cited on page 130.]

Guainazzi, M., Risaliti, G., Awaki, H., et al. 2016, Mon. Not. R. Astron. Soc., 460, 1954, doi: 10.1093/mnras/stw1033 [Cited 2 times on pages 128 and 176.]

Gull, S., & Daniell, G. 1978, Nature, 272, 686, doi: 10.1038/272686a0 [Cited on page 24.]

Gupta, Y., Ajithkumar, B., Kale, H. S., et al. 2017, Curr. Sci., 113, 707, doi: 10.18520/cs/v113/i04/707-714 [Cited on page 26.]

Haardt, F., & Maraschi, L. 1991, Astrophys. J., 380, L51, doi: 10.1086/186171 [Cited on page 5.]

Haardt, F., Maraschi, L., & Ghisellini, G. 1994, Astrophys. J., 432, L95, doi: 10.1086/187520 [Cited on page 5.]

Hale, C. L., Williams, W., Jarvis, M. J., et al. 2019, Astron. Astrophys., 622, doi: 10.1051/0004-6361/201833906 [Cited on page 42.]

Harrison, F. A., Craig, W. W., Christensen, F. E., et al. 2013, Astrophys. J., 770, doi: 10.1088/0004-637X/770/2/103 [Cited 3 times on pages 30, 35, and 131.]

Helfand, D. J., White, R. L., & Becker, R. H. 2015, Astrophys. J., 801, doi: 10.1088/0004-637X/801/1/26 [Cited on page 40.]

Helou, G., Soifer, B. T., & Rowan-Robinson, M. 1985, ApJL, 298, L7, doi: 10.1086/184556 [Cited on page 39.]

Heywood, I., Hale, C. L., Jarvis, M. J., et al. 2020, Mon. Not. R. Astron. Soc., 496, 3469, doi: 10.1093/MNRAS/STAA1770 [Cited 3 times on pages 42, 91, and 184.]

Heywood, I., Jarvis, M. J., Hale, C. L., et al. 2022, Mon. Not. R. Astron. Soc., 509, 2150, doi: 10.1093/mnras/stab3021 [Cited on page 81.]

Högbom, J. A. 1974, Astron. Astrophys. Suppl., 15, 417 [Cited on page 24.]

Högbom, J. A., & Cornwell, T. J. 2009, Astron. Astrophys., 500, 65, doi: 10.1051/0004-6361/200912148 [Cited on page 24.]

Hönig, S. F. 2019, Astrophys. J., 884, 171, doi: 10.3847/1538-4357/ab4591 [Cited on page 126.]

Hönig, S. F., & Kishimoto, M. 2010, Astron. Astrophys., 523, doi: 10.1051/0004-6361/200912676 [Cited on page 9.]

Hönig, S. F., Kishimoto, M., Antonucci, R., et al. 2012, Astrophys. J., 755, 149, doi: 10.1088/0004-637X/755/2/149 [Cited on page 126.]

Hoormann, J. K., Martini, P., Davis, T. M., et al. 2019, Mon. Not. R. Astron. Soc., 487, 3650, doi: 10.1093/mnras/stz1539 [Cited on page 7.]

Hopkins, P. F., Hernquist, L., Cox, T. J., et al. 2006, Astrophys. J. Suppl. Ser., 163, 1, doi: 10.1086/499298 [Cited 2 times on pages 2 and 37.]

Hopkins, P. F., Hernquist, L., Cox, T. J., et al. 2006, ApJS, 163, 1, doi: 10.1086/499298 [Cited on page 88.]

Hopkins, P. F., Hernquist, L., Cox, T. J., & Kereš, D. 2008, Astrophys. J. Suppl. Ser., 175, 356, doi: 10.1086/524362 [Cited 3 times on pages 12, 39, and 88.]

Ilbert, O., Arnouts, S., McCracken, H. J., et al. 2006, Astron. Astrophys., 457, 841, doi: 10.1051/0004-6361:20065138 [Cited 2 times on pages 93 and 94.]

Isbell, J. W., Meisenheimer, K., Pott, J. U., et al. 2022, A&A, 663, A35, doi: 10.1051/0004-6361/202243271 [Cited 2 times on pages 169 and 172.]

Ishibashi, W., Fabian, A. C., Ricci, C., & Celotti, A. 2018, MNRAS, 479, 3335, doi: 10.1093/mnras/sty1620 [Cited on page 120.]

Ishwara-Chandra, C. H., Taylor, A. R., Green, D. A., et al. 2020, Mon. Not. R. Astron. Soc., 497, 5383, doi: 10.1093/mnras/staa2341 [Cited on page 61.]

Jarvis, M. J., Bonfield, D. G., Bruce, V. A., et al. 2013, Mon. Not. R. Astron. Soc., 428, 1281, doi: 10.1093/mnras/sts118 [Cited on page 91.]

Jithesh, V., Maqbool, B., Misra, R., et al. 2019, ApJ, 887, 101, doi: 10.3847/1538-4357/ab4f6a [Cited on page 135.]

Kaiser, C. R., & Alexander, P. 1997, Mon. Not. R. Astron. Soc., 286, 215, doi: 10.1093/mnras/286.1.215 [Cited on page 9.]

Kalberla, P. M., Burton, W. B., Hartmann, D., et al. 2005, Astron. Astrophys., 440, 775, doi: 10.1051/0004-6361:20041864 [Cited on page 129.]

Kamraj, N., Harrison, F. A., Baloković, M., Lohfink, A., & Brightman, M. 2018, Astrophys. J., 866, 124, doi: 10.3847/1538-4357/AADD0D [Cited on page 177.]

Kara, E., Alston, W. N., Fabian, A. C., et al. 2016, Mon. Not. R. Astron. Soc., 462, 511, doi: 10.1093/mnras/stw1695 [Cited on page 5.]

Kaspi, S., Smith, P. S., Netzer, H., et al. 2000, Astrophys. J., 533, 631, doi: 10.1086/308704 [Cited on page 7.]

Kauffmann, G., & Haehnelt, M. 2000, Mon. Not. R. Astron. Soc., 311, 576, doi: 10.1046/j.1365-8711.2000.03077.x [Cited on page 37.]

Kayal, A., Singh, V., Chandra, C. H. I., Wadadekar, Y., & Dutta, S. 2022, Journal of Astrophysics and Astronomy, 43, 84, doi: 10.1007/s12036-022-09873-0 [Cited 2 times on pages 91 and 92.]

Kirkpatrick, A., Hall, K., Nyland, K., Lacy, M., & Prandoni, I. 2018. https://arxiv.org/abs/1809.01199 [Cited on page 82.]

Klein, M. J., & Stelzried, C. T. 1976, AJ, 81, 1078, doi: 10.1086/111988 [Cited on page 21.]

Knoll, G. F. 2000, Book, 816 [Cited on page 28.]

Kormendy, J., & Gebhardt, K. 2001, in American Institute of Physics Conference Series, Vol. 586, 20th Texas Symp. Relativ. Astrophys., ed. J. C. Wheeler & H. Martel, 363–381 [Cited on page 2.]

Kormendy, J., & Ho, L. C. 2013, Annu. Rev. Astron. Astrophys., 51, 511, doi: 10.1146/annurev-astro-082708-101811 [Cited 2 times on pages 2 and 129.]

Kormendy, J., & Richstone, D. 1995, Annu. Rev. Astron. Astrophys., 33, 581, doi: 10.1146/annurev.aa.33.090195.003053 [Cited on page 2.]

Koss, M., Trakhtenbrot, B., Ricci, C., et al. 2017, Astrophys. J., 850, 74, doi: 10.3847/1538-4357/aa8ec9 [Cited 3 times on pages 2, 129, and 177.]

Koss, M. J., Assef, R., Baloković, M., et al. 2016, ApJ, 825, 85, doi: 10.3847/0004-637X/825/2/85 [Cited on page 90.]

Koyama, K., Tsunemi, H., Dotani, T., et al. 2007, Publ. Astron. Soc. Japan, 59, doi: 10.1093/pasj/59.sp1.s23 [Cited on page 137.]

Krolik, J. H. 1999, Active galactic nuclei : from the central black hole to the galactic environment, princeton edn. (Princeton University Press), 632 [Cited 2 times on pages 1 and 6.]

Krolik, J. H., & Begelman, M. C. 1988, Astrophys. J., 329, 702, doi: 10.1086/166414 [Cited on page 171.]

Kumar, A., Ghosh, S. K., Hutchings, J., et al. 2012, Sp. Telesc. Instrum. 2012 Ultrav. to Gamma Ray, 8443, 84431N, doi: 10.1117/12.924507 [Cited on page 35.]

Lacy, M., & Sajina, A. 2020, Nat. Astron., 4, 352, doi: 10.1038/s41550-020-1071-x [Cited on page 37.]

Lacy, M., Storrie-Lombardi, L. J., Sajina, A., et al. 2004, Astrophys. J. Suppl. Ser., 154, 166, doi: 10.1086/422816 [Cited 2 times on pages 70 and 71.]

Lacy, M., Baum, S. A., Chandler, C. J., et al. 2020, Publ. Astron. Soc. Pacific, 132, doi: 10.1088/1538-3873/ab63eb [Cited on page 43.]

Lansbury, G. B., Banerji, M., Fabian, A. C., & Temple, M. J. 2020, Mon. Not. R. Astron. Soc., 495, 2652, doi: 10.1093/mnras/staa1220 [Cited 5 times on pages 73, 104, 116, 117, and 120.]

Lanzuisi, G., Piconcelli, E., Fiore, F., et al. 2009, A&A, 498, 67, doi: 10.1051/0004-6361/200811282 [Cited 2 times on pages 89 and 92.]

Lanzuisi, G., Ranalli, P., Georgantopoulos, I., et al. 2015, A&A, 573, A137, doi: 10.1051/0004-6361/201424924 [Cited on page 90.]

Le Fèvre, O., Cassata, P., Cucciati, O., et al. 2013, Astron. Astrophys., 559, A14, doi: 10.1051/0004-6361/201322179 [Cited 2 times on pages 52 and 93.]

Leftley, J. H., Tristram, K. R. W., Hönig, S. F., et al. 2018, Astrophys. J., 862, 17, doi: 10.3847/1538-4357/aac8e5 [Cited on page 126.]

Longair, M. S. 2011, 880 [Cited on page 3.]

Lonsdale, C. J., Smith, H. E., Rowan-Robinson, M., et al. 2003, Publ. Astron. Soc. Pacific, 115, 897, doi: 10.1086/376850 [Cited 2 times on pages 43 and 91.]

Lonsdale, C. J., Lacy, M., Kimball, A. E., et al. 2015, Astrophys. J., 813, 45, doi: 10.1088/0004-637X/813/1/45 [Cited on page 40.]

Lyden-Bell, D. 1969, Nature, 223, 690, doi: 10.1038/223690a0 [Cited 3 times on pages 1, 2, and 3.]

Madsen, K. K., Beardmore, A. P., Forster, K., et al. 2016, Astron. J., 153, 2, doi: 10.3847/1538-3881/153/1/2 [Cited on page 155.]

Magorrian, J., Tremaine, S., Richstone, D., et al. 1998, Astron. J., 115, 2285, doi: 10.1086/300353 [Cited on page 2.]

Malkan, M. A. 1983, Astrophys. J., 268, 582, doi: 10.1086/160981 [Cited on page 3.]

Maraschi, L., Ghisellini, G., & Celotti, A. 1992, Astrophys. J., 397, L5, doi: 10.1086/186531 [Cited on page 10.]

Marchesi, S., Ajello, M., Zhao, X., et al. 2019, Astrophys. J., 872, 8, doi: 10.3847/1538-4357/aafbeb [Cited on page 128.]

Marchesi, S., Zhao, X., Torres-Albà, N., et al. 2022, Astrophys. J., 935, 114, doi: 10.3847/1538-4357/ac80be [Cited 2 times on pages 128 and 178.]

Marconi, A., Risaliti, G., Gilli, R., et al. 2004, MNRAS, 351, 169, doi: 10.1111/j.1365-2966.2004.07765.x [Cited on page 88.]

Martínez-Sansigre, A., Rawlings, S., Bonfield, D. G., et al. 2007, MNRAS, 379, L6, doi: 10.1111/j.1745-3933.2007.00323.x [Cited on page 89.]

Mason, K. O., Breeveld, A., Much, R., et al. 2001, A&A, 365, L36, doi: 10.1051/0004-6361:20000044 [Cited on page 34.]

Massaro, F., Bianchi, S., Matt, G., D'Onofrio, E., & Nicastro, F. 2006, Astron. Astrophys., 455, 153, doi: 10.1051/0004-6361:20054772 [Cited on page 156.]

Mateos, S., Carrera, F. J., Barcons, X., et al. 2017, Astrophys. J., 841, L18, doi: 10.3847/2041-8213/aa7268 [Cited on page 10.]

Matt, G., Matt, & G. 1997, MmSAI, 68, 127, doi: 10.48550/ARXIV.ASTRO-PH/9612002 [Cited on page 10.]

Matt, G., Perola, G. C., & Piro, L. 1991, Astron. Astrophys. Vol. 247, p. 25, 247, 25 [Cited on page 5.]

Matt, G., Fiore, F., Perola, G. C., et al. 1996, Mon. Not. R. Astron. Soc., 281, L69, doi: 10.1093/mnras/281.4.L69 [Cited on page 130.]

Mauduit, J.-C., Lacy, M., Farrah, D., et al. 2012, Publ. Astron. Soc. Pacific, 124, 714, doi: 10.1086/666945 [Cited on page 91.]

McConnell, N. J., & Ma, C. P. 2013, Astrophys. J., 764, doi: 10.1088/0004-637X/764/2/184 [Cited on page 2.]

McHardy, I. M., Gunn, K. F., Uttley, P., & Goad, M. R. 2005, Mon. Not. R. Astron. Soc., 359, 1469, doi: 10.1111/j.1365-2966.2005.08992.x [Cited on page 177.]

McLure, R. J., Pearce, H. J., Dunlop, J. S., et al. 2013, MNRAS, 428, 1088, doi: 10.1093/mnras/sts092 [Cited on page 93.]

Melbourne, J., Soifer, B. T., Desai, V., et al. 2012, Astron. J., 143, 125, doi: 10.1088/0004-6256/143/5/125 [Cited 3 times on pages 38, 39, and 88.]

Menzel, M. L., Merloni, A., Georgakakis, A., et al. 2016, MNRAS, 457, 110, doi: 10.1093/mnras/stv2749 [Cited on page 93.]

Merritt, D., & Ferrarese, L. 2001, Mon. Not. R. Astron. Soc., 320, doi: 10.1046/j.1365-8711.2001.04165.x [Cited on page 2.]

Mingo, B., Hardcastle, M. J., Croston, J. H., et al. 2012, Astrophys. J., 758, 95, doi: 10.1088/0004-637X/758/2/95 [Cited on page 149.]

Miniutti, G., & Fabian, A. C. 2004, Mon. Not. R. Astron. Soc., 349, 1435, doi: 10.1111/j.1365-2966.2004.07611.x [Cited on page 5.]

Mitsuda, K., Bautz, M., Inoue, H., et al. 2007, Publ. Astron. Soc. Japan, 59, doi: 10.1093/pasj/59.sp1.s1 [Cited on page 137.]

Mohan, N., & Rafferty, D. 2015, PyBDSM: Python Blob Detection and Source Finder. https://ui.adsabs.harvard.edu/abs/2015ascl.soft02007M [Cited on page 42.]

Momcheva, I. G., Brammer, G. B., van Dokkum, P. G., et al. 2016, ApJS, 225, 27, doi: 10.3847/0067-0049/225/2/27 [Cited on page 93.]

Mondal, S., Róańska, A., Bagińska, P., Markowitz, A., & De Marco, B. 2021, Astron. Astrophys., 651, A54, doi: 10.1051/0004-6361/202140459 [Cited 2 times on pages 131 and 147.]

Moorwood, A. F., Lutz, D., Oliva, E., et al. 1996, Astron. Astrophys., 315, L109 [Cited on page 129.]

Moran, E. 2007, in Astronomical Society of the Pacific Conference Series, Vol. 373, Cent. Engine Act. Galact. Nucl., ed. L. Ho & J. W. Wang, 425 [Cited on page 125.]

Morgan, C. W., Hainline, L. J., Chen, B., et al. 2012, Astrophys. J., 756, 52, doi: 10.1088/0004-637X/756/1/52 [Cited on page 126.]

Morić, I., Smolčić, V., Kimball, A., et al. 2010, ApJ, 724, 779, doi: 10.1088/0004-637X/724/1/779 [Cited on page 39.]

Murphy, K. D., & Yaqoob, T. 2009, Mon. Not. R. Astron. Soc., 397, 1549, doi: 10.1111/j.1365-2966.2009.15025.x [Cited on page 154.]

Narayan, R., & Yi, I. 1994, Astrophys. J., 428, L13, doi: 10.1086/187381 [Cited on page 3.]

Narayanan, D., Dey, A., Hayward, C. C., et al. 2010, MNRAS, 407, 1701, doi: 10.1111/j.1365-2966.2010.16997.x [Cited on page 88.]

Nenkova, M., Sirocky, M. M., Ivezić, Ž., & Elitzur, M. 2008, Astrophys. J., 685, 147, doi: 10.1086/590482 [Cited 3 times on pages 8, 126, and 165.]

Netzer, H. 2013, The Physics and Evolution of Active Galactic Nuclei (Cambridge University Press), 1–361, doi: 10.1017/CBO9781139109291. https://www.cambridge.org/core/books/physics-and-evolution-of-active-galactic-nuclei/2A36453A413D67311D59A8A5CEA7117C [Cited 2 times on pages 3 and 5.]

—. 2015, Annu. Rev. Astron. Astrophys., 53, 365, doi: 10.1146/annurev-astro-082214-122302 [Cited on page 126.]

Ni, Q., Brandt, W. N., Chen, C.-T., et al. 2021, ApJS, 256, 21, doi: 10.3847/1538-4365/ac0dc6 [Cited on page 94.]

Noboriguchi, A., Nagao, T., Toba, Y., et al. 2019, Astrophys. J., 876, 132, doi: 10.3847/1538-4357/ab1754 [Cited on page 38.]

Noguchi, K., Terashima, Y., Ishino, Y., et al. 2010, Astrophys. J., 711, 144, doi: 10.1088/0004-637X/711/1/144 [Cited on page 10.]

Norris, R. P., Marvil, J., Collier, J. D., et al. 2021, Publ. Astron. Soc. Aust., 38, e046, doi: 10.1017/pasa.2021.42 [Cited on page 81.]

Nyland, K., Lacy, M., Brandt, W. N., et al. 2023, Research Notes of the American Astronomical Society, 7, 33, doi: 10.3847/2515-5172/acbc72 [Cited 3 times on pages 93, 94, and 96.]

Nyland, K., Lacy, M., Sajina, A., et al. 2017, ApJS, 230, 9, doi: 10.3847/1538-4365/aa6fed [Cited on page 94.]

O'Dea, C. P., & Saikia, D. J. 2021, Astron. Astrophys. Rev., 29, 3, doi: 10.1007/s00159-021-00131-w [Cited on page 64.]

Oke, J. B., & Gunn, J. E. 1983, Astrophys. J., 266, 713, doi: 10.1086/160817 [Cited on page 45.]

Oliver, S. J., Bock, J., Altieri, B., et al. 2012, MNRAS, 424, 1614, doi: 10.1111/j.1365-2966.2012.20912.x [Cited on page 91.]

Osterbrock, D. E. 1978, Phys. Scr., 17, 285, doi: 10.1088/0031-8949/17/3/024 [Cited on page 6.]

Osterbrock, D. E., & Ferland, G. J. 2006, Astrophysics of gaseous nebulae and active galactic nuclei. (University Science Books), 461 [Cited on page 7.]

Pacaud, F., Pierre, M., Refregier, A., et al. 2006, Mon. Not. R. Astron. Soc., 372, 578, doi: 10.1111/j.1365-2966.2006.10881.x [Cited on page 95.]

Packham, C., Radomski, J. T., Roche, P. F., et al. 2005, Astrophys. J., 618, L17, doi: 10.1086/427691 [Cited on page 8.]

Padovani, P., Alexander, D. M., Assef, R. J., et al. 2017, Astron. Astrophys. Rev., 25, doi: 10.1007/s00159-017-0102-9 [Cited on page 9.]

Patil, P., Nyland, K., Whittle, M., et al. 2020, Astrophys. J., 896, 18, doi: 10.3847/1538-4357/ab9011 [Cited 4 times on pages 40, 63, 69, and 85.]

Patra, N., Bray, J. D., Roberts, P., & Ekers, R. D. 2017, Experimental Astronomy, 43, 119, doi: 10.1007/s10686-017-9523-8 [Cited on page 22.]

Perley, R. A., Schwab, F. R., Bridle, A. H., & Ekers, R. D. 1986, Synthesis imaging. Course notes from an NRAO summer school, held at Socorro, New Mexico, USA, 5 - 9 August 1985. [Cited on page 23.]

Peterson, B. M. 1997, An Introd. to Act. Galact. Nucl., doi: 10.1017/cbo9781139170901 [Cited on page 7.]

—. 2006, Lect. Notes Phys., 693, 77, doi: 10.1007/3-540-34621-X_3 [Cited on page 6.]

—. 2008, New Astron. Rev., 52, 240, doi: 10.1016/j.newar.2008.06.005 [Cited on page 7.]

Peterson, B. M., Denney, K. D., De Rosa, G., et al. 2013, Astrophys. J., 779, 109, doi: 10.1088/0004-637X/779/2/109 [Cited on page 7.]

Pierre, M., Pacaud, F., Adami, C., et al. 2016, A&A, 592, doi: 10.1051/0004-6361/201526766 [Cited on page 95.]

Pope, A., Bussmann, R. S., Dey, A., et al. 2008, ApJ, 689, 127, doi: 10.1086/592739 [Cited on page 89.]

Pringle, J. E. 1981, Annu. Rev. Astron. Astrophys., 19, 137, doi: 10.1146/annurev.aa.19.090181.001033 [Cited on page 3.]

Pringle, J. E., Rees, M. J., Pacholczyk, A. G., et al. 1973, A&A, 29, 179 [Cited 2 times on pages 1 and 2.]

Pringle, J. E., Rees, M. J., Pringle, J. E., & Rees, M. J. 1972, A&A, 21, 1 [Cited on page 2.]

Puccetti, S., Fiore, F., Risaliti, G., et al. 2007, Mon. Not. R. Astron. Soc., 377, 607, doi: 10.1111/j.1365-2966.2007.11634.x [Cited on page 126.]

Puccetti, S., Comastri, A., Fiore, F., et al. 2014, Astrophys. J., 793, 26, doi: 10.1088/0004-637X/793/1/26 [Cited on page 128.]

Qiu, Y., Soria, R., Wang, S., et al. 2019, Astrophys. J., 877, 57, doi: 10.3847/1538-4357/ab16e7 [Cited 2 times on pages 142 and 144.]

Quirola-Vásquez, J., Bauer, F. E., Dwarkadas, V. V., et al. 2019, Mon. Not. R. Astron. Soc., 490, 4536, doi: 10.1093/mnras/stz2858 [Cited 2 times on pages 144 and 147.]

Ramos Almeida, C., & Ricci, C. 2017, Nat. Astron., 1, 679, doi: 10.1038/s41550-017-0232-z [Cited 2 times on pages 8 and 125.]

Rees, M. J. 1971, Nature, 229, 312, doi: 10.1038/229312a0 [Cited on page 9.]

—. 1984, Annu. Rev. Astron. Astrophys., 22, 471, doi: 10.1146/annurev.aa.22.090184.002351 [Cited 2 times on pages 1 and 2.]

Reis, R. C., & Miller, J. M. 2013, Astrophys. J. Lett., 769, doi: 10.1088/2041-8205/769/1/L7 [Cited on page 5.]

Ricci, C., Ueda, Y., Koss, M. J., et al. 2015, Astrophys. J. Lett., 815, doi: 10.1088/2041-8205/815/1/L13 [Cited on page 72.]

Ricci, C., Bauer, F. E., Arevalo, P., et al. 2016, Astrophys. J., 820, 5, doi: 10.3847/0004-637x/820/1/5 [Cited on page 175.]

Ricci, C., Bauer, F. E., Treister, E., et al. 2017a, Mon. Not. R. Astron. Soc., 468, 1273, doi: 10.1093/mnras/stx173 [Cited on page 8.]

Ricci, C., Trakhtenbrot, B., Koss, M. J., et al. 2017b, Astrophys. J. Suppl. Ser., 233, 17, doi: 10.3847/1538-4365/aa96ad [Cited 3 times on pages 87, 89, and 126.]

—. 2017c, Nature, 549, 488, doi: 10.1038/nature23906 [Cited on page 172.]

Ricci, C., Privon, G. C., Pfeifle, R. W., et al. 2021, Mon. Not. R. Astron. Soc., 506, 5935, doi: 10.1093/mnras/stab2052 [Cited on page 38.]

Richstone, D., Ajhar, E. A., Bender, R., et al. 1998, Nature, Vol. 385, Issue 6701 (Supplement), p. A14, 1 Oct. 1998, 385, A14, doi: 10.48550/ARXIV.ASTRO-PH/9810378 [Cited on page 2.]

Riguccini, L., Le Floc'h, E., Mullaney, J. R., et al. 2015, Mon. Not. R. Astron. Soc., 452, 470, doi: 10.1093/mnras/stv1297 [Cited on page 39.]

Riguccini, L. A., Treister, E., Menéndez-Delmestre, K., et al. 2019, Astron. J., 157, 233, doi: 10.3847/1538-3881/ab16cd [Cited on page 73.]

Risaliti, G., Elvis, M., Bianchi, S., & Matt, G. 2010, Mon. Not. R. Astron. Soc. Lett., 406, L20, doi: 10.1111/j.1745-3933.2010.00873.x [Cited on page 175.]

Risaliti, G., Elvis, M., Fabbiano, G., Baldi, A., & Zezas, A. 2005, Astrophys. J., 623, L93, doi: 10.1086/430252 [Cited 2 times on pages 126 and 176.]

Risaliti, G., Elvis, M., & Nicastro, F. 2002, Astrophys. J., 571, 234, doi: 10.1086/324146 [Cited on page 176.]

Rivers, E., Baloković, M., Arévalo, P., et al. 2015, Astrophys. J., 815, 55, doi: 10.1088/0004-637X/815/1/55 [Cited on page 126.]

Rowan-Robinson, M. 2000, Mon. Not. R. Astron. Soc., 316, 885, doi: 10.1046/j.1365-8711.2000.03588.x [Cited on page 38.]

Ryle, M., & Hewish, A. 1960, Mon. Not. R. Astron. Soc., 120, 220, doi: 10.1093/mnras/120.3.220 [Cited on page 19.]

Saha, T., Markowitz, A. G., & Buchner, J. 2022, Mon. Not. R. Astron. Soc., 509, 5485, doi: 10.1093/mnras/stab3250 [Cited 2 times on pages 126 and 153.]

Sambruna, R. M., Netzer, H., Kaspi, S., et al. 2001, Astrophys. J., 546, L13, doi: 10.1086/318068 [Cited on page 156.]

Sanders, D. B., & Mirabel, I. F. 1996, ARA&A, 34, 749, doi: 10.1146/annurev.astro.34.1.749 [Cited on page 88.]

Schmitt, H. R., Donley, J. L., Antonucci, R. R., Hutchings, J. B., & Kinney, A. L. 2003, Astrophys. Journal, Suppl. Ser., 148, 327, doi: 10.1086/377440 [Cited on page 125.]

Schuldt, S., Suyu, S. H., Cañameras, R., et al. 2021, Astron. Astrophys., 651, doi: 10.1051/0004-6361/202039945 [Cited 2 times on pages 52 and 93.]

Shakura, N. I., & Sunyaev, R. A. 1973, Symp. - Int. Astron. Union, 55, 155, doi: 10.1017/s007418090010035x [Cited on page 2.]

Shanks, T., Ansarinejad, B., Bielby, R. M., et al. 2021, Mon. Not. R. Astron. Soc., 505, 1509, doi: 10.1093/mnras/stab1226 [Cited on page 38.]

Shapiro, S. L., Teukolsky, S. A., & Lightman, A. P. 1983, Phys. Today, 36, 89, doi: 10.1063/1.2915325 [Cited on page 3.]

Shields, G. A. 1978, Nature, 272, 706, doi: 10.1038/272706a0 [Cited on page 3.]

Singh, K., Stewart, G., Westergaard, N., et al. 2017, J. Astrophys. Astron., 38, 29, doi: 10.1007/s12036-017-9448-7 [Cited 3 times on pages 29, 35, and 135.]

Singh, K. P., Tandon, S. N., Agrawal, P. C., et al. 2014a, in Sp. Telesc. Instrum. 2014 Ultrav. to Gamma Ray, Vol. 9144, International Society for Optics and Photonics, 91441S [Cited on page 35.]

Singh, K. P., Stewart, G. C., Chandra, S., et al. 2016, Sp. Telesc. Instrum. 2016 Ultrav. to Gamma Ray, 9905, 99051E, doi: 10.1117/12.2235309 [Cited on page 35.]

Singh, V., & Chand, H. 2018, Mon. Not. R. Astron. Soc., 480, 1796, doi: 10.1093/mnras/sty1818 [Cited on page 61.]

Singh, V., Ishwara-Chandra, C. H., Wadadekar, Y., Beelen, A., & Kharb, P. 2015, Mon. Not. R. Astron. Soc., 446, 599, doi: 10.1093/mnras/stu2124 [Cited 2 times on pages 45 and 54.]

Singh, V., Shastri, P., & Risaliti, G. 2011, Astron. Astrophys., 532, A84, doi: 10.1051/0004-6361/201016387 [Cited 4 times on pages 8, 87, 103, and 126.]

Singh, V., Beelen, A., Wadadekar, Y., et al. 2014b, Astron. Astrophys., 569, A52, doi: 10.1051/0004-6361/201423644 [Cited on page 91.]

Skelton, R. E., Whitaker, K. E., Momcheva, I. G., et al. 2014, ApJS, 214, 24, doi: 10.1088/0067-0049/214/2/24 [Cited on page 93.]

Stalevski, M., Tristram, K. R. W., & Asmus, D. 2019, MNRAS, 484, 3334, doi: 10.1093/mnras/stz220 [Cited on page 172.]

Stein, W. A., & Weedman, D. W. 1976, Astrophys. J., 205, 44, doi: 10.1086/154248 [Cited on page 6.]

Stern, D., Eisenhardt, P., Gorjian, V., et al. 2005, Astrophys. J., 631, 163, doi: 10.1086/432523 [Cited on page 70.]

Stern, D., Lansbury, G. B., Assef, R. J., et al. 2014, ApJ, 794, 102, doi: 10.1088/0004-637X/794/2/102 [Cited on page 89.]

Strüder, L., Briel, U., Dennerl, K., et al. 2001, Astron. Astrophys., 365, L18, doi: 10.1051/0004-6361:20000066 [Cited 2 times on pages 29 and 34.]

Subramaniam, A., Tandon, S. N., Hutchings, J., et al. 2016, Sp. Telesc. Instrum. 2016 Ultrav. to Gamma Ray, 9905, 99051F, doi: 10.1117/12.2235271 [Cited on page 35.]

Suleiman, N., Noboriguchi, A., Toba, Y., et al. 2022, PASJ, 74, 1157, doi: 10.1093/pasj/psac061 [Cited on page 88.]

Swain, S., Dewangan, G. C., Shalima, P., Tripathi, P., & Latha, K. V. P. 2023, MNRAS, doi: 10.1093/mnras/stad337 [Cited on page 135.]

Swarup, G. 1991, Giant Metrewave Radio Telescope (GMRT), doi: 10.1017/s0252921100013671. https://ui.adsabs.harvard.edu/abs/1991ASPC...19..376S/abstract [Cited on page 25.]

Swarup, G., Sinha, R. P., & Hilldrup, K. 1984, Mon. Not. R. Astron. Soc., 208, 813, doi: 10.1093/mnras/208.4.813 [Cited on page 9.]

Tadhunter, C., & Tsvetanov, Z. 1989, Nature, 341, 422, doi: 10.1038/341422a0 [Cited on page 7.]

Tanaka, M., Coupon, J., Hsieh, B. C., et al. 2018, Publ. Astron. Soc. Japan, 70, S9, doi: 10.1093/pasj/psx077 [Cited 2 times on pages 52 and 93.]

Tang, B., Shang, Z., Gu, Q., Brotherton, M. S., & Runnoe, J. C. 2012, Astrophys. Journal, Suppl. Ser., 201, 38, doi: 10.1088/0067-0049/201/2/38 [Cited on page 6.]

Teng, S. H., & Veilleux, S. 2010, ApJ, 725, 1848, doi: 10.1088/0004-637X/725/2/1848 [Cited on page 89.]

Thompson, A. R., Clark, B. G., Wade, C. M., & Napier, P. J. 1980, Astrophys. J. Suppl. Ser., 44, 151, doi: 10.1086/190688 [Cited on page 26.]

Thompson, A. R., Moran, J. M., & Swenson, George W., J. 2017, Interferometry and Synthesis in Radio Astronomy, 3rd Edition, doi: 10.1007/978-3-319-44431-4 [Cited on page 18.]

Thompson, T. A., Fabian, A. C., Quataert, E., & Murray, N. 2015, MNRAS, 449, 147, doi: 10.1093/mnras/stv246 [Cited on page 118.]

Toba, Y., Nagao, T., Strauss, M. A., et al. 2015, Publ. Astron. Soc. Japan, 67, doi: 10.1093/pasj/psv057 [Cited 2 times on pages 45 and 92.]

Toba, Y., Yamada, S., Ueda, Y., et al. 2020, ApJ, 888, 8, doi: 10.3847/1538-4357/ab5718 [Cited on page 89.]

Torres-Albà, N., Marchesi, S., Zhao, X., et al. 2021, ApJ, 922, 252, doi: 10.3847/1538-4357/ac1c73 [Cited on page 88.]

Torricelli-Ciamponi, G., Pietrini, P., Risaliti, G., & Salvati, M. 2014, Mon. Not. R. Astron. Soc., 442, 2116, doi: 10.1093/mnras/stu969 [Cited on page 126.]

Tozzi, P., Gilli, R., Mainieri, V., et al. 2006, A&A, 451, 457, doi: 10.1051/0004-6361:20042592 [Cited on page 103.]

Treister, E., Urry, C. M., & Virani, S. 2009a, ApJ, 696, 110, doi: 10.1088/0004-637X/696/1/110 [Cited on page 88.]

Treister, E., Cardamone, C. N., Schawinski, K., et al. 2009b, ApJ, 706, 535, doi: 10.1088/0004-637X/706/1/535 [Cited on page 89.]

Tristram, K. R., Burtscher, L., Jaffe, W., et al. 2014, Astron. Astrophys., 563, A82, doi: 10.1051/0004-6361/201322698 [Cited 6 times on pages 126, 127, 130, 169, 172, and 177.]

Tristram, K. R., Meisenheimer, K., Jaffe, W., et al. 2007, Astron. Astrophys., 474, 837, doi: 10.1051/0004-6361:20078369 [Cited on page 130.]

Truebenbach, A. E., & Darling, J. 2017, Mon. Not. R. Astron. Soc., 468, 196, doi: 10.1093/mnras/stx456 [Cited on page 38.]

Tsai, C. W., Eisenhardt, P. R., Wu, J., et al. 2015, Astrophys. J., 805, doi: 10.1088/0004-637X/805/2/90 [Cited 2 times on pages 39 and 89.]

Turner, M. J., Abbey, A., Arnaud, M., et al. 2001, Astron. Astrophys., 365, L27, doi: 10.1051/0004-6361:20000087 [Cited on page 29.]

Ueda, Y., Watson, M. G., Stewart, I. M., et al. 2008, Astrophys. J. Suppl. Ser., 179, 124, doi: 10.1086/591083 [Cited on page 95.]

Uematsu, R., Ueda, Y., Tanimoto, A., et al. 2021, Astrophys. J., 913, 17, doi: 10.3847/1538-4357/abf0a2 [Cited on page 172.]

Urry, C. M., & Padovani, P. 1995, Publ. Astron. Soc. Pacific, 107, 803, doi: 10.1086/133630 [Cited 4 times on pages 8, 10, 87, and 125.]

Ursini, F., Marinucci, A., Matt, G., et al. 2023, MNRAS, 519, 50, doi: 10.1093/mnras/stac3189 [Cited on page 171.]

Vito, F., Brandt, W. N., Stern, D., et al. 2018, MNRAS, 474, 4528, doi: 10.1093/mnras/stx3120 [Cited 4 times on pages 12, 89, 121, and 122.]

Walton, D. J., Fuerst, F., Harrison, F., et al. 2013, Astrophys. J., 779, 148, doi: 10.1088/0004-637X/779/2/148 [Cited 2 times on pages 141 and 147.]

Wernecke, S. J. 1977, Radio Sci., 12, 831, doi: 10.1029/RS012i005p00831 [Cited on page 24.]

White, R. L., Helfand, D. J., Becker, R. H., Glikman, E., & de Vries, W. 2007, Astrophys. J., 654, 99, doi: 10.1086/507700 [Cited on page 76.]

Wiita, P. J. 1978, Astrophys. J., 221, 41, doi: 10.1086/156003 [Cited on page 9.]

Wilkins, D. R., & Gallo, L. C. 2015, Mon. Not. R. Astron. Soc., 448, 703, doi: 10.1093/mnras/stu2524 [Cited on page 5.]

Willott, C. J., Rawlings, S., Jarvis, M. J., & Blundell, K. M. 2003, Mon. Not. R. Astron. Soc., 339, 173, doi: 10.1046/j.1365-8711.2003.06172.x [Cited on page 67.]

Winn, J. N., Patnaik, A. R., & Wrobel, J. M. 2003, ApJS, 145, 83, doi: 10.1086/345541 [Cited on page 22.]

Wootten, A., & Thompson, A. 2009, Proc. IEEE, 97, 1463, doi: 10.1109/JPROC.2009.2020572 [Cited on page 82.]

Wu, J., Tsai, C. W., Sayers, J., et al. 2012, Astrophys. J., 756, 96, doi: 10.1088/0004-637X/756/1/96 [Cited on page 40.]

Wu, J., Jun, H. D., Assef, R. J., et al. 2018, ApJ, 852, 96, doi: 10.3847/1538-4357/aa9ff3 [Cited on page 121.]

Yadav, J. S., Agrawal, P. C., Antia, H. M., et al. 2016, Sp. Telesc. Instrum. 2016 Ultrav. to Gamma Ray, 9905, 99051D, doi: 10.1117/12.2231857 [Cited on page 35.]

Yamaki, H., Kameno, S., Beppu, H., Mizuno, I., & Imai, H. 2012, PASJ, 64, 118, doi: 10.1093/pasj/64.5.118 [Cited on page 22.]

Yang, Y., Wilson, A. S., Matt, G., Terashima, Y., & Greenhill, L. J. 2009, Astrophys. J., 691, 131, doi: 10.1088/0004-637X/691/1/131 [Cited on page 130.]

Yutani, N., Toba, Y., Baba, S., & Wada, K. 2022, arXiv e-prints, arXiv:2205.00567. https://arxiv.org/abs/2205.00567 [Cited 2 times on pages 39 and 88.]

Zaino, A., Bianchi, S., Marinucci, A., et al. 2020, Mon. Not. R. Astron. Soc., 492, 3872, doi: 10.1093/mnras/staa107 [Cited 3 times on pages 128, 176, and 177.]

Zakamska, N. L., Lampayan, K., Petric, A., et al. 2016, MNRAS, 455, 4191, doi: 10.1093/mnras/stv2571 [Cited on page 39.]

Zappacosta, L., Piconcelli, E., Duras, F., et al. 2018, A&A, 618, A28, doi: 10.1051/0004-6361/201732557 [Cited on page 89.]

Zhao, X., Marchesi, S., Ajello, M., et al. 2021, Astron. Astrophys., 650, A57, doi: 10.1051/0004-6361/202140297 [Cited on page 87.]

Zou, F., Brandt, W. N., Vito, F., et al. 2020, MNRAS, 499, 1823, doi: 10.1093/mnras/staa2930 [Cited 7 times on pages 89, 103, 104, 116, 117, 118, and 120.]

Zou, F., Brandt, W. N., Lacy, M., et al. 2021, Research Notes of the American Astronomical Society, 5, 31, doi: 10.3847/2515-5172/abe769 [Cited on page 94.]

Zou, F., Brandt, W. N., Chen, C.-T., et al. 2022, ApJS, 262, 15, doi: 10.3847/1538-4365/ac7bdf [Cited on page 94.]